UDK 669+666+678+53

ISSN 1580-2949
MTAEC9, 48(3)313–450(2014)

MATER. TEHNOL.	LETNIK VOLUME 48	ŠTEV. NO. 3	STR. P. 313–450	LJUBLJANA SLOVENIJA	MAY–JUNE 2014

VSEBINA – CONTENTS

IZVIRNI ZNANSTVENI ČLANKI – ORIGINAL SCIENTIFIC ARTICLES

STROKOVNI ČLANKI – PROFESSIONAL ARTICLES

UDK 678.7:66.017
Original scientific article/Izvirni znanstveni članek

ISSN 1580-2949
MTAEC9, 48(3)315(2014)

EFFECT OF THE QUENCHING TEMPERATURE ON THE IZOD IMPACT STRENGTH OF POLYCARBONATE: EXPERIMENTAL DATA AND EMPIRICAL MODELING

VPLIV TEMPERATURE KALJENJA NA IZOD UDARNO TRDNOST POLIKARBONATA: EKSPERIMENTALNI PODATKI IN EMPIRIČNO MODELIRANJE

Farid Rouabah[1], Abdallah Bouguettoucha[2], Laurent Ibos[3], Nacerddine Haddaoui[1]

[1]Laboratoire de Physico-Chimie des Hauts Polymères, Université Ferhat Abbes, 19000 Sétif, Algérie
[2]Laboratoire de Génie des Procédés Chimique (LGPC), Université Ferhat Abbes, 19000 Sétif, Algérie
[3]Université Paris-Est, CERTES, 61 Avenue du Général De Gaulle, 94010 Créteil, France
f_rouabah2002@yahoo.fr

Prejem rokopisa – received: 2012-07-04; sprejem za objavo – accepted for publication: 2013-08-27

In this study, the development of a mathematical model of the effects of free quenching on the Izod impact strength of polycarbonate (PC) has been investigated. Three different thermal treatments were used: the first quenching from the melt state to different temperatures, the second quenching from T_g + 15 °C and, finally, the annealing. The results have shown that an improvement in the impact strength can be obtained after the second quenching at 40 °C. The impact tests experimentally performed on the molding prototypes yield useful data for a particular structural and impact-loading case. But, it is generally not practical, in terms of time and cost, to experimentally characterize the effects of a wide range of design variables. A successful numerical model for the Izod impact strength of polymers can provide convenient and useful guidelines on product design and, therefore, decrease the disadvantages arising from purely experimental trial and error. It is expensive to prepare the samples for the tests. Therefore, it is necessary to develop a mathematical model that will predict the fracture toughness of polycarbonate as a function of the quenching temperature. Mathematical models for the mechanical properties like the tensile strength, Young's modulus and Izod impact strength as functions of the quenching temperature are not available. There is no sign that they can be built up from a simple theory; a polynomial interpolation was, therefore, used to generate a fracture-toughness model using the data obtained from the experiments. The shifted model represents the Izod impact of the samples as a function of the first- and second-quenching temperatures.

Keywords: Izod impact strength, polycarbonate, quenching temperature, mathematical modeling

Ta študija preučuje razvoj matematičnega modela vpliva prostega kaljenja na Izod udarno trdnost polikarbonata (PC). Uporabljeni so bili trije različni načini toplotne obdelave: najprej prosto kaljenje iz staljenega stanja na različne temperature, nato drugo kaljenje iz T_g + 15 °C in nato končno žarjenje. Rezultati so pokazali, da je mogoče doseči izboljšanje Izod udarne trdnosti po drugem kaljenju pri 40 °C. Eksperimentalno izvedeni preizkusi na modeliranih prototipih so dali uporabne podatke za posebne primere strukturno in udarno obremenjenih primerov. Vendar pa na splošno ni praktično – s stališča časa in stroškov – eksperimentalno določanje vplivov različnih oblik. Uspešen numerični model za Izod udarno trdnost polimerov lahko zagotovi zanesljive in uporabne napotke za načrtovanje proizvodov in s tem zmanjša pomanjkljivosti, ki izvirajo iz eksperimentalnih preizkusov in napak. Priprava vzorcev za preizkuse je draga. Zato je treba razviti matematični model, ki bo napovedoval lomno žilavost polikarbonata v odvisnosti od temperature kaljenja. Na razpolago ni modelov za mehanske lastnosti, kot so natezna trdnost, Youngov modul in Izod udarna trdnost, v odvisnosti od temperature kaljenja. Ni znamenj, da se lahko postavijo z enostavno teorijo: zato je bila z uporabo eksperimentalnih podatkov uporabljena interpolacija polinomov za izdelavo modela lomne žilavosti. Predstavljeni model predstavlja Izod udarno trdnost v odvisnosti od prve in druge temperature kaljenja.

Ključne besede: Izod udarna trdnost, polikarbonat, temperatura kaljenja, matematično modeliranje

1 INTRODUCTION

Engineering polymers have been increasingly used in the applications such as housings for electronic appliances, lenses and windows that have to sustain accidental impact without showing signs of damage. Due to good thermal- and electrical-insulation properties, low density, high resistance to chemicals and ease of manufacturing, engineering polymers have been increasingly used in the applications where the impact performance is the primary concern.[1–4] One of the biggest advantages of polycarbonate (PC) is its impact strength. It is widely used as a transparent protective material because of its low density and excellent mechanical properties. However, when defects such as cracks or notches are introduced, it is subject to a dramatic brittle failure at relatively low loads. PC applications are also limited to thin molded articles because its impact strength is highly sensitive to the presence of notches. The presence of sharp notches, or even small notches, caused by a microscopic surface degradation decreases the impact strength.[5] However, an addition of appropriate polymers or terpolymers and core-shell impact modifiers can be an effective toughening method for the PCs used in thick sections.[6,7] To expand the usefulness of PC in a variety of applications, it is important to explore the ways to prevent or minimize the loss of toughness during sub-T_g annealing and to reduce the sensitivity to the presence of notches and, consequently, the loss of the impact strength. Residual-stress (*RS*) generation with the quenching process under severe conditions (0 °C) is known to be an effective method of toughening glassy polymers.[8–11] Recently, our study showed that, in the case of polycarbonate, the improvement of the impact strength after the second quench at 40 °C is linked to the existence of the relaxation mode located around 35 °C.[12]

Notched Izod testing is a common qualitative measure of the toughness of a material, measuring the energy absorbed prior to failure under high triaxiality and high-rate loading conditions. In industrial applications, it is important to know the impact behavior and the safe operating limits of polymeric structures. In our case, the evaluation of the impact-design failure of polymeric structures has to be experimentally performed on molding prototypes. The experimental trial-and-error method significantly delays the design progress and optimization, wasting a lot of time, money and efforts.

There are several types of standard tests to evaluate the impact strength of polymers. The most commonly used are the Charpy and Izod tests.[13] A successful numerical model for an impact deformation and failure of polymers can provide convenient and useful guidelines on the product design, therefore decreasing the disadvantages arising from just experimental trial and error. In this work, we have investigated the development of a mathematical model predicting the effects of the first- and second-quenching temperatures on the Izod impact strength of PC.

2 EXPERIMENTAL PROCEDURE

2.1 Materials

The polymer used in this study is a commercial polycarbonate, Makrolon® 2620, supplied by Bayer (Germany) with the average molecular mass of about 57 400. The melt index at 300 °C is 19.6 g/(10 min), the polydispersity index is 2.16 and the glass transition temperature is about 144 °C (the value obtained from DMA measurements[14]).

2.1.1 First-quench procedure

Pellets were dried in an oven at 120 °C and then put into the mold and pressed at 25 bar for 12 min at 230 °C. Then the samples were immediately quenched from the moulding temperature in the water baths at three different temperatures of (0, 20 and 80) °C or in the air at room temperature for 15 min. All the samples have a thickness of 3 mm and this step was named "the first quench".

2.1.2 Second-quench procedure

Another free quenching was carried out only for the samples molded at 230 °C at different quenching temperatures. These specimens were heated in the oven at 160 °C (T_g + 15 °C) for 3 h and were immediately quenched for the second time in the water baths at different temperatures (0, 20, 30, 35, 40, 45 and 60) °C for 15 min. This procedure was named "the second quench".

2.1.3 Annealed samples

Finally, in order to get reference samples, an annealing was performed. The annealed specimens were prepared using the samples first quenched in air at 25 °C. Then, these samples were heated at 160 °C for a period of 2 h and, finally, slowly cooled in the oven at room temperature at a rate of about 0.5 °C min^{-1}. These samples were named "annealed samples".

2.2 Notched Izod impact strength

Izod impact-strength properties were determined at room temperature with a CEAST 6546/000 machine with a 15 J pendulum according to ASTM D256-73. The specimens with the dimensions of 3 mm × 12.7 mm × 63 mm were compression molded. Parts of them were milled with a notch radius of 0.5 mm. This radius was chosen so that the tip of the notch was located in the residual compressive zone. These stress zones were determined with a photoelastic examination of a sample between the cross Polaroids under white light. In the case of the thermal stress (symmetrical free quenching), due to the non-uniform cooling of the outer and central layers, compressive and tensile stresses are formed in the material. Two neutral lines symmetrically separate the stress zones. The extension of this zone can reach a certain percentage of the sample thickness.[14]

These stresses are frozen in, and the material conserves some internal stresses, revealed in the polarized light by certain colors. Using a standard polariscope, the photoelastic color sequence, with the increasing stress, observed from the neutral line includes: black (zero), yellow, red, blue-green, yellow, red, green, yellow, red, green and so on.[14] At least five specimens were tested and the average value was used for plotting the experimental data.

2.3 Numerical method

The polynomial curve-fitting technique was used to derive analytical terms that match the given data points.[15] Polynomial curve fitting is a mathematical procedure for finding the best fitting curve for a given set of points by minimizing the sum of the squares of the offsets of the points from the curve. This includes finding the coefficients of polynomial $p(x)$ of degree n that fits the computed values $p(x_i)$ with experimental data y_i, where $i \in \{1, 2, ..., N\}$ and N is the number of experimental data points. The following definition has been used for determining the residual standard deviation (*RSD*), which is a statistical term used to describe the standard deviation of the points formed around a function, and it is an estimate of the accuracy of the dependent variable being measured. The lower the *RSD*, the greater is the agreement between the experimental data and the model. The *RSD* is computed as follows:

$$RSD=\sqrt{\frac{\sum_{i=1}^{N}\left[y_i-p(x_i)\right]^2}{N-q}} \tag{1}$$

where q is the number of estimated parameters (note that for a polynomial fit, $q = n + 1$) and the y_i values correspond to the experimental results of the Izod impact strength (a_k).

3 RESULTS AND DISCUSSIONS

3.1 *Effects of the first and second quenching on the Izod impact strength*

The evolution of the milled notched Izod impact strength is presented as the function of the second-quenching temperature (**Figure 1**). In both cases, the maximum second-quenching temperature is 40 °C. The second thermal treatment including a heat treatment for 3 h at 160 °C (i.e., at T_g + 15 °C) has not totally erased the first thermal treatment. Indeed, the same evolution is observed for the samples that were first quenched in water at (0, 20 and 80) °C and in air at room temperature (25 °C). The influence of the first quenching is reflected on all the properties. The properties obtained after the first quenches at 0 °C and 20 °C are close; they correspond to the rapid first quench. Again, the properties corresponding to the first-quenching temperature of 80 °C and to the cooling in air are close, indicating a slower first quench.

In a previous work,[12] the minimum density observed for the second-quenching temperature of 35 °C was associated with an increase in the free volume. This increase leads to a higher molecular mobility. This explains the increase in the Izod impact strength. The maximum ductility reached during the second quenching from 160 °C to 40 °C is linked to the existence of the β_1 molecular relaxation at around 35 °C.[12]

As already reported for the PMMA and PS,[14] the Izod impact-strength values are maximum at the same second-quenching temperature, i.e., at 40 °C. However, with polycarbonate, the improvement in the Izod impact strength is more pronounced.

3.2 *Comparison of the experimental data with the empirical model*

In order to obtain an analytical expression of the variation of the Izod impact strength of PC with the thermal-treatment parameters, i.e., the first- and second-quenching temperatures, we decided to use an empirical model. First of all, the model chosen in this study to fit the experimental behavior as the function of the second-quenching temperature has a third-degree polynomial form as follows:

$$a_k = a_0 + a_1 \times T_2 + a_2 \times T_2^2 + a_3 \times T_2^3 \qquad (2)$$

where a_k is the notched Izod impact strength (expressed in kJ m^{-2}), T_2 is the absolute second-quenching temperature (in K) and a_0, a_1, a_2 and a_3 are the constants obtained by fitting.

The parameters estimated from the polynomial model (equation 2) are displayed in **Table 1**. The expression chosen to describe the experimental result, with the usual meanings for constants a_0, a_1, a_2, and a_3, gives a fairly good agreement between the calculated and the experimental values, as seen in **Figure 1**. Indeed, it can be seen that the model matched the experimental data for the entire process. This is supported by the low *RSD* values obtained. However, we must note a slightly higher value of the *RSD* for the first quench in water at 80 °C, indicating a lower agreement between the experimental data and the model in this particular case.

Close values of the estimated parameters were obtained for both the samples first quenched in water at 0 °C and the ones first quenched in air. Moreover, the values of the Izod impact strength are higher for the samples first quenched at 0 °C than for the ones first

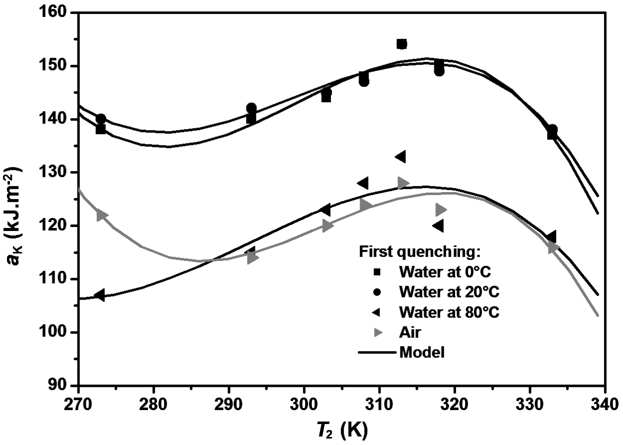

Figure 1: Milled notched Izod impact strength of PC as a function of second-quenching temperature T_2 of the PC first quenched in water at (■) 0 °C, (●) 20 °C, (◄) 80 °C and (►) in air at 25 °C; for the milled annealed sample, a_k = 45 kJ m^{-2}

Slika 1: Izod udarna trdnost brušenega in z zarezo PC-vzorca v odvisnosti od druge temperature kaljenja T_2 PC-vzorca, ki je bil najprej kaljen v vodi pri (■) 0 °C, (●) 20 °C, (◄) 80 °C in (►) na zraku pri 25 °C; pri brušenem žarjenem vzorcu je bila a_k = 45 kJ m^{-2}

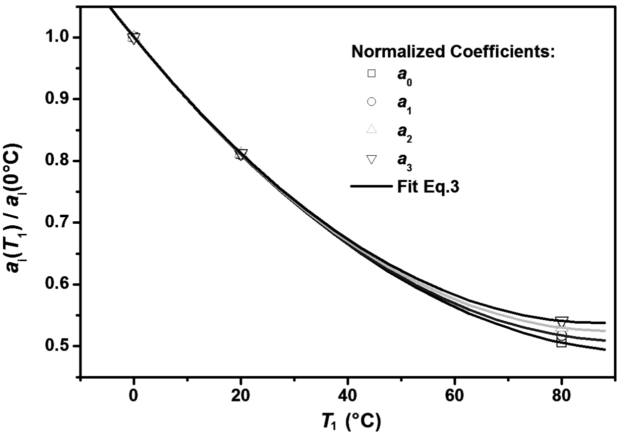

Figure 2: Plot of the normalized a_i coefficients from equation 2 as a function of first-quenching temperature T_1 (for the samples quenched in water)

Slika 2: Prikaz normaliziranih koeficientov a_i iz enačbe 2 v odvisnosti od kalilne temperature T_1 prvega kaljenja (za vzorce, kaljene v vodi)

Table 1: Parameters estimated from the model and residual standard deviation between the experimental Izod impact strength (a_k) and the calculated one, for the PC first quenched at different temperatures (T_1) in air and water

Tabela 1: Parametri, določeni iz modela in preostale standardne deviacije med eksperimentalno določeno Izod udarno trdnostjo (a_k) in izračunano za polikarbonat, ki je bil najprej kaljen pri različnih temperaturah (T_1) na zraku in v vodi

Sample	First quenched in water			First quenched in air
T_1/°C	0 °C	20 °C	80 °C	25 °C
a_0 (kJ m^{-2})	20422	16556	10326	21591
a_1 (kJ m^{-2} K^{-1})	–204.89	–166.00	–105.97	–214.28
a_2 (kJ m^{-2} K^{-2})	0.68764	0.55780	0.36427	0.71084
a_3 (kJ m^{-2} K^{-3})	-7.6663×10^{-4}	-6.2266×10^{-4}	-4.1476×10^{-4}	-7.8382×10^{-4}
RSD	1.25	1.61	4.02	2.22

Table 2: Parameters b_i of equation 3 estimated from the plots of normalized coefficients a_i presented in **Figure 2**

Tabela 2: Parametri b_i iz enačbe 3, določeni iz odvisnosti od normaliziranih koeficientov a_i, predstavljenih na **sliki 2**

Estimated parameter of Eq. 3	Values for each Eq. 2 polynomial coefficient a_i			
	a_0	a_1	a_2	a_3
b_1/°C^{-1}	-1.056×10^{-2}	-1.064×10^{-2}	-1.063×10^{-2}	-1.061×10^{-2}
b_2/°C^{-2}	5.476×10^{-5}	5.759×10^{-5}	5.938×10^{-5}	6.088×10^{-5}

quenched in air. The selected first quench in ambient atmosphere is generally preferred because it is moderate and less costly than the first quench in water at 0 °C, which requires more resources and is more expensive. These results are supported by the model used. It has to be noted that we could not find a model in the literature to compare it with our results.

Even if the model proposed is in agreement with the experimental behavior, we must note that the fitting parameters a_i obtained do not have, at this time, any physical significance. However, it seems interesting to study their dependence upon first-quenching temperature T_1, when the samples are first quenched in water. In order to describe the general variation of these parameters with T_1, we present, in **Figure 2,** a plot of the a_i values normalized to the values obtained for the first quenching at 0 °C as the function of T_1. We can see that the normalized values of polynomial coefficients a_i of equation 2 seem to obey the general rule that can be approximated using the following relationship:

$$a_i(T_1) = a_i(0°C) \times \left[1 + b_1 \times T_1 + b_2 \times T_1^2\right] \quad \forall i \in \{1,2,3,4\} \qquad (3)$$

where T_1 is the first-quenching temperature expressed in °C, while b_1 and b_2 are the coefficients, whose values are given in **Table 2**. The values of the b_1 parameter seem to be quite independent of the polynomial coefficient order *i,* whereas a slight dependence on this coefficient order can be noted for the b_2 parameter. By using equations 2 and 3, along with the empirical values of parameters a_i and b_i reported in **Tables 1** and **2**, it is now possible to compute the Izod impact strength of PC as the function of the first- and second-quenching temperatures, namely, T_1 and T_2. The results of this computation are presented in **Figure 3**. This kind of simple modeling can be useful for manufacturing polymers since it can predict the value of the impact strength as the function of the parameters characterizing the thermal treatments imposed on the material. This kind of modeling can be carried out on the basis of the experiments performed for a limited number of the selected quenching temperatures.

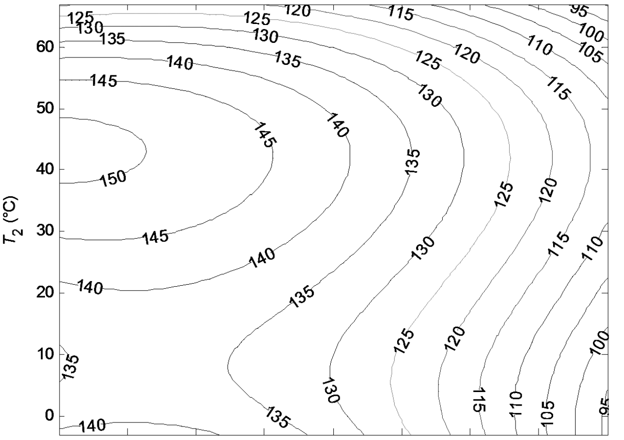

Figure 3: Chart of Izod impact strength a_k (expressed in kJ m^{-2}) of PC as a function of the first- and second-quenching temperatures, namely T_1 and T_2 (quenching in water); computation done using equations 2 and 3, the model and data from **Tables 1** and **2**

Slika 3: Diagram Izod udarne trdnosti a_k (izražene v kJ m^{-2}) polikarbonata v odvisnosti od prve in druge temperature kaljenja T_1 in T_2 (kaljeno v vodi); izračun je izdelan z uporabo enačb 2 in 3, modela in podatkov iz **tabele 1** in **2**

4 CONCLUSION

The effect of the quenching process on the mechanical properties of PC was investigated via Izod impact measurements. The predicted Izod impact strength as the function of the second-quenching temperature was compared with the experimental data and a good agreement was obtained. The results indicated that a generalized constitutive model accurately predicts the Izod impact strength of PC over a wide range of first- and second-quenching temperatures. This kind of modeling could be useful for manufacturers as it can reduce the number of experimental tests necessary to design a manufacturing process. It should be interesting, in future research, on the one hand, to check if this kind of behavior can be extrapolated to the other polymers (e.g., PMMA, polystyrene) and, on the other hand, to find a physical significance of some of these empirical parameters.

5 REFERENCES

[1] O. Delatycki, Mechanical performance and design in polymers, Interscience Publishers, New York 1971

[2] S. M. Walley, J. E. Field, P. H. Pope, N. A. Safford, J. Phys. III France, 1 (**1991**) 12, 1889

[3] S. Kalpakjian, Manufacturing engineering and technology, 3rd ed., Addison-Wesley, Reading, Massachusetts 1995

[4] E. M. Arruda, M. C. Boyce, R. Jayachandran, Mech. Mater., 19 (**1995**), 193

[5] J. C. Falk, K. W. Narducy, M. S. Cohen, R. Brunner, Polym. Eng. Sci., 20 (**1980**) 11, 763

[6] A. F. Yee, R. P. Kambour, In Proceedings of International Conference, Toughening of Plastics, Plastics and Rubber Institute Conference, London, 1978, 20

[7] A. F. Yee, J. Mater. Sci., 12 (**1977**), 757

[8] L. J. Broutman, S. M. Krishnakumar, Polym. Eng. Sci., 16 (**1976**) 2, 74

[9] B. D. Aggarwala, E. Saibel, Phys. Chem. Glass., 2 (**1961**), 137

[10] E. H. Lee, T. G. Rogers, T. C. Woo, J. Am. Ceram. Soc., 48 (**1965**), 480

[11] A. I. Isayev, Polym. Eng. Sci., 23 (**1983**), 271

[12] F. Rouabah, M. Fois, L. Ibos, A. Boudenne, C. Picard, D. Dadache, N. Haddaoui, J. Appl. Polym. Sci., 109 (**2008**), 1507

[13] W. G. Perkins, Polymer. Eng. & Sci., 39 (**1999**), 2445

[14] F. Rouabah, PhD Thesis, University of Sétif, 2007

[15] W. H. Press, S. A. Teukolsky, W. T. Vetterling, B. P. Flannery, Numerical Recipes – The Art of Scientific Computing, 3rd edition, Cambridge University Press, 2007

UDK 669.715:539.374
Original scientific article/Izvirni znanstveni članek

ISSN 1580-2949
MTAEC9, 48(3)321(2014)

SUPERPLASTIC DEFORMATION OF AN X7093 Al ALLOY

SUPERPLASTIČNA DEFORMACIJA Al-ZLITINE X7093

Srdjan Tadić[1], Aleksandar Sedmak[2], Radica Prokić-Cvetković[2], Abdsalam M. Eramah[1], Rebeka Rudolf[3]

[1]Innovation Center, Faculty of Mechanical Engineering, Kraljice Marije 16, 11000 Belgrade, Serbia
[2]Faculty of Mechanical Engineering, University of Belgrade, Kraljice Marije 16, 11000 Belgrade, Serbia
[3]Faculty of Mechanical Engineering, University of Maribor, Smetanova 17, 2000 Maribor, Slovenia
srdjantadic26@gmail.com

Prejem rokopisa – received: 2012-10-01; sprejem za objavo – accepted for publication: 2013-07-17

We have investigated the superplastic deformation mechanism of a powder-metallurgy, high-zinc X7093 Al alloy. The objective was to examine the rate-controlling mechanisms that govern its superplastic deformation. The investigations were carried out in the temperature range 490–524 °C and strain rates of 4.17×10^{-5} s^{-1} to 2.1×10^{-2} s^{-1}. The maximum ductility was slightly more than 500 % at 524 °C and 4.2×10^{-4} s^{-1}. The values of the stress exponent (n) and the activation energy (Q) indicated that the deformation is rate-controlled by the climb within the grain-boundary diffusion path. The existence of a temperature-dependent threshold stress was confirmed.

Keywords: superplasticity, 7xxx Al alloys, deformation mechanisms

Izvršena je bila študija mehanizma superplastične deformacije Al-zlitine 7093 s cinkom, izdelane po postopku metalurgije prahov. Cilj je bila preiskava mehanizma kontrole hitrosti, ki ureja superplastično deformacijo zlitine. Preiskave so bile izvršene v temperaturnem območju 490–524 °C in hitrostih obremenjevanja $4{,}17 \times 10^{-5}$ – $2{,}1 \times 10^{-2}$ s^{-1}. Maksimalna duktilnost je bila malo nad 500-odstotna pri 524 °C in $4{,}2 \times 10^{-4}$ s^{-1}. Vrednosti napetostnega eksponenta (n) in aktivacijska energija (Q) so pokazale, da je hitrost deformacije kontrolirana s plezanjem po difuzijskih poteh v mejah zrn. Potrjen je tudi obstoj temperaturno odvisnega praga napetosti.

Ključne besede: superplastičnost, 7xxx Al-zlitine, mehanizmi deformacije

1 INTRODUCTION

The ability of crystalline solids to undergo extremely large tensile deformations at elevated temperatures is commonly referred to as superplasticity. At least two requirements have to be fulfilled for superplastic deformation[1]: (i) a very small grain size (typically less then 10 µm) and (ii) a proper combination of temperature (T) and strain rate ($\dot{\varepsilon}$). Superplastic flow can be described by the creep-derived Dorn[2] equation:

$$\dot{\varepsilon} = \frac{AD_0G}{kT}\left(\frac{b}{d}\right)^{\mathrm{p}}\left(\frac{\sigma-\sigma_0}{E}\right)^{\mathrm{n}}\exp\left(\frac{-Q_{\mathrm{ap}}}{RT}\right) \qquad (1)$$

where $\dot{\varepsilon}$ is the strain rate, A is a microstructure-dependent coefficient, D_{o} is the diffusion coefficient, G and E are, respectively, the shear and elastic modulus, k is Boltzmann's constant, while R and T have their usual meanings. The influence of the grain size is described by $(b/d)^{\mathrm{p}}$, where b is the Burger's vector and d is the average grain size, while p is the 'grain size exponent', σ is the flow stress and σ_{o} refers to the so-called threshold stress, while n is the 'stress exponent' (the reciprocal integer value of strain-rate-sensitivity, m); Q_{ap} is the apparent thermal activation energy for the diffusion process that controls the superplastic deformation. Both n and Q can be simply determined[3] from experimental results:

$$m=\frac{1}{n}=\left(\frac{\partial \ln \sigma}{\partial \ln \dot{\varepsilon}}\right)_{\mathrm{T}} \qquad Q=-R\left(\frac{\partial \ln \dot{\varepsilon}}{\partial (1/\mathrm{T})}\right)_{\sigma} \qquad (2)$$

The basic mechanism of superplastic deformation is grain-boundary sliding (GBS)[4] – the cause of the high strain-rate sensitivity m, which is, in turn, responsible for the delayed necking during the tensile deformation. In general, $m > 0.35$ is regarded[5] as the condition for superplasticity. Regardless of the m value, GBS requires some kind of stress accommodation at the triple points of the grain boundaries.[6] It is stated that the rate of accommodation mechanisms controls the overall superplastic strain rate.[7]

Previous studies[8–11] have shown that 7xxx Al alloys can be readily thermomechanically processed to attain superplastic capabilities. The optimum conditions for superplasticity are mostly achieved at testing temperatures of T = 500–530 °C and slow strain rates of about 10^{-4} s^{-1}.[12,13] It is, however, highly dependent on the grain size. Tensile elongations as high as 2000 % have been reported.

The objective of this paper is to characterize the superplastic deformation behavior of the second-generation, powder-metallurgy x7093 Al alloy. Based on strain-rate change tests and superplastic tensile tests, a thermal activation analysis was applied to identify the governing and rate-controlling deformation mechanisms. The alloy used in this research has an average grain size d = 10.7 µm.

2 EXPERIMENT

The material was supplied by the manufacturer in the form of a hot-worked billet. The nominal chemical composition of the alloy is given as follows (in mass fractions, *w*/%): Zn - 9, Mg – 2.2, Mg – 1.5, Zr – 0.14, Ni – 0.1 and O – 0. 35. Zinc, magnesium and copper are the main alloying elements for 7xxx [14] alloys. A specific feature of this alloy is the exceptionally high level of zinc. Apart from the Zn, the oxygen level, typically for powder-metallurgy alloys, is rather high. Oxygen, as well as zirconium and nickel, forms a series of insoluble dispersoids.

In order to achieve a fine-grained microstructure, a thermo-mechanical treatment, often used for high-strength 7xxx alloys, is utilized in the present study. It was made in four steps: (i) solid-solution treatment at 490 °C followed by water quenching, (ii) over-aging at 400 °C for 16 h, (iii) warm rolling from h_o = 10 mm down to h_f = 1 mm at 200 °C and, (iv) recrystallization at 480 °C for 30 min. The rolling was conducted on a laboratory two-roll high-rolling mill with the rolls preheated at 70 °C. Between the two successive rolling passes, the material was held in a furnace for 5 min at 200 °C. During every pass the thickness reduction was Δh = –1 mm so the accumulated deformation was progressively increasing as the thickness of the plate was reduced. In the final pass, the thickness reduction was –50 %, while the overall accumulated true strain was ε = –2.3.

Flat tensile samples of 8-mm gauge length, typical for superplastic examinations, were machined from the plate with the axis parallel to the rolling direction. Tensile specimens were tested at temperatures of 490–524 °C and the initial strain rates in the range 4.17×10^{-5} s^{-1} to 2.1×10^{-2} s^{-1}. For each test, the force *vs*. elongation was recorded and converted to true stress (σ) – true strain (ε) and the instantaneous true strain rate ($\dot{\varepsilon}$).[15] The tests were conducted using an Instron testing machine with a constant cross-head displacement. The machine was equipped with a three-zone furnace and the temperature was controlled by three independent chromel-alumel thermocouples. The temperature accuracy was held within ± 2 °C.

Two kinds of tensile tests were carried out: (i) continuous elongation-to-failure tests and (ii) strain-rate-change tests. In the second type of tests, the flow stresses were recorded at a number of different cross-head speeds. Initially, the specimens were deformed to ε = 0.15 at the testing temperature to ensure a homogenous deformation. Then, the tests were carried out over small strain-rate increments and repeated several times.

3 RESULTS

The stress dependence of the strain rate, under isothermal conditions, is shown in the double logarithmic plot of **Figure 1**. An apparent linear dependence can be observed within the range of the applied strain rates and temperatures. The experimental data were fitted with the least-squares procedure using Equation (3):

$$\sigma = K\dot{\varepsilon}^{m} \Rightarrow \log\sigma = \log K + m\log\dot{\varepsilon} \tag{3}$$

where K denotes the strength coefficient (e.g., $K = \sigma$ when $\dot{\varepsilon}$ = 1 s^{-1}), all other symbols are already mentioned. The results of the analysis are inserted into **Figure 1**. Both m and K are reciprocally influenced by the temperature and the applied strain rate. The

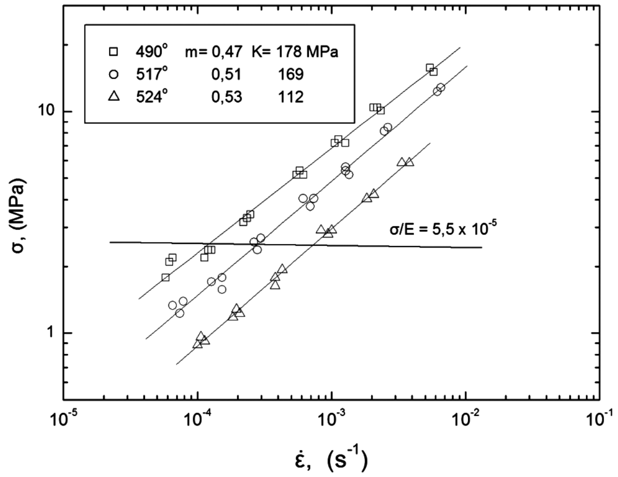

Figure 1: The strain rate as a function of the stress, double logarithm scale. The results of the least-square analysis are inserted into the plot.
Slika 1: Hitrost obremenjevanja kot funkcija napetosti, dvojna logaritemska skala. Rezultati analize najmanjših kvadratov so vstavljeni v diagram.

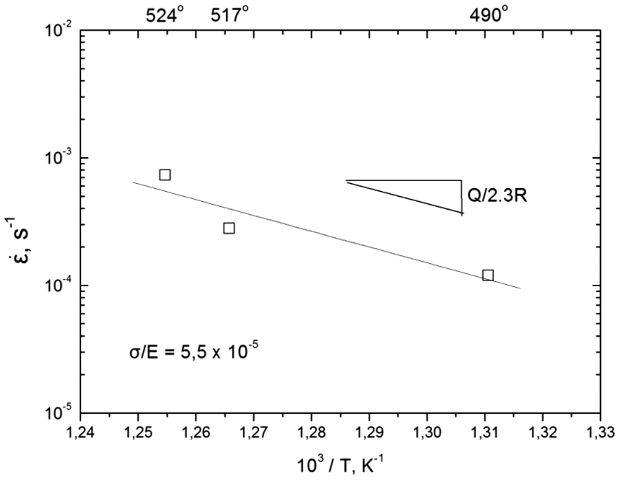

Figure 2: The apparent activation energy vs. the deformation. Indicated stress corresponds to the full line in **Figure 1**.
Slika 2: Navidezna aktivacijska energija proti deformaciji. Prikazana napetost ustreza polni liniji na **sliki 1**.

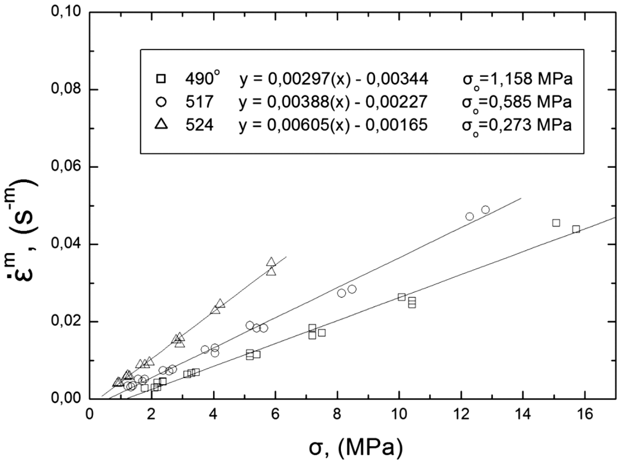

Figure 3: The strain rate as a function of the stress. The least-squares analysis for the threshold stress determination.

Slika 3: Hitrost obremenjevanja kot funkcija napetosti. Analiza najmanjših kvadratov za določitev praga napetosti.

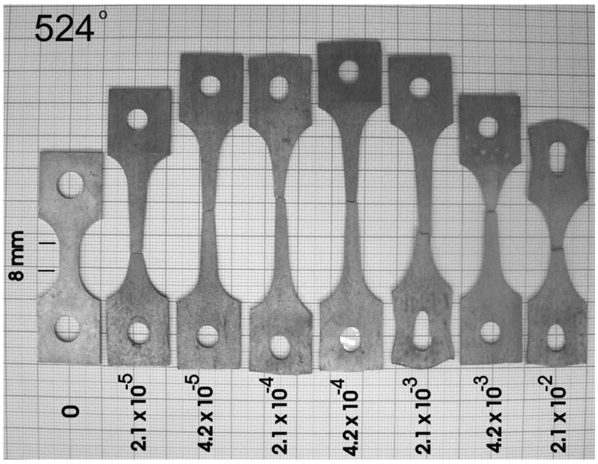

Figure 5: Specimens continuously (stress-strain) tested at 524 °C with various applied strain rates

Slika 5: Vzorci, kontinuirno preizkušeni (napetost-hitrost) na 524 °C z uporabljenimi različnimi hitrostmi obremenjevanja

calculated m-values can be regarded as being typical for the superplastic behavior of Al alloys.

The apparent activation energy for the deformation, Q_{ap}, was determined by plotting the logarithm of strain rate *vs.* 1/T at a constant stress level, i.e., the modulus-normalized stress $\sigma/E = 5.5 \times 10^{-5}$. Such a plot is depicted in **Figure 2**. The straight line, obtained by the least-squares method, reveals a slope equal to $Q/(2.303R)$. The calculated value of Q is 95 kJ/mol. This is close to the value of the activation energy for grain-boundary diffusion in aluminum (84 kJ/mol) and far less than for the lattice diffusion (142 kJ/mol).[16] The same results (with scatter of ± 4 kJ/mol) were calculated for other stress levels (in the range of σ = 2–10 MPa), indicating that Q is not stress dependent.

Among the phenomena governing superplastic deformation, the existence and origins of the threshold stress (σ_o) are the subjects of wide dispute.[17–19] Experimentally, the threshold stress can be determined by plotting $\dot{\varepsilon}^{1/n}$ *vs.* σ (with n being true-stress exponent) and linearly extrapolating values to zero strain rate. Such a plot, as shown in **Figure 3** for $n = 2$, reveals that the threshold stress exists in this alloy and that the values decrease with increasing temperature. The existence of the threshold stress implies that the superplastic deformation is driven by the effective stress $\sigma_{\rm eff} = \sigma - \sigma_{\rm o}$, rather than by the nominal applied stress.

After rearranging Dorn's equation (Eq.1) into the dimensionless, normalized form, it can be used to further clarify the superplastic deformation behavior. Tensile test data are plotted in **Figure 4** as $[\dot{\varepsilon}kT/(D_{\rm GB}Gb)]$ *vs.* $(\sigma - \sigma_0)/E$. Here, $D_{\rm GB}$ refers to grain-boundary diffusion, $D_{\rm GB} = 5\times10^{-14} \exp(84.000/8.314T)$ (m³/s), $G = 3.0 \times 10^4 - 16T$ MPa, $E = 2G(1 + \nu)$, $b = 2.86 \times 10^{-10}$ m and $k = 1.381 \times 10^{-23}$ J/K. Several features on this plot deserve to be emphasized: all the experimental data merged into a

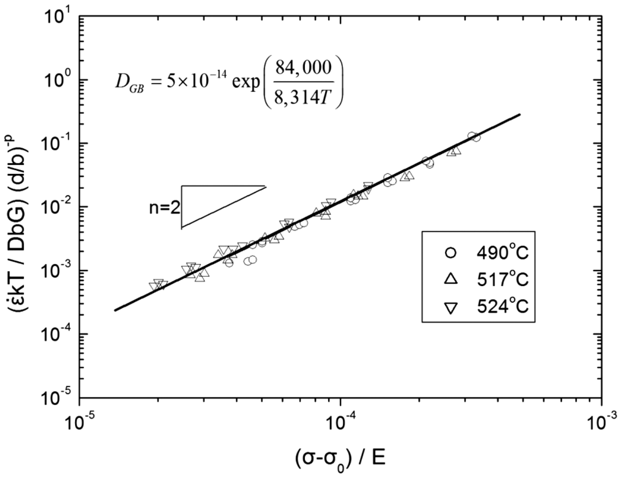

Figure 4: The normalized strain rate vs. the normalized effective stress

Slika 4: Normalizirana hitrost obremenjevanja proti normalizirani efektivni napetosti

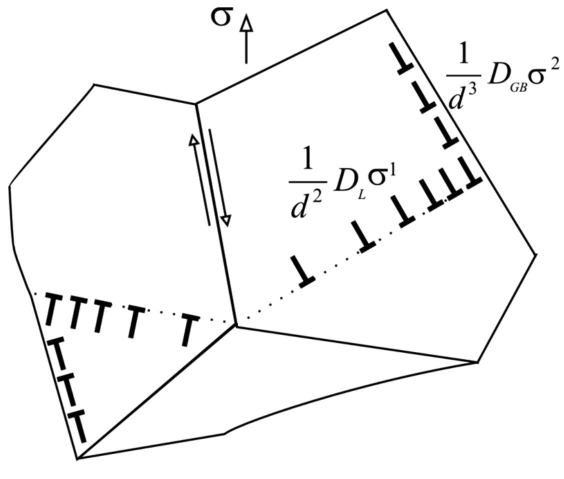

Figure 6: The sketch of grain-boundary sliding accommodated by dislocation glide and climb

Slika 6: Shema drsenja meje zrna zaradi drsenja in plezanja dislokacij single line, thereby proving that the activation energy and the threshold stress are correctly determined[20]; the slope of the line confirms the stress dependence $\dot{\varepsilon} \propto \sigma^2$, i.e., the stress exponent $n = 2$; the experimental data reveal the best fit with the grain size dependence $\dot{\varepsilon} \propto d^{-3}$.

In accordance with the determined strain-rate sensitivity (m), elongation-to-failure tests have revealed superplastic behavior with moderate elongations in the range 100–500 %. The best superplastic properties were observed at 524 °C. **Figure 5** shows a set of tensile specimens tested at this temperature. The highest elongation, 525 %, was achieved at the strain rate 4.2×10^{-4} s^{-1}. However, rather large elongations were observed across a very broad spectrum of strain rates –4.2×10^{-5} to 4.2×10^{-3} s^{-1} , which is two orders of magnitude. This can perhaps be attributed to the presence of insoluble dispersoids that inhibit grain growth during deformation.[21–23] In addition, it can be observed that all the specimens exhibit no-necking.

4 DISCUSSION

Over past decades, considerable efforts in physical metallurgy have been focused on superplasticity.[24] A number of mechanisms (and speculations) have been proposed to explain the mechanisms and kinetics of the process. Nevertheless, a consensus was attained long ago that superplasticity is essentially a grain-boundary sliding phenomenon.[25] Dispute has been raised about the nature of the accommodation processes that relieve the stress concentrations at the grain boundaries. Stress relief by diffusional flow was proposed as a 'grain switching' mechanism accommodated by diffusion mass transfer.[26] The model predicts $m = 1$, which is far higher than the results in **Figure 1**. The majority of superplastic aluminum alloys, within the appropriate temperatures and strain rates, exhibit $n = 2$ ($m \approx 0.5$) behavior, as also confirmed in this paper. Furthermore, it was suggested that at stresses higher than $\sigma > 10^{-5}$E, accommodations by slip are a more probable mechanism.[27] Based on accommodation by dislocation slip, quite a few theoretical models have been proposed.[28–33] Despite the distinctions based on a particular dislocation configuration during deformation, all the models describe a rate-controlling equation in the form of Eq.1. The differences are reflected in the values of n, Q and p. In short, the differences can be summarized as follows. The stress exponent is related to the dislocation movement through the glide and climb. When the glide is rate-controlling (class I solid-solution alloys), the stress exponent $n = 1$ [34,35] or 3.[36] In this case, the activation energy for the deformation is expected to be close to the lattice self-diffusion D_{L} or chemical diffusivity D_{chem}. When climb is the rate-controlling mechanism (typically for class II solid-solution alloys), the stress exponent $n = 2$ [6] and grain-boundary diffusion D_{GB} is prevailing. However, it should be stressed that during the deformation, both glide and climb take place. These are sequential processes,[4] meaning that glide happens before climb. Thus, the slower one will determine the rate of grain-boundary sliding:

$$\frac{1}{\dot{\varepsilon}_{\mathrm{total}}} = \frac{1}{\dot{\varepsilon}_{\mathrm{glide}}} + \frac{1}{\dot{\varepsilon}_{\mathrm{climb}}} \tag{4}$$

Only when $\dot{\varepsilon}_{\mathrm{climb}} >> \dot{\varepsilon}_{\mathrm{glide}} \Rightarrow \dot{\varepsilon}_{\mathrm{total}} \approx \dot{\varepsilon}_{\mathrm{climb}}$, as is the case with the presented results.

The climb itself is diffusion driven, both by lattice and grain-boundary diffusion. These are parallel, independent processes and the faster one is rate-controlling. If the lattice diffusion is faster, the grain-size exponent should be $p = 2$.[1,37] If the rate of grain-boundary diffusion is a controlling process, then $p = 3$.[38,39] (It is necessary to mention the superplastic analogy to Nabarro-Herring *vs.* Coble diffusional creep[1,4,5]). In symbolic notation, the model can be set up as in Eq.5, which seems to properly explain the deformation behavior of the investigated alloy:

$$\dot{\varepsilon}_{\mathrm{climb}} >> \dot{\varepsilon}_{\mathrm{glide}} \Rightarrow \dot{D}_{\mathrm{GB}} > \dot{D}_{\mathrm{L}} \Rightarrow \dot{\varepsilon}_{\mathrm{total}} \propto \frac{1}{d^3} \dot{D}_{\mathrm{GB}} \sigma^2 \tag{5}$$

Equation 5 envisages sequential strain rates of glide and climb as well as the diffusion rates (D-dotted) of the lattice and grain-boundary path. The sketch of the proposed model, based on ref.[25,27–30], is plotted in **Figure 6**. In brief, grain-boundary sliding is impeded at the triple grain boundaries. It generates local stress concentrations and, at some critical intensity of resolved shear stress, dislocation slip is initiated. The emission of new dislocations relieves stresses at the triple points and the GBS continues. Generated dislocations further glide on favorable slip systems and pile-up at the opposite side of the grain. At some level of dislocation pile-up, the climb kicks off and initiates the dynamic recovery. As a final consequence, the overall superplastic strain rate is controlled by the dynamic recovery, which is, *ipso facto*, dependent on the climb rate along the grain-boundary diffusion path.

5 CONCLUSIONS

The superplastic behavior of a high-zinc aluminum x7093 alloy was investigated. The calculated values of the stress exponent ($n = 2$), strain-rate sensitivity ($m = \approx 0.5$), thermal activation energy for deformation (Q – close to activation energy for grain-boundary diffusion) and grain size exponent ($p = 3$) suggest that the superplastic strain rate is controlled by the rates of climb and grain-boundary diffusion. A rate-dependent deformation model was proposed.

Acknowledgments

Thanks to Milutin Nikačević from VTI-Belgrade for the provision of materials. The work was supported by the Serbian Ministry of Education, Science and Technology.

6 REFERENCES

[1] T. G. Nieh, J. Wadsworth, O. D. Sherby, Superplasticity in Metals and Alloys, Cambridge University Press, Cambridge 1997

[2] J. Harper, J. E. Dorn, Acta Metall., 5 (**1957**), 654

[3] J. P. Pilling, N. Ridley, Superplasticity in Crystaline Solids, The Institute of Metals, London 1989

[4] T. H. Courtney, Mechanical Behavior of Materials, McGraw-Hill, London 1990

[5] T. G. Langdon, The interpretation of creep mechanisms in high Temperature Flow, In: E. M. Taleff, C. K. Syn, D. R. Lesuer (Eds.), Deformation, Processing and Properties of Structural Materials, TMS, Warrendale, 2000, 109

[6] O. D. Sherby, E. M. Taleff, Mat. Sci. and Eng., A322 (2002), 89–99

[7] J. C. M. Li, A. K. Mukherjee (Eds.), Rate Processes in Plastic Deformation of Materials, Proceedings of the John E. Dorn Symposium, Metals Park, 1975

[8] F. C. Liu, Z. Y. Ma, Scripta Mater., 58 (**2008**), 667

[9] R. B. Vastava, T. G. Langdon, Acta Metall., 27 (**1979**), 251

[10] P. Shariat, R. B. Vastava, T. G. Langdon, Acta Metall., 30 (**1982**), 285

[11] F. A. Mohamed, S. A. Shei, T. G. Langdon, Acta Metall., 23 (**1975**), 1443

[12] P. K. Chaudhury, F. A. Mohamed, Acta Metall., 36 (**1988**), 1099

[13] P. K. Chaudhury, V. Sivaramakrishnan, F. A. Mohamed, Metall. Trans., 19A (**1988**), 2741

[14] J. A. Wert, N. E. Paton, C. H. Hamilton, M. W. Mahoney, Metall. Trans., 12A (**1981**), 1267

[15] G. E. Dieter, Mechanical Metallurgy, McGraw-Hill, London 1988

[16] H. Frost, M. F. Ashby, The Plasticity and Creep of Metals and Ceramics, Pergamon Press, Oxford 1982

[17] P. K. Chaudhury, F. A. Mohamed, Acta Mater., 36 (**1988**), 1099

[18] G. S. Murty, M. Koczak, Mat. Sci. Eng., 100 (**1988**), 37

[19] Y. Li, T. G. Langdon, Scripta Mater., 36 (**1997**), 1457

[20] A. K. Mukherjee, T. B. Bieler, A. H. Chokshi, Superplasticity in Metals and Ceramics, 10th Riso International Symposium om Metallurgy and Materials Science, Roskilde, Dennmark, 1989

[21] D. W. Kum, W. J. Kim, G. Frommeyer, Scripta Mater., 40 (**1999**), 223

[22] K. Matsuki, G. Stanick, H. Natagawa, M. Tokizawa, Z. Metallkde., 79 (**1988**), 231

[23] W. J. Kim, K. Higashi, J. K. Kim, Mater. Sci. Eng., A260 (**1999**), 170

[24] T. G. Langdon, Seventy five years of superplasticity: historic developments and new opportunitie, J. Mater. Sci., 44 (**2009**), 5998

[25] A. Ball, M. M. Hutchison, Metal. Sci. J., 3 (**1969**), 1

[26] M. F. Ashby, R. A. Verrall, Acta Metall, 21 (**1973**), 149

[27] O. D. Sherby, J. Wadsworth, Mat. Sci. Tech., 1 (**1985**), 925

[28] R. C. Gifkins, Strength of Metals and Alloys, Pergamon Press, Oxford 1982

[29] A. K. Mukherjee, Mater. Sci. Eng., 8 (**1971**), 83

[30] R. C. Gifkins, Metall. Trans., 7A (**1976**), 1225

[31] J. H. Gittus, J. Eng. Mat. Tech., 99 (**1977**), 244

[32] A. Arieli, A. K. Mukherjee, Mat. Sci. Eng., 45 (**1980**), 61

[33] V. Paidar, S. Takeuchi, Acta. Metall., 40 (**1992**), 1773

[34] O. D. Sherby, P. M. Burke, Prog. Mater. Sci., 13 (**1968**), 325

[35] H. Fukuyo, H. C. Tsai, T. Oyama, O. D. Sherby, Iron Steel Inst, 31 (**1991**), 76

[36] J. Weertman, Trans. ASM, 61 (**1968**), 681

[37] G. Krauss (ed.), Deformation Processes and Structure, ASM, Metals Park, 1984, 355

[38] C. H. Hamilton, N. A. Paton (ed.), Superplastic forming of structural materials, The Metallurgical Society of AIME, Warrendale, 1982, 241

[39] G. Frommeyer, W. Kowalski, R. Rablbauer, Met. and Mater. Trans., 37A (**2006**), 3511

UDK 669.18:669.187.28
Original scientific article/Izvirni znanstveni članek

ISSN 1580-2949
MTAEC9, 48(3)327(2014)

MODELLING OF THE SULPHIDE CAPACITY OF STEELMAKING SLAGS

MODELIRANJE SULFIDNE KAPACITETE JEKLARSKIH ŽLINDER

Zarko Radovic, Nebojsa Tadic, Milisav Lalovic, Dragoljub Blecic
University of Montenegro, Faculty of Metallurgy and Technology, Cetinjski put bb, 81000 Podgorica, Montenegro
zarkor@ac.me

Prejem rokopisa – received: 2012-12-06; sprejem za objavo – accepted for publication: 2013-08-27

In this paper the influence of the CaF_2 amount in steelmaking slags on the CaO and Al_2O_3 activities is presented. The new analytical model (RMJ) for determining the sulphide capacity was derived. The aim of this model is to adjust and correct some models, according to Tsao, Daffy and Young, that had limitations regarding the presence of CaF_2 in the slag. Using the RMJ model, the effect of CaF_2 on the sulphide capacity and desulphurisation degree is more precisely defined. Calcium fluoride decreases the negative effect of Al_2O_3 on the sulphide capacity. For an investigation under production conditions, several types of carbon and low-alloy steels were chosen. The steels used for the analysis of specified process parameters were produced using a mixture of CaF_2-CaO and CaO-CaF_2-white bauxite (WB) as the flux. For specified cases, the results obtained with the RMJ model as well as with the Young model, were presented. The RMJ model defines correction factors $k_{1(CaF2)}$ and $k_{2(CaF2)}$. It can be seen that the certainty factor of linear dependence is a bit larger in the case of the RMJ model than the one obtained with the Young model.

Keywords: calcium fluoride, sulphide capacity, RMJ model

V tem članku je predstavljen vpliv vsebnosti CaF_2 v jeklarskih žlindrah na aktivnost CaO in Al_2O_3. Izpeljan je bil nov analitični model (RMJ) za določanje sulfidne kapacitete. Namen modela je prilagoditev in poprava modelov po Tsaoju, Daffyju in Youngu, ki imajo omejitve glede prisotnosti CaF_2 v žlindri. Z uporabo modela RMJ je mogoče bolj natančno opredeliti vpliv CaF_2 na sulfidno kapaciteto in stopnjo razžvepljanja. Kalcijev fluorid zmanjša negativni vpliv Al_2O_3 na sulfidno kapaciteto. Več vrst ogljikovih in malo legiranih jekel je bilo izbranih za industrijski preizkus. Jekla, izbrana za analizo specifičnih procesnih parametrov, so bila izdelana z uporabo mešanice CaF_2-CaO in CaO-CaF_2-beli boksit (WB) kot talilo. Za določene primere so predstavljeni rezultati RMJ-modela, kot tudi Youngovega modela. RMJ-model določa korekcijske faktorje $k_{1(CaF2)}$ in $k_{2(CaF2)}$. Opazi se, da je faktor zanesljivosti linearne odvisnosti nekoliko večji pri RMJ-modelu v primerjavi z dobljenim pri Youngovem modelu.

Ključne besede: kalcijev fluorid, sulfidna kapaciteta, RMJ-model

1 INTRODUCTION

Synthetic-slag practice is employed to obtain clean steels and to desulphurize molten steel (50–60 % of the original sulphur). These slags contain CaO, CaF_2, Al_2O_3 and a small amount of SiO_2. Besides, slag contains insoluble particles (CaO, MgO) and a chemical analysis of the slag gives unrealistic results for the slag basicity. In this case, the calculated basicity is significantly higher than the basicity of fully liquid slags. An important parameter to characterize synthetic slag with respect to its suitability to desulphurize molten steel is the sulphide capacity. On the basis of the ionic theory, the sulphide capacity and sulphur activity must be correlated with the optical basicity because the standard calculation methods neglect the influence of many oxides, except for CaO, MgO and SiO_2.[1] The model by Tsao[2] has been used for defining the chemical-composition influence on the sulphide capacity:

$$\lg C_{\rm S} = 3.44(X_{\rm CaO} + 0.1X_{\rm MgO} - 0.8X_{\rm Al_2O_3} - X_{\rm SiO_2}) - \\ - \frac{9894}{T} + 2.05 \tag{1}$$

where: X_i is the molar fraction of oxide i, T is the slag temperature in K.

However, the above correlation is not applicable to the metallurgical slags containing CaF_2 because the effect of CaF_2 must be substituted with an oxide. On the basis of the optical-basicity index, the following correlation was suggested by Gaye[3]:

$$\lg C_{\rm S} = \frac{B}{D} + 1.445 - \frac{12364}{T} \tag{2}$$

where: B = 5.62 (% CaO) + 4.15 (% MgO) – 1.15 (% SiO_2) + 1.46 (% Al_2O_3), D = (% CaO) + 1.39 (% MgO) + 1.87 (% SiO_2) + 1.65 (% Al_2O_3).

In this case the amount of CaF_2 is assumed to be part of the CaO amount. Since aluminum was used for steel deoxidation, the activity of Al_2O_3 and the Al amount are considered while calculating the sulphur-distribution coefficient[4]:

$$\lg L_{\rm S} = \lg C_{\rm S} - \frac{1}{3}\lg(a_{\rm Al_2O_3}) + \frac{2}{3}(\%{\rm Al}) + \frac{20397}{T} - 5.482 \tag{3}$$

In the secondary-metallurgy processes Si was used as a deoxidizer. Therefore, the formation of a stable SiO_2, its interaction with the other oxides and its influence on the sulphide capacity should not be neglected. This correlation can be empirically defined with the Young expression[5]:

$$\lg C_S = -13.913 + 48.84\Lambda - 23.82\Lambda^2 - \left(\frac{11710}{T}\right) - -0.02223(\%\mathrm{SiO_2}) - 0.02275(\%\mathrm{Al_2O_3}) \quad (4)$$

where Λ is the theoretical optical basicity of the slag calculated with the Nakamura method[6]. An experimental analysis of EAF steelmaking slags shows that this model can be used as the basis for further consideration. Young et al.[5] showed that equation (4) can be applied only to the range of $\Lambda < 0.8$, i.e., to the slags examined in the experimental part of this research. Larger values of the CaF_2 amount cause high values of C_s and L_s. In this way, it is possible to obtain a value of L_s that is higher than 1000, and the literature reports show that such large values are indeed obtained in industrial practices[7].

The main aim of this paper is to derive a new model (RMJ) that will more precisely define the impact of CaF_2 on the sulphide capacity of steelmaking slags.

2 EXPERIMENTAL WORK

The first stage of the experimental investigations is a chemical analysis of the slag samples. The chemical compositions of the investigated slags for the two slag mixtures are given in **Table 1**. The steels are produced in a EAF 60 t, while Si and Al are used as deoxidizers. The slag and metal were manually sampled by the EAF operator at the temperature of ≈1570 °C, after a vacuum treatment of the steel, 10–12 min before casting. The mixture for the synthetic slag contains CaO, CaF_2 and white bauxite in the mass ratio of 3 : 1 : 2, with the ratio of 3 : 1 for the CaO-CaF_2 mixture.

For degassing the steel, a vacuum treatment and stirring with argon purging from the ladle bottom are used.

The aim of using a triple slag mixture is to investigate the impact of CaF_2 in the case of an increased presence of Al_2O_3 in white bauxite.

3 RESULTS AND DISCUSSION

A presence of CaF_2 increases the CaO saturation in the slags. For example, at comparable CaO concentrations, activity $a_{(\mathrm{CaO})}$ in the CaO-CaF_2 slag is much higher than in the CaO-Al_2O_3 and CaO-SiO_2 systems. The slags in secondary steelmaking are basically unstable at high temperatures since two or more components in the slag react[8] and the composition changes continuously while the fluorides and oxides react as follows:

$$3\mathrm{CaF_2} + \mathrm{Al_2O_3} = 2\mathrm{AlF_3}\ (g) + 3\mathrm{CaO} \quad (5)$$

The slag composition shows a steady increase in the CaO concentration and a decrease in Al_2O_3, so that the part of expression (4) that is correlated with Al_2O_3 must be corrected with $k_{1(\mathrm{CaF2})}$. Besides, the effect of moisture when dealing with the slags containing CaF_2 is very important because of the following reaction:

$$\mathrm{CaF_2} + \mathrm{H_2O} = \mathrm{CaO} + 2\mathrm{HF(g)} \quad (6)$$

In this case, CaF_2 increases together with the CaO activity. Therefore, the Young model (equation 4) must be adjusted with the correction factors, $k_{1(\mathrm{CaF2})}$ and $k_{2(\mathrm{CaF2})}$, defining the secondary influence of CaF_2 on C_s as follows:

$$\lg C_S = -13.913 + 48.84\Lambda - 23.82\Lambda^2 - \left(\frac{11710}{T}\right) - -0.02223(\%\mathrm{SiO_2}) - 0.02275(\%\mathrm{Al_2O_3}) \cdot k_{1(\mathrm{CaF2})} + k_{2(\mathrm{CaF2})} \quad (7)$$

Figure 1 shows sulphide capacities in the CaO-CaF_2-Al_2O_3 ternary system at 1500 °C, as determined by Kor and Richardson[4].

Using the correlations shown in **Figure 1** for the chemical compositions of the investigated slags (**Table 1**), obtained with the regression-analysis method, the following expressions are obtained:

$$k_{1(\mathrm{CaF_2})} = -0.0001(\%\mathrm{CaF_2})^2 + 0.024(\%\mathrm{CaF_2}) + 0.031 \quad (8)$$

$$k_{2(\mathrm{CaF_2})} = -0.0002(\%\mathrm{CaF_2})^2 + 0.015(\%\mathrm{CaF_2}) + 0.015 \quad (9)$$

Table 1: Chemical compositions of the investigated slags after steel vacuuming (mass fractions, *w*/%)
Tabela 1: Kemijska sestava preiskovanih žlinder po obdelavi jekla v vakuumu (masni deleži, *w*/%)

Slag mixture	Steel (EN)	Amounts of components (*w*/%)								
		CaO	MnO	MgO	SiO_2	Al_2O_3	FeO	Fe_2O_3	CaF_2	S
CaO-CaF_2	1.6582	40.00	1.90	13.70	18.20	16.90	1.77	1.30	5.00	0.27
	1.2714	43.52	0.87	11.31	13.77	21.20	1.14	1.90	4.65	0.50
	1.1181	40.5	0.1	18.1	16.5	15.6	0.6	1.4	6.00	2.50
	1.7147	56.5	0.3	7.8	15.1	6.2	0.9	0.9	8.90	2.30
	1.0503	51.0	0.6	10.6	16.6	7.1	1.1	1.3	9.20	1.20
	1.7005	39.2	1.9	24.3	17.2	9.5	1.5	0.2	5.10	0.30
	1.1191	41.8	3.8	12.3	21.1	20.1	1.9	0.2	5.80	0.30
	1.7225	50.7	0.8	10.1	18.2	13.1	1.2	0.9	4.90	0.50
CaO-CaF_2-WB	1.6582	41.2	0.3	14.7	27.2	12.30	2.30	1.0	2.30	0.40
	1.7225	44.0	0.5	9.2	23.1	9.1	1.8	1.1	2.5	0.32
	1.1141	45.3	0.8	19.1	18.5	18.8	1.33	0.92	3.1	0.41
	1.7147	46.5	0.6	17.8	15.1	9.2	1.4	1.4	3.9	0.39
	1.0503	42.2	0.52	16.8	22.2	13.1	1.21	1.32	2.9	0.35
	1.2714	39.52	0.87	19.31	21.8	20.1	1.94	1.8	2.95	0.33

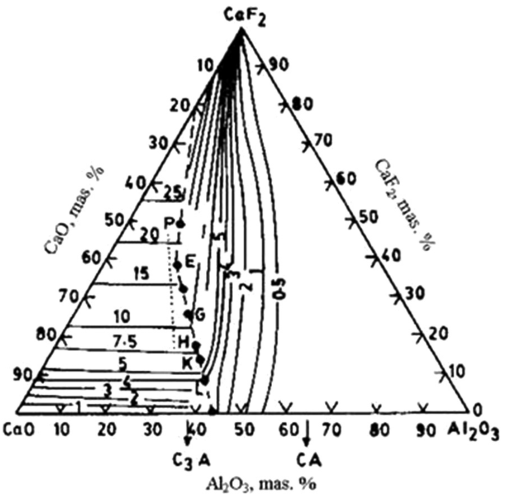

Figure 1: Sulphide capacity for the CaO-CaF_2-Al_2O_3 system at 1500 °C
Slika 1: Sulfidna kapaciteta sistema CaO-CaF_2-Al_2O_3 pri 1500 °C

Equation 8 shows that CaF_2 decreases the negative effect of Al_2O_3 on CaS and it is defined by $k_{1(CaF2)}$. With a calculation using equations 8 and 9, the effect of CaF_2 on C_s, for the constant amounts of Al_2O_3 and CaO, was examined. Therefore, equations 7, 8 and 9 provide the basis for deriving the RMJ model.

The procedure was repeated for different amounts of these components under the conditions of secondary metallurgy that are analyzed. The values of C_s were analyzed cumulatively so that the influence of Al_2O_3 and CaO was presented indirectly through CaF_2. Equations 8 and 9 show that the $k_{1(CaF2)}$ and $k_{2(CaF2)}$ values are always positive. This is in accordance with the fact that an increase in the CaF_2 amount increases the sulphide capacity. The primary effect of CaF_2 was defined on the basis of the optical-basicity values. However, the secondary effect of CaF_2 can be considered through a decrease in the slag viscosity and an increase in the CaO activity.

Based on the above-mentioned procedure, the $C_{s'}$ values, using the RMJ model (eq.7), and C_s, using the Young model (eq.4), were determined. On the basis of the chemical composition of the slag, optical basicity was calculated with the Nakamura method[4].

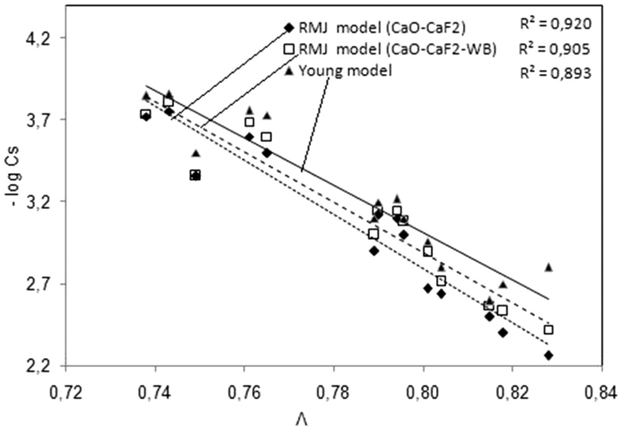

Figure 2: Sulphide capacity as the function of optical basicity
Slika 2: Sulfidna kapaciteta v odvisnosti od optične bazičnosti

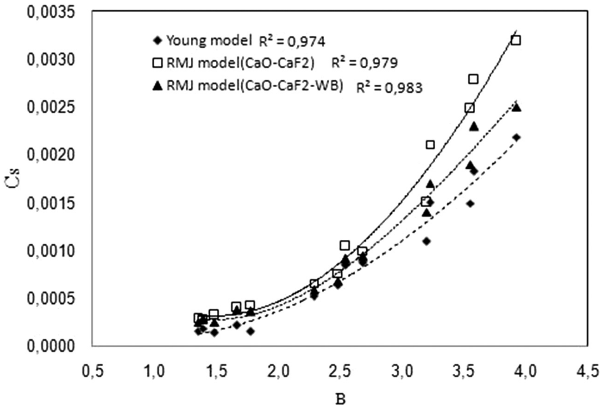

Figure 3: Influence of basicity on sulphide capacity
Slika 3: Vpliv bazičnosti na sulfidno kapaciteto

In all the considered cases, the compared values of $C_{s'}$ are higher than the C_s values. The relationship between the sulphide capacity and the optical basicity for the two above-mentioned models is shown in **Figure 2**.

It is likely that the C_s values increase with an increase in the optical basicity. This is the basis of the CaF_2 effect on the sulphide capacity and desulphurisation. All the values of the sulphide capacity calculated with the new RMJ model are higher than the ones calculated with the Young model. It was noticed that C_s increases faster with the increasing CaF_2 amount when the RMJ model is used because of its effect on $k_{1(CaF2)}$ and $k_{2(CaF2)}$. **Figure 3** shows the variation of C_s as the function of the slag basicity, indicating that the sulphide capacity increases with the increased B values.

For the slag with $B < 2$, the values of C_s obtained with the RMJ and Young models are approximately equal. This is a direct result of the small values of correction factors $k_{1(CaF2)}$ and $k_{2(CaF2)}$ in the RMJ model. In the later stages, for $B > 2$, its values significantly increase and the differences between the C_s values of the two models are higher. The C_s values are higher for the CaO-CaF_2 mixture than for the triple CaO-CaF_2-WB mixture because of the Al_2O_3 presence in white bauxite.

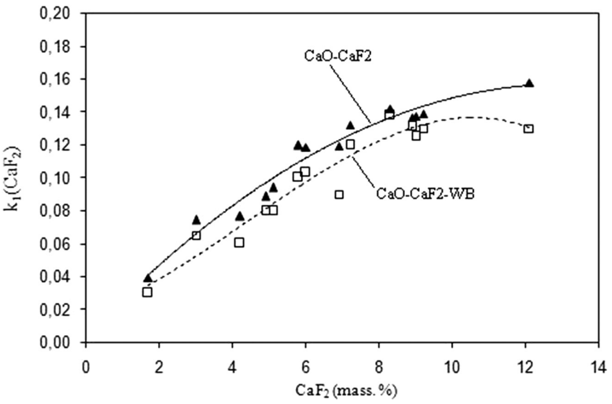

Figure 4: Influence of CaF_2 on the values of $k_{1(CaF2)}$ factor
Slika 4: Vpliv CaF_2 na vrednosti faktorja $k_{1(CaF2)}$

Table 2: Coefficient of sulphur distribution for the investigated slags
Tabela 2: Koeficient razporeditve žvepla pri preiskovanih žlindrah

Slag	1	2	3	4	5	6	7	8
L_s	53.7	73.3	69.1	76.6	80.8	129.3	111.4	99.8
$L_{s'}$(CaO-CaF_2)	58.8	79.2	75.6	83.8	88.5	141.6	122.0	109.8
$L_{s'}$(CaO-CaF_2-WB)	54.1	75.3	71.1	81.1	85.0	131.2	–	–

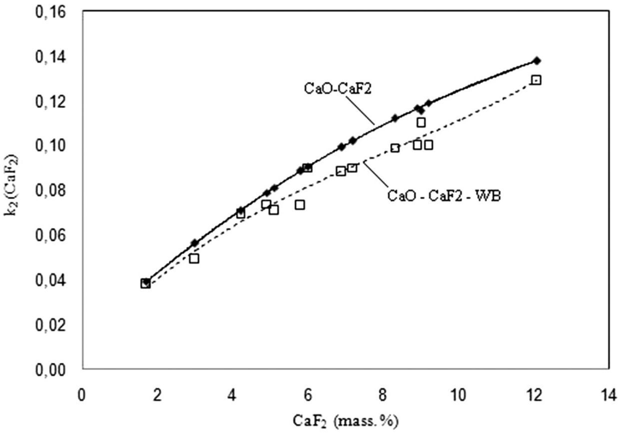

Figure 5: Influence of CaF_2 on the values of $k_{2(CaF2)}$ factor
Slika 5: Vpliv CaF_2 na vrednosti faktorja $k_{2(CaF2)}$

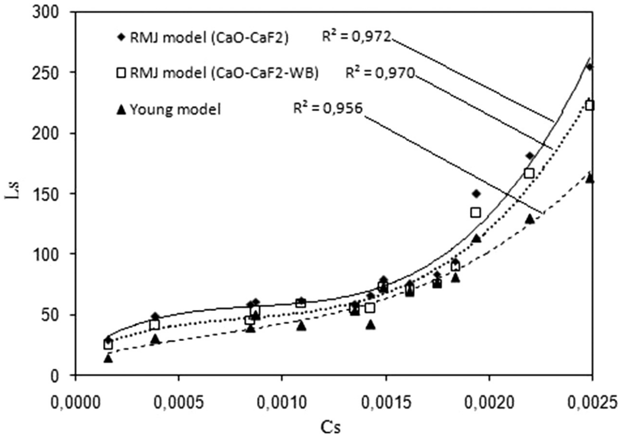

Figure 6: Effect of C_s on sulphur distribution
Slika 6: Vpliv C_s na razporeditev žvepla

The typical values of $k_{1(CaF2)}$ and $k_{2(CaF2)}$, as functions of the CaF_2 amount, are shown in **Figures 4** and **5**.

In general, it may be noticed that $k_{1(CaF2)}$ and $k_{2(CaF2)}$ are proportional to the CaF_2 amount. Besides, for $w(CaF_2) < 8$ %, the relationship is approximately linear, but for $w(CaF_2) > 8$ %, the intensity of the k_{CaF2} changes is lower. The values of $k_{1(CaF2)}$ and $k_{2(CaF2)}$ are lower for CaO-CaF_2-WB than for the CaO-CaF_2 slag mixture. It is noticeable that a higher amount of CaF_2 and a lower Al_2O_3 amount cause an increase in the correction-factor values. Besides, the results in the case of the CaO-CaF_2-WB mixture are more scattered than for CaO-CaF_2.

The coefficient of sulphur distribution is calculated with equation 3. The values of L_s (the RMJ model) and $L_{s'}$ (the Young model) are presented in **Table 2**.

The effect of L_s on the sulphide capacity for the two considered models is shown in **Figure 6**. It can be seen that, at the lower C_s values, the relation between L_s and C_s is almost linear.

However, at $C_s > 0.0015$, the L_s values strongly increase, and the results are more scattered in all the cases. It is likely that the degree of desulphurisation is higher for the RMJ model than for the Young model. This is because positive values of $k_{1(CaF2)}$ and $k_{2(CaF2)}$ allow a larger CaO activity that is generally observed in practice. The probability factors of polinomial dependence are higher for the RMJ model ($R^2 = 0.97$ and $R^2 = 0.972$) than for the Young model ($R^2 = 0.956$).

4 CONCLUSION

The results of the new analytical RMJ model, presented in this paper, indicate that a usage of correction factors $k_{1(CaF2)}$ and $k_{2(CaF2)}$ is required. The secondary effect of CaF_2 on the degree of desulphurisation is fully defined with these factors. Using white bauxite as a slag component, the values of $k_{2(CaF2)}$ decrease and the degree of desulphurisation is lower. The relative effect of CaF_2 on the values of k_{CaF2} and L_s at the basicity of $B > 2$ was indicated. The differences in the values of C_s for the RMJ and Young models increase with the increasing k_{CaF2}. This difference was caused by the secondary effect of CaF_2 on the CaO and Al_2O_3 activities as well as the properties of the slag. The presence of Al_2O_3 in white bauxite causes a lower sulphide capacity, and an optimum component amount in the steelmaking slag mixture is a condition for good desulphurisation.

5 REFERENCES

[1] A. Mc Lean, Y. Yang, I. Sommervile, The Science and Technology of Slags for Iron and Steelmaking, Proceedings of 6th Int. Conference, Stockholm, 2000, 127

[2] T. Tsao, H. G. Katayama, Trans. ISIJ, 26 (**1986**), 717

[3] H. Gaye, P. Riboud, Proceed. of 5th Int. Iron and Steel Con., 6 (**1986**), 631

[4] A. Gosh, Secondary Metallurgy, CRC Press, New York 2000, 195

[5] W. Young, A. Duffy, Use of optical basicity concept for determining sulphur slag-metal partitions, Ironmaking and Steelmaking, 19 (**1992**), 201

[6] M. M. Nzotta, M. Andersson, P. Jonsson, S. Seetaraman, A study on the sulphide capacities of steelmaking slags, Scand. Journal of Metallurgy, 29 (**2000**), 177

[7] N. Bannenberg, H. Lachmud, Proceedings of Steelmaking Conf. Proc., Chicago, 77 (**1994**), 135

[8] K. Mills, The estimation of slag properties, Journal of The Southern African Institute of Mining and Metallurgy, 111 (**2011**), 649

UDK 666.3/.7:620.178
Original scientific article/Izvirni znanstveni članek

ISSN 1580-2949
MTAEC9, 48(3)331(2014)

THE EFFECT OF THE FIRING TEMPERATURE ON THE HARDNESS OF ALUMINA PORCELAIN

VPLIV TEMPERATURE ŽGANJA NA TRDOTO PORCELANA IZ ALUMINIJEVEGA OKSIDA

Igor Štubňa[1], Peter Šín[2], Mart Viljus[3], Anton Trník[1,4]

[1]Department of Physics, Constantine the Philosopher University, A. Hlinku 1, 94974 Nitra, Slovakia
2Department of Physics, Faculty of Civil Engineering, Slovak University of Technology, Radlinského 11, 813 68 Bratislava, Slovakia
[3]Center for Materials Research, Tallinn University of Technology, Ehitajate tee 5, 19086 Tallinn, Estonia
[4]Department of Materials Engineering and Chemistry, Czech Technical University, Thákurova 7, 16629 Prague, Czech Republic
atrnik@ukf.sk; anton.trnik@fsv.cvut.cz

Prejem rokopisa – received: 2013-02-12; sprejem za objavo – accepted for publication: 2013-07-23

Green alumina porcelain samples containing kaolin (27 %), Al_2O_3, grog (50 %) and feldspar (23 %) were fired at temperatures between 300 °C and 1250 °C with a heating and cooling rate of 5 °C/min. The Shore hardness and the Vickers hardness of the fired samples were measured at room temperature. Both hardnesses of the green alumina porcelain samples are low and remain approximately constant up to 400 °C when dehydroxylation begins. Between 400 °C and 700 °C both hardnesses slightly increase. Above 700 °C, they increase exponentially. This is explained by sintering and high-temperature reactions in metakaolinite. The dependencies between both hardnesses, Shore and Vickers, and the firing temperature are very similar, i.e., the Shore hardness and the Vickers hardness reflect changes in the sample in the same manner. The Vickers hardness is much more sensitive to the firing temperature. Its values after firing at 1250 °C are 130 times higher than those measured at room temperature. However, the values of the Shore hardness are only four times higher. The relationship between the Young's modulus and the Shore hardness and the Vickers hardness can be fitted by power-regression functions.

Keywords: Shore hardness, Vickers hardness, alumina porcelain, Young's modulus

Surovi vzorci porcelana, ki vsebujejo kaolin (27 %), Al_2O_3 in gline (50 %) ter glinenec (23 %), so bili žgani pri temperaturah med 300 °C in 1250 °C s hitrostjo ogrevanja in ohlajanja 5 °C/min. Pri sobni temperaturi je bila pri žganih vzorcih izmerjena trdota po Shoreu in Vickersu. Obe trdoti surovega porcelana na osnovi aluminijevega oksida sta nizki in ostajata relativno konstantni do temperature 400 °C, ko se začne dehidroksilacija. Med 400 °C in 700 °C obe trdoti nekoliko narasteta. Nad 700 °C trdoti naraščata eksponencialno. To si razlagamo s sintranjem in z visokotemperaturnimi reakcijami v metakaolinitu. Odvisnosti med obema trdotama po Shoreu in Vickersu ter temperaturo žganja so zelo podobne, kar pomeni, da trdoti po Shoreu in Vickersu izražata spremembe v vzorcu na enak način. Trdota po Vickersu je bolj občutljiva za temperaturo žganja. Njena vrednost po žganju pri 1250 °C je 130-krat višja kot trdota, izmerjena pri sobni temperaturi. Vrednosti trdote po Shoreu so samo 4-krat višje. Odvisnost med Youngovim modulom, trdoto po Shoreu in trdoto po Vickersu je mogoče ugotoviti s funkcijami regresije.

Ključne besede: trdota po Shoreu, trdota po Vickersu, porcelan na osnovi aluminijevega oksida, Youngov modul

1 INTRODUCTION

The desired mechanical properties of ceramics are achieved in a relatively complex technological process in which firing is the most important part. During firing, a ceramic kaolin-based body, such as porcelain, passes from the green state to the final ceramic state through several phase transitions, during which both composition and structure change significantly. It is important to know how the mechanical properties develop during firing, so one group of research projects is focused on different mechanical properties measured during the firing.[1] Some projects deal with the same properties, but measured at room temperature after firing at chosen temperatures. This second way is experimentally simpler and is often used as a measurement of the Young's modulus, the mechanical strength, hardness, and other mechanical parameters.

The hardness is an important property of the ceramic body that often determines its application. For example, the hardness of porcelain determines whether this material is suitable for floor tiles. There are different kinds of hardness, which is more a technical parameter than physical, and consequently different methods are used for their measurement. A quick and simple method, the Shore method, uses an indenter that falls down vertically on a sample.[2] This type of hardness is related to the material's elasticity. A measure of the Shore hardness is the maximum height reached by the indenter after the rebound off the sample. The principle of this method is simple and can be used at elevated temperatures. Although the Shore hardness is mostly measured on elastomers, this parameter is also used for rocks[3–5] as well as for ceramics and metals in high-temperature conditions.[6] If a steel ball is used as the indenter, it is necessary to obtain an accurate horizontal position of the sample as well as an optical measurement of the maximum vertical position of the indenter after the rebound.[7] Another mechanical arrangement is exploited in[6], where the steel ball falls on a tilted sample and the hardness is determined from the time between two impacts, recorded by electromechanical receivers. One of them is placed on the sample and the other on a metallic reflector situated above it.

Another hardness test that is often used for ceramics is the Vickers hardness.[8] Its principle is based on the load of a diamond-pyramided indenter over the sample surface for the dwell time. The Vickers hardness is calculated from the loading force and indentation area. For example, the Vickers hardness of ceramic floor tiles was measured in[9] and alumina composites were tested in[10]. It was found that the Vickers hardness increases with the sintering temperature.

Since the macroscopic hardness as well as the Young's modulus are generally determined by interatomic bonds inside the crystals and interface forces between the crystals in a polycrystalline body, one may expect a close relationship between these quantities. This can be exploited for an estimation of the Young's modulus through a hardness measurement, which is simpler. For example, it is known that the Shore hardness is related to the elasticity and there are formulae that link the Young's modulus and the Shore hardness of elastomers.[11,12] A power relationship between the Young's modulus and the hardness (obtained from the Schmidt hammer test, which is also a rebound method) was found in[13] for different rocks. A logarithmic relationship between them was derived in[14]. A linear as well as an exponential relationship between the values of the Young's modulus and the hardness were presented.[3,4,15,16] Our findings imply that no unambiguous relationship exists between the Young's modulus and the hardness for the measured material. Experimental points in the plots of the hardness vs. Young's modulus are usually very scattered, which makes these relationships questionable. We did not succeed in finding such a relationship for ceramic materials.

The aim of this work is to measure the Shore hardness and the Vickers hardness at room temperature on ceramic samples fired at different temperatures and to compare the Shore hardness with the Vickers hardness.

2 EXPERIMENTAL

The samples for the hardness test were cut from a green alumina porcelain plastic blank (diameter 300 mm) intended for high-voltage insulators. The blank consists of kaolin (27 %), Al_2O_3, milled fired waste (50 %), and feldspar (23 %). Its chemical composition is in **Table 1**.

Table 1: The chemical composition of the green sample material in mass fractions, *w*/%

Tabela 1: Kemijska sestava surovega materiala vzorcev v masnih deležih, *w*/%

SiO_2	Al_2O_3	Fe_2O_3	TiO_2	CaO	MgO	K_2O	Na_2O	L.O.I.
40.22	48.99	0.81	0.20	0.23	0.27	3.60	0.59	4.93

The blank was cut into samples with dimensions of 10 mm × 30 mm × 30 mm. The samples were dried in the open air and both 30 mm × 30 mm faces were smoothed with fine sandpaper. After that the sets of three samples were fired at (300, 400, 425, 450, 475, 500, 550, 600, 700, 800, 900, 1000, 1100, 1200, and 1250) °C with a heating and cooling rate of 5 °C/min.

To measure the Shore hardness, we designed an apparatus where the indenter (a steel ball Ø = 4 mm) hits a sample, tilted by an angle between the sample and the horizontal plane of 22.5°, and falls down on a soft plasticine surface. Here the indenter creates a circular imprint. The hardness was calculated from the geometrical quantities denoted as h_1 (the vertical distance between the initial position of the indenter and the sample), h_2 (the vertical distance between the sample and the plasticine surface), and l (the horizontal length of the indenter's trajectory after the rebound). Since the distances $h_1 = h_2 = 0.25$ m are fixed, only l is measured. The Shore hardness (HSC) is defined as HSC = $10^4 h_3/65h_1$, where h_3 is the maximum vertical height reached by the indenter after the rebound.[2] When the vertical rebound is expressed through l as $h_3 = 12/[2(l + h_2)]$, we obtain HSC = $10^4 l_2/[130h_1(l + h_2)]$ and after substituting numerical values we have:

$$HSC = \frac{307.7l^2}{l+0.25} \qquad (1)$$

where l is in metres.

The plausibility of the results obtained using the described apparatus was verified by Vickers sclerometer Indentamet 1105 Buehler (Germany). For the Vickers hardness (HV) measurement a loading force of 10 N and a dwell time of 10 s were used.

We used three samples for every firing temperature and the measurement was repeated five times at different places of the sample, so we had 15 sets of experimental data of the hardness for each firing temperature.

Young's modulus was measured at room temperature using the sonic resonant method[17] with cylindrical samples of dimensions Ø 11 mm × 150 mm fired at temperatures between 300 °C and 1250 °C.

3 RESULTS AND DISCUSSION

The dependence of the Shore hardness on the firing temperature is depicted in **Figure 1**. As noted above, the Vickers hardness was also measured (**Figure 2**) to find the similarities between both the results. The Vickers hardness is more sensitive to changes in the sample structure developed during heating from room temperature to 1250 °C. In contrast to the Shore hardness, which increased by only ≈4 times, the Vickers hardness increased by ≈130 times. Both the Shore hardness and the Vickers hardness reflect the main processes in the samples in the same manner.

During the heating from room temperature up to 400 °C, the hardness is approximately the same as the green sample hardness. This supports the idea that no structural and compositional changes in the sample occur in this temperature interval.[18,19]

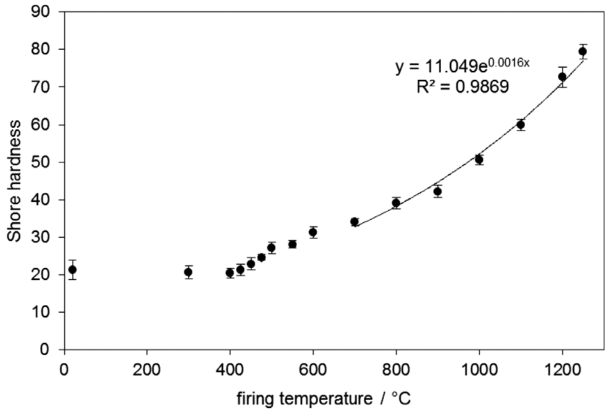

Figure 1: The Shore hardness versus firing temperature
Slika 1: Trdota po Shoreu v odvisnosti od temperature žganja

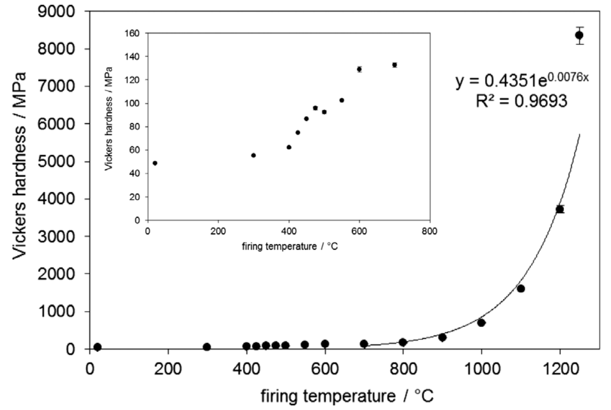

Figure 2: The Vickers hardness versus firing temperature
Slika 2: Trdota po Vickersu v odvisnosti od temperature žganja

Another interesting occurrence is found between 400 °C and 600 °C, where dehydroxylation runs in the kaolinite component. Dehydroxylation creates the highly defective porous metakaolinite,[18–20] which represents ≈ 23 % of the sample mass. Consequently, the mechanical properties of the metakaolinite crystals are weaker, and these properties must also be weaker for the porcelain mixture containing metakaolinite. The total porosity of the sample (consisting of metakaolinite, alumina, feldspar, and grog) increases by 3–4 % after dehydroxylation.[18,21] In spite of these facts, we do not observe a significant decrease in the hardness, as would be logically expected, but an increase occurs instead. We observe only a very low decrease of the Vickers hardness in **Figure 2** and a decelerating of the increase of the Shore hardness above 500 °C in **Figure 1**. We note that similar results were obtained in the dehydroxylation region using a measurement of the Brinell hardness on the green quartz porcelain samples that contained 50 % of kaolin, 25 % of feldspar, and 25 % of quartz.[21] Such behaviour can be explained only by an improvement of the crystal interfaces, because the crystal interiors remain unchanged.

To explain this peculiar behaviour of the hardness in the dehydroxylation region, we propose a mechanism based on additional electrostatic forces between electrically charged defects on the surfaces of the metakaolinite crystals that fortify the sample.[19] The idea is based on the fact that dehydroxylation is a source of the electrically charged defects inside the crystals.[20,22] Many of them are supposedly located on the crystal faces, and, consequently, they become a source of the additional attractive electrostatic forces between metakaolinite crystals. We may also suppose a solid-state sintering as another source of the fortification of the samples.

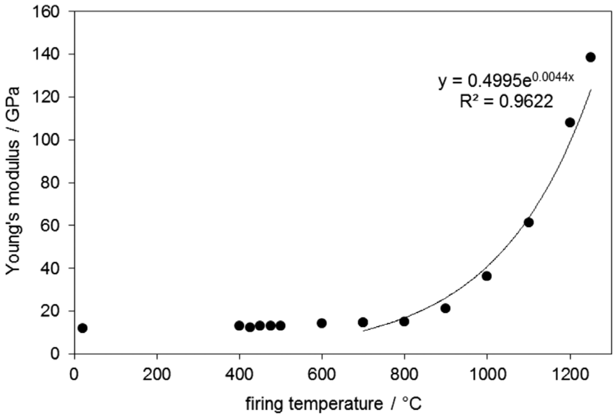

Figure 3: The Young's modulus versus firing temperature
Slika 3: Youngov modul v odvisnosti od temperature žganja

At temperatures of 700–1250 °C, the relationships between the hardness and the firing temperature can be expressed by exponential functions, $HSC = 11.049 \exp(0.0016t)$ and $HV = 0.435 \exp(0.0076t)$. This can be explained by sintering.[23–25]

As follows from **Figure 3**, the relationship between the Young's modulus and the firing temperature is very similar[25] to those of the Shore hardness and the Vickers hardness (**Figures 1** and **2**). The comparison between the Shore hardness and the Vickers hardness is depicted in **Figure 4**. It is clear that the dependence between them is not linear. Nonlinearity is probably caused by multiple processes that take place in the material during measurement. To create an imprint in the Vickers test, the irreversible crush and redisposition of the crystals

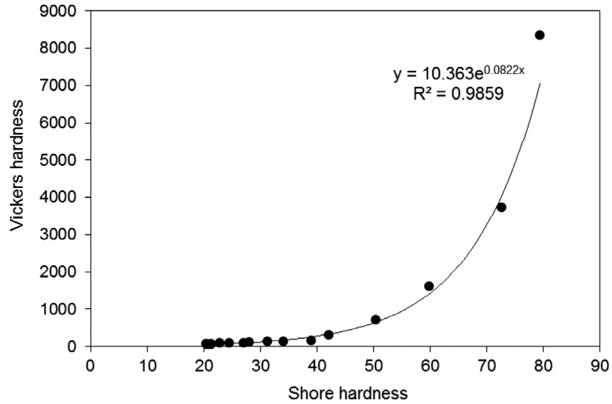

Figure 4: Comparison of the Shore and the Vickers hardnesses
Slika 4: Primerjava trdot po Shoreu in Vickersu

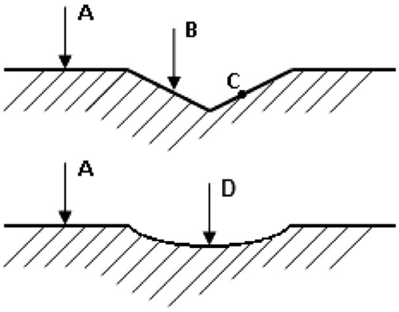

Figure 5: Positions of the sample points visualized by SEM
Slika 5: Položaji točk na vzorcu, prikazani s SEM

occur in the area closest to the sharp pyramidal indenter. This is visible in SEM pictures taken from different points (**Figure 5**) of the sample fired at 950 °C. The sample surface out of the imprint (point A) is shown in **Figure 6**. The surface inside the imprint (point B in **Figure 5**) is clearly ordered: the plate-like crystals are placed and pressed in the plane parallel to the faces of the Vickers pyramid (**Figure 7**). Then the sample was broken to show a fracture surface close to the imprint (point C in **Figure 5**). The thickness of the ordered layer (under the arrows in **Figure 8**) can be estimated, its magnitude being ≈ 3 µm.

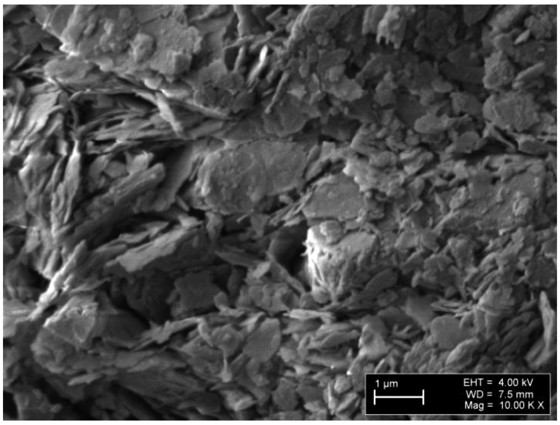

Figure 6: A view of the sample surface at the point A
Slika 6: Videz površine v točki A

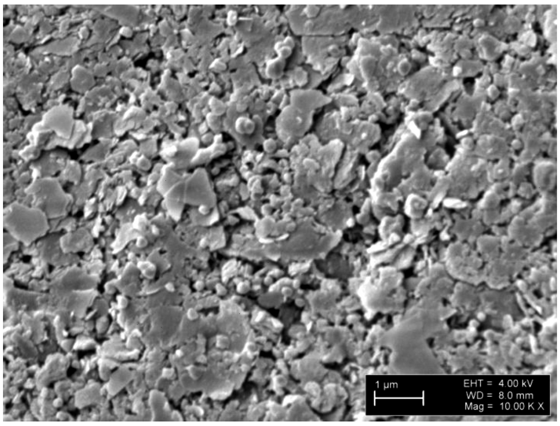

Figure 7: A view of the surface inside the imprint at the point B
Slika 7: Videz površine v vtisku v točki B

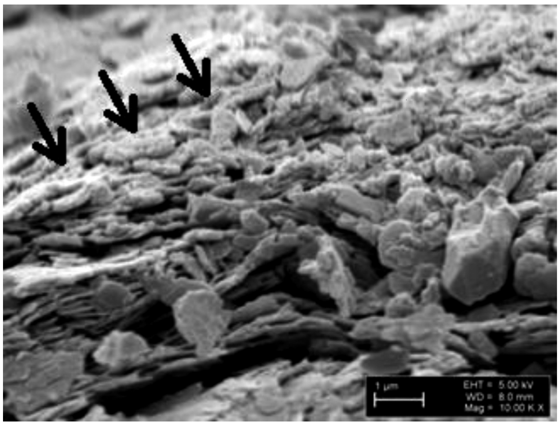

Figure 8: View of the pressed layer (under arrows) at the point C
Slika 8: Videz stisnjene plasti (pod puščicami) v točki C

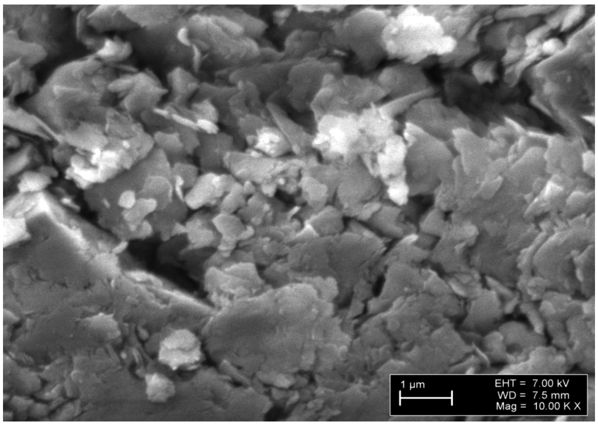

Figure 9: A view of the surface inside the imprint at the point D
Slika 9: Videz površine v vtisku v točki D

In contrast to this, in the Shore test the irreversible changes in the impact area are not so extensive as in the case of the Vickers test, as is shown in **Figure 9** where a sample fired at 950 °C is depicted. The surface inside the imprint (point D in **Figure 5**) is partly ordered: the plate-like crystals are placed and partly pressed in the plane parallel to the spherical imprint. However, a part of the change is reversible. Here the material is partially

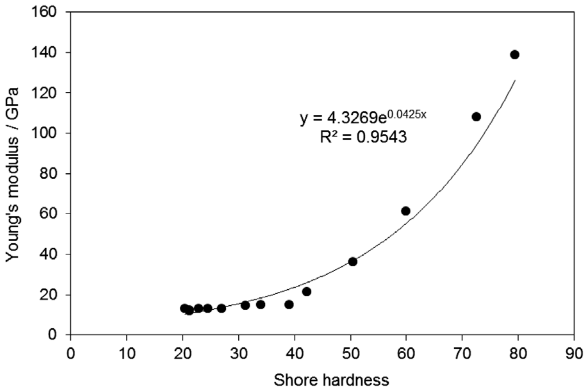

Figure 10: Relationship between the Young's modulus and the Shore hardness
Slika 10: Odvisnost med Youngovim modulom in trdoto po Shoreu

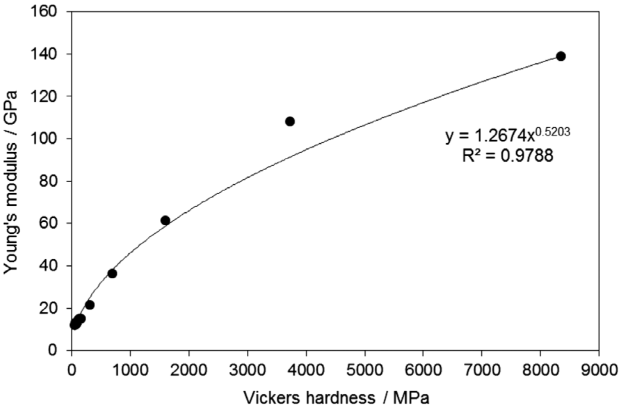

Figure 11: Relationship between the Young's modulus and the Vickers hardness
Slika 11: Odvisnost med Youngovim modulom in trdoto po Vickersu

compressed and decompressed like an elastic spring at the collision between the indenter and the sample.

As noted in the Introduction, we made attempts to find a relationship between the hardness and the Young's modulus. The relationships between the Shore hardness and the Young's modulus as well as between the Vickers hardness and the Young's modulus are shown in **Figures 10** and **11**. They were derived from the results presented in **Figures 1**, **2** and **3**. The experimental data in **Figure 10** can be fitted with an exponential function and the experimental data in **Figure 11** can be fitted with a power function. Both functions have relatively high coefficients of determination.

4 CONCLUSIONS

From the results obtained by the measurement of the hardness on alumina porcelain samples fired at different temperatures we can conclude the following.

The dependencies of the Shore hardness and the Vickers hardness types of hardness on the firing temperature exhibit the same patterns within the three temperature ranges 20–400 °C, 400–700 °C, and 700–1250 °C.

The hardness of the samples fired at temperatures less than 400 °C is approximately the same as the green hardness. This supports the fact that no structural or compositional changes in the sample occur in the 20–400 °C interval.

When dehydroxylation begins (≈ 400 °C), the hardness begins to increase. Until 700 °C the linear increase of the hardness is inhibited by dehydroxylation, which produces electrically charged defects on the surfaces of the kaolinite crystals. The van der Waals forces that act between these defects strengthen the sample structure.

Above 700 °C the hardness increases exponentially, which is related to the sintering and the high-temperature reactions in metakaolinite.

The relationship between the Shore hardness and the Young's modulus can be well fitted with an exponential function (a coefficient of determination $R^2 = 0.9543$), and the relationship between the Vickers hardness and the Young's modulus with a power function (coefficient of determination $R^2 = 0.9788$).

Acknowledgements

This work was supported by grant VEGA 1/0464/12 and VEGA 1/0689/13. The authors are indebted to the ceramic plant PPC Čab for providing the green samples and the chemical analysis, and also to Dr. R. Moravčík (Slovak University of Technology) for help with the Vickers test. A. T. gratefully acknowledges the financial support of the Czech Science Foundation, Project No. P105/12/G059. M. V. acknowledges the support of the Estonian Ministry of Education and Research by the project No. SF0140062s08.

5 REFERENCES

[1] I. Štubňa, A. Trník, F. Chmelík, L. Vozár, Mechanical properties of kaolin-base ceramics during firing, In: C. Sikalidis (Ed.), Advances in Ceramics – characterization, raw materials, processing, properties, degradation and healing, InTech, Rijeka, 2011, 229–244

[2] ASTM E-448, Standard practice for scleroscope hardness testing of metallic materials, 2008

[3] E. Yasar, Y. Erdogan, Eng. Geol., 71 (**2004**), 281

[4] F. I. Shalabi, E. J. Cording, O. H. Al-Hattamleh, Eng. Geol., 90 (**2007**), 138

[5] R. J. Goble, S. D. Scott, Can. Mineral., 23 (**1985**), 273

[6] J. V. Miloserdin, V. M. Baranov, High-temperature testing of reactor materials, Atomizdat, Moskva 1978

[7] J. S. Zvorono, (Dpt. of Applied Mechanics, St. Petersburg State Electrotechnical University): private information

[8] ASTM E 1327-99, Standard Test Method for Vickers Indentation Hardness of Advanced Ceramics, 2008

[9] L. Sidjanin, D. Rajnovic, J. Ranogajec, E. Molnar, J. Eur. Ceram. Soc., 27 (**2007**), 1767

[10] N. A. Travitzky, A. Goldstein, O. Avsian, A. Singurindi, Mat. Sci. Eng. A-Struct., 286 (**2000**), 225

[11] British Standard BST 903, Methods of testing vulcanized rubber, Part 19, 1950 and Part A7, 1957

[12] H. J. Qi, K. Joyce, M. C. Boyce, Rubber Chem. Technol., 76 (**2003**), 419

[13] S. Yagiz, B. Eng. Geol. Environ., 68 (**2009**), 55

[14] O. Katz, Z. Reches, J. C. Roegiers, Evaluation of mechanical rock properties using a Schmidt hammer, Int. J. Rock Mech. Min., 37 (**2000**), 723

[15] G. Vasconcelos, P. B. Laurenco, C. S. A. Alves, J. Pamplona, Prediction of the mechanical properties of granites by ultrasonic pulse velocity and Schmidt hammer hardness, Proc. 10th North American Masonry Conference, St. Louis, Missouri, 2007, 980–991

[16] I. Yilmaz, H. Sendir, Eng. Geol., 66 (**2002**), 211

[17] I. Štubňa, A. Trník, L. Vozár, Acta Acus. united Ac., 97 (**2011**), 1

[18] F. H. Norton, Fine ceramics – technology and applications, McGraw-Hill Book Co., New York 1970

[19] V. Hanykýř, J. Kitzendorfer, Technologie keramiky, Silis Praha and Vega Hradec Králové, Praha, 2000 (in Czech)

[20] F. Freund, Ber. Deutsche Keram. Ges., 44 (**1967**), 5

[21] I. Štubňa, T. Kozík, Ceram. Int., 23 (**1997**), 247

[22] F. Freund, The defect structure of metakaolinite, In: Proc. Int. Clay Conf., Madrid, 1972, 13–25

[23] I. Štubňa, P. Šín, A. Trník, R. Veinthal, Key Engineering Materials, 527 (**2013**), 14

[24] P. Šín, R. Veinthal, F. Sergejev, M. Antonov, I. Štubňa, Mater. Sci. – Medzg., 18 (**2012**), 90

[25] I. Štubňa, A. Trník, P. Šín, R. Sokolář, I. Medveď, Mater. Tehnol., 45 (**2011**) 4, 375–378

UDK 666.3/.7:666.3.017
Original scientific article/Izvirni znanstveni članek

ISSN 1580-2949
MTAEC9, 48(3)337(2014)

BIOMECHANICAL INTERACTIONS BETWEEN BONE AND METAL-CERAMIC BRIDGES COMPOSED OF DIFFERENT TYPES OF NON-NOBLE ALLOYS UNDER VERTICAL LOADING CONDITIONS

BIOMEHANSKA INTERAKCIJA MED KOSTJO IN KOVINSKO-KERAMIČNIM MOSTIČKOM IZ RAZLIČNIH VRST NEPLEMENITIH ZLITIN PRI VERTIKALNIH OBREMENITVAH

Ivan Tanasić, Ljiljana Tihaček Šojić, Aleksandra Milić Lemić
University of Belgrade, School of Dental Medicine, Department of Prosthodontics, Doktora Subotića 8, 11000 Belgrade, Serbia
doktorivan@hotmail.com

Prejem rokopisa – received: 2013-05-21; sprejem za objavo – accepted for publication: 2013-08-29

The purpose of this study was to compare the mechanical properties of three metal-ceramic bridges of different types of dental alloys and to present and evaluate the possible biomechanical interactions between a marginal bone and metal-ceramic bridges during vertical loading. The research was done as an experimental study. A mandible with an intact anterior region was used. The preparation of the remaining teeth for receiving three types of porcelain-fused-to-metal (PFM) restorations was performed. Vita VMK 95 was used for all three metal-ceramic restorations. These three metal-ceramic bridges composed of different alloys, nickel and non-nickel, served as different models: the Niadur-nickelferous model, the Wiron 99-nickel model and the Wirobond C-cobalt-chrome model. The maximum compressive strain of 5 % for all three virtual models is observed in the region of central incisors. The Niadur model has the lowest mean strain (2.62 %) in comparison with the other two models. The mean strain of Wiron 99 is lower, by 0.10 %, than the mean strain of the Wirobond model. Biomechanical behavior of the presented models caused by the vertical-loading conditions is explained as an interaction between the marginal bone and the metal-ceramic bridges. All of them, nickel and non-nickel models, indicate a similar strain (deformation) distribution; however, from the biomechanical perspective, Niadur is more favorable than the other two materials.

Keywords: basic alloys, deformation, biomechanics

Namen te študije je bila primerjava mehanskih lastnosti treh kovinsko-keramičnih mostičkov z različnimi vrstami dentalnih zlitin ter predstavitev in ocenitev morebitne biomehanske interakcije med navidezno kostjo in kovinsko-keramičnim mostičkom med vertikalnim obremenjevanjem. Raziskava je bila opravljena kot eksperimentalna študija. Uporabljena je bila čeljust z nepoškodovanim področjem. Izvršena je bila priprava preostalih zob za namestitev 3 vrst nadomestkov (PFM) iz porcelana, spojenega na kovino. Za vse tri kovinsko-keramične nadomestke je bil uporabljen porcelan Vita VMK 95. Ti trije kovinsko-keramični mostički so bili sestavljeni iz različnih zlitin, z nikljem in brez njega, za pridobitev različnih modelov: Niadur-nikelj železo, Wiron 99-nikelj in Wirobond C-kobalt-krom. Opažen je bil največji tlačni raztezek do 5 % v območju centralnega sekalca pri vseh treh navideznih modelih. V primerjavi z drugima dvema modeloma je imel Niadur najmanjši raztezek 2,62 %. Povprečni raztezek pri Wiron 99 je bil za 0,10 % manjši kot pri modelu Wirobond. Biomehanično vedenje predstavljenih modelov pri vertikalnih obremenitvah je razloženo z interakcijo med navidezno kostjo in kovinsko-keramičnim mostičkom. Vsi modeli z nikljem ali brez njega kažejo podoben raztezek (deformacijo), razen Niadura, ki je s stališča biomehanike bolj ugoden.

Ključne besede: osnovne zlitine, deformacija, biomehanika

1 INTRODUCTION

Besides aesthetics[1] and biocompatibility,[2] dental metal ceramics used for prosthetic reconstruction should have good biomechanical properties.[3,4] As other restorative materials, dental ceramics have disadvantages mostly due to their inability to resist the functional masticatory forces that are present in the oral cavity.[5,6] From the mechanical view point, the life-time of a metal-ceramic bridge depends on the ceramic and alloy mechanical properties.[7] In a ceramic system, the stress intensity (K_1) may exceed the fracture toughness (K_{1c}).[8,9] The toughness that is defined as the discrete (i.e., critical) stress intensity level (K_c) is more expressed in an all-ceramic system than in metal-ceramic restorations.[10] During mastication, compressive, flexural, shear and tensile stresses acting on the ceramic are exerted on the alloy framework, too.[11] Unlike the ceramic responsible for the aesthetics, the alloy framework should be able to withstand the masticatory forces.[12,13] The entire metal-ceramic construction should preserve the marginal-bone integrity to a certain extent.[14]

The following study describes biomechanical behaviors of three different types of dental alloys under vertical-loading conditions, identifying the best one from the biomechanical perspective. The digital image correlation method (DIC) was used for a detailed strain analysis. The purpose of this study was to compare the mechanical properties of three metal-ceramic bridges of different types of dental alloys and to present and evaluate the possible biomechanical interactions between the marginal bone and metal-ceramic bridges during vertical loading.

2 MATERIAL AND METHOD

The research was performed as an experimental study. A mandible with an intact anterior region was used. The mandible was borrowed from the Laboratory for Anthropology, Institute of Anatomy, School of Medicine. According to the data from the Laboratory archive, the mandible donor was female, in her late 60s. The mandible was previously prepared and exposed to occlusal loading.

The preparation procedure was followed by placing the mandible in a saline solution, the drying process and the preparation of the anterior abutment teeth.[15] The preparation of the remaining teeth for receiving three types of the porcelain-fused-to-metal (PFM) restorations was performed. Vita VMK 95 was used as the "ceramic of choice" for all three metal-ceramic restorations. Nevertheless, these three metal-ceramic bridges were composed of different alloys: Niadur-nickelferous (a Cr-Ni alloy), Wiron 99 (a Ni-Cr alloy) and Wirobond C (a Co-Cr alloy). After the first metal-ceramic bridge (Niadur + Vita 95) was obtained, it was pressed with elastomer gum in a standard tray to get an elastomer mold (**Figure 1**) for the next two metal-ceramic bridges. In this way, three models with similar forms were obtained.

The narrow space between the dental roots and the alveoli was coated with a silicone membrane, similar to a periodontal ligament, to reduce the vertical force to a certain extent (**Figure 2**).The mandible with the metal-ceramic bridges positioned in situ was used for obtaining three experimental models: the Niadur model, the Wiron 99 model and the Wirobond C model. Each model had a metal-ceramic bridge made of a different type of alloy. After the preparation procedure, the model was exposed to vertical loading. The average masticatory force was reported to vary between 11 and 150 N, whereas the force peaks were reported to be 200 N in the anterior, 350 N in the posterior and 1000 N in the subjects with parafunctional habits. The load of 300 N was used for the in-vitro experimental analyses. A vertically directed load was applied onto the incisal and occlusal surfaces of

Figure 2: Thin silicone layer imitating a periodontal ligament
Slika 2: Tanek sloj silikona posnema parodontalne vezi

Figure 1: Elastomer mold (impression) for shaping equal metal-ceramic bridges
Slika 1: Forma za elastomer (odtisek), ki se uporablja za enake kovinsko-keramične mostičke

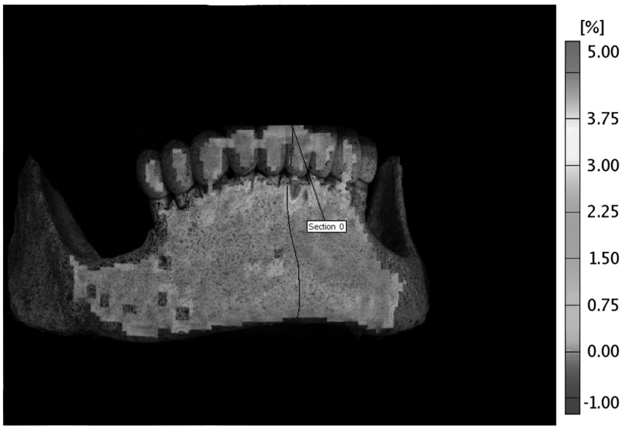

Figure 3: Mandible restored with a metal-ceramic bridge composed of Niadur
Slika 3: Obnovljena čeljust s kovinsko-keramičnim mostičkom iz Niadura

Table 1: Strain values (*e*) and fracture toughness for three mandible models restored with metal-ceramic bridges composed of different base alloys
Tabela 1: Raztezki (*e*) in lomna žilavost pri treh čeljustnih modelih, obnovljenih s kovinsko-keramičnimi mostički iz zlitin z različno osnovo

Tested model (F = 300 N)	$e_{\min}$/%	$e_{\max}$/%	mean strain (%)	No. of measurements before a fracture of the ceramic or marginal bone
NIADUR	0.25	5	2.62	6
WIRON 99	0.5	5	2.75	5
WIROBOND C	0.7	5	2.85	9

the metal-ceramic bridges. The measuring was performed three times for each model, but for each new measurement the next model was used. So, every metal-ceramic model was loaded three times with a gap of 10 min between the measurements. After three cycles of the preliminary loading of different models, they were being loaded until a fracture occurred. The numbers of the cycles leading to the fractures are presented in **Table 1**.

The strain measurement was performed using the equipment from the GOM manufacturer.[16] When a model was loaded, a camera photographed the model stage and the Aramis software processed the obtained data and visualized the strain field. This is represented with virtual models (**Figures 3** to **5**).

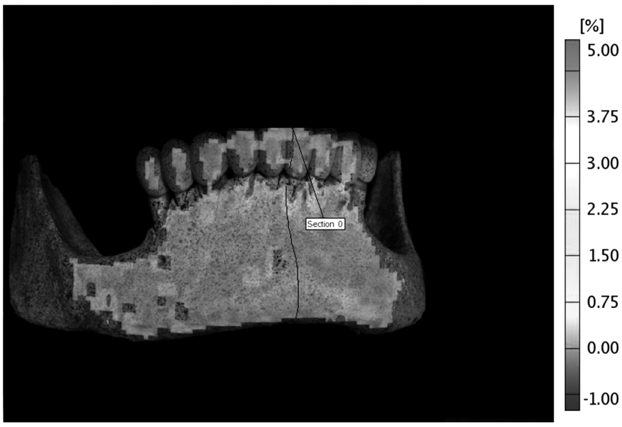

Figure 5: Mandible restored with a metal-ceramic bridge composed of Wirobond C

Slika 5: Obnovljena čeljust s kovinsko-keramičnim mostičkom iz Wirobonda C

3 RESULTS

The maximum compressive strain of 5 % in all three virtual models is observed in the region of the central incisors. All three models have the same strain propagation in the upper part of the mandible body. Nevertheless, the marginal bone in the Wirobond model suffered from a greater overall strain in comparison with the other two Ni-Cr models. This can be explained with the fact that the marginal bone of almost every abutment of the Wirobond model deforms to a greater extent (**Figure 5**) than in the other two cases. The strain values detected on the vestibular surfaces of the metal-ceramic bridge framework are slightly higher in the Wirobond model. Nevertheless, the strain may exceed 3 % in the contact region between the central incisors in the Co-Cr model. The Vita 95 ceramic in the Wirobond model was fractured after nine cycles of the vertical-loading exposure which is slightly better than in the other two models (**Table 1**). Niadur does not induce a higher strain than Wiron 99 (**Figures 3** and **4**). Also, it is noticed that the Niadur model has the lowest mean strain (2.62 %) in comparison with the other two models (**Table 1**). The highest strain in all three virtual models is mainly concentrated in the region of the anterior teeth, especially the incisors. In this region, just below the marginal edge of the metal-ceramic bridge, we notice the highest strain of 5 %, presented with line section 0. **Figure 6** shows the variations in the strain within the section line connecting the two points with the shortest distance (43.9 mm): the incisal edge of the metal-ceramic bridge and the lowest point of the mandible body. The diagram in **Figure 6** indicates that the section line in the region of the metal-ceramic bridge and the marginal bone has the highest strain value in the Wiron 99 model. Although the overall strain in the Wirobond model has a similar distribution to the one in the Wiron 99 model, the mean strain for Wiron 99 is by 0.10 % lower than for the Wirobond model.

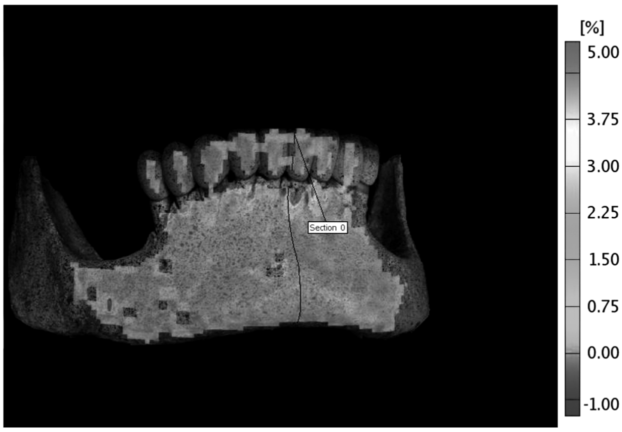

Figure 4: Mandible restored with a metal-ceramic bridge composed of Wiron 99

Slika 4: Obnovljena čeljust s kovinsko-keramičnim mostičkom iz Wirona 99

4 DISCUSSION

For the elderly, losing posterior teeth may influence their chewing ability or cause an abrasion of the anterior teeth and a loss of the vertical dimension. In such a situation, fully covering porcelain-fused-to-metal crowns

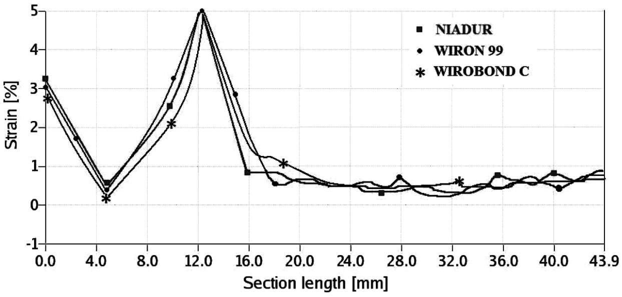

Figure 6: Diagram of the strains within the section lines positioned by the software for every model

Slika 6: Diagram raztezkov vzdolž odsekov, ki jih določi programska oprema za vsak posamezni model or metal-ceramic bridges may be the best choice, having advantages over an all-ceramic system because the fracture failure is more expressed in an all-ceramic system than in metal-ceramic restorations.[17] It is known that most of the elderly persons are not so interested in a removable partial denture because of its discomfort,[18] also rejecting implants in conventional therapy, probably because their expensiveness or surgical procedure. Thus, they occasionally choose a simple solution, deciding not to have all 28 teeth but to save or restore what is left. This study took into account the fact that 8–10 teeth in a jaw (with a minimum of 2 premolars) are enough for elderly persons.[19] As elderly persons with shortened dental arches mostly bite with the anterior teeth, these teeth have to be restored because of the damages (the teeth wear) on their incisal and vestibular surfaces.[20,21]

Many in-vitro techniques for evaluating the mechanical properties of dental alloys or ceramics have been proposed.[22,23] In spite of their apparent simplicity, indentation techniques are burdened with a number of shortcomings related to the specimen preparation, analytical techniques and mathematical analyses.[24] This in-vitro study tends to evaluate and measure the strains caused by loaded metal-ceramic bridges consisting of different alloys. The novelty in this research is that DIC visualizes biomechanical impacts of the frameworks of various alloys on the mandible under vertical loading. This is an elegant and innovative method for researching dental biomechanics that can better explain a distribution of exerted vertical loads. Due to the fact that the applied model (mandible+fixed restorations) is most similar to natural circumstances, it has a great advantage over a standardized specimen.

The study is not a conventional investigation with a standardized specimen. It is an in-vitro investigation where a cadaveric mandible model is loaded within the boundary conditions.[25] A silicone layer was used for the amortization of the applied loads, simulating the periodontal ligament and physiological conditions.[26] Also, a silicon mold was used for standardizing the metal-ceramic frameworks of three different alloys. In this way, similar metal-ceramic models could be obtained and the investigation was conducted with high precision and under the same conditions. The number of loading cycles exerted before the ceramic fracture indicates the fracture toughness[27] of the applied metal-ceramic bridges.

Niadur and Wiron 99 are non-precious alloys, very often used in contemporary dental practice because of their low costs. In dentistry, cobalt-chromium alloys are frequently used for partial denture frameworks. Aditionally, Co-Cr alloys have a substantially higher biocompatibility than Ni-Cr alloys[11,28,29] and, for this reason, they are much more favorable in dental practice. As can be seen in **Table 1**, the Co-Cr model is more resistant to the ceramic fracture than the other two models. This may be explained with the fact that the bond strength is higher in Co-Cr alloys, which is in correlation with the previous finding.[30] This is why the Co-Cr alloy was the alloy of choice when compared with Ni-Cr alloys.

Besides other factors (the metal-ceramic bond strength and the elastic modulus) the extent of the marginal-bone loss may influence the rate of clinical survival of metal-ceramic bridges.[11,31] The study examined and compared three types of ceramics and their impacts on the marginal bone and it was found that there is no significant difference in the strain distribution between the nickel and non-nickel alloys. It was found that a wider strain field is detected on the loaded Co-Cr alloy than on the Ni alloys (**Figure 3**). In this case, every abutment suffered from the same strain intensity. Nevertheless, both nickel alloys (Niadur and Wiron 99) have a similar strain distribution with the highest strain in the region of central incisors (**Figures 1** and **2**). Although dental Co-Cr alloys are widely used in dental practice due to their good mechanical properties and excellent corrosion resistance,[32] this study does not give an advantage to one over the other alloy. However, it is good to know that a Co-Cr based alloy may be an excellent alternative, especially when combining fixed and removable prostheses.[33]

5 CONCLUSION

Within the limitations of this study the following conclusions may be reached:

- The biomechanical behaviors of the presented models caused by vertical-loading conditions are explained as the interactions between the marginal bone and metal-ceramic bridges;
- The aforementioned biomechanical interactions are described as the force-induced strains in the upper part of the mandible bone tissue;
- All the Ni-Cr and Co-Cr models indicate a similar strain distribution, but Niadur is more favorable than the other two from the biomechanical perspective;
- Wiron 99 has a larger impact on the marginal bone than the Wirobond C or Niadur alloys;
- The overall strain has a larger impact in the upper part of the mandible in the case of the Wirobond C model;
- The maximum strains in all the virtual models have the same PIC values that do not exceed 5 %;
- All three semicircular metal-ceramic bridges show the highest strain in the central position between the first incisors.

6 REFERENCES

[1] H. T. Shillingburg, S. Hobo, L. D. Whitsett, R. Jacobi, S. E. Brackett, Fundamentals of fixed prosthodontics, 3rd ed., Quintessence Publishing Co., 1997, 181–210

[2] T. E. Donovan, G. C. Cho, Predictable aesthetics with metal-ceramic and all-ceramic crowns: the critical importance of soft-tissue management, Periodontol 2000, 27 (**2001**), 121–30

[3] M. Persson, M. Bergman, Metal-ceramic bond strength, Acta Odontol Scand, 54 (**1996**), 160–165

[4] G. Libby, M. R. Arcuri, W. E. LaVelle, L. Hebl, Longevity of fixed partial dentures, J Prosthet Dent., 78 (**1997**), 127–131

[5] H. Yilmaz, C. Aydin, B. E. Gul, Flexural strength and fracture toughness of dental core ceramics, J Prosthet Dent., 98 (**2007**) 2, 120–128

[6] A. J. Raidgrodski, Contemporary all-ceramic fixed partial dentures: a review, Dent Clin North Am., 48 (**2004**) 8, 531–544

[7] N. H. J. Creugers, A. F. Käyser, M. A. van't Hof, A meta-analysis of durability data on conventional fixed bridges, Community Dent Oral Epidemiol, 22 (**1994**), 448–452

[8] J. B. Quinn, V. Sundar, I. K. Lloyd, Influence of microstructure and chemistry on the fracture toughness of dental ceramics, Dent Mater., 19 (**2003**), 603–611

[9] H. Fischer, R. Marx, Fracture toughness of dental ceramics: comparison of bending and indentation method, Dent Mater., 18 (**2002**), 12–19

[10] J. J. Mecholsky, Fracture mechanics principles, Dent Mater., 11 (**1995**), 111–2

[11] C. J. Goodacre, G. Bernal, K. Rungcharassaeng, J. Y. K. Kan, Clinical complications in fixed prosthodontics, J Prosthet Dent., 90 (**2003**) 1, 31–41

[12] R. G. Craig, J. M. Powers, J. C. Wataha (editors), Dental materials – properties and manipulations, 7th ed., Mosby-Year Book, St. Louis 2000

[13] M. Ozcan, Fracture reasons in ceramic-fused-to-metal restorations, J Oral Rehabil., 30 (**2003**) 3, 265–269

[14] C. Field, Q. Li, W. Li, M. Thompson, M. Swain, Prediction of mandibular bone remodelling induced by fixed partial dentures, J Biomech., 43 (**2010**), 1771–1779

[15] Lj. Tihacek-Sojic, A. Milic-Lemic, I. Tanasic, N. Mitrovic, M. Milosevic, Compressive strains and displacement in a partially dentate lower jaw rehabilitated with two different treatment modalities, Gerodontol., 29 (**2012**) 2, e851–e857

[16] GOM: http://www.gom.com/

[17] I. Denry, J. R. Kelly, State of the art of zirconia for dental applications, Dent Mater., 24 (**2008**) 3, 299–307

[18] N. Jepson, P. F. Allen, Short and sticky options in the treatment of the partially dentate patient, Br Dent J., 187 (**1999**), 646–652

[19] A. F. Käyser, Minimum number of teeth needed to satisfy functional and social demands, In: A. Frandsen (ed.), Public Health Aspects of Periodontal Disease, Quintessence, Chicago, IL 1984, 135–147

[20] P. T. Sarita, C. M. Kreulen, D. Witter, N. H. Creugers, Signs and symptoms associated with TMD in adults with shortened dental arches, Int J Prosthodont, 16 (**2003**) 3, 265–270

[21] D. J. Witter, N. H. Creugers, C. M. Kreulen, A. F. de Haan, Occlusal stability in shortened dental arches, J Dent Res., 80 (**2001**) 2, 432–436

[22] J. M. Scolaro, A. L. do Valle, Bonding ceramic to metal: A comparison using shear test, Rev Fac Odontol Bauru, 10 (**2002**) 1, 57–62

[23] W. J. Garbelini, G. E. Henriques, M. Jr. Troia, M. F. Mesquita, C. C. Dezan, Evaluation of low-fusing ceramic systems combined with titanium grades II and V by bending test and scanning electron microscopy, J Appl Oral Sci., 11 (**2003**) 4, 354–60

[24] S. S. Scherrer, I. L. Denry, H. W. A. Wiskott, Comparison of three fracture toughness testing techniques using a dental glass and a dental ceramic, Dent Mater., 14 (**1998**), 246–255

[25] I. Tanasic, A. Milic-Lemic, Lj. Tihacek-Sojic, I. Stancic, N. Mitrovic, Analysis of the compressive strain below the removable and fixed prosthesis in the posterior mandible using a digital image correlation method, Biomech Model Mechanobiol., 11 (**2012**) 6, 751–758

[26] M. Kaku, K. Uoshima, Y. Yamashita, H. Miura, Investigation of periodontal ligament reaction upon excessive occlusal load – osteopontin induction among periodontal ligament cells, J Periodontal Res., 40 (**2005**) 1, 59–66

[27] H. Wang, P. Pallav, G. Isgrò, J. Albert Feilzer, Fracture toughness comparison of three test methods with four dental porcelains, Dent Mater., 23 (**2007**) 7, 905–910

[28] J. W. McLean, Evolution of dental ceramics in the twentieth century, J Prosthet Dent., 85 (**2001**) 1, 61–66

[29] A. S. Hiyasat, O. M. Bashabsheh, H. Darmani, Elements released from dental casting alloys and their cytotoxic effects, Int J Prosthodont, 15 (**2002**) 5, 473–478

[30] J. Lenz, S. Schwarz, H. Schwickerath, F. Sperner, A. Schafer, Bond strength of metal-ceramic systems in three-point flexure bond test, J Appl Biomater., 6 (**1995**) 1, 55-64

[31] M. Ozcan, W. Niedermeier, Clinical study on the reasons for and location of failures of metal-ceramic restorations and survival of repairs, Int J Prosthodont, 15 (**2002**) 3, 299–302

[32] A. Carek, J. Živko-Babic, Z. Schauperl, M. Jakovav, Mechanical properties of Co-Cr welded alloy, J Dent Res., 89 (**2010**), 745

[33] S. Viennot, F. Dalard, G. Malquarti, B. Grosgogeat, Combination fixed and removable prostheses using a CoCr alloy: a clinical report, J Prosthet Dent., 96 (**2006**) 2, 100–103

UDK 539.42:620.178.1
Original scientific article/Izvirni znanstveni članek

ISSN 1580-2949
MTAEC9, 48(3)343(2014)

WEAR RESISTANCE AND DYNAMIC FRACTURE TOUGHNESS OF HYPOEUTECTIC HIGH-CHROMIUM WHITE CAST IRON ALLOYED WITH NIOBIUM AND VANADIUM

ODPORNOST PROTI OBRABI IN DINAMIČNA LOMNA ŽILAVOST PODEVTEKTIČNEGA BELEGA LITEGA ŽELEZA, LEGIRANEGA Z NIOBIJEM IN VANADIJEM

Mirjana Filipović[1], Željko Kamberović[1], Marija Korać[1], Zoran Anđić[2]
[1]Department of Metallurgical Engineering, Faculty of Technology and Metallurgy, University of Belgrade, Karnegijeva 4, 11120 Belgrade, Serbia
[2]Innovation Centre of the Faculty of Chemistry, University of Belgrade, Studentski trg 12-16, 11000 Belgrade, Serbia
mirjanaf@tmf.bg.ac.rs

Prejem rokopisa – received: 2013-06-03; sprejem za objavo – accepted for publication: 2013-08-27

The influence of mass fractions 1.5 % Nb and 1.5 % V, added singly and in combination, on the microstructural characteristics and properties relevant to the service performance of the hypoeutectic high-chromium white iron containing 18 % Cr and 2.9 % C, namely, the wear resistance and the fracture toughness, has been examined. The Fe-Cr-C-Nb-V alloy gives the best compromise between the wear resistance and the fracture toughness. The dynamic fracture toughness of this alloy is larger by about 42 % and the abrasion wear resistance is larger by about 33 % than the properties of the basic Fe-Cr-C alloy. The presence of NbC carbides in the structure, caused by adding niobium to the alloy, contributes to an improvement of the wear resistance and the dynamic fracture toughness. On the other hand, the higher fracture toughness was attributed to the strengthening during fracture, since very fine secondary carbide particles were present, mainly in the austenitic matrix (as a result of the vanadium addition). The secondary carbides that precipitate in the matrix regions also influence the abrasion behaviour. By increasing the matrix strength through a dispersion-hardening effect, the fine secondary carbides can increase the mechanical support of M_7C_3 eutectic carbides.

Keywords: Fe-Cr-C-Nb-V alloy, NbC carbides, secondary carbides, wear resistance, fracture toughness

Preučevan je bil vpliv dodatka masnega deleža Nb 1,5 % in V 1,5 %, posamezno in v kombinaciji, na značilnosti mikrostrukture in uporabne lastnosti podevtektičnega kromovega belega železa z 18 % Cr in 2,9 % C ter na obrabno odpornost in lomno žilavost. Zlitina Fe-Cr-C-Nb-V je najboljši kompromis med odpornostjo proti obrabi in lomno žilavostjo. V primerjavi z osnovno Fe-Cr-C-zlitino ima ta zlitina okrog 42 % večjo dinamično lomno žilavost in okrog 33 % večjo odpornost proti abraziji. Prisotnost NbC-karbidov zaradi dodatka niobija zlitini prispeva k izboljšanju odpornosti proti obrabi in povečanju dinamične lomne žilavosti. Po drugi plati se višjo lomno žilavost pripisuje utrjevanju med širjenjem preloma, ker so zelo drobni delci sekundarnih karbidov pretežno v avstenitni osnovi (kot posledica dodatka vanadija). Sekundarni karbidi, ki se izločajo v osnovi, tudi vplivajo na vedenje pri obrabi. S povečanjem trdnosti osnove zaradi učinka disperzijskega utrjevanja drobni sekundarni karbidi lahko povečajo mehansko podporo evtektičnih karbidov M_7C_3.

Ključne besede: zlitina Fe-Cr-C-Nb-V, NbC-karbidi, sekundarni karbidi, odpornost proti obrabi, lomna žilavost

1 INTRODUCTION

High-chromium white cast irons constitute an important class of wear-resistant materials currently used in a variety of applications where the stability in an aggressive environment is the principal requirement, including the mining and mineral processing, cement production, slurry pumping, and the pulp and paper manufacturing industries.

In the case of high-chromium white cast irons, important microstructural parameters for the wear resistance include the volume fraction, hardness, orientation and morphology of carbides[1–5] and the type of matrix.[1,2,6] These factors also influence the hardness and fracture toughness of the material.[1,2,7]

Extensive industrial applications of high-chromium white cast irons have attracted researchers to try different carbide-forming elements such as tungsten,[8,9] vanadium,[8–16] niobium,[8,10,17–22] titanium[10,19,23–26] and boron[27] to further improve this type of material. An addition of an alloying element which confines carbon in the form of a carbide, with a greater hardness and a more favorable morphology, and which reduces the carbon content of the matrix, allows a simultaneous improvement of both toughness and abrasion resistance.[1,9,13,24] By controlling the morphology of the carbide phase and the matrix structure in these materials, a significant improvement in the toughness and service life may be achieved.

An introduction of niobium to these alloys resulted in a preferential formation of NbC which is appreciably harder than the other carbides present and which forms efficiently since niobium is fully partitioned to these phases.[17–19,21] Vanadium appears to be of special interest, due to its double effect on both the matrix structure and stereological characteristics of carbides.[12,14] Subsequently, niobium and vanadium improve the hardness and wear resistance.[10,11,13,20] However, there is little information[1] available concerning the influence of niobium and vanadium on the fracture toughness or explaining how much of these elements should be combined with high-chromium white iron to obtain the optimum fracture toughness and abrasive-wear resistance.

In this study the influence of the mass fractions 1.5 % Nb and 1.5 % V, added singly and in combination, on the microstructural characteristics and properties relevant to the service performance of the hypoeutectic high-chromium white iron containing 18 % Cr and 2.9 % C, namely, the wear resistance and the fracture toughness, was examined.

2 EXPERIMENTAL PROCEDURE

The chemical compositions of the tested alloys are listed in **Table 1**. An induction furnace was used for melting, and rods with a length of 200 mm and a diameter of 30 mm were cast in sand molds. Samples for the structural analysis, hardness, wear, and fracture-toughness tests were cut from the cast rods.

The microstructure was examined using conventional light microscopy (LM) and transmission electron microscopy (TEM). The samples for the light-microscope examinations were prepared using the standard metallographic technique (etched with a picric acid solution (1 g) in methanol (100 mL) with an addition of 5 mL of hydrochloric acid). The sizes and volume fractions of the phases present in the structure were determined using an image analyzer.

The Cr K_α radiation was used for measuring the amount of the retained austenite by means of X-rays, as it is considered to be more appropriate for the structures containing greater amounts of carbides (in order to increase the dispersion, if there are interference peaks, for example).[28] A continuously rotating/tilting specimen holder was used to eliminate the effect of the preferred orientation of the columnar structure, which was shown to affect the results (as described in detail in[29]). At a scanning rate of 1° min^{-1}, the integrated intensities under the peaks of $(200)\alpha$, $(220)\alpha$, $(220)\gamma$ and $(331)\gamma$ were measured with a diffractometer.

The hardness of nickel-chromium and high-chromium white cast-iron alloys was examined with the Vickers method at a load of 294 N. The abrasive wear resistance was evaluated according to the ASTM Standard Practice G-65, Procedure B (dry-sand/rubber wheel abrasion test). Rounded quartz-grain sand with a mesh of 50–70 was used as an abrasive particle. The volume loss, ΔV, was then calculated by dividing the mass loss by the alloy density. The reciprocal value of the volume loss, ΔV, due to the wear is called the wear resistance, ΔV^{-1}. The dynamic fracture toughness was measured at room temperature using an impact test machine equipped with an instrumented Charpy tub. The testing methodology selected was based on the three-point bending tests. The specimens with the dimentions of 10 mm × 10 mm × 55 mm were notched and precracked by fatigue following the ASTM E399 recommendations. The dynamic-stress-intensity factor, K_{Id}, was determined using the following equation:[30,31]

$$K_{\mathrm{Id}} = \left(\frac{P_{\max} S}{BW^{3/2}}\right) f\left(\frac{a}{W}\right) \tag{1}$$

where $P_{\max}$ is the maximum load, S is the span, B is the specimen thickness, W is the specimen width, a is the initial crack length and $f(a/W)$ is the geometry factor.

3 RESULTS

The as-cast microstructure of the tested hypoeutectic white cast irons with a high-chromium content consists primary of austenite dendrites and eutectic colonies,

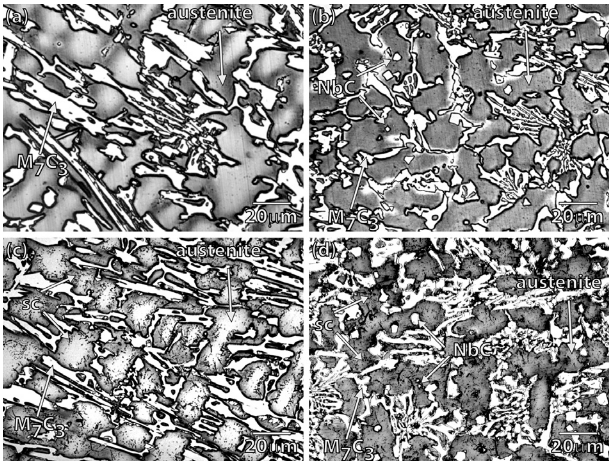

Figure 1: LM micrographs of the: a) basic Fe-Cr-C alloy, b) Fe-Cr-C-Nb alloy containing 1.58 % Nb, c) Fe-Cr-C-V alloy containing 1.55 % V and d) Fe-Cr-C-Nb-V alloy containing 1.53 % Nb and 1.47 % V

Slika 1: Mikrostruktura: a) osnovne Fe-Cr-C-zlitine, b) Fe-Cr-C-Nb-zlitine z 1,58 % Nb, c) Fe-Cr-C-V-zlitine z 1,55 % V in d) Fe-Cr-C-Nb-V-zlitine z 1,53 % Nb in 1,47 % V

Table 1: Chemical compositions of the tested alloys in mass fractions (*w*/%)

Tabela 1: Kemijska sestava preizkušanih zlitin v masnih deležih (*w*/%)

Alloy	C	Si	Mn	Cr	Ni	Mo	Cu	Nb	V
Fe-Cr-C	2.93	0.55	0.85	17.93	0.73	0.92	0.83	–	–
Fe-Cr-C-Nb	2.94	0.59	0.84	17.97	0.71	0.91	0.87	1.58	–
Fe-Cr-C-V	2.89	0.58	0.79	18.12	0.75	0.96	0.86	–	1.55
Fe-Cr-C-Nb-V	2.91	0.51	0.81	18.01	0.70	0.91	0.84	1.53	1.47

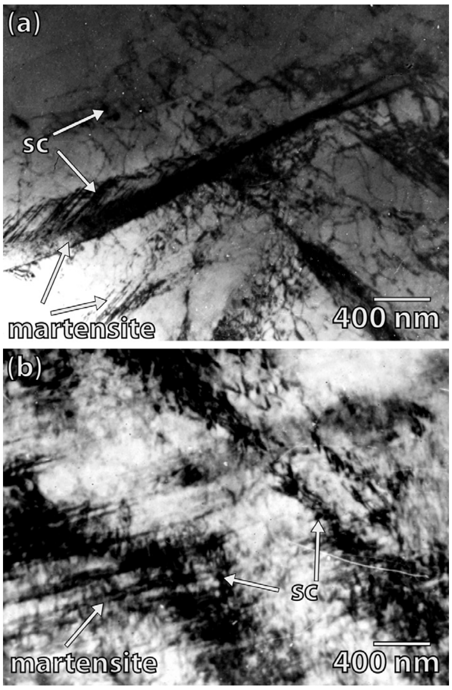

Figure 2: TEM micrographs of the: a) Fe-Cr-C-V alloy and b) Fe-Cr-C-Nb-V alloy showing secondary carbides and martensite
Slika 2: TEM-posnetka: a) Fe-Cr-C-V-zlitine in b) Fe-Cr-C-Nb-V-zlitine s sekundarnimi karbidi in martenzitom

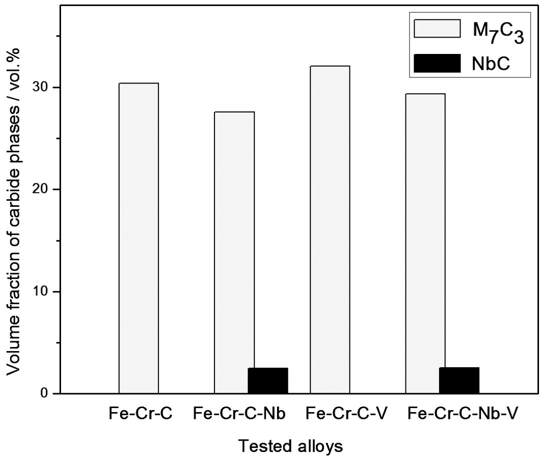

Figure 4: Volume fractions of carbide phases in the tested alloys
Slika 4: Volumenski deleži karbidnih faz v preizkusnih zlitinah

composed of M_7C_3 carbide and austenite (**Figure 1**). Also, nodular- or hexagonal-disc NbC carbides were observed to form in the tested alloys containing niobium (**Figures 1b** and **1d**).

The primary austenite in the basic Fe-Cr-C and Fe-Cr-C-Nb white irons, is mainly stable when cooling down to room temperature (**Figures 1a** and **1b**). Very fine particles are observed in the primary austenite dendrites of Fe-Cr-C-V and Fe-Cr-C-Nb-V alloys (**Figures 1c** and **1d**). In a previous paper[12] these particles precipitating in the matrix were identified to be the carbides of the $M_{23}C_6$ type. Martensite is noticed around the carbide particles (**Figures 2a** and **2b**). The volume fraction of the retained austenite in the tested Fe-Cr-C-Nb alloy is approximately the same as in the basic Fe-Cr-C alloy (**Figure 3**). On the other hand, the amount of the retained austenite is found to decrease in the tested high-chromium white irons, alloyed with vanadium (Fe-Cr-C-V and Fe-Cr-C-Nb-V alloys, **Figure 3**).

The influence of niobium and vanadium on the volume fractions of the carbide phases in the tested alloys is shown in **Figure 4**. The volume fraction of M_7C_3 eutectic carbides decreases with a niobium addition, whereas it increases with a vanadium addition in the tested Fe-Cr-C white iron. The Fe-Cr-C-Nb-V type alloy has approximately the same volume fraction of M_7C_3 carbides as the basic Fe-Cr-C alloy.

Niobium and vanadium influenced the refinement of the structure of high-chromium white cast iron (**Figure 5**). The matrix microhardness of the Fe-Cr-C and Fe-Cr-C-Nb alloys is lower compared to the Fe-Cr-C-V and Fe-Cr-C-Nb-V alloys (**Figure 6**).

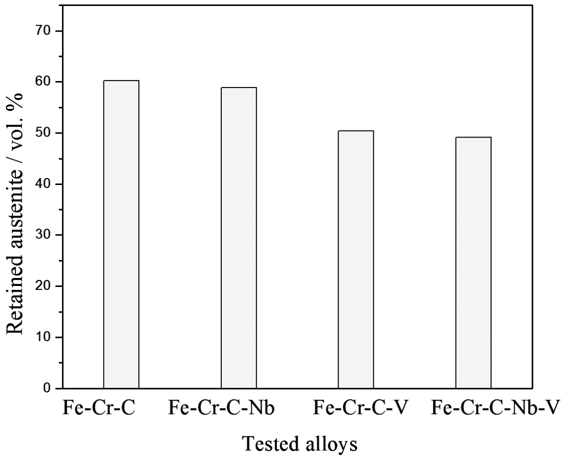

Figure 3: Volume fraction of the retained austenite in the tested alloys
Slika 3: Volumenski delež zaostalega avstenita v preizkusnih zlitinah

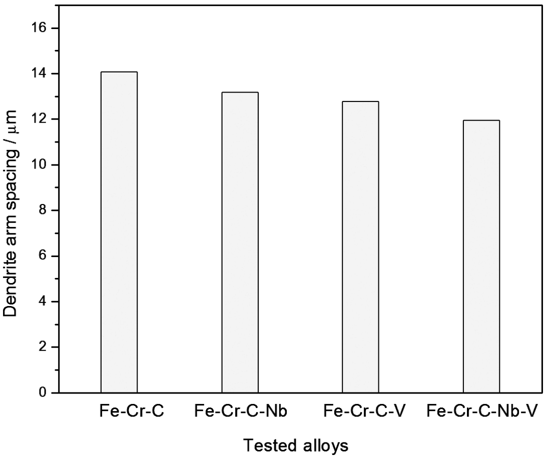

Figure 5: Dendrite arm spacing in the tested alloys
Slika 5: Razdalja med dendritnimi vejami v preizkusnih zlitinah

An addition of 1.5 % Nb and 1.5 % V, singly or in combination, to the Fe-Cr-C alloy with a high chromium amount results in an increase in the hardness, wear resistance and dynamic fracture toughness (**Figures 7**, **8** and **9**, respectively). Niobium makes a greater contribution to the improvement of the wear resistance, whereas vanadium makes a greater contribution to the improvement of the hardness and toughness of the tested alloys in the as-cast condition.

4 DISCUSSION

For the present study, all the alloys were solidified at the same rate and the differences observed are attributed to the effect of the alloying elements.

The changes in the volume fractions (**Figure 4**) and sizes (**Figure 5**) of the phases in the structures of the tested alloys indicate that niobium and vanadium affect the crystallization process in hypoeutectic high-chromium white irons.

Niobium in the Fe-Cr-C-Nb and Fe-Cr-C-Nb-V alloys with high-chromium amounts forms niobium carbides of the MC type. The solubility of niobium in austenite and M_7C_3 carbide is very low, so the majority of the niobium present in the alloy is in the form of an MC carbide.[8,10,17] MC carbides are formed before M_7C_3,[17,21] causing a depletion of the carbon in the liquid. Since carbon is the primary element determining the amount of carbide in high-chromium iron, the amount of M_7C_3 carbide is lower in the Fe-Cr-C-Nb alloy when compared to the basic Fe-Cr-C alloy (**Figure 4**).

As a consequence of alloying high-chromium white iron with vanadium, the solidification-temperature interval is narrower. This effect was considered previously in detail.[14] The eutectic-colony growth rate increases significantly with the increasing eutectic temperature, i.e., with the decreasing solidification-temperature interval, thus stimulating the formation of a larger amount of finer M_7C_3 carbides (**Figure 4**).

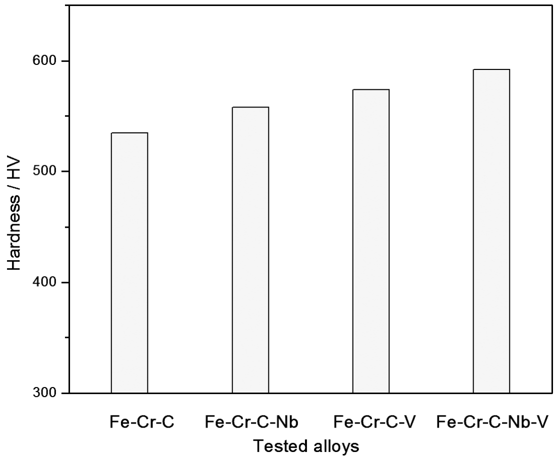

Figure 7: Hardness of the tested alloys
Slika 7: Trdota preizkusnih zlitin

The volume fraction of the M_7C_3 eutectic carbides in the tested Fe-Cr-C-Nb-V alloy is approximately the same as in the basic Fe-Cr-C alloy (**Figure 4**), since, on the one hand, a niobium addition causes a reduction, while vanadium, on the other hand, causes an increase in the amount of the M_7C_3 carbides in the structure.

Vanadium was found to affect the transformation of the austenite in the as-cast condition of the tested Fe-Cr-C-V and Fe-Cr-C-Nb-V alloys (**Figures 1c**, **1d** and **2**). At the temperatures below the solidus, in the course of further cooling after the solidification, $M_{23}C_6$ carbides precipitate in the austenite in the tested alloys containing vanadium (**Figures 1c**, **1d** and **2**). The transformation of the austenite into martensite in these alloys is closely related to the precipitation of secondary carbides. The precipitation of $M_{23}C_6$ carbides minimizes the carbon and chromium amounts in the matrix, and increases the Ms temperature.

Niobium and vanadium altered the microstructure characteristics of the high-chromium white iron and affected its properties.

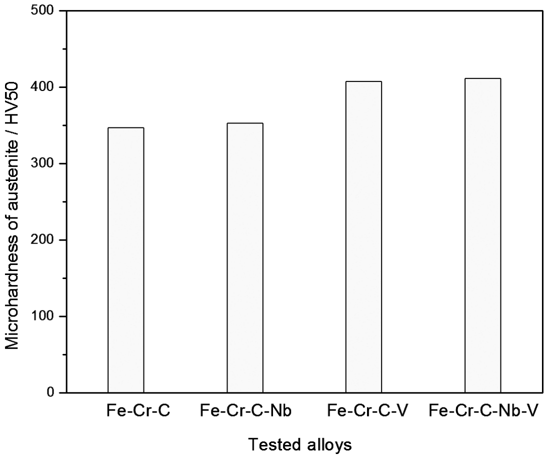

Figure 6: Microhardness of the tested alloys
Slika 6: Mikrotrdota preizkusnih zlitin

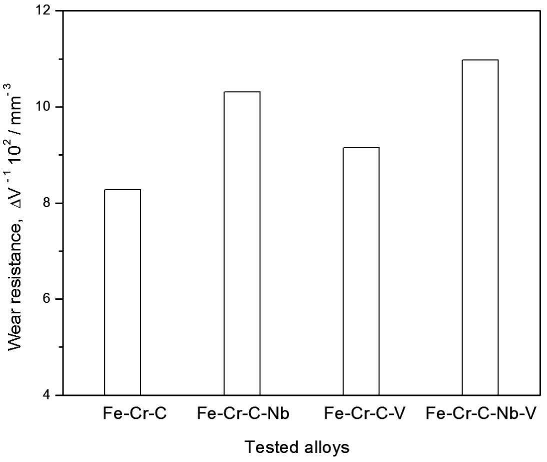

Figure 8: Wear resistance of the tested alloys
Slika 8: Obrabna odpornost preizkusnih zlitin

The improved hardness of the tested Fe-Cr-C-Nb alloy (**Figure 7**) is the result of a presence of hard NbC carbides in the structure (**Figures 1b** and **1d**).

The increased volume fraction of the eutectic M_7C_3 carbides (**Figure 4**), caused by adding vanadium to the Fe-Cr-C white iron, contributes to the improvement of the hardness (**Figure 7**). Moreover, the martensite present in the structure (**Figure 2**), improves the matrix microhardness (**Figure 6**) and, consequently, the alloy macrohardness (**Figure 7**).

The hard NbC carbide phase present in the microstructure (as the result of the niobium addition) and the martensite, together with a reduction in the volume fraction of the retained austenite (as the result of the vanadium addition) contribute to the improvement of the hardness of the tested Fe-Cr-C-Nb-V alloy.

The increase in the volume fraction of the M_7C_3 eutectic carbides in the tested Fe-Cr-C-V alloy and the NbC carbides present in Fe-Cr-C-Nb and Fe-Cr-C-Nb-V alloys (**Figure 4**) reduce the volume loss caused by the abrasive wear (**Figure 8**). The abrasion resistance of the carbide phase was more effective than the matrix in high-chromium white cast irons since, among other things, the hardness values of M_7C_3 carbides (1200–1800 HV)[1,10] and NbC carbides (2370 HV)[10] were greater than the hardness of the abrasive used (960 HV)[1]. Besides, NbC carbides, due to their characteristic morphology, show a higher wear resistance than M_7C_3 carbides. The wear under low-stress abrasion conditions, and in the case of a quartz abrasive, was apparently controlled by the rate of removing the carbide phase, while the protruding carbides protected the matrix from a direct attack of the abrasive particles.

In addition to the volume fraction of the carbides, the size of the phases present in the structure was another microstructure variable that affected the abrasive resistance of the Fe-Cr-C white iron alloyed with niobium and vanadium. The smaller size of the primary austenite dendrites, i.e., the average distance between the carbide particles, caused by adding niobium and vanadium to the alloy (**Figure 5**), protected the matrix better from a direct attack of the abrasive particles.

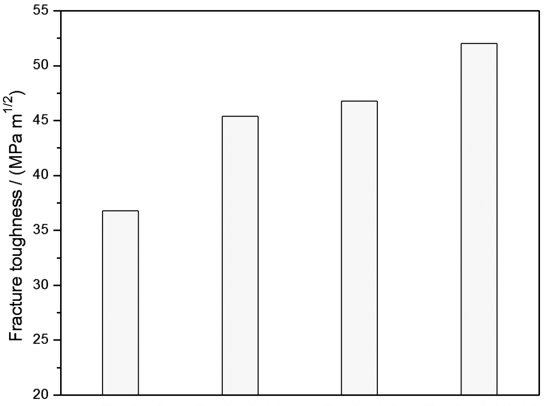

Figure 9: Dynamic fracture toughness of the tested alloys
Slika 9: Dinamična lomna žilavost preizkusnih zlitin

The wear resistance under low-stress abrasion conditions also depended on the matrix microstructure. In addition to the fact that the matrix helped control the penetration depth of the abrasive particles, it also played an important role in preventing a bodily removal of smaller carbides and cracking the massive ones.[3,5,6] Experimental results indicate that the secondary carbides that precipitate in the matrix regions of the tested high-chromium iron containing vanadium influence the abrasion behaviour. By increasing the matrix strength through a dispersion-hardening effect, the fine secondary carbides can increase the mechanical support of the carbides. These results agree with those of Liu et al.[32] and Wang et al.[33] who found that the precipitation of fine $M_{23}C_6$ carbides, as a result of the cryogenic treatment, is responsible for the improved wear resistance of high-chromium white irons.

A brittle failure involved a crack initiation and propagation, the latter being controlled by the fracture toughness. Since the crack moved easily through eutectic carbides, decreasing the volume fraction of the brittle M_7C_3 carbide phase (**Figure 4**), caused by adding niobium to the Fe-Cr-C white iron, it increased the fracture toughness (**Figure 9**). In addition, NbC carbides, due to their characteristic morphology (**Figures 1b** and **1d**), have a higher toughness than M_7C_3 carbides and they, consequently, contribute to an improved fracture toughness of the tested Fe-Cr-C-Nb alloy.

In addition, the results of the fracture-toughness tests (**Figure 9**) show that the dynamic fracture toughness of the tested white irons is also determined by the properties of the matrix. The primary role of the matrix in the fracture process of the high-chromium white cast irons was to prevent the brittle cracks from propagating from one carbide particle to another. The matrix, therefore, had a crack-blunting effect, which subsequently increased the critical stress-intensity factor necessary to continue crack propagation.[1,2]

The vanadium addition to the tested high-chromium white iron increases the volume fraction of the M_7C_3 eutectic carbides and reduces the fracture toughness. Further, the amount of the retained austenite decreases (**Figure 3**), subsequently reducing the toughness. However, the tested alloy containing 1.55 % V showed a greater dynamic fracture toughness when compared to the basic Fe-C-Cr alloy (**Figure 9**). The fracture toughness was determined mainly with the energy that had to be consumed while the crack was extending through the ligaments of the matrix.[1,7] Since the austenite in these alloys contained very fine $M_{23}C_6$ carbide particles, the higher fracture toughness was attributed to the strengthening of the austenite during fracture. The improvement of the fracture toughness of the alloy containing 1.55 % V, due to the presence of fine $M_{23}C_6$ carbides within the austenite, was considerably higher than the reduction caused by an increase in the amount of M_7C_3 carbides and a reduction in the volume fraction of the retained austenite.

Due to the presence of NbC carbides in the structure (as a result of the niobium addition) and the presence of fine $M_{23}C_6$ carbides within the matrix (as a result of the vanadium addition), the tested Fe-Cr-C-Nb-V white iron showed a greater dynamic fracture toughness than the other experimental alloys (**Figure 9**).

It follows from the present results that the alloy containing 1.53 % Nb and 1.47 % V gives the best compromise between the wear resistance and fracture toughness (**Figures 8** and **9**). This alloy shows a dynamic fracture toughness that is greater by about 42 % and an abrasion wear resistance greater by about 33 % than the values for the basic Fe-Cr-C alloy. It may be used to produce dents and hammers for the fibrizer equipment recovering asbestos fibres, and in many other applications where good abrasion resistance and toughness are necessary.

5 CONCLUSIONS

Niobium and vanadium altered the microstructure characteristics of the hypoeutectic high-chromium white cast iron containing mass fractions 18 % Cr and 2.9 % C and affected its mechanical properties.

The alloy containing 1.53 % Nb and 1.47 % V gives the best compromise between the wear resistance and the fracture toughness. The dynamic fracture toughness of this alloy is larger by about 42 % and the abrasion wear resistance is larger by about 33 % than the properties of the basic alloy with no niobium and vanadium additions.

NbC carbides, due to their characteristic morphology, show a higher wear resistance and toughness than M_7C_3 carbides. The presence of this type of carbides in the structure, caused by an addition of niobium to the alloy, contributes to the improvement of the wear resistance and dynamic fracture toughness.

Besides, the higher fracture toughness is attributed to the strengthening during fracture, since very fine secondary carbide particles were present mainly in the austenitic matrix (as the consequence, in this case, of alloying high-chromium white iron with vanadium). The secondary carbides precipitating in the matrix regions also influence the abrasion behaviour. By increasing the matrix strength through a dispersion-hardening effect, the fine secondary carbides can increase the mechanical support of the eutectic carbides.

Acknowledgements

This research was carried out with the financial support for the project No. 34033, "Innovative synergy of by-products, waste minimization and clean technologies in metallurgy", provided by the Ministry of Education, Science and Technological Development of the Republic of Serbia.

6 REFERENCES

[1] C. P. Tabrett, I. R. Sare, M. R. Ghomashchi, Int. Mater. Rev., 41 (**1996**) 2, 59

[2] K. H. Zum Gahr, D. V. Doane, Metall. Trans. A, 11 (**1980**) 4, 613

[3] Ö. N. Doğan, J. A. Hawk, G. Laird II, Met. Mat. Trans. A, 28A (**1997**) 6, 1315

[4] A. Wiengmoon, T. Chairuangsri, J. T. H. Pearce, ISIJ Int., 44 (**2004**) 2, 396

[5] J. J. Coronado, Wear, 270 (**2011**) 11–12, 287

[6] M. Kazemipour, H. Shokrollahi, S. Sharafi, Tribol. Lett., 39 (**2010**) 2, 181

[7] A. Kootsookos, J. D. Gates, Mater. Sci. Eng. A, 490A (**2008**) 1–2, 313

[8] A. Sawamoto, K. Ōgi, K. Matsuda, AFS Trans., 94 (**1986**), 403

[9] Y. P. Wang, D. Y. Li, L. Parent, H. Tian, Wear, 271 (**2011**) 9–10, 1623

[10] A. Bedolla-Jacuinde, Int. J. Cast Metals Res., 13 (**2001**), 343

[11] H. Liu, J. Wang, B. Shen, H. Yang, S. Gao, S. Huang, Mater. Des., 28 (**2007**) 3, 1059

[12] M. Filipovic, E. Romhanji, Z. Kamberovic, M. Korac, Mater. Trans., 50 (**2009**) 10, 2488

[13] M. Filipovic, E. Romhanji, Wear, 270 (**2011**) 11–12, 800

[14] M. Filipovic, Z. Kamberovic, M. Korac, Mater. Trans., 52 (**2011**) 3, 386

[15] M. Filipovic, E. Romhanji, Z. Kamberovic, ISIJ Int., 52 (**2012**) 12, 2200

[16] R. Junsamoot, S. Inthidech, K. Sriprateep, P. Sricharoenchai, Y. Matsubara, J. Met. Mater. Min., 21 (**2011**) 2, 13

[17] R. Kesri, M. Durand-Charre, J. Mater. Sci., 22 (**1987**) 8, 2959

[18] H. K. Baik, C. R. Loper, AFS Trans., 96 (**1988**), 405

[19] C. R. Loper, H. K. Baik, AFS Trans., 97 (**1989**), 1001

[20] C. He-Xing, C. Zhe-Chuan, L. Jin-Cai, L. Huai-Tao, Wear, 166 (**1993**) 2, 197

[21] X. Zhi, J. Xing, H. Fu, B. Xiao, Mater. Lett., 62 (**2008**) 6–7, 857

[22] G. H. Coelho, J. A. Golczewski, H. F. Fischmeister, Met. Mat. Trans. A, 34A (**2003**) 9, 1749

[23] A. Bedolla-Jacuinde, R. Correa, J. G. Quezada, C. Maldonado, Mater. Sci. Eng. A, 398A (**2005**) 1–2, 297

[24] A. Bedolla-Jacuinde, R. Correa, I. Mejía, J. G. Quezada, W. M. Rainforth, Wear, 263 (**2007**) 1–6, 808

[25] X. Wu, J. Xing, H. Fu, X. Zhi, Mater. Sci. Eng. A, 457A (**2007**) 1–2, 180

[26] X. Zhi, J. Xing, H. Fu, Y. Gao, Mater. Charact., 59 (**2008**) 9, 1221

[27] Y. Taşgin, M. Kaplan, M. Yaz, Mater. Des., 30 (**2009**) 8, 3174

[28] J. Durnin, K. A. Ridal, J. Iron Steel Inst., 206 (**1968**) 1, 60

[29] C. Kim, J. Heat. Treat., 1 (**1979**) 2, 43

[30] H. Qiu, M. Enoki, K. Hiraoka, T. Kishi, Eng. Fract. Mech., 72 (**2005**) 10, 1624

[31] K. Prasad, S. V. Kamat, J. Alloys Compd., 491 (**2010**) 1–2, 237

[32] H. Liu, J. Wang, H. Yang, B. Shen, Mater. Sci. Eng. A, 478A (**2008**) 1–2, 324

[33] J. Wang, J. Xiong, H. Fan, H. S. Yang, H. H. Liu, B. L. Shen, J. Mater. Process. Technol., 209 (**2009**) 7, 3236

UDK 669.715:621.7
Original scientific article/Izvirni znanstveni članek

ISSN 1580-2949
MTAEC9, 48(3)349(2014)

MICROSTRUCTURE OF RAPIDLY SOLIDIFIED AND HOT-PRESSED Al-Fe-X ALLOYS

MIKROSTRUKTURA HITRO STRJENIH IN VROČE STISKANIH ZLITIN Al-Fe-X

Milena Voděrová, Pavel Novák, Dalibor Vojtěch

Institute of Chemical Technology, Department of Metals and Corrosion Engineering, Technická 5, 166 28 Prague 6, Czech Republic
voderovm@vscht.cz

Prejem rokopisa – received: 2013-06-07; sprejem za objavo – accepted for publication: 2013-08-28

Rapidly solidified aluminium alloys are promising materials for many technical applications. The main advantages of aluminium alloys alloyed with transition metals, such as Ni, Fe, Cr or Mn, are a good strength-to-weight ratio, a relatively low price, improved mechanical properties and a thermal stability. Mechanical properties of these alloys can be improved with rapid-solidification techniques. In this work, a production method employing melt spinning, cryogenic milling of melt-spun ribbons and the subsequent hot pressing was tested. The Al-11Fe, Al-7Fe-4Cr and Al-7Fe-4Ni alloys were processed in this way. The microstructure and mechanical properties of the prepared alloys were compared with the cast materials of the same composition. The results showed that the proposed technology can lead to a significant microstructure refinement and hardness improvement of the investigated alloys, when compared with the as-cast state. In the case of the Al-Fe alloy, a local coarsening of the $Al_{13}Fe_4$ particles was observed. Hot pressing is suggested to be a promising method for processing rapidly solidified alloys with respect to maintaining a fine structure and satisfactory hardness.

Keywords: rapid solidification, aluminium alloys, hot pressing, microstructure

Hitro strjene aluminijeve zlitine so obetajoč material za različno tehnično uporabo. Glavne prednosti aluminijevih zlitin, legiranih s prehodnimi kovinami, kot so Ni, Fe, Cr ali Mn, so ugodno razmerje med trdnostjo in maso, relativno nizka cena, izboljšane mehanske lastnosti in termična stabilnost. Mehanske lastnosti teh zlitin se lahko izboljša s tehniko hitrega strjevanja. Preizkušena je bila metoda izdelave z uporabo ulivanja tankega traku, kriogeno mletje tankega ulitega traku in končno vroče stiskanje prahu. Tako so bile izdelane zlitine Al-11Fe, Al-7Fe-4Cr in Al-7Fe-4Ni. Mikrostruktura in mehanske lastnosti izdelanih zlitin so bile primerjane z litim materialom z enako sestavo. Rezultati so pokazali, da predložena tehnologija, v primerjavi z litim stanjem, povzroča občutno drobnejšo mikrostrukturo in povišanje trdote. Pri zlitini Al-Fe je bilo opaženo lokalno povečanje delcev $Al_{13}Fe_4$. Domneva se, da je vroče stiskanje obetajoča metoda za obdržanje drobnozrnate strukture in zadovoljive trdote.

Ključne besede: hitro strjevanje, aluminijeve zlitine, vroče stiskanje, mikrostruktura

1 INTRODUCTION

Rapidly solidified aluminium alloys alloyed with transition metals are promising materials for the technical applications requiring improved mechanical properties and a thermal stability.[1,2] However, to be applicable, the powders obtained with atomisation or the thin ribbons obtained with melt spinning have to be compacted. To produce a dense material, several methods are recommended: hot isostatic pressing (HIP), hot extrusion, spark-plasma sintering (SPS) or hot pressing (HP).[3–6] The main request about the manufacturing method for producing a bulk material is to keep the particle size at the lowest possible level. All the listed methods require relatively high temperatures and pressures. Although HIP is beneficial in engineering, it is quite complicated for a laboratory use because of the complex equipment required. For the aluminium alloys investigated in this paper, hot extrusion or hot pressing are the most suitable compaction technologies. Recently, the extrusion of rapidly solidified aluminium alloys has been widely investigated.[7,8] However, in the case of the alloys containing high amounts of intermetallics, such as the investigated Al-Fe-X alloys, hot extrusion requires high temperatures and pressures. In this work, hot pressing as a less demanding alternative was tested. In recent years, the consumption of aluminium alloys in engineering has been rising and this is closely connected with the issue of a waste disposal. Aluminium scrap is often contaminated with a mixture of the elements coming from the steel parts, e.g., Fe, Ni, Cr, Mn, that are very difficult and costly to remove. However, these elements are often recommended to improve the thermal stability of aluminium alloys. The idea that powder metallurgy can be used to recycle the aluminium contaminated with a mixture of elements was already mentioned in[7]. The alloys used in this experiment serve as a model leading to the development of a process for recycling aluminium scrap containing iron and stainless steel.

2 EXPERIMENTAL WORK

The samples of the Al-11Fe, Al-7Fe-4Ni and Al-7Fe-4Cr (mass fractions, *w*/%) alloys were prepared by conventional casting, melt spinning and hot pressing. The chemical compositions of the investigated alloys were chosen in order to model the metallic waste containing, e.g., the stainless steel including relatively high amounts of nickel and chromium. The alloys were prepared by melting the Al-11Fe master alloy and the master alloy with an addition of pure nickel or chromium. In the first step, the alloys were melted in an electric-resistance furnace at 1000 °C and cast into a non-preheated brass mould. After that, the alloys were subjected to a rapid solidification with the melt-spinning technique. In this process, a molten alloy was cast onto a copper-alloy wheel. The melting was carried out under argon protective atmosphere; the temperature of the melt was 1200 °C because of the high liquidus temperatures of the used alloys. The process yields aluminium-alloy ribbons, 30 μm thick. The rotation velocity of the cooling wheel in the melt-spinning process was 1420 r/min, which corresponds to the circumferential speed of 38 m/s. The rapidly solidified alloys were cryogenically milled in a planetary ball mill RETSCH PM 100 in liquid nitrogen in order to ensure an embrittlement of the ribbons and to simplify the milling. The milling was performed for 10 min at 400 r/min. For compacting the material, a universal testing machine LabTest5.250SP1 was used. The milled powders were cold pre-pressed under the pressure of 220 MPa and then heated at 500 °C for 20 min to ensure temperature homogeneity. Hot pressing was performed for 5 min at 500 °C with the maximum pressure of 530 MPa. After hot pressing, a sample was cooled on air. The microstructures of all the samples were investigated with a TESCAN VEGA 3 LMU scanning electron microscope (SEM) equipped with an Oxford Instruments INCA 350 EDS analyser. The mechanical properties of the investigated alloys were examined by measuring the Vickers hardness and microhardness with the 5 kg (HV 5) and 0.005 kg (HV 0.005) loads at room temperature. The results are presented in the form of the average of ten values. The phase composition was determined with X- ray diffraction (XRD, PANalytical X´Pert Pro).

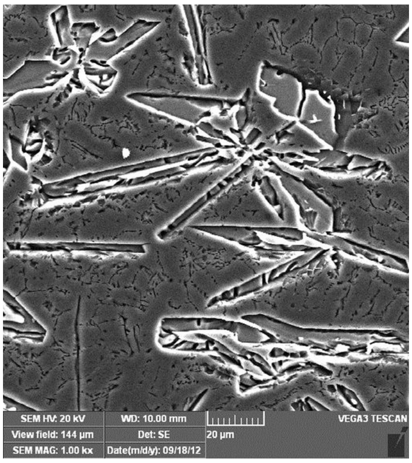

Figure 1: Microstructure of as-cast Al-11Fe (SEM)
Slika 1: Mikrostruktura litega Al-11Fe (SEM)

3 RESULTS AND DISCUSSION

3.1 Microstructure

The microstructures of the as-cast alloys obtained with the scanning electron microscope are shown in the figures, acquired in the backscattered electron mode (BSE). A slow solidification rate causes the evolution of large amounts of irregularly shaped, coarse intermetallic phases. As seen in **Figure 1**, the conventionally cast Al-11Fe consists of large grains of a solid solution of Fe in Al and coarse $Al_{13}Fe_4$ intermetallics (also referred to as $FeAl_3$ in[9]). The nickel added to the as-cast alloy (**Figure 2**) remains dissolved together with the iron in aluminium, while the iron forms coarse particles of $Al_{13}Fe_4$. In an as-cast alloy, chromium is partly dissolved in aluminium or it forms Al_5Cr and $Al_{13}Cr_2$ intermetallics together with stable $Al_{13}Fe_4$, as seen in the **Figure 3**. After increasing the solidification rate, the microstructures of the investigated alloys change significantly. The microstructure of the rapidly solidified ribbon in a longitudinal cut is composed of two main areas; the wheel side and the free side. The wheel side is in the direct contact with

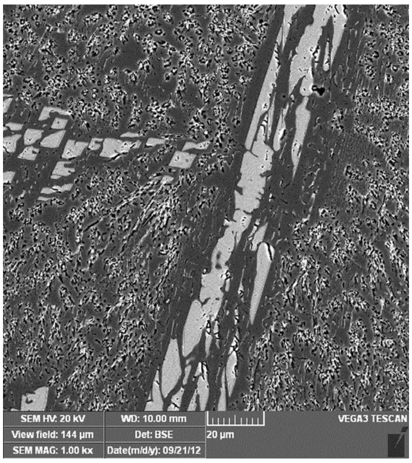

Figure 2: Microstructure of as-cast Al-7Fe-4Ni (SEM)
Slika 2: Mikrostruktura litega Al-7Fe-4Ni (SEM)

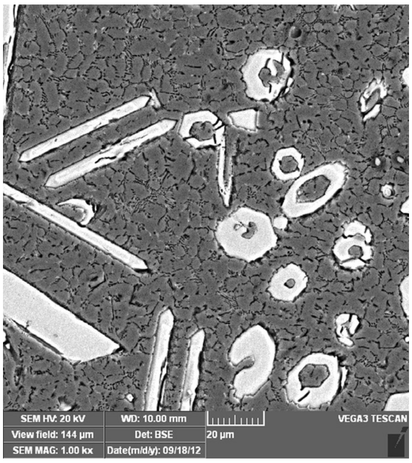

Figure 3: Microstructure of as-cast Al-7Fe-4Cr (SEM)
Slika 3: Mikrostruktura litega Al-7Fe-4Cr (SEM)

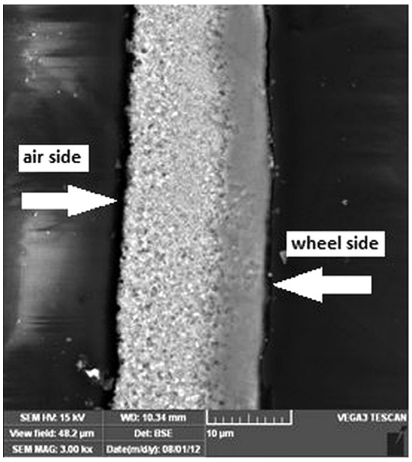

Figure 4: Microstructure of melt-spun Al-11Fe (SEM)
Slika 4: Mikrostruktura hitro strjenega traku iz Al-11Fe (SEM)

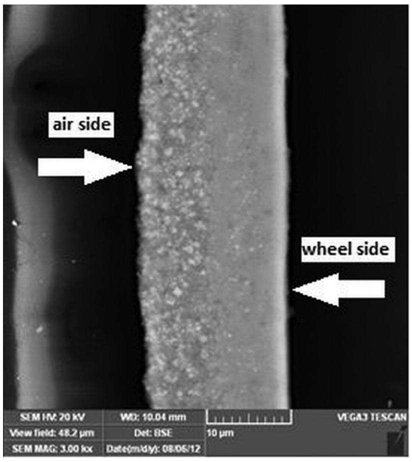

Figure 5: Microstructure of melt-spun Al-7Fe-4Ni (SEM)
Slika 5: Mikrostruktura hitro strjenega traku iz Al-7Fe-4Ni (SEM)

the cooling wheel and it is usually composed of a supersaturated solid solution of the alloying elements in aluminium and low amounts of stable and metastable intermetallics and/or quasicrystals. The free side is cooled less intensely. This area contains more intermetallics that are very fine and round-shaped. The microstructure of the rapidly solidified Al-11Fe alloy in **Figure 4** is composed of a supersaturated solid solution of Fe in Al and nanometre-sized intermetallic phases on the wheel side, while the stable $Al_{13}Fe_4$ and metastable Al_6Fe phases are located on the free side. Both regions of the RS Al-Fe-Ni alloy are composed of a supersaturated solid solution of Ni and Fe in Al, quasicrystalline $Al_{75}Ni_{10}Fe_{15}$ and stable $Al_{13}Fe_4$ and Al_3Ni_2 phases (**Figure 5**). The microstructure of the melt-spun alloy containing chromium in **Figure 6** is composed of a supersaturated solid solution, $Al_{13}Cr_2$ and $Al_{13}Fe_4$ on both sides of the ribbon.

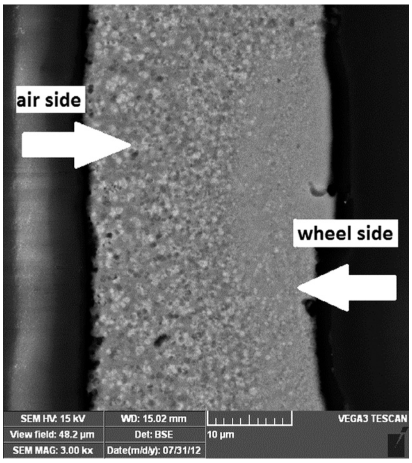

Figure 6: Microstructure of melt-spun Al-7Fe-4Cr (SEM)
Slika 6: Mikrostruktura hitro strjenega traku iz Al-7Fe-4Cr (SEM)

3.2 Milling of rapidly solidified alloys

Rapidly solidified alloys were milled in liquid nitrogen to ensure the embrittlement of the ribbons. The optimum time for milling was determined as 10 min. After 5 min of milling, there was still a large amount of unmilled ribbons, while after 15 min all the nitrogen evaporated; the product became very hot, forming clusters instead of the required powder. The microstructure of milled ribbons is shown in **Figure 7**. From these micrographs it can be seen that the cryogenic milling of RS ribbons does not produce round, but irregularly shaped porous particles of various sizes.

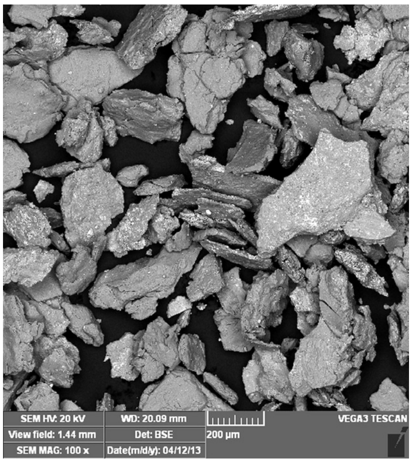

Figure 7: Al-11Fe powder obtained with cryogenic milling (SEM)
Slika 7: Al-11Fe-prah, dobljen s kriogenim mletjem (SEM)

3.3 Hot pressing of rapidly solidified milled powders

The microstructures of the hot-pressed alloys are shown in **Figures 8** to **10**. It is obvious that the microstructure of the hot-pressed Al-11Fe coarsened significantly. The metastable Al_6Fe and supersaturated solution were decomposed to form a large amount of $Al_{13}Fe_4$. Al-7Fe-4Ni has a fine microstructure including fine particles of $Al_{13}Fe_4$ and Al_4Ni_3. The microstructure of the hot-pressed Al-7Fe-4Cr does not change significantly. It contains fine, homogeneously distributed particles of the solid solution, and the $Al_{13}Fe_4$ and $Al_{13}Cr_2$ intermetallic phases. These results suggest a better thermal stability of the ternary alloys. The phase compositions of the investigated alloys in the as-cast, rapidly solidified and hot-pressed state are compared in **Figures 11** to **13**. In the case of Al-11Fe, the as-cast alloy contains a high amount of $Al_{13}Fe_4$ which is transformed, due to a lack of diffusion time, into Al_6Fe after rapid solidification. This metastable phase is then decomposed during hot pressing and a high fraction of $Al_{13}Fe_4$ is formed. The quasicrystals of $Al_{75}Ni_{10}Fe_{15}$ present in the rapidly solidified Al-7Fe-4Ni decompose after hot pressing. The phase

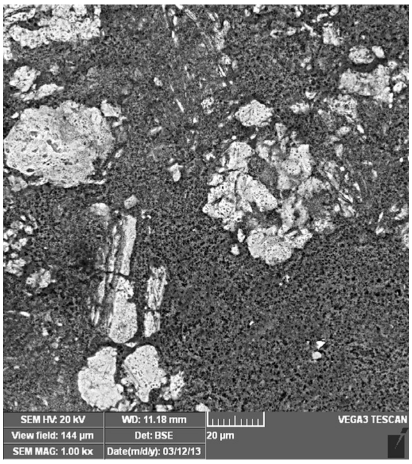

Figure 8: Microstructure of hot-pressed Al-11Fe (SEM)
Slika 8: Mikrostruktura vroče stisnjene zlitine Al-11Fe (SEM)

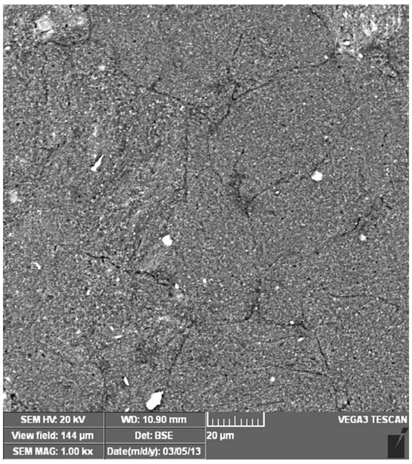

Figure 9: Microstructure of hot-pressed Al-7Fe-4Ni (SEM)
Slika 9: Mikrostruktura vroče stisnjene zlitine Al-7Fe-4Ni (SEM)

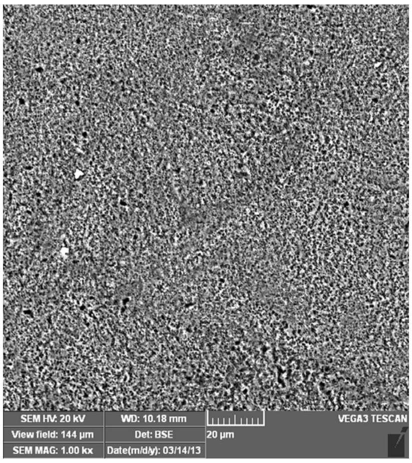

Figure 10: Microstructure of hot-pressed Al-7Fe-4Cr (SEM)
Slika 10: Mikrostruktura vroče stisnjene zlitine Al-7Fe-4Cr (SEM)

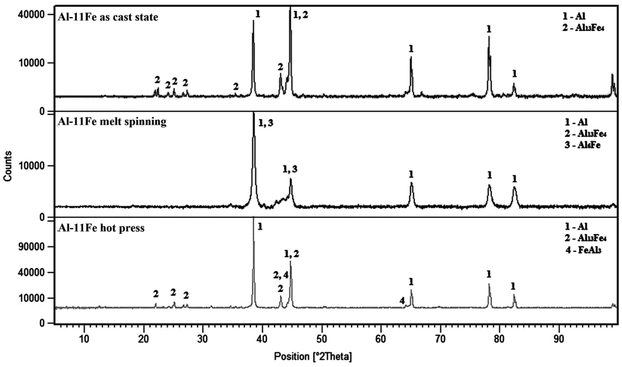

Figure 11: XRD patterns of Al-11Fe prepared with different methods
Slika 11: XRD-posnetki zlitine Al-11Fe, pripravljene z različnimi metodami

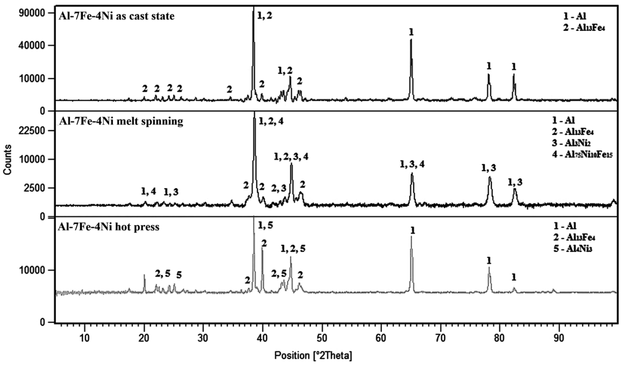

Figure 12: XRD patterns of Al-7Fe-4Ni prepared with different methods
Slika 12: XRD-posnetki zlitine Al-7Fe-4Ni, pripravljene z različnimi metodami

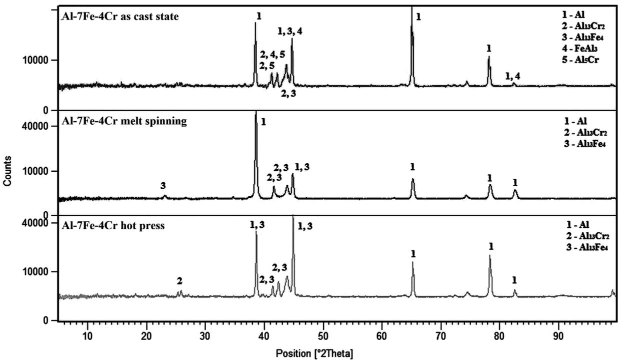

Figure 13: XRD patterns of Al-7Fe-4Cr prepared with different methods
Slika 13: XRD-posnetki zlitine Al-7Fe-4Cr, pripravljene z različnimi metodami

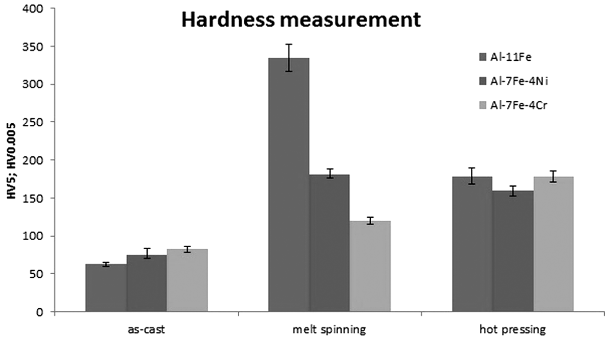

Figure 14: Hardness measurement
Slika 14: Izmerjene trdote

composition of Al-7Fe-4Cr changes after melt spinning but remains the same after further processing.

3.4 Hardness measurement

The results obtained with the hardness and microhardness measurements are summarized in **Figure 14**. The as-cast and hot-pressed materials were measured with the load of 5 kg, while the RS ribbons were measured with the load of 0.005 kg. The microhardness measurement was realised in the centre of the ribbons to avoid interference between the material and the epoxy surrounding the samples. From the diagram it is evident that the increasing solidification rate, resulting in a refined microstructure, increased the hardness as well. A significantly higher value of Al-11Fe is probably caused by a large amount of the hard metastable Al_6Fe. On the other hand, the hardness of Al-11Fe and Al-Fe-Ni decreased after hot pressing, while the hardness of Al-Fe-Cr increased. The decrease in the hardness can be explained as the result of intermetallic coarsening, a decomposition of the metastable Al_6Fe in Al-11Fe and a decomposition of the quasicrystals in Al-7Fe-4Ni. On the contrary, the $Al_{13}Cr_2$ formed in the rapidly solidified Al-7Fe-4Cr is probably more stable and its hardening effect remains present even after hot pressing. In addition, chromium has a lower diffusivity in aluminium than iron and nickel, thus blocking the coalescence and recrystallization of the phases.

However, the elevated temperatures caused a moderate decrease in the hardness. A significant change in the hardness occurred in the case of Al-Fe-Cr, where the values for the rapidly solidified samples increased up to 180 HV, probably due to a precipitation of the $Al_{13}Cr_2$ intermetallic phase.

4 CONCLUSION

In this work, the processing of Al-Fe-X alloys with powder-metallurgy technology including melt spinning and hot pressing was tested. Traditionally, cast alloys are composed of an aluminium matrix containing partly dissolved aluminium elements and coarse intermetallics such as $Al_{13}Fe_4$ in the case of Al-11Fe and Al-7Fe-4Ni, and $Al_{13}Cr_2$ and Al_5Cr in Al-7Fe-4Cr. The rapid-solidification results are given for fine-grained microstructures consisting of supersaturated solid solutions, stable and metastable intermetallic phases. In Al-11Fe, a supersaturated solid solution and metastable phase Al_6Fe are formed, which is probably the main reason for a higher microhardness of the melt-spun ribbons. The melt-spun Al-7Fe-4Ni alloy contains Al_3Ni_2 and a quasicrystalline phase ($Al_{70}Ni_{10}Fe_{15}$). The microstructure of the RS chromium alloy differs only in the amount of intermetallics, which is decreased due to the suppressed diffusion. Rapidly solidified alloys reach the highest values of microhardness primarily due to a very fine microstructure. The microstructures of hot-pressed alloys are fine and homogeneous, except for Al-11Fe where the microstructure coarsened significantly, presumably because of a decomposition of metastable Al_6Fe to the more stable $Al_{13}Fe_4$. This is also the reason for a rapid decrease in the microhardness, while Al-7Fe-4Ni loses only about 10 HV and the microhardness of Al-7Fe-4Cr is even increased. This is probably caused by a large amount of chromium aluminides that did not decompose during milling and hot pressing. All the results show that these alloys can be beneficial in technical engineering and suggest that the processing methods are applicable. The thermal stability of these alloys and mechanical properties at elevated temperatures will be studied further.

Acknowledgement

This research was financially supported by the Czech Science Foundation, project No. P108/12/G043.

5 REFERENCES

[1] E. J. Lavernia, T. S. Srivatsan, Journal of Materials Science and Technology, 45 (**2010**), 287–325

[2] P. Jurči, M. Dománková, M. Hudáková, B. Šuštaršič, Mater. Tehnol., 41 (**2007**) 6, 283–287

[3] S. Billard, J. P. Fondere, B. Bacroix, G. F. Dirras, Acta Materialia, 54 (**2006**), 411–421

[4] N. L. Loh, K. Y. Sia, Journal of Materials Processing Technology, 30 (**1992**), 45–65

[5] L. Wang, J. Zhang, W. Jiang, Int. Journal of Refractory Metals and Hard Materials, 39 (**2013**), 103–112

[6] F. Vollertsen, A. Sprenger, J. Kraus, H. Arnet, Journal of Materials Processing Technology, 87 (**1999**), 1–27

[7] F. Průša, D. Vojtěch, Materials Science and Engineering, A, 565 (**2013**), 13–20

[8] D. Vojtěch, A. Michalcová, F. Průša, K. Dám, P. Šedá, Materials Characterization, 56 (**2012**), 83–97

[9] C. Chen, J. Wang, D. Shu, P. Li, J. Xue, B. Sun, Materials Transactions, 52 (**2011**), 1629–1633

UDK 678.7
Original scientific article/Izvirni znanstveni članek

ISSN 1580-2949
MTAEC9, 48(3)355(2014)

PREPARATION AND CHARACTERIZATIONS OF A NOVEL COPOLYMER BASED ON AN EMULSION SOLVENT EVAPORATION METHOD

PRIPRAVA IN KARAKTERIZACIJA NOVEGA KOPOLIMERA IZDELANEGA Z IZHLAPEVANJEM TOPILA IZ EMULZIJE

Yiqi Huang, Zhaoyu Luo
College of Mechanical Engineering, Guangxi Universitiy, 530004 Nanning, China
hyqgxu@126.com

Prejem rokopisa – received: 2013-06-15; sprejem za objavo – accepted for publication: 2013-07-25

A novel copolymer was synthesized by modifying starch-g-polylactic acid (MSt-g-PLA). The results indicated that the starch was efficiently esterified by maleic anhydride (MAH) (mass fractions, $w = 2\ \%$) with polyethylene glycol-400 (PEG-400, $w = 1\ \%$) as the dispersant. Then MSt-g-PLA was synthesized by employing the modified starch to react with D, L-lactic acid. The copolymer was amphiphilic and its molecular mass and molecular-mass distribution were 4.789×10^4 (M_n), 6.921×10^4 (M_w) and 1.445, respectively. Subsequently, CTX/MSt-g-PLA microspheres containing the model drug and cefotaxime sodium (CTX) were achieved. The appearance of the microspheres was smooth and regular. Some 90 % of the particle size was under 150.3 µm, and the mean diameter was 99.3 µm. The degradation rates of the microspheres increased with the increase of the pH value of the buffer. With the amphiphilic copolymer MSt-g-PLA as a drug carrier, the microspheres had no burst during the drug release, and had a similar sustainable release to the PLA carrier.

Keywords: modified starch-g-polylactic acid (MSt-g-PLA), microspheres, degradation, sustainable release

Nov kopolimer je bil sintetiziran z modificiranjem škroba-g-poli mlečne kisline (MSt-g-PLA). Rezultati so pokazali, da je bil škrob učinkovito esterificiran z anhidridom maleinske kisline (MAH) (masni delež $w = 2\ \%$) in polietilen glikolom-400 (PEG-400, $w = 1\ \%$) kot disperzantom. Nato je bila sintetizirana MSt-g-PLA z uporabo modificiranega škroba, ki je reagiral z D, L-mlečno kislino. Kopolimer je bil amfifiličen in z razporeditvijo molekulske mase $4{,}789 \times 10^4$ (M_n), $6{,}921 \times 10^4$ (M_w) in 1,445. Pozneje so bile dobljene mikrokroglice CTX/MSt-g-PLA, ki so vsebovale modelno zdravilo in natrijev cefotaksim (CTX). Pojav mikrokroglic je bil tekoč in enakomeren. Devetdeset odstotkov delcev je bilo manjših od 150,3 µm in povprečni premer je bil 99,3 µm. Hitrost degradacije mikrokroglic je naraščala z naraščanjem pH-vrednosti pufra. Z amfifiličnim kopolimerom MSt-g-PLA kot nosilcem zdravila se mikrokroglice niso razpočile med sproščanjem zdravila in so omogočale podobno trajno sproščanje kot PLA-nosilec.

Ključne besede: modificiran škrob-g-poli mlečna kislina (MSt-g-PLA), mikrokroglice, razgradnja, trajnostno sproščanje

1 INTRODUCTION

Polymers are used more and more in biotechnology as drug carriers,[1] playing an important role in drug production and in connection with each other, such as protein, amino acid and glycoprotein, especially as polymer anticancer drugs, showing a more promising prospect for applications. Starch is a biodegradable and natural macromolecular material and has wide applications in many industries, especially in pharmacy. For example, starch is assigned as drug forms because of its good biodegradability and biocompatibility, while starch is easy to disintegrate in the mouth, forming hydrogen bonds under saliva. So as to avoid the strong first-pass effect, a lot of research has been done on the modification of starch, of which the esterification reaction is a major part. Polylactic acid (PLA) has been widely used as a biomedical material for good biocompatibility, to be the most promising material in tissue engineering scaffolds, but its high hydrophobicity produces a poor adhesion property, accordingly limiting its application scope. Therefore, studies on PLA copolymer come to be hot topics.[2–4]

It has been reported that starch can be grafted by PLA from lactic acid directly[5,6] or indirectly,[7,8] while starch and PLA are incompatible and their reaction is very weak. However, modification to starch beforehand may improve it.[9–11] There is no report about starch being modified beforehand and much less about the copolymer used as drug carrier in medicine. In this work an biodegradable, biocompatible and amphiphilic copolymer of modified starch-g-polylactic acid (MSt-g-PLA) was prepared efficiently via in-situ graft copolymerization, and CTX/MSt-g-PLA microspheres were synthesized with CTX as a model drug and MSt-g-PLA as a drug carrier. The degradation products of glucose and lactic acid from MSt-g-PLA are innoxious and even necessary for the body, and CTX is a broad-spectrum antibacterial water soluble drug, but an over exact concentration inside the body will cause anaphylaxis. This work has studied how to wrap the drug with sustained-release materials MSt-g-PLA, because the starch chain terminal can enhance solubility and bioavailability, and the PLA terminal can retard the drug dissolving out, and thus it can reach sustained release. MSt-g-PLA will be an ideal drug carrier.

2 EXPERIMENTAL

2.1 Materials

Soluble starch was obtained from the Junle Chemical Plant, Sichuan province, China. DL-Lactic acid (85–90 %), zinc oxide, dichloromethane and acetic ether were from Hongyan Chemical Reagent Plant, Tianjin city. Cis-butenedioic anhydride was from Dengfeng Chemical Reagent Plant, Tianjin city. Tin octoate was from the chemical reagent plant of Tianjin.

2.2 Preparation of MSt-g-PLA

The soluble starch was first modified by solving the soluble starch with 30 % water and a certain amount of esterifier and plastifier, stirring for 2 h at 60 °C, air-drying for 24 h, and standing by for the second step. Secondly, 7 g of modified starch was added to 50 mL of lactic acid, stirring for 1.5 h at 80 °C. After the modified starch was gelatinized by free water (10–15 %) in lactic acid, heating up to 100 °C, when no bubbles came out, a certain amount of catalysts (zinc-oxide and tin octoate) were added, then heating up to 130 °C for 5 h, and 140 °C for 10 h. All the above processes were under continued stirring and vacuum. Thirdly, the product was purified by being solved in acetone, and then the copolymer was precipitated and separated out from the solution by adding ethanol. This procedure was repeated five times. Finally, the MSt-g-PLA was obtained by vacuum drying.

2.3 Synthesis of MSt-g-PLA microspheres

The MSt-g-PLA microspheres were synthesized by an emulsion solvent evaporation method. The organic phase was prepared by solving CTX (0.05 g) and the copolymer (0.2 g) in 10 mL of organic solvent, and dispersed under ultrasonic vibration. The aqueous phase was 50 mL 0.02 g/mL polyvinyl alcohol (PVA) solution. The oil phase was dripped into the aqueous phase slowly in 10 min while stirring at high speed, then slowing down and stirring for 4 h at a moderate speed until the organic solvent evaporated completely. Finally, the microspheres were separated off from the emulsion by centrifuging, washing and vacuum freeze drying.

2.4 Characterization of MSt-g-PLA

The IR spectra were measured on an IR Prestige-21-type apparatus (Japan Shimadzu), scanning in the range of 500–4000 cm^{-1}. The ^1H NMR spectra were recorded on a Bruker TOPSPIN 2.0 spectrometer, with TMS as internal standard, 500 MHz, and DMSO-d6 as a solvent. The morphology of the surface of the microspheres was studied with a JSM-6380 SEM (Japan JEOL), and the particle size of the MSt-g-PLA microspheres was analyzed using a Beckman Counlter LS-230 granulometer (United Kingdom). The adsorbance of the glucose was measured with a UV-visible photometer at 490 nm. The molecular mass of the copolymer was determined on Size-Exclusion Chromatography Coupled with Multi Angle Laser Light Scattering (SEC-MALLS) of DAWN-EOS type, with DMF as solvent, velocity of flow 0.500 mL/min, laser wavelength 690.0 nm at 40 °C (USA, Wyatt).

2.5 In-vitro release of drug-loaded microspheres

Standard curves were formed using the following method. A series of phosphate buffered saline (PBS, pH7.4) solutions containing CTX were prepared, and the CTX concentrations were (40, 20, 10, 5, 2.5, 1.25) mg/mL, respectively. The absorbance was obtained at the maximum absorption wavelength of 213 nm using UV spectrophotometry, and then the standard curve equation of CTX in the PBS was gained, $C = 6.1318A - 1.2822$ (C, mg/mL, $R^2 = 0.9999$).

The drug release rate was measured as follows. A total of 50.0 mg of microspheres and 5 mL of PBS were added to a dialysis bag and sealed, then soaked in 50 mL of PBS (pH 7.4) at 37 °C. Next, a 5 mL sample was taken from the supernatant at (1, 2, 3, 5, 7, 9, 11) h, and a 5 mL of PBS was supplemented immediately, followed by measuring the absorbance of the solution at 213 nm. According to the standard curve equation, the cumulative release percentage of the microspheres could be calculated:

$$\text{release rate} = \frac{\text{the release amount of the drug in solution}}{\text{the total amount of the drug in microspheres}} \cdot 100\%$$

3 RESULTS AND DISCUSSION

3.1 Modification mechanism of the starch

Starch is a water-soluble multi-hydroxy compound, with hydroxyls at the C2, C3 and C6 positions in every glucose unit, possessing plenty of intramolecular as well as intermolecular hydrogen bonds. Two kinds of reactions can occur easily. One is oxidative reaction with a breaking of the bond between the C2 and C3 positions into aldehyde, the other is the esterification of the hydro-

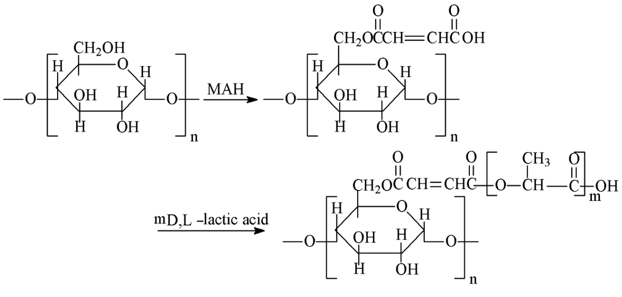

Figure 1: The modification of the starch and the synthesis of the MSt-g-PLA copolymer

Slika 1: Modifikacija škroba in sinteza MSt-g-PLA-kopolimera xyl, much more likely at the C6 position than at the C2 or C3 position (**Figure 1**). It is difficult for hydrophilic starch to react with hydrophobic PLA, so the starch needs to be modified beforehand. PEG-400, containing hydroxyl groups and being hydrophilic and lipophilic, is both a good impregnant and compatibilizer,[11] so as to be a favorable bridge for the increasing affinity of starch with the PLA. MAH, a kind of dicarboxylic anhydride, as an esterifying agent, will introduce a terminal double bond into the starch side-chains, in favor of starch grafting PLA. Thus, the starch was effectively modified with MAH ($w = 2$ %) as the esterifying agent and PEG-400 ($w = 1$ %) as the dispersion medium (**Figure 1**).

3.2 Structural analysis of MSt-g-PLA

Figure 2 is an IR spectra of the MSt-g-PLA (curve b) and the starch esterified by MAH (curve a) in the range 500–4000 cm^{-1}. It can be seen that the carbonyl C=O characteristic absorption peak at 1735 cm^{-1} existed in the curve **Figure 2a**, which also existed in the IR spectra of the MSt-g-PLA at 1755 cm^{-1} (**Figure 2b**), and the methyl peak at 2990 cm^{-1} existed in **Figure 2b** belonging to PLA and the characteristic peak at 2943 cm^{-1} of starch, all of which proved the PLA was grafted onto the modified starch.

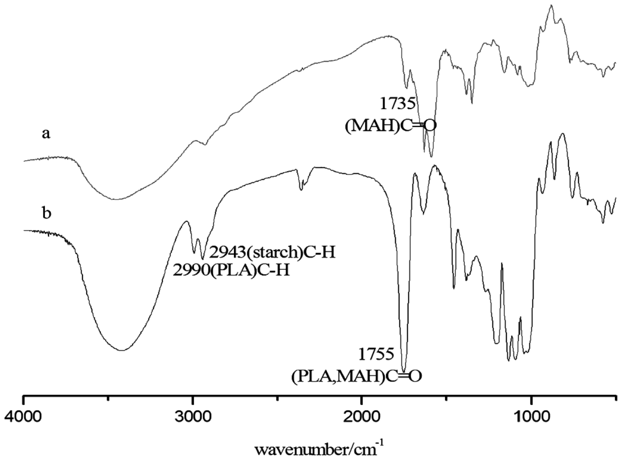

Figure 2: IR spectrum of MSt-g-PLA
Slika 2: IR-spekter MSt-g-PLA

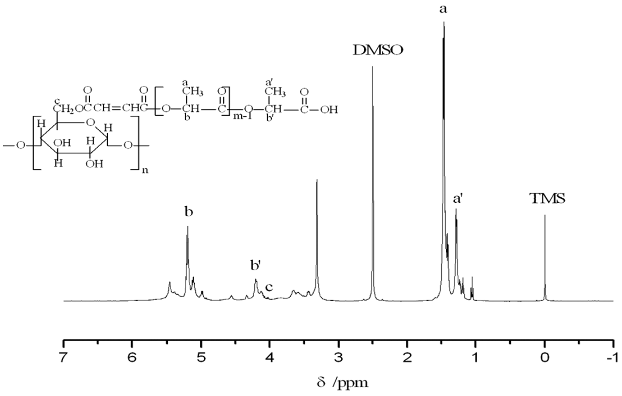

Figure 3: ^{1}H-NMR spectrum of MSt-g-PLA
Slika 3: ^{1}H-NMR-spekter MSt-g-PLA

Figure 3 shows the ^{1}H-NMR spectrum of MSt-g-PLA. The ^{1}H-NMR spectra showed double peaks between $1.46 \cdot 10^{-6}$ and $1.47 \cdot 10^{-6}$ (**Figure 3a**) and four peaks between $5.18 \cdot 10^{-6}$ and $5.22 \cdot 10^{-6}$ (**Figure 3b**), which were resonance peaks of the methyl and methylidyne hydrogen atoms of the PLA interior chain, and the integral intensity ratio was 102 : 36 = 3 : 1, corresponding to the ratio of the number of hydrogen atoms. The peaks at $1.29 \cdot 10^{-6}$ and $4.33 \cdot 10^{-6}$ belong to those of the methyl and methylene hydrogen atoms of the PLA chain terminal, respectively. The peaks between $3.3 \cdot 10^{-6}$ and $5.5 \cdot 10^{-6}$ belong to the methylene and methylidyne hydrogen atoms of the starch main chain. The results showed that the MSt-g-PLA was synthesized effectively. The mean grafting length of the lactic acid was 4.46, counting by the integral intensity ratio of the hydrogen of the interior and the terminal chain of the PLA. The mean hydroxyl number of every anhydroglucose unit (AGU) substituted by PLA was 0.89, counting with the integral intensity ratio of the hydrogen of the PLA side-chain and the starch main chain, and the mol fraction of AGU in the copolymer was 1 : 1.89, which was equivalent to 34 % starch.

The content of starch in the MSt-g-PLA was determined by the phenol-sulfuric acid method. Firstly, the starch was hydrolyzed into glucose and then the content of the glucose was determined by colorimetry. According to the relationship between the glucose concentration (C_G) and the absorbance (A) at a wavelength of 490 nm, the standard curve was drawn as $C_G = 0.017 + 0.302A$. The absorbance of the MSt-g-PLA hydrolysate at 490 nm was 0.56. By using the relationship of C_G and A, the glucose content in the MSt-g-PLA was calculated to be 37 %.

The total mass of starch increased after the hydrolysis due to water absorption based on the equation $(C_6H_{10}O_5)_n + nH_2O \rightarrow nC_6H_{12}O_6$, and this was also proved by the results from the above two methods. Therefore, the biodegradable and amphiphilic copolymer MSt-g-PLA was synthesized and characterized by IR and ^{1}H-NMR.

3.3 Molecular masses of MSt-g-PLA

The molecular masses of the MSt-g-PLA were measured by SEC-MALLS (**Figure 4**). As is clear from **Figure 4**, it was evident that the two peaks were well overlapped to be a single peak. The molecular masses (M_n, M_w) and molecular-mass distribution (M_w/M_n) of the MSt-g-PLA were 4.789×10^4 (M_n), 6.921×10^4 (M_w) and 1.445 (polydispersity index, PDI), respectively. Being of single peak and PDI 1.445 < 2, the results proved that the sample of MSt-g-PLA was a copolymer with a low polydispersity.[9]

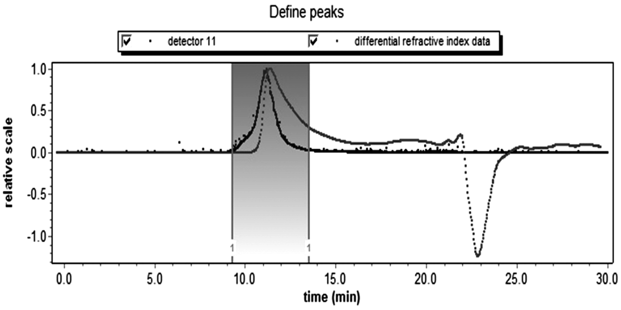

Figure 4: Area graph of laser peaks and differential peaks of starch-g-PLA

Slika 4: Področje laserskega vrha in diferenčnega vrha škrob-g-PLA

3.4 The surface features and qualities of the microspheres

Two organic solvents, dichloromethane and ethyl acetate, were employed to synthesize the MSt-g-PLA microspheres. The comparison of the qualities and micro-morphology of the microspheres was characterized by SEM and particle size analyzer.

It was clear from the SEM (**Figure 5**) that the microsphere surface prepared in dichloromethane was rough, while the surface was smooth and microsphere shape was regular when ethyl acetate was employed as a solvent, and the dispersity was also better (**Figures 5b** and **5d**). This can be attributed to the volatility of the dichloromethane, which was too fast for the microspheres to form into a regular spherical shape (**Figures 5a** and **5c**), while the ethyl acetate volatilized more slowly and displayed much better compatibility with the aqueous phase, so the microspheres had enough time to form into a regular appearance.

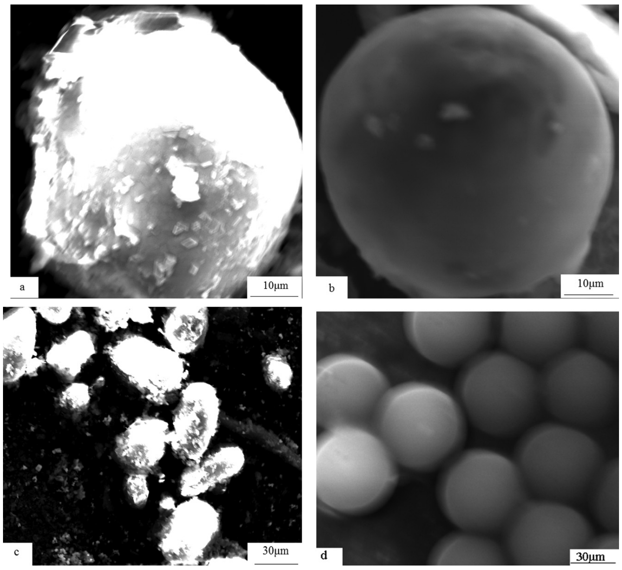

Figure 5: SEM images of microspheres with: a), c) dichloromethane and b), d) ethyl acetate as a solvent

Slika 5: SEM-posnetki mikrokroglic s topilom: a), c) diklormetan in b), d) etil acetat

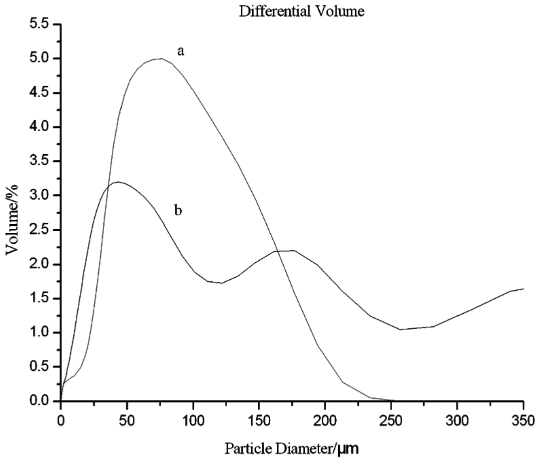

Figure 6: The particle diameter curves of the microspheres with: a) ethyl acetate or b) dichloromethane as a solvent

Slika 6: Krivulje premera mikrokroglic s topilom: a) etil acetat ali b) diklormetan

It was clear that the particle size distribution of the microspheres with ethyl acetate as a solvent (**Figure 6a**) was different from that with dichloromethane as a solvent (**Figure 6b**). There was only one peak displayed in the former curve, while there were two peaks in the latter one at around 0.2 μm and 300 μm. The mean diameter, median diameter and diameter disparity of the former were (99.31, 62.57 and 36.74) μm, respectively, while those of the latter were (111.9, 52.04 and 59.86) μm, respectively, greater than the former, i.e., the microspheres particle distribution in ethyl acetate was uniform and narrow, while to be dispersant and non-uniform in the dichloromethane.

3.5 Hydrolysis rate of the microspheres in different buffer solutions

The hydrolysis of the microspheres in four buffer solutions (**Figure 7**), including Na_2CO_3-$NaHCO_3$ (pH =

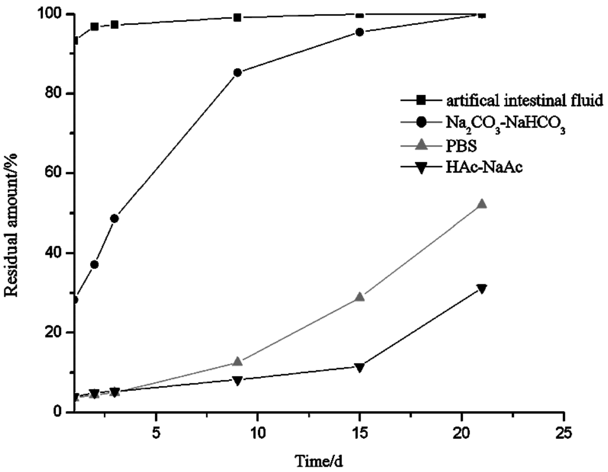

Figure 7: The influence of solvents and pH on the hydrolysis rate of MSt-g-PLA

Slika 7: Vpliv topil in pH na hitrost hidrolize MSt-g-PLA

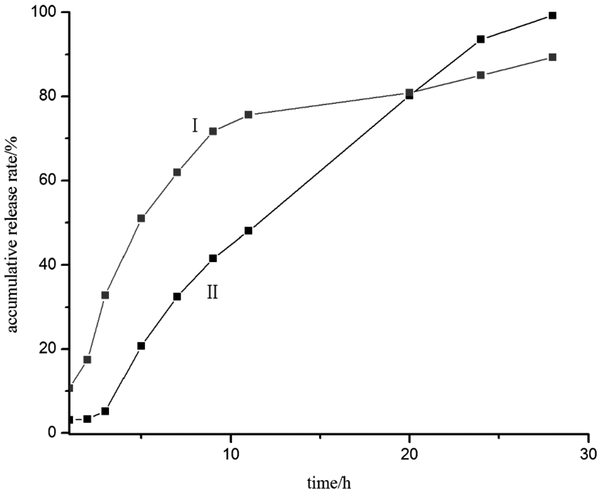

Figure 8: Fraction of cefotaxime sodium in vitro released from the microspheres
Slika 8: Deleža sproščanja natrijevega cefotaksima iz mikrokroglic pri in vitro preizkusu

10.23), phosphate (PBS, pH = 7.4), Simulated Intestinal Fluid (SIF, pH = 6.8), and HAc-NaAc (pH = 4.0), was studied. It was clear that the hydrolytic rate of the microspheres was the fastest in SIF, second in Na_2CO_3-$NaHCO_3$, third in PBS and the slowest in HAc-NaAc. It was easy to see that the stability of the microspheres increased with decreasing pH values, except in the SIF, which was possibly because the SIF contained a mixture of the enzymes of pancreatic juice, such as amylase, lipase, and trypsin, converting starch to sugars and so accelerating the hydrolysis rate.

3.6 Sustained-release behavior of CTX/MSt-g-PLA microspheres in PBS

In order to determine the effect of the MSt-g-PLA microspheres on the CTX release behavior, PLA was selected for the comparison, and the drug-release behavior of the CTX/PLA (I) and CTX/MSt-g-PLA (II) microspheres was evaluated in PBS (**Figure 8**). It was clear that the CTX of I released more quickly than that of II in the initial phase in 10 h. At this stage the drug entered into the water, mainly in the form of diffusion. The interaction between the CTX and MSt-g-PLA was stronger than that with PLA, because the CTX contains nitrogen and oxygen, and there was a hydrogen bond between the cefotaxime sodium and the MSt-g-PLA, while only physical adsorption by van der Waals forces existed between the CTX and the PLA. Therefore, the interaction of the former was stronger than that of the latter. Accompanying the drug release, the microspheres began to swell and the polymer was degraded. Obviously, the amphiphilic MSt-g-PLA degraded faster than the hydrophobic PLA, until the skeleton of the carrier was corroded out in the end, so it was clear that the CTX release rate of II was faster than that of I from 10 h, and after 28 h, nearly the whole drug of II was released. By contrast, the drug of I was released by just less than 90 % because the PLA was degrading more slowly. In short, the drug release of the CTX/MSt-g-PLA microspheres showed no distinct burst phenomenon, and the MSt-g-PLA could be a good drug carrier.

4 CONCLUSIONS

The amphiphilic, biodegradable copolymer, MSt-g-PLA, was successfully synthesized and characterized. Then, MSt-g-PLA microspheres with a regular shape, smooth surface and uniform particle size distribution were prepared, and the properties for the drug release were studied. It was found that the CTX/MSt-g-PLA microspheres exhibited sustained-release performance for the drug CTX. The starch is biocompatible and hydrophilic, and the PLA is highly hydrophobic, indicating a vital role in delaying the decomposition and controlling the drug release. The microspheres composed by such an amphiphilic copolymer can also be applied for a fat-soluble drug. This study provides a preliminary result that will be helpful in the field of medicine.

Acknowledgement

This work was financially supported by the Guangxi Key Laboratory of Manufacturing System & Advanced Manufacturing Technology (Grant No. 10-046-07S04) and Guangxi University of Science and Technology research projects (30131x002).

5 REFERENCES

[1] G. L. Ringsdorf et al., Dipl-Chem, 93 (**2006**) 4, 311–332
[2] G. S. Das, R. F. Wilson, G. H. R. Rao et al., J. Biomed. Mater. Res., 55 (**2001**), 96–103
[3] L. Liu, C. Li, X. Li et al., J. Appl. Polym. Sci., 80 (**2001**), 1976–1982
[4] F. T. Meng, W. Z. Zhang, G. H. Ma et al., Artificial cells, Blood substitutes and Biotechnology, 31 (**2003**) 3, 281–295
[5] L. Chen, X. Y. Qiu, M. X. Deng et al., Polymer, 46 (**2005**) 15, 5723–5729
[6] J. Shao, Y. M. Zhao, China plastics, 23 (**2009**) 10, 15–20
[7] Q. X. Gong, K. H. Tu, L. Q. Wang, Acta Polymerica Sinica, (**2006**) 9, 1045–1049
[8] L. Q. Huang, W. Zeng, J. P. Qu, Plastics Science and Technology, 37 (**2009**) 4, 55–58
[9] H. F. Ma, J. S. He, Herald of Medicine, 22 (**2003**) S1, 132–133
[10] X. H. Chen, Chinese Journal of Primary Medicine and Pharmacy, (**2006**) 9, 1552–1553
[11] F. Yang, Y. Han, Y. M. Zhao et al., Journal of China Pharmacy University, 35 (**2004**) 3, 207–210

UDK 669.018.95:620.178.1
Original scientific article/Izvirni znanstveni članek

ISSN 1580-2949
MTAEC9, 48(3)361(2014)

OPTIMIZATION OF THE PROCESS PARAMETERS FOR DRY-SLIDING WEAR OF AN Al 2219-SiC$_p$ COMPOSITE USING THE TAGUCHI-BASED GREY RELATIONAL ANALYSIS

OPTIMIRANJE PROCESNIH PARAMETROV PRI SUHI OBRABI Z DRSENJEM KOMPOZITA Al 2219-SiC$_p$ S TAGUCHIJEVO SIVO RELACIJSKO ANALIZO

Radhakrishnan Ganesh[1], **Kesavan Chandrasekaran**[2], **Mohammed Ameen**[2], **Raja Pavan Kumar**[2]

[1]Department of Mechanical Engineering, Anna University, Chennai, Tamilnadu, India
[2]Dept. of Mechanical Engineering, R.M.K. Engineering College, Kavaraipettai, Tamilnadu, India
ganesh_akmcmc@yahoo.co.in

Prejem rokopisa – received: 2013-06-18; sprejem za objavo – accepted for publication: 2013-09-04

This article focuses on an approach based on the Taguchi method with grey relational analysis for optimizing the process parameters for the dry-sliding wear of Al 2219-SiC particulate composites with multi-performance characteristics. The grey relational grade obtained with the grey relational analysis is used to optimize the process parameters. The optimum process parameters can then be determined with the Taguchi method using the grey relational grade as the performance index. The composite was fabricated via a powder-metallurgy route with the mass fractions of (10, 15 and 20) % and precipitated at (500, 550 and 600) °C. The dry-sliding-wear test was conducted on a pin-on-disc wear-testing machine for the normal loads of (10, 20 and 30) N and at disc speeds of (400, 500 and 600) r/min. The performance indicators of the wear test were the wear rate, the coefficient of friction, the friction force and the temperature rise of the pin. Further, optimization of the process parameters was performed using the Taguchi-based grey relational analysis followed by ANOVA to determine the percentage contributions of the process parameters to the wear performance of the composites. An L_9 orthogonal array was used for the optimization study. The influences of individual process parameters on the wear performances of the composites are analyzed and presented in this study.

Keywords: optimization, grey relational analysis, wear rate, temperature rise of the pin

Članek obravnava približek, ki temelji na Taguchijevi metodi sive relacijske analize za optimiranje procesnih parametrov pri obrabi s suhim drsenjem zrnatega kompozita Al 2219-SiC z več zmogljivostmi. Za optimiranje procesnih parametrov so bile uporabljene sive relacijske stopnje, dobljene iz sive relacijske analize. Optimalne procesne parametre je mogoče določiti s Taguchijevo metodo z uporabo sive relacijske stopnje kot indeksom zmogljivosti. Kompozit je bil izdelan po postopku prašne metalurgije z masnim deležem (10, 15 in 20) % in izločenem pri (500, 550 in 600) °C. Preizkus obrabe pri suhem drsenju je bil izvršen na napravi "pin on disc" za preizkušanje obrabe pri obremenitvah (10, 20 in 30) N in hitrosti vrtenja plošče s (400, 500 in 600) r/min. Indikatorji zmogljivosti pri preizkusu obrabe so: hitrost obrabe, koeficient trenja, sila trenja in naraščanje temperature preizkušanca. Nadaljnja optimizacija parametrov procesa je bila izvršena s Taguchijevo sivo relacijsko analizo, ki ji je sledila ANOVA za določanje deleža parametrov procesa na vedenje kompozita pri obrabi. Ortogonalna namestitev L_9 je bila vzeta za študij optimiranja. V tej študiji je predstavljen vpliv posameznih parametrov procesa na vedenje obrabe kompozita.

Ključne besede: optimiranje, siva relacijska analiza, hitrost obrabe, narastek temperature preizkušanca

1 INTRODUCTION

Particulate-reinforced aluminium metal-matrix composites are increasingly used in many areas. They are found in the automobile, mining, mineral, aerospace and other applications owing to their very good properties such as high specific stiffness, high specific modulus, low density, good corrosion resistance, wear resistance, etc.[1] Discontinuously reinforced aluminium metal-matrix composites (MMCs) have isotropic properties offering a higher specific stiffness than aerospace metal alloys.[2] Most of the aluminium MMCs have reinforcements such as SiC, alumina, fine graphite, etc.[3–5] An extensive research was done, both experimentally and analytically, on these materials to better understand their mechanical behavior and wear resistance. The presence of hard reinforced particulates has given these composites superior tribological characteristics.[6] The wear resistance, along with a good specific resistance, makes the composites suitable for the applications where a sliding contact is expected. As the wear resistance is a property of primary importance to assess the performance of such components, the tribological behavior of aluminium-alloy-based composites has received strong interest, and work on the sliding and abrasive wears of these materials was comprehensively reviewed by Deuis et al.[7,8] The effects of different parameters such as load, volume fraction, size of reinforcement, sliding distance and velocity on the dry-sliding wear of SiC$_p$-reinforced aluminium alloys have been studied. The sliding speed and load affect the wear mechanism and its rate. As the load and sliding speed increase, the wear rate increases,[9,10] and at high sliding speeds the composites with a higher reinforcement amount show a higher wear resistance.[11] During the wear experiments, the values of the wear rate may reach the minimum for the optimum values of the input variables. The goal of the optimization is to determine the optimum input values for obtaining the minimum or maximum values of the output variable. A successful optimization requires a cause-and-effect relationship (an input-output relationship) between the predictors and the response variables. In the literature several techniques like the Taguchi's approximation, artificial neural networks, genetic algorithms, etc., are described to construct a cause-effect relationship between the variables of a process to optimize the predictor variables. The Taguchi's approximation aims to determine the optimum choice of the levels of the controllable factors in a process of manufacturing a product. The principle of choosing the levels focuses, to a great extent, on the variability around the pre-chosen target for the process response.[12–14]

2 EXPERIMENTATION

The step-by-step procedure of the grey relational analysis is shown in **Figure 1**. **Table 1** shows the chemical composition of the Al 2219 alloy. The control factors considered and their levels are presented in **Table 2**. For conducting the experiments, an L_9 orthogonal array was chosen. Orthogonal arrays are a simplified method of putting together an experiment. It simplifies the number of experiments to be conducted. The L_9 orthogonal array was chosen from the standard array-selector table based on the number of factors, their levels and degrees of freedom. The responses and *S*/*N* ratios are presented in **Tables 3** and **4**. The materials used for the experimentation were the Al 2219 alloy and SiC particulates (with the average particle size of 23 μm) of different mass fractions such as (10, 15 and 20) %. The workpieces were fabricated via a powder-metallurgy technique and the precipitation hardening of all the workpieces was carried out at different temperatures such as (500, 550 and 600) °C. A SEM (scanning electron microscope) image of Al 2219 is shown in **Figure 2**. The wear performance of the aluminum-matrix composites were studied by conducting a wear test using a pin-on-disc wear tester (Ducom, Bengaluru) under dry running conditions shown in **Figure 3**. The responses studied for evaluating the wear behavior of the composites were the wear rate, coefficient of friction, friction force and temperature rise of the pin. The process parameters during the wear test were optimized using the grey relational analysis. The grey relational analysis can effectively manage discrete data sets, uncertainty and multi-response characteristics.[9] The grey relational analysis is a method for measuring the absolute value of a data difference between sequences and it can be used to measure the approximate correla-

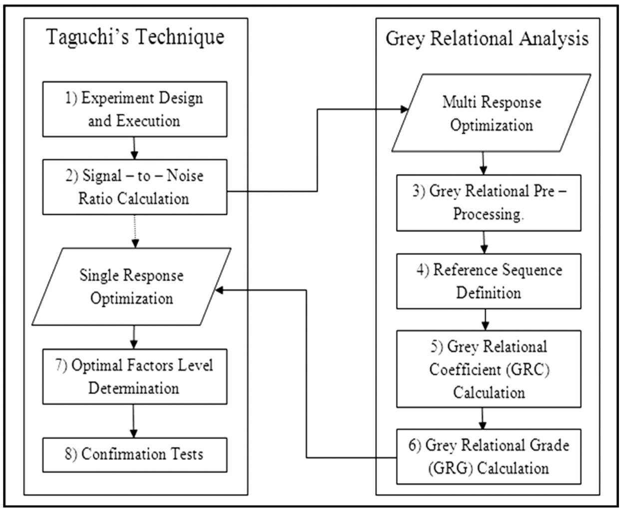

Figure 1: Step-by-step procedure of a grey relational analysis
Slika 1: Koraki postopka sive relacijske analize

Table 1: Chemical composition of the Al 2219 alloy in mass fractions, *w*/%
Tabela 1: Kemijska sestava zlitina Al 2219 v masnih deležih, *w*/%

Alloy composition	Si	Cu	Mn	Zn	Ti	Mg	V	Zr	Al
	0.20	6.00	0.30	0.10	0.10	0.02	0.05	0.10	balance

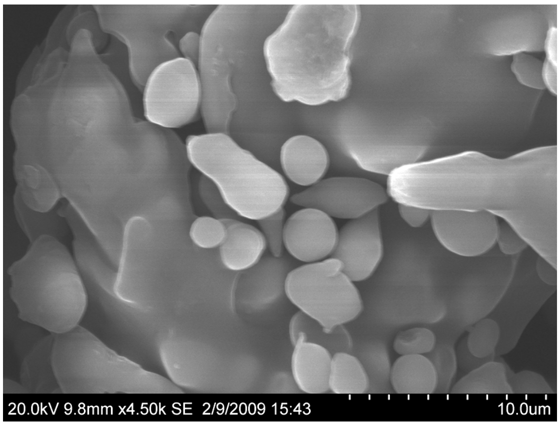

Figure 2: SEM micrograph of an unreinforced aluminium alloy
Slika 2: SEM-posnetek zrn aluminijeve zlitine brez dodatkov

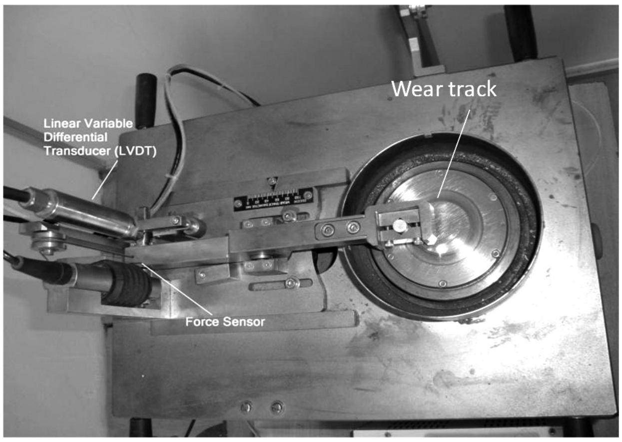

Figure 3: Photograph of a pin-on-disc wear-test set up
Slika 3: Posnetek naprave "pin-on-disc" za preizkus obrabe

tion between sequences.[10] In a grey relational analysis, the experimental observations of the wear rate, coefficient of friction, friction force and temperature rise of the pin are first normalized to be in the range of zero to one. This is called the data pre-processing[10] shown in **Table 5**. It is required because the range and the unit of observation differ from the other indicators. The grey relational coefficient is the measure of relevance between two systems or sequences. The calculated grey relational coefficients for different wear-test conditions are presented in **Table 6**. The grey relational grade is also calculated by taking the average value of the grey relational coefficients and it is presented in **Table 6**.

The signal-to-noise (*S/N*) ratios for the responses are calculated using the following equations:[15]

Nominal the better,

$$S/N \text{ ratio} = 10\lg_{10}\left(\frac{y^2}{s^2} - \frac{1}{n}\right) \tag{1}$$

Smaller the better,

$$S/N \text{ ratio} = -10\lg \frac{1}{\text{n}} \sum_{i=1}^{n} y_i^2 \tag{2}$$

Higher the better,

$$S/N \text{ ratio} = -10\lg \frac{1}{\text{n}} \sum_{i=1}^{n} \frac{1}{y_i^2} \tag{3}$$

where n = the number of trials, y_i = the signal factor or performance characteristic and s^2 = the noise factor. Noise factors are the factors that are impossible or too expensive to control during an experiment. The smaller-the-better criterion was used for the parameters of the wear rate and the temperature rise of the pin and the higher-the-better criterion was used for the parameters of the coefficient of friction and the friction force. The normalization process in the grey relational analysis was done using the following equations:[16]

Nominal the better,

$$Y(k) = \frac{\left|x_i^0(k) - x^0\right|}{\max x_i^0(k) - x_i^0(k)} \tag{4}$$

Smaller the better,

$$Y(k) = \frac{\max x_i^0(k) - x_i^0(k)}{\max x_i^0(k) - \min x_i^0(k)} \tag{5}$$

Higher the better,

$$Y(k) = \frac{x_i^0(k) - \min x_i^0(k)}{\max x_i^0(k) - \min x_i^0(k)} \tag{6}$$

where $Y(k)$ = the normalized value for the k^{th} trial, $x_i^0\,(k)$ = the value of the output parameter for the k^{th} trial, min $x_i^0\,(k)$ = the smallest value of the output parameter x for the k^{th} trial and max $x_i^0\,(k)$ = the largest value of the output parameter x for the k^{th} trial. The grey relational coefficient (*GRC*) for any output parameter can be calculated using the following formula:

$$\delta j = \frac{\Delta_{\min} + \zeta\Delta_{\max}}{\Delta_{oi} + \zeta\Delta_{\max}} \tag{7}$$

where δj = the *GRC* for the j^{th} output parameter,

$\Delta_{oi} = \left|x_i^*(k) - x_i^0(k)\right|$ = the deviation sequence,

$x_0^*\,(k)$ = the reference sequence,

$\Delta_{\min} = \min \left|x_i^*(k) - x_i^0(k)\right|$

$\Delta_{\max} = \max \left|x_i^*(k) - x_i^0(k)\right|$ and

ζ = the mass coefficient. The grey relational grade (*GRG*) is calculated using the following equation:[17]

$$GRG = \frac{1}{\text{n}} \sum_{i=1}^{n} \delta j \tag{8}$$

where n = the number of output parameters.

Table 2: Control factors and their levels
Tabela 2: Kontrolni faktorji in njihovi nivoji

S. No.	Control factor	Coding	Level
1	Mass fraction, %	A	10, 15 & 20
2	Precipitation temperature, °C	B	500, 550 & 600
3	Normal load, N	C	10, 20 & 30
4	Speed of disc, r/min	D	400, 500 & 600

Table 3: L_9 orthogonal array and the values of responses
Tabela 3: Ortogonalna namestitev L_9 in vrednosti odzivov

A	B	C	D	Wear rate (μm/s)	Coefficient of friction	Friction load (N)	Temperature rise of pin (°C)
1	1	1	1	0.0741	0.449	2.339	4.6
1	2	2	2	0.1489	0.4512	8.55	10.2
1	3	3	3	0.1243	0.3292	10.746	13.4
2	1	2	3	0.1708	0.5452	9.775	14.2
2	2	3	1	0.1833	0.486	18.62	13
2	3	1	2	0.1027	0.5699	6.545	7.8
3	1	3	2	0.173	0.5727	15.312	16.6
3	2	1	3	0.0812	0.6435	6.405	12.2
3	3	2	1	0.1864	0.5412	10.292	12.4

Table 4: *S/N* ratio of responses
Tabela 4: Razmerje odzivov *S/N*

A	B	C	D	Wear rate	Coefficient of friction	Friction force	Temperature rise of pin
1	1	1	1	22.60364	–6.95507	7.380604	–13.2552
1	2	2	2	16.54211	–6.91262	18.63932	–20.172
1	3	3	3	18.11058	–9.6508	20.62494	–22.5421
2	1	2	3	15.35024	–5.26888	19.80234	–23.0458
2	2	3	1	14.73675	–6.26727	25.39959	–22.2789
2	3	1	2	19.76859	–4.88403	16.31819	–17.8419
3	1	3	2	15.23908	–4.84146	23.70064	–24.4022
3	2	1	3	21.80888	–3.82903	16.13038	–21.7272
3	3	2	1	14.59108	–5.33284	20.25	–21.8684

Table 5: Normalized values and deviation sequences of responses
Tabela 5: Normalizirane vrednosti in deviacijske sekvence odzivov

Exp. number	Normalized values of responses				Deviation sequences			
	Wear rate (μm/s)	Coefficient of friction	Friction load (N)	Temperature rise of pin (°C)	Wear rate (μm/s)	Coefficient of friction	Friction load (N)	Temperature rise of pin (°C)
1	1.0000	0.3812	0.0000	1.0000	0.0000	0.6188	1.0000	0.0000
2	0.3339	0.3882	0.3815	0.5333	0.6661	0.6118	0.6185	0.4667
3	0.5530	0.0000	0.5164	0.2667	0.4470	1.0000	0.4836	0.7333
4	0.1389	0.6872	0.4567	0.2000	0.8611	0.3128	0.5433	0.8000
5	0.0276	0.4989	1.0000	0.3000	0.9724	0.5011	0.0000	0.7000
6	0.7453	0.7658	0.2583	0.7333	0.2547	0.2342	0.7417	0.2667
7	0.1193	0.7747	0.7968	0.0000	0.8807	0.2253	0.2032	1.0000
8	0.9368	1.0000	0.2497	0.3667	0.0632	0.0000	0.7503	0.6333
9	0.0000	0.6745	0.4885	0.3500	1.0000	0.3255	0.5115	0.6500

Table 6: Grey relational coefficient and grey relational grade
Tabela 6: Sivi relacijski koeficient in siva relacijska stopnja

Experiment number	Grey relational coefficient				Grey relational grade
	Wear rate (μm/s)	Coefficient of friction	Friction load (N)	Temperature rise of pin (°C)	
1	1.0000	0.4469	0.3333	1.0000	**0.6951**
2	0.4288	0.4497	0.4470	0.5172	0.4607
3	0.5280	0.3333	0.5083	0.4054	0.4438
4	0.3674	0.6152	0.4793	0.3846	0.4616
5	0.3396	0.4994	1.0000	0.4167	0.5639
6	0.6625	0.6810	0.4027	0.6522	0.5996
7	0.3621	0.6894	0.7111	0.3333	0.5240

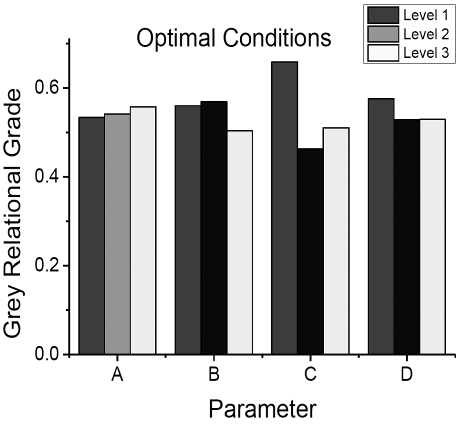

Figure 4: Grey relational grades for optimal conditions
Slika 4: Sive relacijske stopnje pri optimalnih razmerah

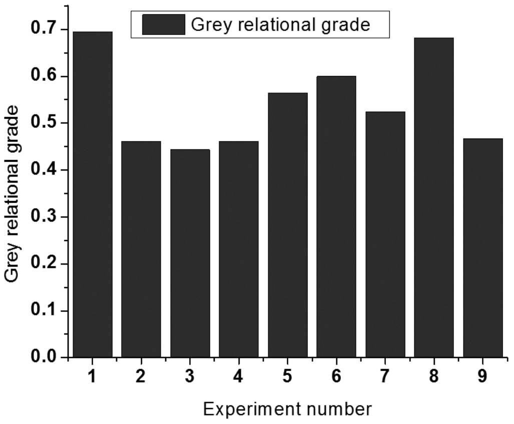

Figure 5: Grey relational grade versus experiment number
Slika 5: Siva relacijska stopnja proti številki preizkusa

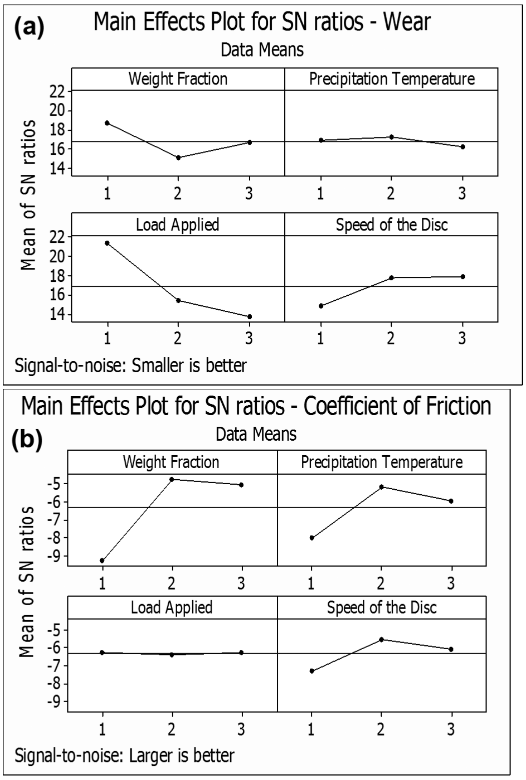

Figure 6: Main effects plot for *S/N*: a) wear, b) coeffition of friction
Slika 6: Glavni učinki razmerja *S/N* na: a) hitrost obrabe in b) koeficient trenja

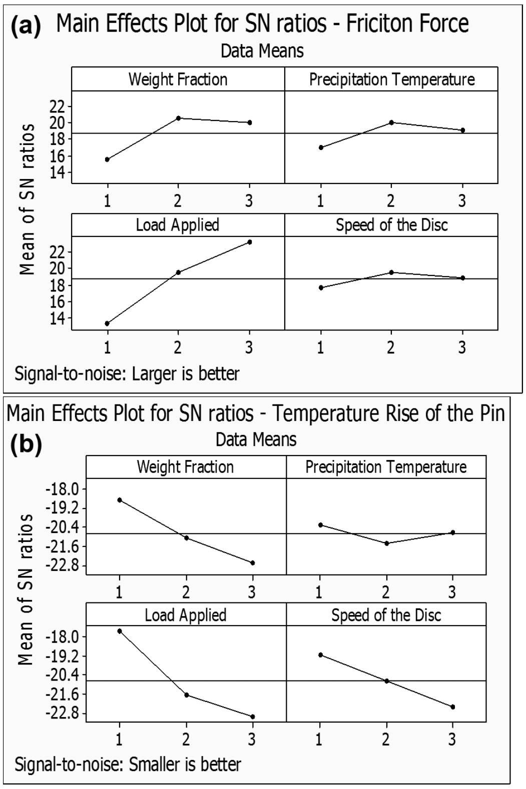

Figure 7: Main effects plot for *S/N* ratios of: a) friction force and b) temperature rise of pin
Slika 7: Glavni učinki razmerja *S/N* na: a) silo trenja in b) dvig temperature vzorca

Table 7: Optimum conditions of control factors
Tabela 7: Optimalne razmere kontrolnih faktorjev

Factor	Level 1	Level 2	Level 3
Mass fraction	0.5332	0.5417	**0.5577**
Precipitation temperature	0.5602	**0.5689**	0.5035
Load	**0.6590**	0.4631	0.5106
Speed	**0.5753**	0.5281	0.5292
Average value = **0.5442**			

Table 8: ANOVA for control factors
Tabela 8: ANOVA za kontrolne faktorje

Testing parameter	Degrees of Freedom	Sum of squares	Mean sum of squares	Percentage contribution
Mass fraction, %	2	0.0010	0.0005	0.0144
Precipitation temperature, °C	2	0.0149	0.0074	0.2197
Load, N	2	0.0485	0.0242	0.7160
Disc speed, r/min	2	0.0034	0.0017	0.0499
Error	72	0.0000	0.0000	0.0000
Total	80	0.0677		

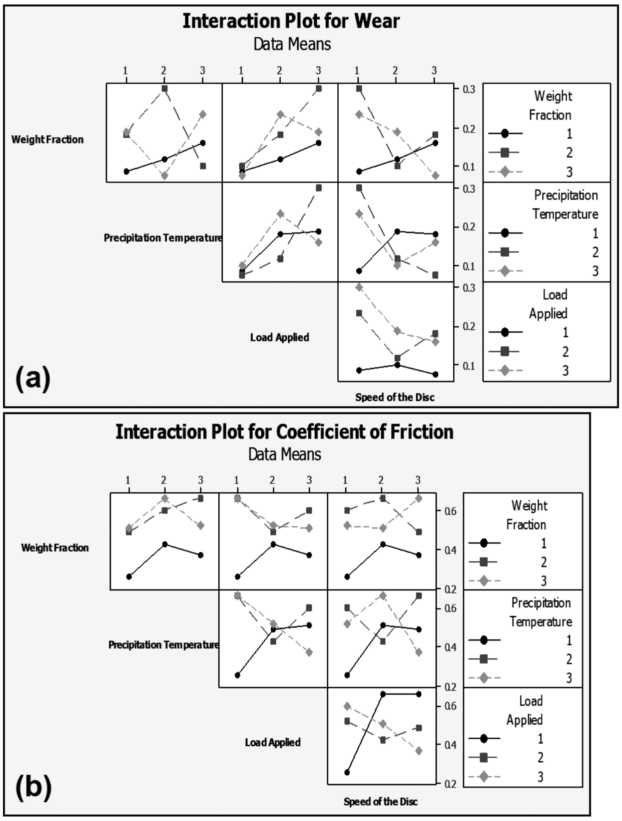

Figure 8: Interaction plot for data means of: a) wear rate and b) coefficient of friction
Slika 8: Prikaz interakcije glavnih podatkov na: a) hitrost obrabe in b) koeficient trenja

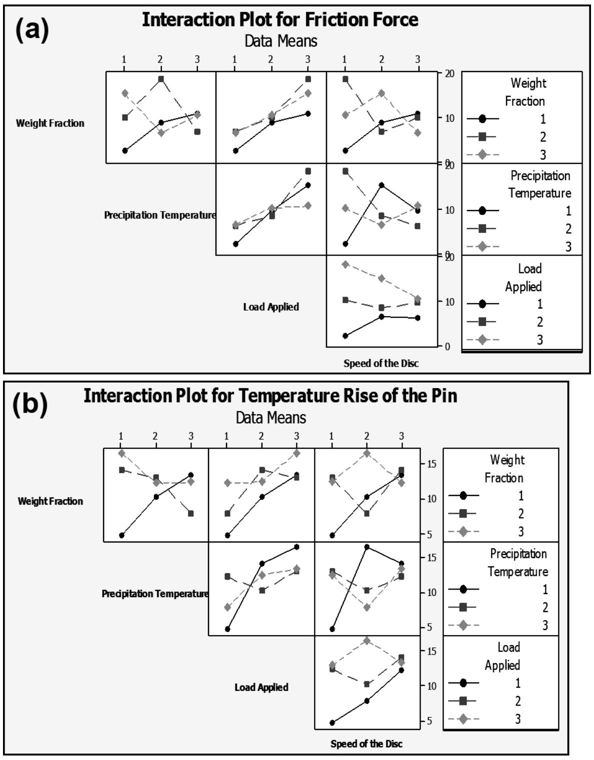

Figure 9: Interaction plot for data means of: a) friction force and b) temperature rise of pin

Slika 9: Prikaz interakcije glavnih podatkov na: a) silo trenja in b) dvig temperature vzorca

3 RESULTS AND DISCUSSIONS

Typically, a low wear rate, high coefficient of friction and friction force and a low temperature rise of the pin are desirable for a good wear-resistant material. According to the grey relational analysis, the experiment exhibiting the highest grey relational grade has the optimum experimental conditions.[16] From **Table 6**, it is clear that experiment number 1 (A1B1C1D1) had the most optimum condition with regard to the orthogonal array. From **Table 7**, we find that the optimum conditions, with regard to the entire experiment, were provided in the case of A3B2C1D1, i.e., the samples with 20 % mass fraction, precipitated at 550 °C, run at an applied load of 10 N and a speed of 400 r/min satisfy the given optimization conditions. The optimum conditions are also illustrated in **Figure 4**. The grey relational grades for the nine experiments are illustrated in **Figure 5**. The purpose of using ANOVA is to find which process parameter significantly affects the wear performance of the composites. ANOVA for the *GRG* is shown in **Table 8**. It has been observed that the normal load acting on the pin significantly influences the wear performance, followed by the precipitation temperature. The mass fraction of the reinforcement and the disc speed are less significant. This may be attributed to the fact that a finer particle size (600 mesh or 23 µm) of the reinforcement eliminates the effect of the mass fraction on the wear characteristics. Usually, fine-particle reinforcement has a good bonding strength with the matrix with all mass fractions, but it may lose it when the precipitation temperature is changed. This is in agreement with the results shown in ANOVA. The main effect plots of the output parameters such as wear, coefficient of friction, friction force and temperature rise of pin are illustrated in **Figures 6a, 6b 7a** and **7b**. The optimum conditions are also easily determined from these figures. The interaction plots for the output parameters are shown in **Figures 8a, 8b**, **9a** and **9b**. All these plots agree with the above arguments.

4 CONCLUSIONS

A grey relational analysis was used for optimizing the process parameters during a dry-sliding wear test of aluminium MMCs. The recommended levels of the process parameters for a better wear performance of the composites are the mass fraction of 20 %, the precipitation temperature of 550 °C, the applied load of 10 N and the speed of the disc of 400 r/min. Of the four process parameters considered during the study, only two factors, the normal load acting on the pin and the precipitation temperature, significantly influence the wear performance, much more than the mass fraction of the reinforcement and the disc speed. This is due to the particle size of the reinforcement (23 µm). A finer particle size leads to a good bonding with the matrix for all mass fractions and, therefore, the performance is the least influenced by the mass fraction. The grey relational analysis was more convenient for optimizing the process parameters as it simplifies the optimization procedure.

5 REFERENCES

[1] A. P. Sannino, H. J. Rack, Wear, 189 (**1995**), 1–19

[2] D. B. Miracle, ASM International, (**2001**), 1043–1049

[3] T. S. Srivatsan, Al-Hajri Meslet, C. Smith, M. Petraoli, Mater Sci Eng., 346 (**2003**), 91–100

[4] T. S. Srivatsan, J. Mater. Sci., 31 (**1996**), 1375–88

[5] K. H. W. Seah, S. C. Sharma, B. M. Girish, Composites Part A, 28A (**1997**), 251–6

[6] S. Basavarajappa, G. Chandramohan, J. Paulo Davim, Materials and design, 28 (**2007**), 1393–1398

[7] R. L. Deuis, C. Subramanian, J. M. Yellup, Composite Sci. Technol., 57 (**1997**), 415–35

[8] R. L. Deuis, C. Subramanian, J. M. Yellup, Wear, 201 (**1996**), 132–44

[9] S. Basavarajappa, G. Chandramohan, K. Mukund, M. Ashwin, M. J. Prabu, Mater. Eng. Perform., 15 (**2006**) 6, 668–74

[10] J. K. M. Kwok, C. Lim, Compos. Sci. Technol., (**1999**), 5955–63

[11] Z. Y. Ma, Y. N. Liang, Y. Z. Zhang, Y. X. Lu, J. Bi, Mater. Sci. Technol., 12 (**1996**), 751–6

[12] S. Basavarajappa, G. Chandramohan, J. Paulo Davim, Mater Des., 28 (**2007**), 1393–8

[13] Y. O. Sahin, Mater. Des., 27 (**2006**), 455–60

[14] Y. Sahin, Mater. Sci. Eng. A, 408 (**2005**), 1–8

[15] K. Palanikumar, Measurement, 44 (**2011**), 2138–2148

[16] U. Esme, Mater. Tehnol., 44 (**2010**) 3, 129–135

[17] H. Aydin, A. Bayram, U. Esme, Y. Kazancoglu, O. Guven, Mater. Tehnol., 44 (**2010**) 4, 205–211

UDK 669.15-194.57:537.622
Original scientific article/Izvirni znanstveni članek

ISSN 1580-2949
MTAEC9, 48(3)367(2014)

EFFECT OF ISOTHERMAL ANNEALING ON THE MAGNETIC PROPERTIES OF COLD-ROLLED LOW-CARBON STEEL WITH MAGNETIC HYSTERESIS-LOOP MEASUREMENTS

VPLIV IZOTERMNEGA ŽARJENJA NA MAGNETNE LASTNOSTI HLADNO VALJANEGA MALOOGLJIČNEGA JEKLA Z MERITVAMI MAGNETNE HISTEREZNE ZANKE

Amir Ansaripour, Hossein Monajatizadeh, Jamshid Amighian
Department of Materials Engineering, Najafabad Branch, Islamic Azad University, P.O. Box 517, Isfahan, Iran
ansaripour@outlook.com

Prejem rokopisa – received: 2013-06-24; sprejem za objavo – accepted for publication: 2013-09-04

The magnetic properties of ferritic steels including the coercive field and the remanent induction are sensitive to microstructural features such as the grain size and the dislocation density. In this paper the effect of isothermal-annealing treatments at different temperatures on the coercive field and the remanent induction of industrially cold-rolled low-carbon steel samples was investigated. The specimens were annealed at low (500 °C) and high temperatures (640 °C) in order to promote the recovery and recrystallization, respectively. A hysteresis-loop measuring apparatus, specifically designed and assembled for plate samples was used under different annealing conditions. Furthermore, microstructural changes were investigated using light microscopy and hardness measurement and were compared with the data extracted from the device. The result showed that the variation in measured H_c is an appropriate magnetic parameter for following the microstructural evolutions such as recovery and recrystallization.

Keywords: non-destructive testing, annealing, magnetic hysteresis

Magnetne lastnosti feritnih jekel, vključno s koercitivnim poljem in remanentno indukcijo, so občutljive za pojave v mikrostrukturi, kot sta velikost zrn in gostota dislokacij. V tem članku je bil preiskovan vpliv obdelave z izotermnim žarjenjem na koercitivno polje in remanentno indukcijo industrijsko hladno valjanih vzorcev malooglji̇čnega jekla pri različnih temperaturah preiskovanja. Vzorci so bili žarjeni pri nizki (500 °C) in visoki temperaturi (640 °C) z namenom, da bi pospešili popravo in rekristalizacijo. Uporabljena je bila naprava za merjenje histerezne zanke, posebno prirejena za ploščate vzorce v različnih razmerah žarjenja. Spremembe mikrostrukture so bile preiskovane s svetlobnim mikroskopom in izmerjena trdota je bila primerjana s podatki, dobljenimi iz naprave. Rezultati so pokazali, da je spreminjanje izmerjenega H_c pravi magnetni parameter za spremljanje razvoja mikrostrukture, kot sta poprava in rekristalizacija.

Ključne besede: neporušne preiskave, žarjenje, magnetna histereza

1 INTRODUCTION

It is well known that work-hardened steel sheets require an annealing process, during which the material softens and recovers its ductility and formability.[1] The main softening mechanisms in metallic materials are recovery and recrystallization. The former leads to an annihilation of dislocations and their re-arrangement into low-energy sub-boundaries and the latter results in a nucleation and growth of new strain-free grains.[2,3] Numerous studies have been published regarding the study of the recovery and recrystallization kinetics using different methods such as the thermal analysis, TEP (thermo-electrical power), X-ray diffraction, metallography and, in recent years, magnetic techniques.[4,5] Among them, the last set of techniques is potentially able to be used non-destructively. This is of great importance because different amounts of softened material at various points of the steel coil that are inherently characteristic of box annealing, may lead to a variation in the mechanical properties and formability of sheets.[6] An application of a magnetic measuring technique on a production line of steel coils can give an appropriate evaluation of the variation in the mechanical properties along a coil.

Magnetic properties of steels depend on microstructural features such as dislocation density, grain and subgrains size, precipitates and other structural defects.[7–9] The first two parameters are affected mainly during the annealing process[3]. Little has been published about the evaluation of annealing cold-rolled low-carbon steels by means of magnetic parameters. Martinez et al.[10–12] surveyed the recovery and the onset of recrystallization, using non-destructive magnetic tests, in low-carbon steels. They measured the coercive force (H_c) and found that this parameter is sensitive to the evolution of microstructure during annealing, using equation $H_c \propto \sqrt{\rho/d}$, in which ρ is the dislocation density and d is the average grain diameter. However, the annealing progress in the form of a recrystallization volume fraction and a grain growth still needs to be examined.

In the present work, a measuring direct pickup coil and a Hall-sensor system were applied to the plate samples to estimate the magnetic properties of the steels that have different microstructures consisting of cold-worked and also fully and partially recrystallized grains. The aim was to find the effect of the microstructure change during annealing on H_c and B_r and to follow the non-destructive characterization of the microstructural changes produced due to the recovery and recrystallization during the annealing of the cold-rolled low-carbon steel presented above.

2 EXPERIMENTAL PROCEDURE

2.1 Materials

The composition of the studied steel is shown in **Table 1**. The samples selected from the industrially produced coils were cold rolled to a final thickness of 0.8 mm through a 75 % reduction.

Table 1: Chemical composition of the samples (mass fractions, *w*/%)
Tabela 1: Kemijska sestava vzorcev (masni deleži, *w*/%)

C	Si	Mn	Al	N (10^{-6})	Fe
0.044	0.008	0.229	0.049	25	balance

The samples were isothermally annealed in the laboratory heat-treatment furnace, in which they were heated up in an argon atmosphere at a rate of 10 °C/h according to the cycle shown in **Table 2**. Then the samples were cooled in air to ambient temperature.

2.2 Hardness and metallographic measurement

Superficial Rockwell-hardness (HR30T) measurements were performed on the sheet of the annealed samples with a steel indenter in the form of a sphere with a 1.58 mm (1/16 in.) diameter subjected to a load of 30 kg. The full load was applied for 30 s according to ASTM E18, while the Vickers-hardness measurements were carried out on the transverse section according to ASTM E92. Each sample was measured five times and the average values were calculated.

Longitudinal sections of the investigated steels were prepared for microscopic examinations with the standard metallographic technique. Having been ground and polished, the metallographic samples were etched with 3 % Nital and examined using an optical microscope.

2.3 Magnetic measuring system

The magnetic measuring system consisted of a U-shaped magnetizing (Fe-Si laminated) core with an excitation coil (200 turns), supplied with a sinusoidal (0.5 Hz) exciting current. The field was measured using a Hall probe placed on the surface of the sample and the direct pickup coil (50 turns) that was wound around the specimen, as depicted in **Figure 1**. The latter was used to compare and validate the flux density measured with the coil. The system is based on a PC, through which an input-output A/D card transfers the signals of the measured magnetic-field strength (*H*) and the flux density (*B*).

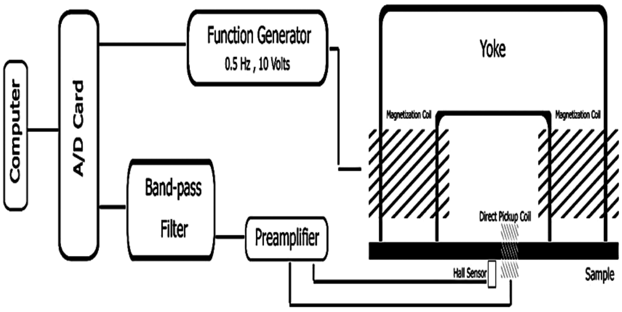

Figure 1: Schematic diagram of the system for measuring magnetic parameters
Slika 1: Shematski prikaz sistema za merjenje magnetnih parametrov

The field in a tested sample was evaluated to be proportional to the exciting current (*I*) and calculated from equation 1:

$$H = \frac{NI}{l} \tag{1}$$

where *N* is the number of the exciting-coil turns, and *l* is the effective magnetic path.

The magnetic induction signal was obtained with an integration of the induced voltage on a 50-turn encircling coil wound around the samples. The flux density (*B*) was obtained after integrating the pickup-coil induced voltage, and calculated from equation 2:

$$B = \frac{NI}{N_\mathrm{p} S} \int V \mathrm{d}t = \frac{1}{N_\mathrm{p} S F_\mathrm{s}} \sum_{i=1}^{N} Vi \tag{2}$$

where N_P is the number of pickup coil turns, *S* is the total section area of the pickup coil, F_s is the sampling frequency and *V* is the voltage induced in the pickup coil.

3 RESULTS AND DISCUSSION

Figure 2 shows the evolution of the microstructures of the samples during isothermal annealing at 500 °C. As can be seen in the figure, the structures consist of elongated grains along the rolling direction and microbands

Table 2: Annealing cycles used in this study
Tabela 2: Uporabljeni cikli žarjenja

L (500 °C)	L1	L2	L3	L4	L5	L6	L7	L8	L9	L10
H (640 °C)	H1	H2	H3	H4	H5	H6	H7	H8	H9	H10
Annealing time (s)	100	300	600	1200	1800	2700	3600	5400	7200	10800

*L: Low-temperature annealing, *H: High-temperature annealing

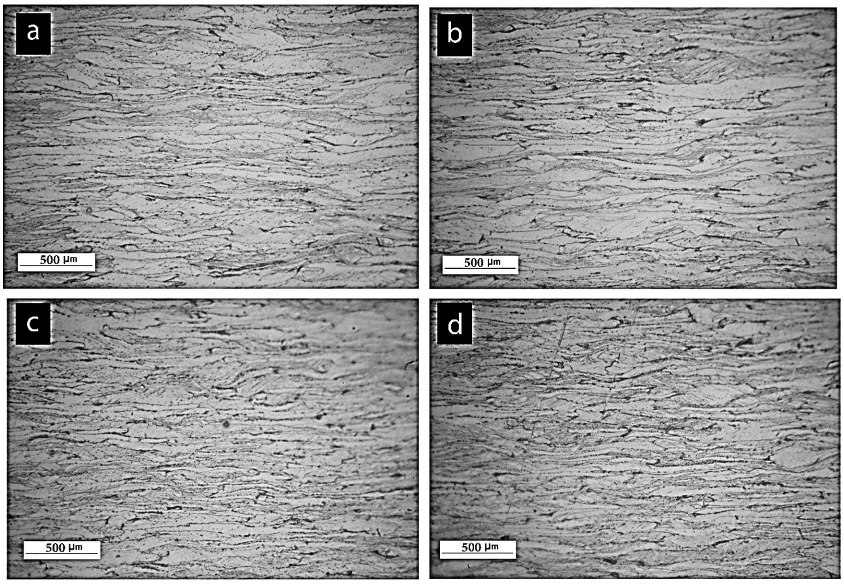

Figure 2: Light micrographs showing the microstructures of the samples after the isothermal annealing at 500 °C: a) 100 s, b) 600 s, c) 1800 s, d) 10800 s

Slika 2: Posnetki mikrostrukture vzorcev po izotermnem žarjenju pri 500 °C: a) 100 s, b) 600 s, c) 1800 s, d) 10800 s

are evident inside them. The soaking time increased up to 10800 s does not noticeably change this structure.

As can be seen, **Figure 3a** reveals the initially deformed grains elongated in the rolling direction without any signs of recrystallization but, during the annealing carried out at 640 °C after about 600 s of soaking (**Figure 3b**), newly recrystallized grains take place. A more increased soaking time (**Figure 3c**), increases the fraction of recrystallized grains, with nearly 90 % of the structure recrystallized after 1800 s. The recrystallization process is completed after 2700 s and the grain growth (**Figure 3d**), is observed after 10800 s.

Figure 4 illustrates the evolution of the hardness of a sample during isothermal annealing. It can be seen in the figure that the hardness is approximately insensitive to the annealing temperature at 500 °C when the softening of the material is governed by the recovery. The Vickers-hardness tests carried out on the transverse section of the sheet give the same type of result. As an example, HV for L1 is 220 and after a 10800 s soaking time at 500 °C it only decreases to 212 HV. At 640 °C after a 300 s soaking time, when the static recrystallization is started, a sudden decrease in the hardness is observed. As the hardness tests of the present steel do not give any infor-

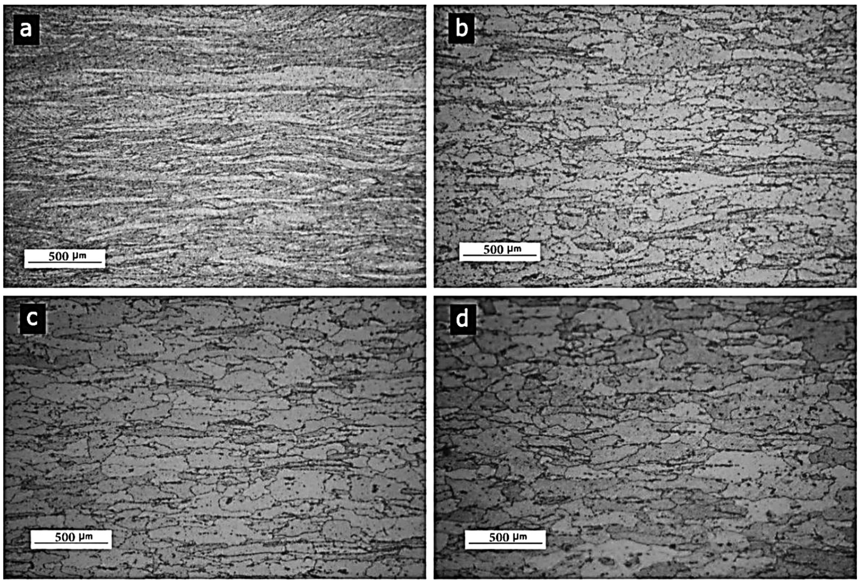

Figure 3: Light micrographs showing the microstructures of the samples after the isothermal annealing at 640 °C: a) 100 s, b) 600 s, c) 1800 s, d) 10800 s

Slika 3: Posnetki mikrostrukture vzorcev po izotermnem žarjenju pri 640 °C: a) 100 s, b) 600 s, c) 1800 s, d) 10800 s

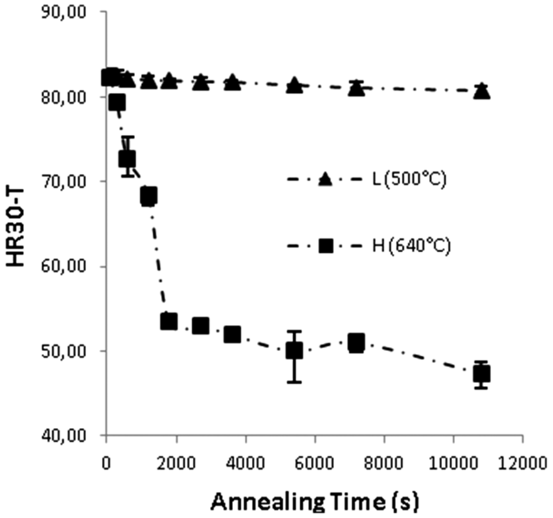

Figure 4: Evolution of the hardness as a function of the annealing time and temperature

Slika 4: Razvoj trdote v odvisnosti od časa in temperature žarjenja

mation about a possible recovery taking place during the annealing carried out at the lowest temperatures, magnetic methods were applied in order to get a higher degree of resolution and investigate this phenomenon.

The effect of increasing the annealing time in the hysteresis loops is shown in **Figure 5**. The *B–H* loops are found to become steeper with the annealing, providing lower H_c, and higher B_r values.

The general shape of the curves shows a knee in the middle where the difference between the curves is more pronounced, as shown more clearly in the right-hand corner of **Figure 5**. Above and below the knees, the curves become approximately coincident.

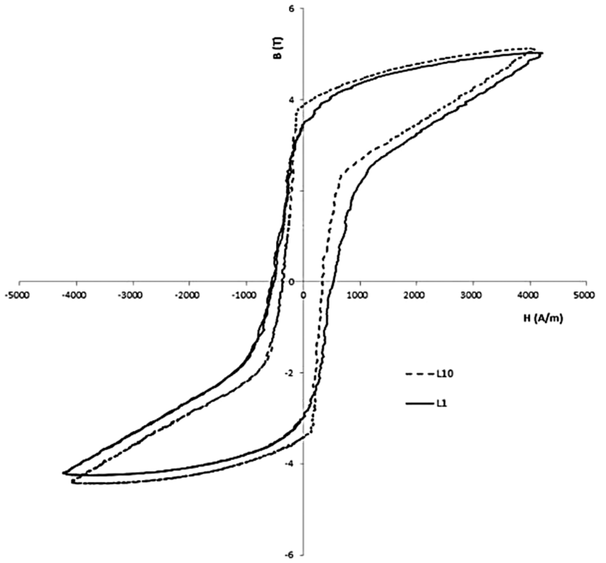

Figure 5: Hysteresis *B–H* loops showing the effect of the annealing treatment at 500 °C

Slika 5: Histerezna zanka *B–H* prikazuje vpliv žarjenja pri 500 °C

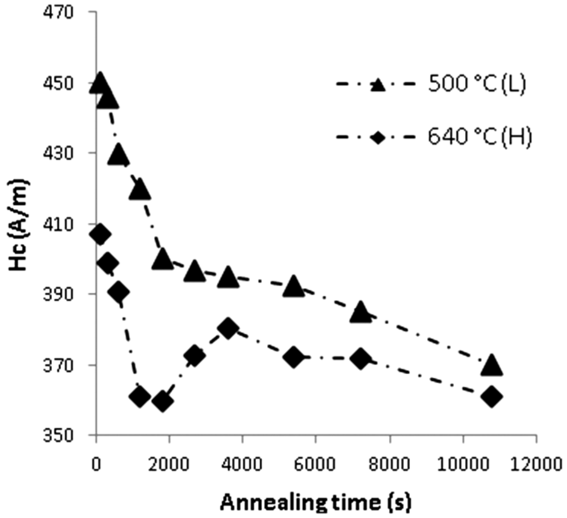

Figure 6: Evolution of the coercive field (H_c) with the annealing time

Slika 6: Razvoj koercitivnega polja (H_c) s časom žarjenja

The evolutions of H_c and B_r with the annealing progress are illustrated in **Figures 6** and **7**. Although both magnetic parameters show an inverse trend, it is observed that an increase in the annealing time from 100 s to 10800 s decreases H_c up to 50 A/m, while the corresponding drop in B_r represents no meaningful change in the high-temperature isothermal annealing. This confirms that H_c is more sensitive to the microstructural evolution during annealing.

A comparison between **Figures 4** and **6** shows that at 500 °C, when the recovery is the governing factor[4] both magnetic parameters are sensitive to the microstructural evolution, whereas the hardness is insensitive to it.

At 640 °C and after about a 1000 s soaking time the rate of decrease in H_c is relatively diminished due to the start of the recrystallization, as can be seen in **Figure 6** (*H*). To explain this diminution, one may refer to the effect of the grain size on H_c according to relation ($H_c \propto$

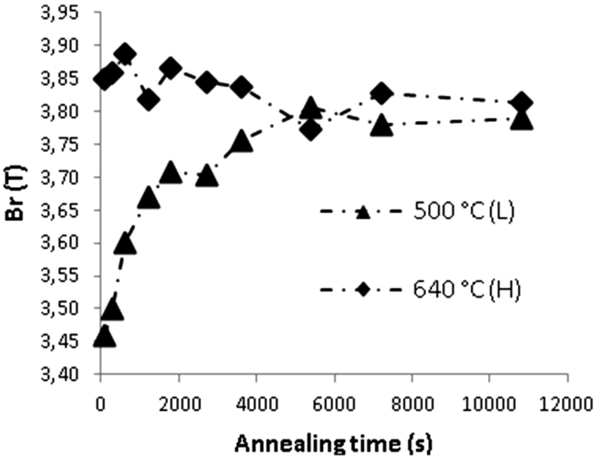

Figure 7: Evolution of the remanent induction (B_r) with the annealing time

Slika 7: Razvoj remanentne indukcije (B_r) s časom žarjenja

$\sqrt{\rho/d}$). When the grain size is reduced, H_c increases[9–19]. The domain-wall motion and rotation under the magnetic field is affected by the microstructural parameters such as grain boundaries, in addition to the dislocation density and inclusions. Grain boundaries present obstacles to the domain-wall motion acting as the pinning centers for the domain walls. As the grain size increases, the number of grains and the total length of grain boundaries decrease and, therefore, the pinning effect of the domain-wall motion decreases.[11–19] The start of the recrystallization leads to a decrease in the average grain size and, thereafter, an increase in the pinning effect of grain boundaries on the domain-wall motion. This is opposite to the effect of an annihilation of dislocations during domain-wall motion and, hence, the rate of decrease in H_c diminishes due to the resultant competition between these two phenomena. At the end of the 1800 s period, the contribution of the pinning effect due to the decreasing average grain size becomes higher than the softening effect of the dislocation annihilation and H_c starts to increase, as depicted above. Due to the growth of the recrystallized grains, this resistance to the domain-wall motion is decreased and H_c starts to decrease again.

These results show that H_c is sensitive enough to the microstructural changes such as recovery and recrystallization.

4 CONCLUSIONS

In the present work, magnetic hysteresis loops of cold-rolled steel-plate samples were measured at different times after isothermal annealing. Two parameters, the coercive force (H_c) and the remnant induction (B_r), in the hysteresis loop were analyzed and compared with the hardness measurement. It was found that both parameters decrease with the increasing time of annealing and the progressing recovery process. Also, while hardness is not sensitive to the microstructural changes during recovery, H_c can be useful for its non-destructive characterization. Moreover, H_c accurately characterizes various stages of recrystallization during the isothermal annealing of cold-rolled low-carbon steel and it can be used as a non-destructive tool for controlling the annealing progress in steel sheets.

Acknowledgements

The technical and financial support of Mobarakeh Steel Complex and the assistance provided by the personnel of the cold-rolling sector are gratefully acknowledged.

5 REFERENCES

[1] R. K. Ray, J. J. Jonas, R. E. Hook, Cold rolling and annealing textures in low carbon and extra low carbon steels, Int. Mater. Rev., 39 (**1994**) 4, 129–171

[2] I. Tanaka, H. Yashiki, Magnetic and mechanical properties of newly developed high-strength nonoriented electrical steel, IEEE Trans. Magn., 46 (**2010**) 2, 290–293

[3] F. J. Humphreys, M. Hatherly, Recrystallization and Related Annealing Phenomena, American Elsevier Publishing Company, New York 1973

[4] J. P. Ferrer, T. De Cock, C. Capdevila, F. G. Caballero, C. Garcia de Andres, Comparison of the annealing behaviour between cold and warm rolled ELC steels by thermoelectric power measurements, Acta. Mater., 55 (**2007**), 2075–2083

[5] C. E. Rodriguez Torres, F. H. Sanchez, A. Gonzalez, F. Actis, R. Herrera, Study of the kinetics of the recrystallization of cold-rolled low-carbon steel, Metall. Mater. Trans. A., 33 (**2002**), 25–31

[6] H. Monajati, D. Asefi, A. Parsapour, Sh. Abbasi, Analysis of the effects of processing parameters on mechanical properties and formability of cold rolled low carbon steel sheets using neural networks, Comput. Mater. Sci., 49 (**2010**), 876–881

[7] E. Gomes, J. Schneider, K. Verbeken, J. Barros, Y. Houbaert, Correlation between microstructure, texture, and magnetic induction in nonoriented electrical steels, IEEE Trans. Magn., 46 (**2010**) 2, 310–313

[8] A. K. Panda, S. K. Das, A. Mitra, D. C. Jiles, C. C. H. Lo, Evaluation of deformation behavior of HSLA-100 steel using magnetic hysteresis technique, IEEE Trans. Magn., 42 (**2006**) 10, 3264–3266

[9] G. V. Bida, A. P. Nichipuruk, Coercive force measurements in nondestructive testing, Russ. J. of Nondestr. Test., 36 (**2000**) 10, 707–727

[10] K. Gurruchaga, A. Martínez-De-Guerenu, M. Soto, F. Arizti, Magnetic barkhausen noise for characterization of recovery and recrystallization, IEEE Trans. Magn., 46 (**2010**) 2, 513–516

[11] A. Martínez-de-Guerenu, F. Arizti, M. Díaz-Fuentes, I. Gutiérrez, Recovery during annealing in a cold rolled low carbon steel. Part I: Kinetics and microstructural characterization, Acta. Mater., 52 (**2004**) 12, 3657–3664

[12] K. Gurruchaga, A. Martínez-De-Guerenu, M. Soto, F. Arizti, Efficacy of magnetic inductive parameters for annealing characterization of cold rolled low carbon steel, IEEE Trans. Magn., 44 (**2008**) 11, 3839–3842

[13] M. J. Sablik, F. J. G. Landgraf, Modeling microstructural effects on hysteresis loops with the same maximum flux density, IEEE Trans. Magn., 39 (**2003**) 5, 2528–2530

[14] M. J. Sablik, T. Yonamine, F. J. G. Landgraf, Modeling plastic deformation effects in steel on hysteresis loops with the same maximum flux density, IEEE Trans. Magn., 40 (**2004**) 5, 3219–3226

[15] T. Liu, S. Takahashi, H. Kikuchi, K. Ara, Y. Kamada, Stray flux effects on the magnetic hysteresis parameters in NDE of low carbon steel, NDT&E Int., 39 (**2006**), 277–281

[16] T. Liu, H. Kikuchi, K. Ara, Y. Kamad, S. Takahashi, Magnetomechanical effect of low carbon steel studied by two kinds of magnetic minor hysteresis loops, NDT&E Int., 39 (**2006**), 408–413

[17] H. Kikuchi, K. Ara, Y. Kamada, S. Kobayashi, Effect of microstructure changes on barkhausen noise properties and hysteresis loop in cold rolled low carbon steel, IEEE Trans. Magn., 45 (**2009**) 6, 2744–2747

[18] H. Hauser, R. Grossinger, F. Keplinger, M. Schonhart, Effect of structural changes on hysteresis properties of steel, J. Magn. Magn. Mater., 320 (**2008**), 983–987

[19] M. J. Sabli, W. J. Geerts, K. Smith, A. Gregory, C. Moore, D. Palmer, A. Bandyopadhyay, F. J. G. Landgraf, M. F. de Campos, Modeling of Plastic Deformation Effects in Ferromagnetic Thin Films, IEEE Trans. Magn., 46 (**2010**) 2, 491–494

UDK 621.937:669.14.018.8 ISSN 1580-2949
Original scientific article/Izvirni znanstveni članek MTAEC9, 48(3)373(2014)

THE EFFECT OF THE CUTTING SPEED ON THE CUTTING FORCES AND SURFACE FINISH WHEN MILLING CHROMIUM 210 Cr12 STEEL HARDFACINGS WITH UNCOATED CUTTING TOOLS

VPLIV HITROSTI REZANJA NA SILE REZANJA IN KVALITETO POVRŠINE PRI REZKANJU KROMOVIH NAVAROV 210 Cr12 Z REZILNIM ORODJEM BREZ PREVLEKE

Abdullah Altin
Van Vocational School of Higher Education, Yuzuncu Yıl University, 65080 Van, Turkey
aaltin@yyu.edu.tr

Prejem rokopisa – received: 2013-06-25; sprejem za objavo – accepted for publication: 2013-07-12

The experimental study presented in this paper aims to select the most suitable cutting and offset parameter combination for a milling process in order to obtain the desired surface roughness value for a machined workpiece of chromium 210 Cr12 steel, in terms of cutting speed, feed rate and depth of cut for the milling process. A series of experiments was performed on chromium material with a cutting width of 50 mm using a round, uncoated, cemented-carbide insert on a engine power 5.5 kW Jhonford VMC550 CNC vertical machining center without any cutting fluid. The experiments were carried out using four different cutting speeds ((70, 90, 110, 130) m/min) at a constant depth of cut (1 mm) and feed rate (0.3 mm/r) and the effects of the cutting speeds on the primary cutting force and the surface roughness were investigated. The cutting force (F_c) and the surface roughness (R_a) decreased with the workpiece material's easy machinability. From the experiments, the highest average primary cutting force was obtained as 658.17 N at a cutting speed of 70 m/min. The lowest average surface roughness was 0.36 μm, which was obtained at a cutting speed of 70 m/min. The experimental results indicated that the obtained chip form is narrow and short stepped.

Keywords: machinability, uncoated cemented-carbide insert, cutting speed, cutting force, surface roughness

Namen predstavljene študije je izbira najprimernejših parametrov rezanja, hitrosti rezanja, hitrosti podajanja in globine reza pri rezkanju in kombinacije parametrov pri postopku rezkanja za doseganje želene hrapavosti površine obdelovancev iz kromovega jekla 210 Cr12. Izvršena je bila serija preizkusov rezanja širine 50 mm na kromovem materialu z vložki iz karbidne trdine brez prevleke na CNC vertikalnem obdelovalnem centru Jhonford VMC550 moči 5,5 kW in brez hladilne tekočine za rezanje. Preizkusi so bili izvršeni pri štirih hitrostih rezanja ((70, 90, 110, 130) m/min) pri konstantni globini rezanja (1 mm) in hitrosti podajanja (0,3 mm/r). Preiskovan je bil vpliv hitrosti rezanja na primarno silo rezanja in hrapavost površine. Sila rezanja (F_c) in hrapavost površine (R_a) sta se zmanjševali z lažjo obdelovalnostjo obdelovanca. Preizkusi so pokazali, da je povprečje največje sile rezanja 658,17 N pri hitrosti rezanja 70 m/min. Povprečje najmanjše hrapavosti površine 0,36 μm je bilo doseženo pri hitrosti rezanja 70 m/min. Rezultati preizkusov so pokazali, da so dobljeni ostružki ravni in kratko stopničasti.

Ključne besede: obdelovalnost, vložki iz karbidne trdine brez prevleke, hitrost rezanja, sila rezanja, hrapavost površine

1 INTRODUCTION

High-chromium steel belongs to the group of corrosion-resistant materials and this leads to its practical applications.[1] High-chromium hardfacing materials are widely used in industry due to their excellent wear resistance.[2] The wear resistance of these materials was mainly achieved by a high hardness and a high carbide content, and this makes the machining of these hardfacings extremely difficult.[3] There is a widespread need for abrassion-resistant materials in industries as diverse as mining and food processing.[2,4] The productivity of machining operations can be expanded and the quality of products can be improved by using higher cutting speeds than are traditionally applied. Developments in cutting tools, work materials and machine tools have resulted in the spread of high-speed cutting technology.[5] The development of ultra-hard CBN materials has opened up the possibility to machine these materials by turning or milling instead of grinding, thus improving the productivity and reducing the cost.[6] Chip formation is one of the most important aspects of the cutting process, with a factor such as tool wear being related to the behaviour of the workpiece material around the cutting edge.[7] The formation mechanism of the chip depends on the thermal properties and the metallurgical state of the workpiece material, as well as on the dynamics of the machine's structure and the cutting process.[8] The chip-formation process of hardfacing and the tool-wear characteristics were previously investigated.[9] This paper further reports on a measurement of the cutting forces and the surface roughness to predict the machining quality of hardfacings at different cutting speeds, which is another key factor in the machinability of chromium steel 210 Cr12 materials. The cutting forces generated during a machining operation are mainly influenced by the properties of the workpiece and the tool material, the machining parameters used and other condition, e.g., the coolant.

Factors such as tool wear, surface quality and chip formation, etc., are all affected by the cutting temperature. In many cases the temperature was a limiting factor for the cutting-tool efficiency.[7,8,10] When cutting some very hard materials using ceramic tools, e.g., case-hardened alloy steel and superalloys, sufficient cutting heat is needed to soften the workpiece material.[11–13] Extensive research work has been done to investigate the machining process of these high-chromium hardfacing materials.[14,15]

2 MATERIALS AND METHOD

2.1 Experimental Specimens

The workpiece material was chromium steel 210 Cr12 with the chemical composition shown in **Table 1**. The machining tests were performed by the single-point milling of this material in flat form with dimension of 100 mm × 50 mm × 30 mm. The milling machine had a continuously variable spindle speed of up to 10000 m/min with a maximum power of 5.5 kW. The mechanical properties and Typical EDS analyses of the specimens are given in **Table 2** and **Figure 1**. The morphology of the surface is given in **Figure 2**.

Table 1: Chemical composition of the workpiece material (chromium steel 210 Cr12), *w*/%

Tabela 1: Kemijska sestava materiala obdelovanca (kromovo jeklo 210 Cr12), *w*/%

C	Si	Mn	P	S	Cr	Cu	Mo	Ni
2.08	0.28	0.39	0.017	0.012	11.48	0.15	0.02	0.31

2.2 Cutting parameters, cutting tool and tool holder

The milling tests were conducted with uncoated cemented-carbide cutting tools. No coolant was used during the tests. The tools were commercial-grade inserts with the geometry *RPHX1204MOEN*. Four different cutting speeds were selected, i.e., 70 m/min, 90 m/min, 110 m/min and 130 m/min, while the cutting parameters, feed rate and depth of cut were kept fixed at 0.30 mm/r and 1 mm, The cutting speeds were chosen by taking into consideration the recommendations of the manufacturing companies. In this study the purpose was to investigate the surface roughness and the material quality on the main cutting force, taking into account the cutting speed. Surtrasonic 3-P measuring equipment was used for the measurements of the surface roughness. The cutting diameter was 50 mm and the cutting width was 30 mm. The experiments were carried out with a 90° lead-angle milling cutter and only one cutting insert was used in the milling cutter. The used tool geometry was as follows: rake angle 0°, clearance angle 7°.

A regression and variance analysis was applied during the experimental study.

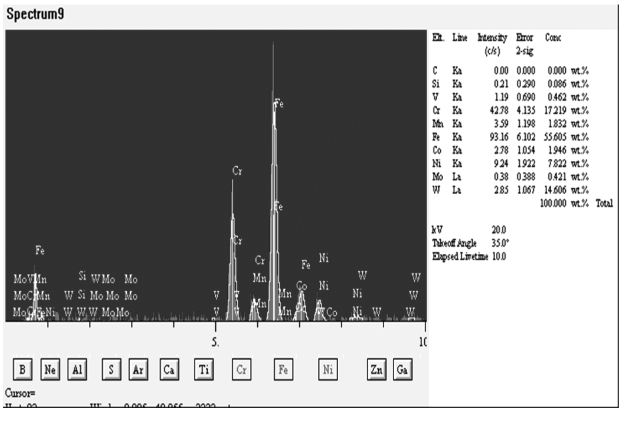

```
Elt.  Line  Intensity  Error   Conc
            (c/s)      2-sig

C     Ka     0.00      0.000    0.000  wt.%
Si    Ka     0.21      0.290    0.086  wt.%
V     Ka     1.19      0.690    0.462  wt.%
Cr    Ka    42.78      4.135   17.219  wt.%
Mn    Ka     3.59      1.198    1.832  wt.%
Fe    Ka    93.16      6.102   55.605  wt.%
Co    Ka     2.78      1.054    1.946  wt.%
Ni    Ka     9.24      1.922    7.822  wt.%
Mo    La     0.38      0.388    0.421  wt.%
W     La     2.85      1.067   14.606  wt.%
                              100.000  wt.%  Total

kV                20.0
Takeoff Angle     35.0°
Elapsed Livetime  10.0
```

Figure 1: Typical EDS analysis of the mechanical workpiece material chromium 210 Crl2 steel

Slika 1: Značilna EDS-analiza obdelovanca iz kromovega jekla 210 Cr12

Table 2: Mechanical properties of chromium steel 210 Cr12

Tabela 2: Mehanske lastnosti kromovega jekla 210 Cr12

Temperature of annealing *T*/°C	Cooling	Hardness HB
800–850	At stove	Max. 250
Hardening °C	Environment	Hardness, after hardening (HRC)
930–960	Weather, lubricant or hot bath 400–450 °C	63–65

2.3 Machine-Tool and Dynamometer type

The milling tests were carried out under orthogonal cutting conditions on a Jhonford VMC550 CNC vertical machining center without any cutting fluid, with a max. power of 5.5 kW and a max. revolution number of 10,000 r/min. During the dry cutting process, a Kistler brand 9257 B-type three-component piezoelectric dynamometer under a tool holder with the appropriate load amplifier is used to measure the three orthogonal cutting forces (F_x, F_y, F_z) acting on the cutting tool in the *X*, *Y*, *Z* directions, data-acquisition software. This allows direct and continuous recording and a simultaneous graphical

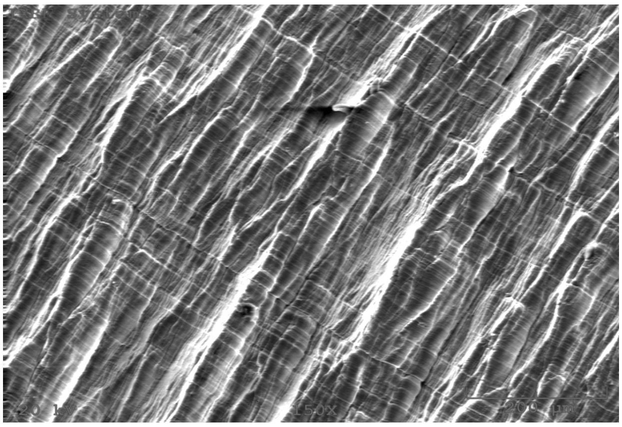

Figure 2: Morphology of surface of the chromium 210 Cr12 steel (SEM)

Slika 2: Značilnosti površine kromovega jekla 210 Cr12 (SEM)

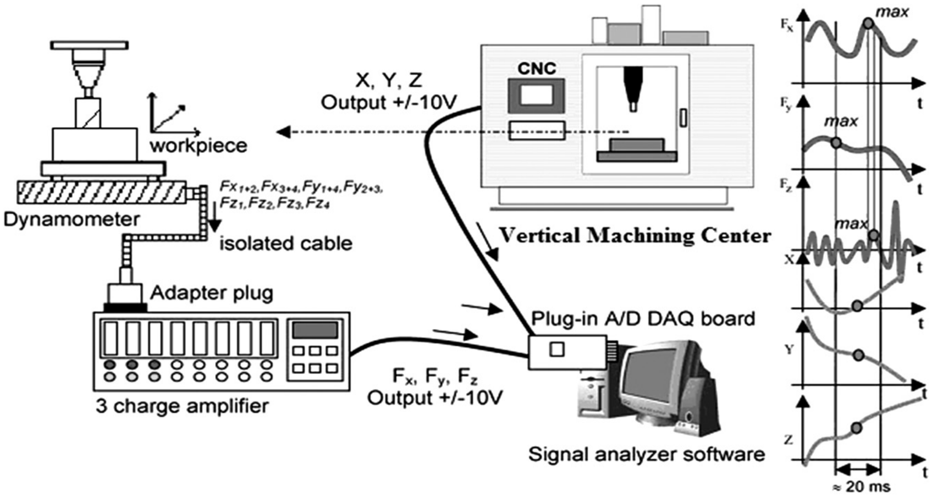

Figure 3: System architecture: left: schematic system scheme; right: data sampled and recorded, each record is composed by 12 values [($F_{x\text{max}}$, F_y, F_z), (F_x, $F_{y\text{max}}$, F_z), (F_x, F_y, $F_{z\text{max}}$), x, y, z]

Slika 3: Zgradba sistema: levo: shematski prikaz sistema; desno: zapis zbranih podatkov; vsak zapis sestoji iz 12 vrednosti [($F_{x\text{max}}$, F_y, F_z), (F_x, $F_{y\text{max}}$, F_z), (F_x, F_y, $F_{z\text{max}}$), x, y, z]

visualization of the three orthogonal cutting forces. The technical properties of the dynamometer and the schematic diagram of the experimental setup are given in **Table 3** and **Figure 3**. Reference system (F_x, F_y) fixed to the cutting tool in the rotating dynamometer and milling process under orthogonal cutting conditions are given in **Figure 4**. Surtrasonic 3-P measuring equipment is used for the measurement of the surface roughness. The measurement processes are carried out with three replications. For measuring the surface roughness on the workpiece during machining, the cut-off sampling lengths are considered as 0.8 mm and 2.5 mm. The ambient temperature is (20 ± 1) °C. The resultant cutting force was calculated to evaluate the machining performance. The reference system (f_x, f_y) was fixed to the cutting tool, in the rotating dynamometer. In this study, the technical properties of dynamometer and the general specifications of the CNC vertical machining center used in the experiments are given in **Tables 3** and **4**. The levels of the independent variables are shown in **Table 5**. The results of the regression and variance analysis in the models are given in **Tables 6** and **7**.

3 RESULTS AND DISCUSSION

3.1 Cutting forces and surface roughness

In this work the aim was to define the variation of the cutting forces related to the cutting speed and the alteration experimentally in order to investigate the effects of the cutting parameters on the surface roughness in the milling process for the chromium steel material. The experiments were successfully carried out and practical results for the milling process were obtained. The main cutting force changed, depending on the cutting speed and the uncoated material of the cutting tool, and while the depth of cut and the feed rate were constant, the cutting speed was changed in all the experiments.[7,16] The main cutting-force values with respect to the cutting speed are given in **Figure 5**. The lowest main cutting force of 212 N is observed at a cutting speed of 110 m/min. **Figure 5** indicates that increasing the cutting speed decreases the main cutting force, excluding the area between 110 m/min and 130 m/min. The obtained main cutting-force values at the cutting speeds of 70 m/min, 90 m/min, 110 m/min and 130 m/min are 244 N, 236 N, 212 N and 231 N, respectively. The results of **Figure 5** show that the cutting speed must be increased in order to reduce the main cutting forces.[16] However, in this study, a decrease is observed in the main cutting force between 70 m/min and 110 m/min. It is considered that this case is caused by plastic deformation, flank edge, crater and notch wear, which are formed at the cutting tool because of the high temperatures of the shear area when using uncoated carbide tools that have a low

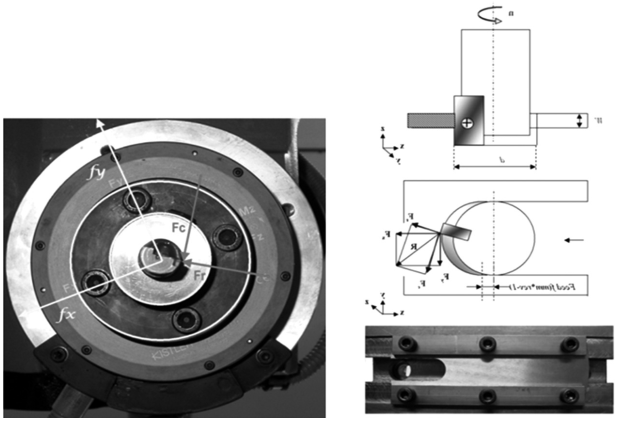

Figure 4: Reference system (F_x, F_y) fixed to the cutting tool in the rotating dynamometer and milling process under orthogonal cutting conditions

Slika 4: Referenčni sistem (F_x, F_y), pritrjen na orodje za rezanje v rotacijskem dinamometru in postopek rezkanja v razmerah ortogonalnega rezanja density at high cutting speeds. The effect of uncoated carbide inserts was found to be important on the main cutting force, but the effect of the cutting speeds was not important in the analysis of variance.[17] The main cutting force increases in spite of increasing the cutting speed at 130 m/min. As a result of an increase of 85.7 % in the cutting speed (130 m/min), while working at low cutting speeds (70 m/min) a decrease of 13.1 % was found in the main cutting force. The high temperature in the flow region and the decreasing contact surface area caused the main cutting force to decrease in comparison to the increased cutting speed. The decrement of the cutting force depends on the material type, the working conditions and the cutting-speed range. It was found that by increasing the cutting speed from 110 m/min to 130 m/min, the main cutting force increases by 9.4 %. Since the rake angle changes due to breakage of the cutting tool, a decrease of the main cutting force in spite of increasing the cutting speed can be attributed to the tool wear. Tool breakage affects the rake angle negatively, which causes an increase of the main cutting force. High temperature in the flow region and a decrease of the contact area and the chip thickness cause the cutting force to decrease depending on the cutting speed. The material properties, working conditions and cutting speed all affect the cutting-force decrement[18]. As a result of the experimental data (**Figure 4**), the main cutting force decrement of 13.1% with an increasing cutting speed of 42.85 % is observed at 110 m/min. The scatter plot between the surface roughness and the cutting speed, as shown in **Figure 6**, indicated that there is linear relationship between the surface roughness and the cutting speed. The results of **Figure 6** show that the average surface roughness increases by 61.1 % with an increasing cutting speed from 70 m/min to 130 m/min. The average surface-roughness values were found to be (0.36, 0.365, 0.425 and 0.58) µm for cutting speeds of (70, 90, 110, and 130) m/min, respectively. As is widely known, the cutting speed must decrease to improve the average surface roughness.[19] According to the round-type insert, the change of the three axes cutting forces and chip formation at $V = 90$ m/min are given in **Figure 7**. The most remarkable result concluded from **Figure 7** is that the main cutting force was decreased in the 110 m/min, the opposite direction of the rake angle, for all cutting speeds, while the cutting force was decreased by increasing the rake angle in a positive direction. This is due to changing the tool/chip contact area. The change of the main cutting force depends on the cutting speed and the uncoating material of the cutting tool. After the prepared test specimens were cut for experimental purposes, they were measured with a three-component piezoelectric dynamometer to obtain the main cutting force. Cemented-carbide tools for the cutting of the chromium steel show a low performance at high cutting speeds.[20] In this study, since chromium steel is used, the cemented-carpide tools showed a weaker performance.[9] The results of this experimental study can be summarized as follows: increasing cutting speed by 85.7 %, (70–130 m/min) causes the main cutting force to decrease by 13.1 %, and increasing the cutting speed by 57.1 % causes the main cutting force to decrease by 13.75 %. The minimum main cutting force value of 212 N was obtained at a cutting speed of 110 m/min. The experimental results indicated that the obtained chip form is narrow and short stepped. Chip formation at $V = 90$ m/min are shown in **Figure 8**.

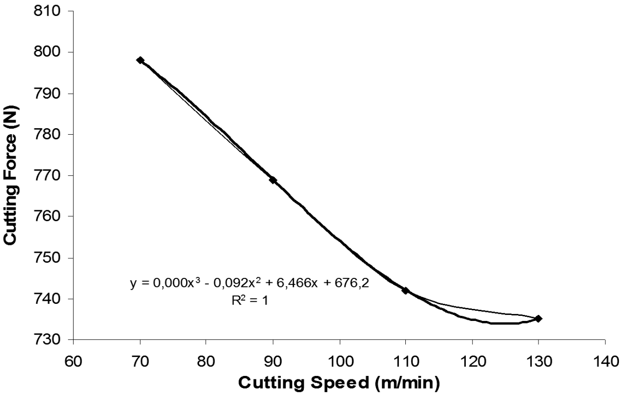

Figure 5: Cutting force ($F_{x\max}$) values (N) with respect to the cutting speeds at a constant feed rate

Slika 5: Vrednosti sile rezanja ($F_{x\max}$) v (N) glede na hitrosti rezanja pri konstantni hitrosti podajanja

Table 3: Technical properties of the dynamometer

Tabela 3: Tehnične značilnosti dinamometra

Force interval (F_x, F_y, F_z)	–5 kN ….. 10 kN
Reaction	< 0.01 N
Accuracy F_x, F_y	≈ 7.5 pC/N
Accuracy F_z	≈ 3.5 pC/N
Natural frequency $f_0(x,y,z)$	3.5 kHz
Working temperature	0 °C ….70 °C
Capacitance	220 pF
Insulation resistance at 20 °C	> 1013 Ω
Grounding insulation	> 108 Ω
Mass	7.3 kg

Table 4: General specifications of the CNC vertical machining center used in the experiments

Tabela 4: Osnovne značilnosti uporabljenega CNC vertikalnega obdelovalnega centra

Model	CNC FANUC 0-M Y.O.M. 1998
Travel *X*, *Y*, *Z*	500 mm × 450 mm × 450 mm
Table Dimensions	705 mm × 450 mm
Tool Changer	18 tools
SPIRSIN	Divisor with tiltable axis
Phase number	3
Frequency	50 Hz
Max revolution number	10000 r/min

Figure 6 clearly shows the effect of feed rate, cutting speed and cutting-tool material on the average surface roughness. According to this figure, in order to obtain the smallest surface roughness, it is necessary to use the *RPHX1204MOEN* cutting tool at low feed rate (0.30 mm/r) and low cutting speed (70 m/min). In addition, in

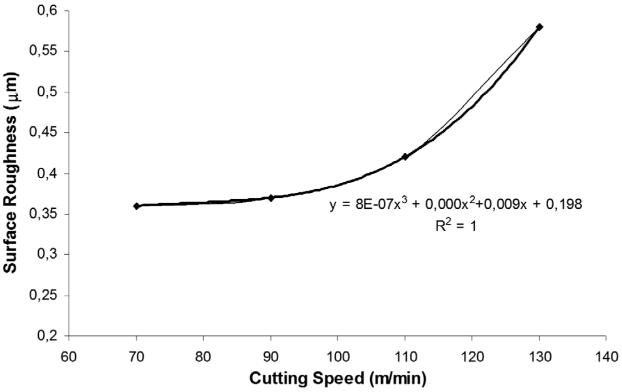

Figure 6: Surface-roughness values (µm) with respect to the cutting speeds at a constant feed rate
Slika 6: Vrednosti za površinsko hrapavost (µm) glede na hitrost rezanja pri konstantni hitrosti podajanja

order to find out which important parameter effects the surface roughness, a variance analysis was made for this aim. According to the results of the ANOVA in **Table 7**, the most efficient cutting parameter that affected the surface roughness was found to be the tool material of the uncoated insert (81.24 %), followed by the cutting speed (4.56 %).

Table 5: Level of independent variables
Tabela 5: Nivo neodvisnih spremenljivk

Variables	Level of variables			
	Lower	Low	Medium	High
Cutting speed, v/(m/min)	70	90	110	130
Feed, f/(mm/r)	0.3	0.3	0.3	0.3
Axial depth, d_a/mm	1	1	1	1

Table 6: Regression analysis of experiment
Tabela 6: Regresijska analiza preizkusov

Regression Analysis: F_x versus V; V_f
* V_f is highly correlated with other X variables
* V_f has been removed from the equation
The regression equation is $F_x = (870 - 1.09)$ V

Predictor	*Coef*	*SECoef*	*T*	*P*
Constant	869.72	18.86	46.12	0.000
V	–1.0862	0.1840	–5.90	0.028

$S = 8.23028$ $R - S_q = 94.6$ % $R - S_q(\text{adj}) = 91.9$ %

Source	*DF*	*SS*	*MS*	*F*	*P*
Regression	1	2359.9	2359.9	34.84	0.028
Residual error	2	135.5	67.7		
Total	3	2495.4			

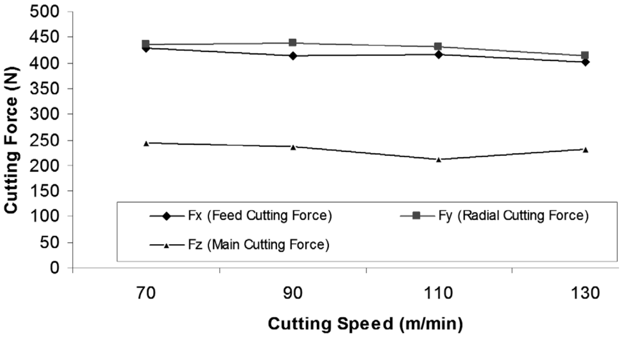

Figure 7: The change of the 3 axis cutting forces for a (1 mm) constant depth of cut and (0.3 mm/r) constant feed rate, dependent on the cutting speed (m/min)
Slika 7: Sprememba 3-osnih sil rezanja pri konstantni globini rezanja (1 mm) in konstantni hitrosti podajanja (0,3 mm/r) v odvisnosti od hitrosti rezanja (m/min)

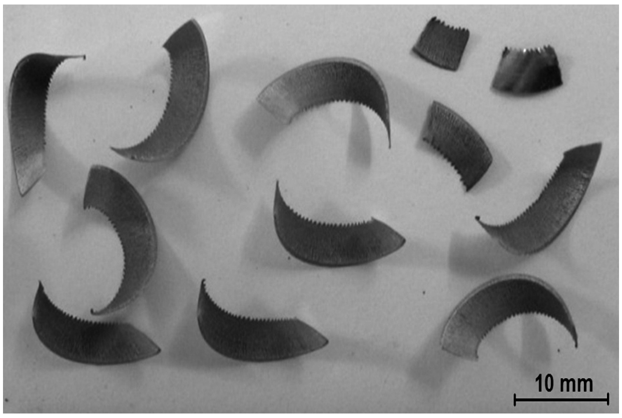

Figure 8: Chip formation at $V = 90$ m/min
Slika 8: Oblika ostružkov pri $V = 90$ m/min

4 CONCLUSIONS

The machinability of chromium-carbide-based hardfacing appears to be strongly related to its microstructural properties, and in particular to the presence and deformation characteristic of the large carbides. The effect of cemented carbide on the main cutting force is much clearer than the effect of the cutting speed. There is an incremental–decremental relationship between the cutting speed and the main cutting force. The breaking on chip contact surface was affected by the tool rake angle in a negative way. The negative chip angle caused an increase in the main cutting force. An increasing relationship between the cutting speed and the arithmetic average surface roughness as well as between the coating

Table 7: Variance analysis of experiment
Tabela 7: Analiza variance preizkusov

Source	D_f	Sum of Squares	Mean square	*F* ratio	Probability	PD
Cutting speeds	3	61906.2	20635.4	0.8436	0.5075	4.56
Uncoated insert	3	1102720.4	367573.5	15.0262	0.0012	81.24
Error	8	195697.0	24462			14.42
Total	14	1357422.4				100

number and the average surface roughness was observed. In the case of the coated tools, the effect of the cutting speed on the surface roughness was much more pronounced than the effect of the different coated cemented-carbide inserts. The experimental results can be used in industry in order to select the most suitable parameter combination in order to achieve the required surface.

5 REFERENCES

[1] K. Ichii, K. Fujimura, T. Takase, Tech. Rep. Kansai Univ., 27 (**1986**), 135

[2] Wear Resistant Surface in Engineering: A Guide to their Production, Properties and Selection, International Research and Development Co. Ltd., Department of Trade and Industry, London, 1985

[3] I. M. Hutchings, A. N. J. Stevenson, Wear of hardfacing white cast irons by solid particle erosion, Wear, 186–187 (**1995**), 150–158

[4] R. Menon, New development in hardfacing alloys, Weld J. (February) (**1996**), 43–48

[5] R. I. King (Ed.), Handbook of high speed mach. technology, Chapman and Hall, London 1985

[6] E. J. Brookes, R. D. James, X. J. Ren, Machining of welded hardfacing materials, In: Proceedings of the Fourth International Conference on Behavior of Materials in Machining: Opportunities and Prospects for Improved Operations, Stratford- Upon-Avon, UK, 1998, 189–198

[7] E. M. Trent, Metal Cutting, 3rd Edition, Butterworths, London 1991

[8] D. A. Stephenson, J. S. Agapiou, Metal Cutting Theory and Practice, Marcel Dekker, New York 1996

[9] X. J. Ren, R. D. James, E. J. Brookes, Wear characteristics of CBN tools in machining hardfacing materials, J. Superhard Mater., 1 (**1999**), 36–45

[10] M. C. Shaw, Metal Cutting Principles, Clarendon Press, Oxford 1984

[11] P. J. Heath, Structure, properties and applications of polycrystalline cubic boron nitride, In: Proceedings of the 14th North American Manufacturing Research Conference, Minneapolis, MN, USA, 1986, 66–80

[12] A. M. Abrao, D. K. Aspinwall, M. L. H. Wise, A review of polycrystalline cubic boron nitride cutting tool developments and application, In: Proceedings of the 13th International Matador Confer., Manchester, UK, 1993, 169–180

[13] W. Konig, A. Berktold, J. Liermann, N. Winands, Top quality components not only by grinding, Ind. Diamond Rev., 3 (**1994**), 127–132

[14] R. M. Hooper, C. A. Brookes, Microstructure and wear of cubic boron nitride aggregate tools, In: Proceedings of the Second International Conference on Science Hard Material, Rhodes, 1984, 907–917

[15] C. A. Brookes, R. D. James, F. Nabhani, A. R. Parry, Structure, composition, and integrity of workpiece: tool interfaces in metal cutting and grinding, In: Proceedings of the IMechE Seminar on Tribology in Metal Cutting and Grinding, 1992, 41–48

[16] G. Boothroyd, Fundamentals of metal machining and machine tools, International Student ed. 5th Printing, McGraw-Hill, New York 1981

[17] E. P. De Garmo, J. T. Black, R. A. Kohser, Material and process in manufacturing, Prentice-Hall International Inc., Englewood Cliffs, NJ 1997

[18] C. Çakır, Modern metal cutting principles, VIPAS, Bursa, 2000

[19] X. J. Ren, R. D. James, E. J. Brookes, L. Wang, Machining of high chromium hardfacing materials, J. Mater. Process. Technol., 115 (**2001**) 3, 423–429

[20] X. J. Ren, Q. X. Yang, R. D. James, L. Wang, Cutting temperatures in hard turning chromium hardfacings with PCBN tooling, Journal of Materials Processing Technology, 147 (**2004**) 1, 38–44

UDK 621.777.2:669.35'71
Original scientific article/Izvirni znanstveni članek

ISSN 1580-2949
MTAEC9, 48(3)379(2014)

PRESSING OF PARTIALLY OXIDE-DISPERSION-STRENGTHENED COPPER USING THE ECAP PROCESS

IZTISKANJE DISPERZIJSKO UTRJENEGA BAKRA PO POSTOPKU ECAP

Matija Kos[1,2], Janko Ferčec[1], Mihael Brunčko[1], Rebeka Rudolf[1,3], Ivan Anžel[1]
[1]Faculty of Mechanical Engineering, University of Maribor, Smetanova 17, 2000 Maribor, Slovenia
[2]Sykofin, d. o. o., Glavni trg 17, 2000 Maribor, Slovenia
[3]Zlatarna Celje, d. d., Kersnikova 19, 3000 Celje, Slovenia
matija.kos@uni-mb.si

Prejem rokopisa – received: 2013-07-01; sprejem za objavo – accepted for publication: 2013-07-26

A combination of internal oxidation (IO) and equal channel angular pressing (ECAP) was used to explore the possibility of uniting the mechanisms of dispersion and deformation strengthening to improve the properties of a Cu-Al alloy with 0.4 % Al. The IO of Cu-Al billets served in the first step of the experiment as a means for dispersion, strengthening the mantle of the billets with a fine dispersion of nanosized oxide particles. The experimental procedure continued with deformation strengthening performed by ECAP, which allowed an intense plastic strain through simple shear.

Material flow in a partly internally oxidized Cu-0.4 % Al billet and in a homogenous reference sample made of modelling mass was also studied to analyse, on the macroscale, the influence of the internal oxidation zone (IOZ) on the material flow behaviour during the ECAP process. The analysis was performed with the aim of revealing the uniformity of the strain distribution and to obtain information about the deformation strengthening across the volume of the billet.

We found that the oxide particles have a minor influence on the material flow on the macroscopic scale during the ECAP process. However, the degree of deformation strengthening in the IOZ was much lower than in the unoxidized core region. The combination of IO and ECAP allows us to produce a Cu composite composed of a hardened oxidized mantle region with good electrical and thermal conductivity and a high- hardened core region. This combination represents a new technological route for the production of high-hardness Cu composites, which could also be used at higher temperatures.

Keywords: ECAP process, internal oxidation, Cu-Al alloy, strengthening mechanism

Kombinacija notranje oksidacije (NO) in postopka ECAP je bila uporabljena za združitev disperzijskega in deformacijskega utrjanja za izboljšanje lastnosti zlitine Cu-Al z 0,4 % Al. Notranja oksidacija je v prvem koraku eksperimenta zagotovila disperzijsko utrjanje plašča preizkušanca s fino disperzijo nano velikih oksidnih delcev. Eksperiment se je nadaljeval z deformacijskim utrjanjem, izvedenim z ECAP-postopkom, ki je omogočil ekstremno plastično deformacijo s čistim strigom.

Preučeno je bilo tudi tečenje materiala na makronivoju v delno notranje oksidiranem Cu-0,4 % Al preizkušancu in homogenem referenčnem vzorcu iz modelirne mase z namenom analize vpliva cone notranje oksidacije na vedenje tečenja materiala med ECAP-postopkom. Analiza je bila izvedena z namenom odkriti enakomernost porazdelitve deformacije in pridobitve informacij o deformacijskem utrjanju po volumnu preizkušanca.

Ugotovili smo, da imajo oksidni delci na makronivoju zelo majhen vpliv na tečenje materiala med ECAP-postopkom, vendar je bila stopnja deformacijskega utrjanja v coni notranje oksidacije veliko nižja kot pa v neoksidiranem jedru. Kombinacija notranje oksidacije in ECAP-postopka nam omogoča izdelavo Cu-kompozita, sestavljenega iz utrjenega oksidiranega plašča z dobro električno in toplotno prevodnostjo ter visoko utrjenega jedra. Ta kombinacija je nova tehnološka pot za izdelavo visokotrdnostnega Cu-kompozita, ki bi se lahko uporabljal tudi pri višjih temperaturah.

Ključne besede: ECAP-postopek, notranja oksidacija, zlitina Cu-Al, mehanizmi utrjanja

1 INTRODUCTION

Considerable interest has been developed in making use of materials with high electrical and thermal conductivity, with microstructural stability and with high-temperature strength. These materials can be used in different segments of the electric and machine-building industry. One of the most promising materials that correspond to the above-mentioned condition is copper, because it has the highest thermal and electrical conductivity among structural materials. Copper has good physical properties but, on the other hand, requires a considerable improvement in strength to be applicable at high temperatures.

To improve its mechanical properties a different strengthening mechanism can be used, such as solid-solution hardening, work hardening, precipitation hardening and dispersion hardening.[1,2] These strengthening mechanisms give engineers the ability to tailor the mechanical properties of materials to suit a variety of different applications. In all these cases the strengthening effect is a consequence of the interactions of gliding dislocations with the barriers (solute atoms, precipitate, dispersoids), and with other dislocations.

An attractive and viable approach for improving the strength of copper is to introduce fine Al_2O_3 particles into the Cu matrix, resulting in an oxide-dispersion strengthening of alloys (ODS alloy). A copper matrix containing fine, nanosized particles is particularly attractive because of its excellent combinations of thermal and electrical conductivity and overall microstructural stability. In order to achieve the fine Al_2O_3 particles in the Cu matrix, powder metallurgy and the IO process are mostly used. However, for non-porous large billets the IO is more suitable. IO is a diffusion-controlled process involving the selective reactions of a less noble solute or second-phase particles with oxygen (also nitrogen or carbon) diffusing in from the surface.[3,4] The problem that occurs during dispersion strengthening with the IO process is to achieve a sufficient depth of the IOZ in a technologically acceptable time.[4]

In engineering practise work hardening is one of the most frequently used methods to improve the strength of metallic products. To achieve a high degree of plastic deformation different techniques have been developed, such as high-pressure torsion (HPT) and equal channel angular pressing (ECAP)[5]. Of these, ECAP is an especially attractive process because the overall billet dimensions do not change during the processing and high shear strains can be accumulated by repeated extrusion through the die.[6–8] The deformation mechanism in the ECAP process depends strongly on many processing parameters, such as the processing route, the geometry of the channel, the presence of friction and the properties of the billet material. These parameters affect the material's flow behaviour, strain distribution and, consequently, the mechanical properties of the pressed material.[9–11]

Significant progress has been made in understanding the fundamental properties and microstructures of ECAPed materials using theoretical analyses and experimental methods. These investigations are based mainly on one-phase materials such as Cu and Al.[12–14] The influence of the second phase particles, such as oxides or precipitates, on the material flow behaviour and on the mechanical properties during ECAP was rarely investigated. In fact the combination of IO and the ECAP process has not yet been studied and no information is available.

This paper describes the possibility of combining the mechanisms of dispersion and deformation strengthening to achieve better mechanical properties of the Cu matrix. The results of material flow in partially internally oxidized Cu-0.4 % Al billet were compared with the flow of a homogenous modelling mass billet to analyse, on the macroscale, the influence of IOZ on the material flow behaviour during the ECAP process.

2 EXPERIMENTAL DETAILS

For the research activities we used a partially internally oxidized Cu-0.4 % Al billet and billets made of modelling mass. Cu-0.4 % Al billets with a cross-section of 10 mm × 10 mm and 50 mm in length were made by vacuum melting, mould casting and calibration rolling. The IO procedure was performed in a mixture of equal parts of copper oxide, copper metal and Al_2O_3 powders enclosed in a glass ampoule and held at 1173 K for 72 h in a tube furnace. This procedure allowed a partial pressure of oxygen equal to the decomposition pressure of copper oxide and maintained the saturation concentration of oxygen in the surface of the billet for longer annealing times. As a result we obtained a billet with thick IOZ 1000 μm.

A simplified, yet representative material system, consisting of different collared modelling mass rings was chosen to simplify the analysis of the macroscopic material flow with homogeneous properties throughout the volume. Two types of modelling billets (MB1, MB2) were used. MB1 was made out of black and white rings in the form of cubes with the dimensions 10 mm × 10 mm × 10 mm to investigate the material flow of homogenous material during the ECAP process (**Figure 1a**). The rings were connected to each other under very low pressure to produce a 10 mm^2 cross-section billet. To simulate the flow of the IOZ billet MB2 was made from horizontal bands that were connected to each other to form a 10 mm^2 cross-section billet (**Figure 1b**). The billets were photographed before extrusion through the die and after each required number of passes.

For the deformation experiments the ECAP toll was designed. Many parameters were taken into consideration regarding the billet shape, the size and the maximum work load. The die with 90° and a square section of 10 mm × 10 mm cross-section and a billet length of 50 mm was used. The outer corner angle was 30°. The die that consisted of two blocks, which were bolted together to give a single internal channel, and the piston were made from UTOP M01 tool steel, hardened to approximately 61 HRc. A simple standard press with 60 t capacity was used. The ECAP pressings were carried out at room

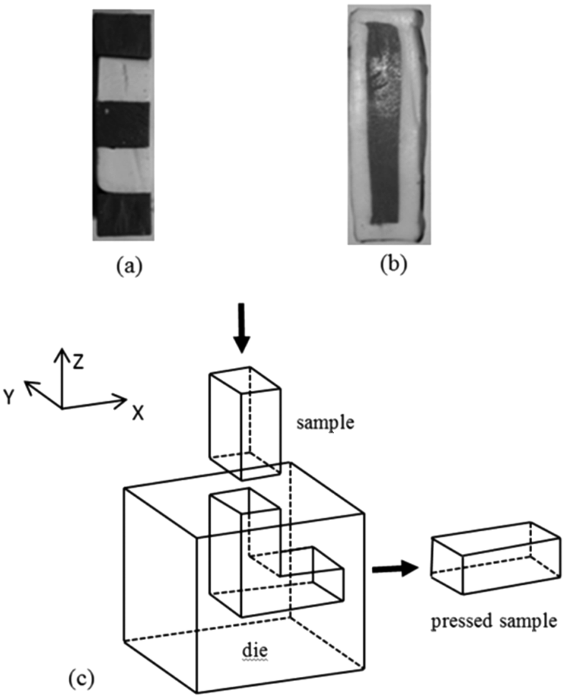

Figure 1: a) Modelling mass billets MB1 and b) MB2, c) schematic illustration of the ECAP process

Slika 1: a) Preizkušanec iz modelirne mase MB1 in b) MB2, c) shematski prikaz ECAP-postopka temperature using route A where the billet is not rotated in any direction[7]. The billet was lubricated with motor oil (OLMALINE SF/CD 20W50). A schematic illustration of the ECAP process is shown in **Figure 1c**.

The samples for the material flow investigation were taken on the $X - Z$ plane according to the coordinate system in **Figure 1c**. The material flow was observed with light microscopy (LM). The samples for LM were prepared with standard metallographic methods and etched with $FeCl_3$. The morphology of the oxide particles (size, shape and distribution) in the IOZ after IO was examined with a scanning electron microscope (SEM) Sirion 400 NC. The metallographic preparations consisted of mechanical wet grinding down to 5 µm with SiC and polishing with an aluminium oxide suspension (0.05 µm). After the ECAP process the IOZ was examined with transmission electron microscopy (TEM) on a Jeol JEM-2100 operated at 200 kV. The samples for TEM were thinned with a Jeol EM-09100IS Ion slicer.

To determine the mechanical properties during the ECAP process we measured the microhardness in a partly internally oxidized Cu-0.4 % Al billet. Microhardness measurements were made before and after the first, second, third, and fourth ECAP passes on the $X - Z$ plane in the IOZ and in the core region.

3 RESULTS AND DISCUSSION

3.1 Internal oxidation

After partial internal oxidation of the sample we obtained IOZ with fine dispersed oxide particles (**Figure 2a**, Area 1). The core of the sample (**Figure 2a**, Area 2) remained a one-phase Cu-0.4 % Al solid solution with slightly increased grains as a consequence of grain coarsening at higher temperatures. In contrast to this, in the IOZ precipitated oxide particles hindered the process of grain growth. The internal oxidation front (IOF) is straight because of the diffusion of oxygen through the volume of the grains, which prevailed against diffusion along the grain boundaries. The mean width of the IOZ was 1000 µm. It is very difficult to achieve such a depth of the IOZ because of the conglomeration of the Cu and Cu_2O powders, which hindered the supply of the oxygen to the surface of the billet. With the addition of Al_2O_3 powders we prevented the conglomeration of powders and maintained the saturation concentration of oxygen in the surface of the billet for longer annealing times.

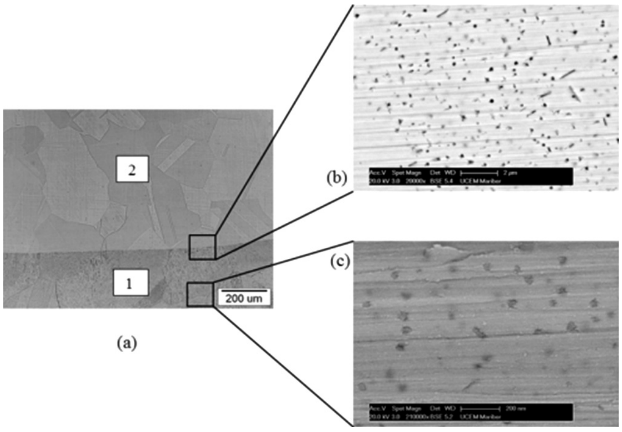

Figure 2: a) LM image of partially internally oxidized Cu-0.4 % Al sample; area 1 is IOZ, area 2 is Cu-0.4 % Al alloy, b) SEM image of the IOF, c) SEM image of the IOZ near the surface area of the billet
Slika 2: a) SM-posnetek delno notranje oksidiranega Cu-0,4 % Al-vzorca; področje 1 je cona notranje oksidacije, področje 2 je Cu-0,4 % Al-zlitina, b) SEM-posnetek fronte notranje oksidacije, c) SEM-posnetek cone notranje oksidacije blizu površine preizkušanca

During the process, oxygen atoms penetrate into the Cu matrix where they react with aluminium. The critical concentration of oxygen for this chemical reaction is very low because of the very high negative free energy of Al oxide formation. Afterwards the solubility product for the oxide ($K_{sp}^{Al_2O_3} = C_{Al}^2 \cdot C_O^3$) is exceeded by the fine oxide particles precipitated from the solid solution.[15]

Figures 2b and **2c** show Al_2O_3 particles at the IOF and in the IOZ near the free surface of the billet. The particles at the IOF have different shapes, from spherical to rod-like, while the particles in the IOZ near the free surface of the billet have a spherical shape. The mean size of the particles increases with the depth of the IOZ, from 50 nm near the free surface (**Figure 2c**) to 300 nm at the IOF (**Figure 2b**). The increase in the mean size of the Al_2O_3 particles with increasing depth of the IOZ is a consequence of the hindered diffusion of oxygen to the IOF that stimulates contra diffusion of the alloying element Al down the concentration gradient towards the IOF. At lower depths of the IOZ the influence of oxide particles on the diffusion of oxygen is negligible. Moreover, with increasing depth of the IOZ the velocity of oxygen diffusion decreases because of the numerous obstacles, i.e., oxide particles. Consequently, there is more time at the IOF for growing the precipitated oxide particles.[4]

3.2 Material flow in modelling mass billets during the ECAP process

Figure 3 shows the flow of the MB1 billet during the first ECAP pass in the $X - Z$ plane. Passing through the deformation zone (dashed lines in **Figure 3**), the horizontal straight bands evolve to inclined bands, which are at an angle with respect to the pressing direction. The angle decreases with the increasing number of passes (**Figure 4**). After the first pass the angle α was 26°, after the second 13°, after the third 10° and after the fourth 6°, which is quite comparable to the angle of inclination of the structural elements mentioned by Segal.[11]

The direction of material flow during the ECAP process was analysed with the changing position of the grey and black dots. The direction of material flow in the outer channel (OC) surface is the opposite of the pressing direction, as shown with a black dot in **Figure 4**. The black dot changes its position in the reverse direction of pressing. In contrast to this, the material flow in the internal channel (IC) surface is in the pressing direction

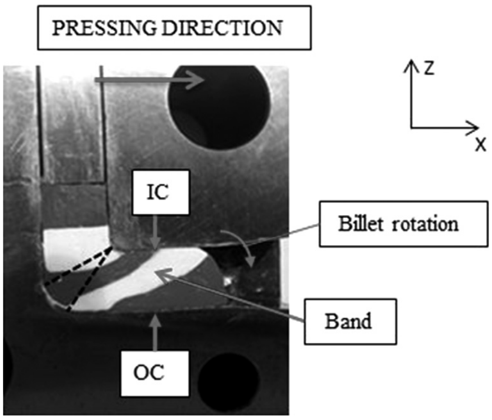

Figure 3: The MB1 billet during the ECAP process
Slika 3: Preizkušanec MB1 med ECAP-postopkom

(grey dot in **Figure 4**). These differences in the material flow from the IC to the OC surface leads to the rotation of the end mass of the billets to the OC surface, as shown in **Figure 3**.

Figure 5 shows the material flow of the MB2 billet during the first ECAP pass. The white layer simulates the flow of the mantle region of the homogenous material. In the OC surface the mean width of the white layer has narrowed and in the IC surface the mean width has increased. As the billet enters the main deformation zone (dash lines in **Figure 5**) the IC layer is subjected to compression in the pressing direction, causing an extension of the white to the centre of the billet. At the same time, the OC surface of the billet is subjected to the tension in the pressing direction, causing narrowing of the white layer with respect to its initial thickness. As a consequence of billets end mass rotation to the OC surface, the grey layer reaches the OC surface. While the white layer was displaced by the grey layer in the OC surface, the white layer's thickness increases slightly (black arrow in **Figure 5**).

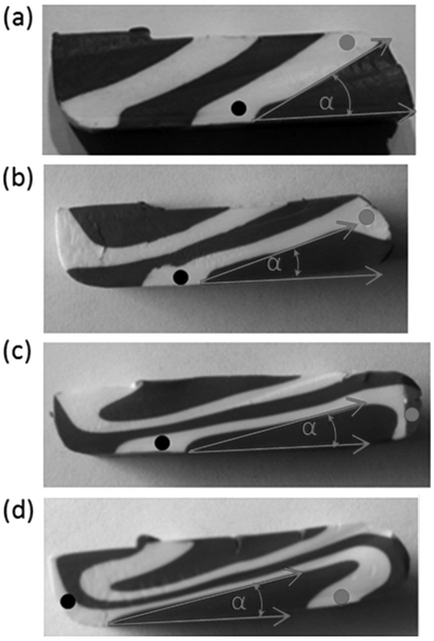

Figure 4: The MB1 billet in the $X – Z$ plane after: a) the first, b) second, c) third and d) fourth ECAP pass
Slika 4: Preizkušanec MB1 v $X – Z$-ravnini po: a) prvem, b) drugem, c) tretjem in d) četrtem ECAP-hodu

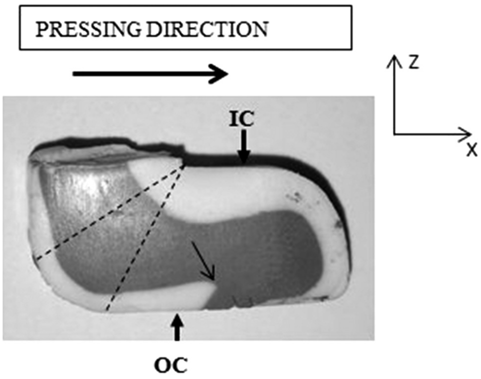

Figure 5: The MB2 billet during the ECAP process
Slika 5: Preizkušanec MB2 med ECAP-postopkom

3.3 Material flow in a partly internally oxidized Cu-0.4%Al billet during the ECAP process

Figure 6 shows a partially internally oxidized Cu-0.4 % Al billet in the $X – Z$ plane during one ECAP pass. The bright area on the edges of the billet is IOZ, which has a similar distribution in the $X – Z$ plane as the white layer in the MB2 billet (**Figure 5**). In the OC surface the mean width of the IOZ has narrowed to 500 µm and in the IC surface the mean width has increased up to 2000 µm. The slight increase in the width of the IOZ in the OC surface (grey arrow in **Figure 6**) is a consequence of the billet's end mass rotation to the OC surface as also shown in billets MB1 and MB2. The rotation of the billets end mass causes high tension in the IC surface, which leads to the formation of cracks (black arrows in **Figure 6**).

The microstructures in **Figure 7** correspond to Areas 1 and 2 indicated in **Figure 6**. In Area 1 (**Figure 7a**) the

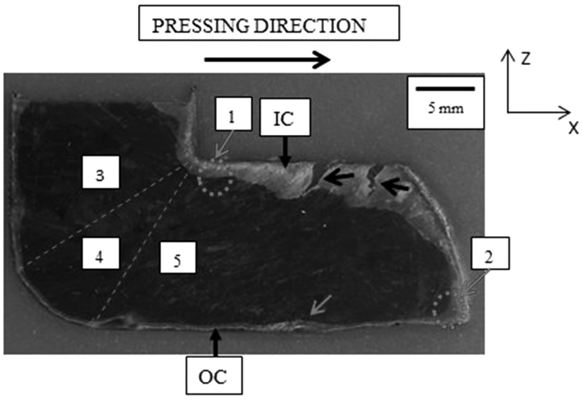

Figure 6: Partially internally oxidized Cu-0.4 % Al billet in the $X –$ Z-plane after one ECAP pass. The black arrows indicate cracks.
Slika 6: Delno notranje oksidiran Cu-0,4 % Al preizkušanec v $X –$ Z-ravnini po prvem ECAP-hodu. Črne puščice kažejo razpoke.

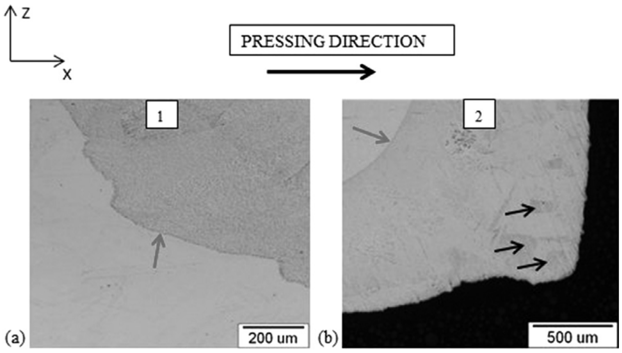

Figure 7: LM image of IOZ in: a) area 1 and b) area 2. The grey arrow indicates the IOF. Black arrows indicate undeformed grains.
Slika 7: SM-posnetek CNO: a) področje 1 in b) področje 2. Sive puščice kažejo fronto notranje oksidacije. Črne puščice kažejo nedeformirana zrna.

IOF is wavy, which indicates that the flow of IOZ is different than the flow of the core region. In Area 2 (**Figure 7b**) the IOF is straight and the un-deformed grains are still visible, indicating that the billet's end part was not subjected to the plastic deformation. The presence of the un-deformed end part of the billet cannot be avoided during the ECAP process because when the billet is inserted into the inlet channel the end part is not in the deformation zone (**Figure 8**).

Variations of material flow from the IC to OC surface are a consequence of a non-uniform strain distribution throughout the cross-section of the billet[11]. The strain distribution in the billet depends on the friction between the channel walls and the billet, die geometry, and properties of the billet material.[9] According to Balasundar et al.[10] the strain distribution in the billet depends on the corner angle in the ECAP die. At lower corner angles (< 40°) the differences in material flow from the IC to OC surfaces leads to the rotation of the end mass of the billet to the OC surface. This rotation was observed in billets MB1, MB2 and in the partially internally oxidized billet.

Prangnell et al.[16] have reported that inhomogeneous deformation increases with friction. As the friction between the billet and the channel walls increases the billet has a tendency to stick to the OC surface. As a consequence the strain at the OC increases and the strain distribution becomes highly inhomogeneous.

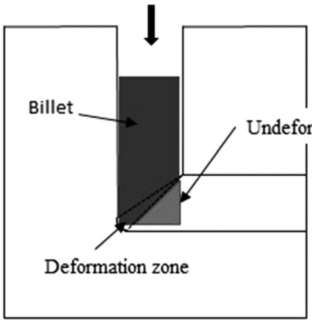

Figure 8: Schematic illustration of undeformed end part of the billet
Slika 8: Shematski prikaz nedeformiranega konca preizkušanca

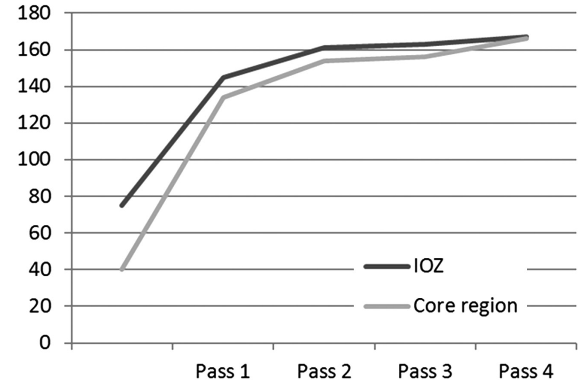

Figure 9: Microhardness of the internal oxidation zone and core region (HV5)
Slika 9: Mikrotrdota cone notranje oksidacije in jedra (HV5)

Numerical analyses have shown that the stress-strain response of the billet material has an influence on the strain distribution during the ECAP process.[10] The modelling mass billets have a flow-softening response, while partially internally oxidized billets have a strain hardening response. The materials with the strain hardening type are subjected to greater strain at the IC than in the OC surface.[17] This can be attributed to the formation of cracks in the partly internally oxidized billet.

On the macroscopic scale the flow of the internally oxidized coat region and the core with the solid solution is similar to the material flow in the billets MB1 and MB2, where the material properties were the same in the mantle and in the core region. The results indicate that oxide particles have a minor influence on the material flow in the IOZ. The differences could be attributed to the different strain distribution in the IC surface as a consequence of the strain-hardening rate of the IOZ.

3.4 Microhardness measurements

The microhardness has been measured in the IOZ and in the core region. Measurements were taken in the centre of the billet where the deformation is the most homogeneous in the IC, OC surface and in the core region.

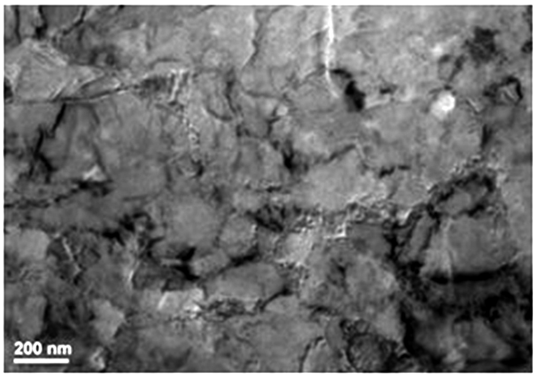

Figure 10: TEM image of the internal oxidation zone
Slika 10: TEM-posnetek cone notranje oksidacije

The results are presented in **Figure 9**. It would be noted that because of the interaction between the Al_2O_3 particles and the sliding dislocations after four passes through the die the ΔHV would be larger in the IOZ. Due to an inhomogeneous strain distribution in the ECAP die the IOZ was subjected to higher strain in the IC surface, which could also contribute to a higher ΔHV in the IOZ. After four passes through the ECAP die the hardness of the IOZ and the core region are the same, which could be attributed to different deformation mechanisms.

During the ECAP process, strong dislocation activities subdivide the original coarse grain into smaller grains[17]. The strength and hardness of the material increases with the decrease of the grain size, as determined by the Hall-Petch equation:

$$\sigma_y = \sigma_0 + \frac{k_y}{\sqrt{d}}$$

where d is the average size of the grain, σ_y is the yield stress, σ_0 is the starting stress and k_y is the strengthening coefficient.

Meyers[18] has analysed the deformation mechanisms in nanostructured materials where grain-boundary sliding has been proposed to be the dominant deformation mechanism at grain sizes < 50 nm. The grain-boundary sliding is a mechanism where the layer of grains slides with respect to the other. This mechanism can lead to a decrease in strength and hardness of the material. Although we have in the IOZ (**Figure 10**) a grain size of approximately 150 nm this effect is present because the Al_2O_3 particles have blocked the dislocation motion. Consequently, from an energy point of view, the sliding was preferable along the grain boundaries. Due to this, deformation strengthening was no longer present in the IOZ.

4 CONCLUSIONS

In our research a combination of IO and ECAP was used to explore the possibility of uniting the mechanisms of dispersion and deformation strengthening to improve the properties of a Cu-Al alloy with 0.4 % Al. Material flow in a partly internally oxidized Cu-0.4 % Al billet and in a homogenous reference sample made of modelling mass was studied to analyse on the macroscale the influence of IOZ on the material-flow behaviour during the ECAP process.

From the obtained results and their analysis several conclusions have been made:

- On the macroscopic scale the material flow in the partly internally oxidized Cu-0.4 % Al billet, which has different material properties in the core and in the mantle region, is the same or similar to that in the homogenous material, where the properties of the mantle region are the same as in the core region. This indicates that the oxide particles have a minor influence on the material flow during the ECAP process.
- Non-uniform strain distribution during the ECAP process leads to an uneven thickness of the internal oxidation zone throughout the mantle region of the billet.
- The combination of IO and ECAP allows us to produce a Cu composite composed of a hardened oxidized mantle region with good electrical and thermal conductivity and a high-hardened core region.
- The combination of dispersion and a deformation strengthening mechanism represents a new technological route for the production of a high-hardness composite that could also be used at higher temperatures, but it is necessary to investigate the solution to achieve an even thickness of the oxidation zone throughout the mantle region of the billet. A possible solution would be the application of back pressure during the ECAP process.
- In an upcoming publication a detailed analysis will be made of the deformation mechanisms in the Cu composite.

Acknowledgment

The operation was partly financed by the European Union, European Social Fund.

5 REFERENCES

[1] E. Arzt, D. S. Wilkinson, Acta Metallurgica, 34 (**1986**) 10, 1863–1898

[2] E. Arzt, P. Grahle, Zeitschrift für Metallkunde, 87 (**1996**) 5, 874–883

[3] I. Anzel, Metalurgija, 13 (**2007**) 4, 325–336

[4] N. Birks, G. H. Meier, F. S. Pettit, Introduction to High Temperature Oxidation of Metals, 2nd edition, Cambridge University Press, Cambridge 2006

[5] Z. Horita, M. Furukawa, M. Nemoto, T. G. Langdon, Mat. Sci. Teh., 16, (**2000**), 1239–1245

[6] V. M. Segal, V. I. Reznikov, A. E. Drobyshevskiy, V. I. Kopylov, Metally, 1 (**1981**), 115

[7] V. M. Segal, V. I. Reznikov, V. I. Kopylov, D. A. Pavlik, V. F. Malyshev, Processes of Structure Formation During Plastic Straining, 1st ed., Scientific and Technical Publishing, Minsk, Belarus 1994, 223

[8] M. Furukawa, Z. Horita, T. G. Langdon, Mater. Sci. and Eng., A332 (**2002**), 97–109

[9] A. Gholina, P. B. Prangnell, M. V. Markushev, Acta. Mater., 48 (**2000**), 1115–1130

[10] I. Balasundar, M. Sudhakara Rao, T. Raghu, Mater. and Design, 30 (**2009**), 1050–1059

[11] V. M. Segal, Mater. Sci. and Eng., A197 (**1995**), 157–164

[12] P. B. Prangnell, A. Gholinia, V. M. Markushev, In: T. C. Lowe, R. Z. Valiev (Eds.), Investigations and Applications of Severe Plastic Deformation, Kluwer Academic Pub., Dordrecht 2000, 65–71

[13] Y. Iwahashi, Z. Horita, M. Nemoto, T. G. Langdon, Acta Mater., 46 (**1998**), 3317–3331

[14] Y. Iwahashi, Z. Horita, M. Nemoto, T. G. Langdon, Acta Mater., 45 (**1997**), 4733–4741

[15] I. Anžel, A. Kneissl, L. Kosec, Z. Metallkd., 90 (**1999**), 621–635

[16] P. B. Prangnell, C. Harris, S. M. Roberts, Scripta Mater., 37 (**1997**), 983

[17] S. J. Oh, S. B. Kang, Mater. Sci. and Eng., A343 (**2003**), 107–115

[18] M. A. Meyers, A. Mishra, D. J. Benson, Progress in Materials Science, 51 (**2006**), 427–556

UDK 669.715:621.777.2
Original scientific article/Izvirni znanstveni članek

ISSN 1580-2949
MTAEC9, 48(3)385(2014)

ENHANCEMENT OF MECHANICAL PROPERTIES OF THE AA5754 ALUMINUM ALLOY WITH A SEVERE PLASTIC DEFORMATION

IZBOLJŠANJE MEHANSKIH LASTNOSTI ALUMINIJEVE ZLITINE AA5754 Z VELIKO PLASTIČNO DEFORMACIJO

Neset Izairi[1], Fadil Ajredini[1], Afërdita Veveçka-Priftaj[2], Mimoza Ristova[3]
[1]Department of Physics, Faculty of Natural Sciences and Mathematics, State University of Tetovo, Tetovo, Republic of Macedonia
[2]Department of Physics, Polytechnic University of Tirana, Sheshi Nënë Tereza, N.4, Tirana, Albania
[3]Institute of Physics, Faculty of Natural Sciences and Mathematics, University Ss. Cyril and Methodius, Skopje, Republic of Macedonia
neset.izairi@unite.edu.mk

Prejem rokopisa – received: 2013-07-15; sprejem za objavo – accepted for publication: 2013-09-05

Mechanical properties of materials with ultrafine grain (UFG) size have attracted considerable scientific attention and technological interest during the last few years. It was well established that the grain size of metallic alloys may be substantially refined with a severe plastic deformation (SPD). The present work focuses on equal-channel angular pressing (ECAP) as the most used method of SPD for grain refinement inducing a significant enhancement to the mechanical and functional properties of the commercial AA5754. ECAP with up to 6 passes resulted in a substantial grain-size reduction from 70 µm of an as-received sample to 5 µm. The aforementioned reduction of the grain size increased the microhardness by a factor of 4. These results were compared to those of AA3004.

Keywords: severe plastic deformation, equal-channel angular pressing (ECAP), mechanical properties, microhardness (HV), tensile test

Zadnjih nekaj let vzbujajo pozornost znanstvenikov in tehnologov mehanske lastnosti materiala z ultradrobnimi zrni (UFG). Ugotovljeno je bilo, da je z uporabo velike plastične deformacije (SPD) mogoče močno zmanjšati velikost zrn v kovinski zlitini. To delo poroča o metodi "equal-channel angular pressing" (ECAP) kot najpogosteje uporabljeni SPD za zmanjšanje zrn, ki povzroči občutno povečanje mehanskih in funkcionalnih lastnosti komercialne zlitine AA5754. ECAP povzroči občutno zmanjšanje velikosti zrn iz 70 µm pri dobavljeni zlitini na 5 µm po 6 prehodih. Omenjeno zmanjšanje velikosti zrn je povečalo mikrotrdoto za faktor 4. Rezultati so bili primerjani z rezultati pri zlitini AA3004.

Ključne besede: velika plastična deformacija, equal-channel angular pressing (ECAP), mehanske lastnosti, mikrotrdota (HV), natezni preizkus

1 INTRODUCTION

The processing, structure and properties of metallic materials with ultrafine grain size have been of increasing interest over the past few years. Grain-size reduction is one of the most attractive ways of improving the mechanical properties of metallic materials. It is known that the strength of all the polycrystalline materials is related to the grain size, through the Hall-Petch equation, predicting an increase in the yield strength (σ_y) with a decrease in the grain size (d):

$$\sigma_y = \sigma_0 + kd^{-1/2} \quad (1)$$

Severe plastic deformation (SPD)[1–5] has gained importance since it offers a direct conversion of bulk metals and alloys with conventional grain sizes to even nanoscaled materials with outstanding new mechanical properties. In order to convert a coarse-grained solid into a material with fine grains, it is necessary to impose an exceptionally high strain in order to introduce a high density of dislocations and to subsequently rearrange the dislocations, forming an array of grain boundaries.[4,6–11] The following are the three SPD methods that attract most of the scientific attention: high-pressure torsion (HPT),[6,7] accumulative roll-bonding (ARB)[10,11] and equal-channel angular pressing (ECAP),[4,8,9] introduced by Segal and co-workers in 1980.[4]

The aim of this paper is to present a grain refinement and the resulting improvement in the mechanical properties using ECAP on the commercial AA5754 Al-alloy. The improvement in the mechanical properties and the grain refinement were studied as functions of the number of ECAP passes.

Figure 1 shows a schematic illustration of the ECAP procedure. In the present experiment a die was constructed as a channel bent at an angle close to 90°. A sample was machined to fit into the channel. The sample was then pressed through the die, using a plunger. The strain imposed on the sample in each passage through the die depended primarily upon the angle, Φ, between the two parts of the channel (90° in **Figure 1**) as well as, to a minor extent, upon the angle of curvature, φ, representing the outer arc of curvature where the two channels intersect (0° in **Figure 1**). If the samples are pressed repeatedly, different slip systems may be introduced by rotating the samples between the consecutive passes through the die. In practice, four separate processing

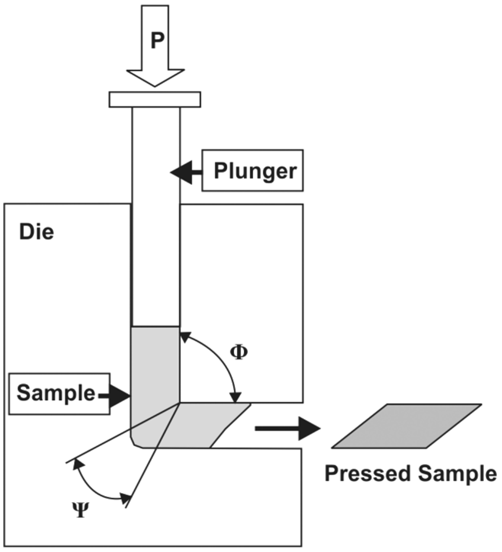

Figure 1: Sectional view of the ECAP die
Slika 1: Prerez skozi ECAP-orodje

routes have been identified for use in ECAP (**Figure 2**). Between each two consecutive passes, a sample can be rotated around the longitudinal axis through the angles of 0° (route A) and 90° in the alternate direction (route B_A), by 90° in the same manner for each pass (route B_C) or by 180° (route C). These different processing routes, along with the number of passes, strongly determine the final microstructure.[4,8,9]

The structural features of the SPD-processed metal are quite complex and they are characterized not only by the formation of ultrafine grains, but also by the presence of non-equilibrium grain boundaries, having a high density of dislocations and vacancies,[12,13] high lattice distortions and possibly also the changes in the local phase composition.[12–14]

In order to examine the potential for using route B_c ECAP for the grain-size refinement and, thus, for the improvement of the mechanical properties, the commercial 5754 Al-alloy was selected for this study. For the sake of comparison, certain results for the AA3004 Al-alloy, the subject of our former research,[15] are given. The AA5754 alloy was chosen because of its technological importance and its relatively low presence in the available ECAP literature.

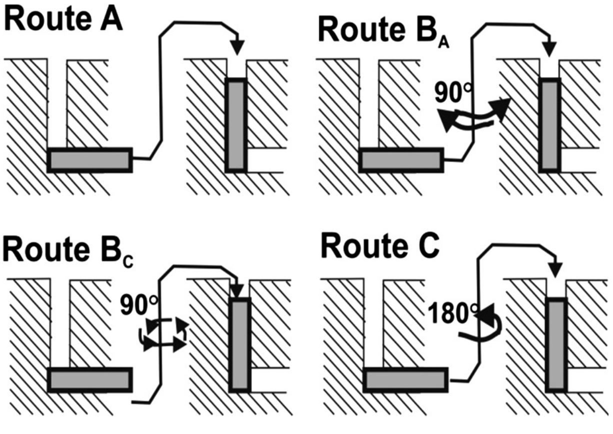

Figure 2: Four processing routes in ECAP
Slika 2: Štiri vrste predelave pri ECAP

2 EXPERIMENTAL WORK

The experiments were conducted on a light-weight commercial Al-alloy, AA5754, supplied from STAMPAL-Torino, Italy, having the composition presented in **Table 1**. According to the manufacturer's declaration, the grain size of the as-prepared samples is about 70 μm. The samples were in a cylindrical form, 10 mm in diameter. Being subjected to ECAP, up to a total of 6 passes at room temperature, they retained the same diameter. Small rectangular pieces suitable for the HV tests were cut from the as-pressed cylinders,[16–21] polished and then subjected to the Vickers-microhardness (HV) measurements, using a load of 300 g, applied for 15 s. For the tensile tests, the samples 100 mm in length and 10 mm in diameter were produced. The samples suitable for the scanning electron microscopy (SEM) were prepared to fit in the sample holder (a diameter of 10 mm and length of 12 mm). Their surfaces were polished with a fine polishing paste and then etched in a 5 % HF solution for 0.5 min to 1 min in order to obtain the visibility of the grain boundaries. The results for the HV and tensile tests performed on the AA3004 aluminum alloy (reported elsewhere)[18] are also given for comparison with the present results for AA5754, the subject to this research. The compositions of both alloys are given in **Table 1**.

Table 1: Chemical compositions of AA5754 and AA3004 (for comparison) in mass fractions, *w*/%
Tabela 1: Kemijska sestava AA5754 in AA3004 (za primerjavo) v masnih deležih, *w*/%

Al-alloy	Al	Mg	Mn	Cr	Fe	Si	Zn
AA5754	96.1–95.4	2.4–2.6	0.1–0.6	0.4	0.4	0.4	0.2
AA3004	97.8	1.2	1	0	0	0	0

A digitalized scanning-electron-microscopy (SEM) system of a JEOL JSM-T220A SEM was used as an imaging tool for three samples (obtained after 2, 5 and 6 passes) to estimate the grain size. The calculations were made with the SPIP V3.2.6.0 software.

3 RESULTS AND DISCUSSION

Figure 3 shows a variation in the microhardness with the number of passes, where the measurements were taken on two orthogonal planes on a specimen surface. The first point in **Figure 3** (the zero passes) refers to the as-received alloy. **Figure 3** shows that HV is essentially independent of the plane of sectioning (longitudinal and perpendicular). HV increases abruptly after the first pass, but thereafter it increases slowly with the progress in the

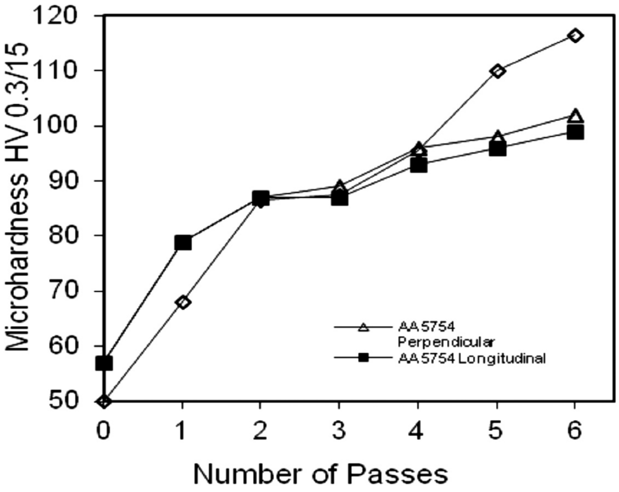

Figure 3: Improvement of the microhardness (HV) depending on the number of ECAP passes measured in two orthogonal planes for AA5754 (70 microns in as-received condition). Evolution of AA3004 (50 microns in as-received condition) is given for comparison.

Slika 3: Povečanje mikrotrdote (HV) v odvisnosti od števila ECAP-prehodov, izmerjeno na dveh ortogonalnih ravninah za AA5754 (70 μm v dobavljenem stanju). Za primerjavo je prikazana mikrotrdota za AA3004 (50 μm v dobavljenem stanju).

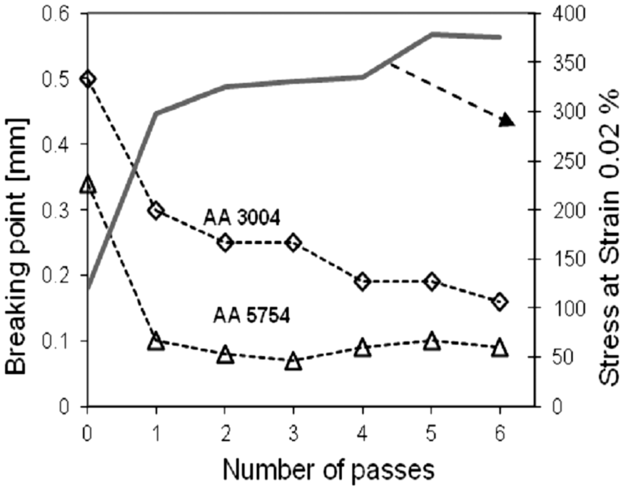

Figure 5: Left *y*-axis: the breaking point changes with the number of ECAP (B_c) passes for AA5754. The change for AA3004 is given for comparison. Right *y*-axis with a gray line: presentation of the stress at a strain of 0.02 % (elastic region, governed by the Hook's law) for the as-received sample and after 1–6 passes.

Slika 5: Leva *y*-os: prelomna točka s številom ECAP-prehodov za AA5754. Za primerjavo je prikazana AA3004. Desna *y*-os s sivo linijo: prikaz napetosti pri raztezku 0,02 % (elastično področje, ki ga določa Hookov zakon) za dobavljeno stanje in po 1–6 prehodih.

pass number (up to 6). A comparison with another widely utilized Al-alloy, AA3004, shows that both alloys achieve the same microhardness after three passes. The results of the tensile testing are shown in **Figure 4**, where the stress is plotted against the strain for a sample in the as-received condition and for the samples after 1 to 6 passes. These curves show that the elongations due to the applied force were significantly reduced after the ECAP processing. It is obvious that the unpressed (as-received) alloy revealed an increase in the stress from about 80 MPa to about 240 MPa after a single ECAP pass, i.e., an increase by a factor of 3. It is also evident that further ECAP passes (2–6) resulted in another stress increase up to 340 MPa (an improvement of more than 4 times). **Figure 5** presents a change in the strength at fracture due to the pass number in the ECAP processing (the results derived from **Figure 4**). It is evident from **Figure 5** that the strength at fracture was substantially reduced with the ECAP processing, from 0.35 mm for the strain of the as-received sample to about 0.11 mm for the sample after a single pass. **Figure 5** revealed that further ECAP (B_c) processing with 2 to 6 passes caused further deterioration of the strength at fracture.

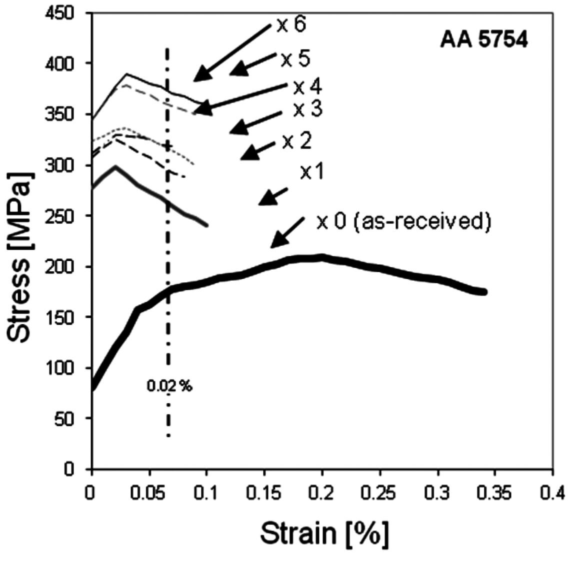

Figure 4: Tensile test: stress versus strain of AA5754 at room temperature for the as-received sample and the samples subjected to 1–6 passes

Slika 4: Natezni preizkus: napetost proti raztezku za AA5754 pri sobni temperaturi za dobavljeno stanje in po 1–6 prehodih

SEM micrograms of the AA5754 surfaces are presented in **Figure 6**. The image in **Figure 6a** shows a network of grain boundaries with thin edges, suggesting small voids among the grains. Furthermore, the calculations of the grain size from **Figure 6** indicate that a single pass causes an abrupt fall from the mean grain size of 70 microns (the value declared by the manufacturer) to about an average of 10 microns, where the standard deviation (SD) appears to be 0.4 μm, suggesting a rather uniform refinement. The following ECAP passes, as seen from **Figures 6b** and **6c**, caused further grain refinement.

A presentation of the grain size versus the pass number, given in **Figure 7**, shows an abrupt fall after the first pass, and thereafter a tendency for saturation at a grain size of 4–5 μm, which is an expected result, in agreement with the Hall-Petch equation (1). Another observation is obvious: further treatment with ECAP cycles (4 and 6 passes) result in a decrease in the grain size.

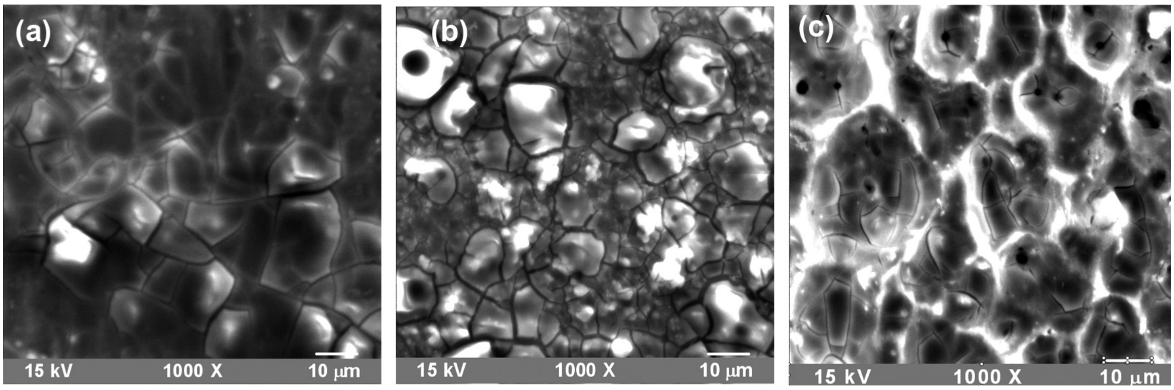

Figure 6: SEM images of the surface of AA3004: a) after a single pass (grain size of (10.3 ± 0.410) μm), b) after 4 passes (grain size of (6 ± 1.9) μm), c) after 6 passes (grain size of (5 ± 2.1) μm)

Slika 6: SEM-posnetki površine AA3004: a) po enem prehodu (velikost zrna (10,3 ± 0,410) μm), b) po 4 prehodih (velikost zrna (6 ± 1,9) μm), c) po 6 prehodih (velikost zrna (5 ± 2,1) μm)

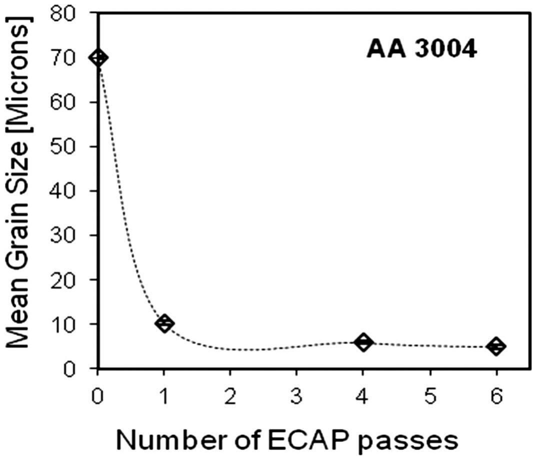

Figure 7: Grain-size evolution of AA3004 with the number of ECAP passes

Slika 7: Spreminjanje velikosti zrn pri AA3004 s številom ECAP prehodov

4 CONCLUSION

In summary, this investigation demonstrates that ECAP was an effective tool for achieving a substantial reduction in the GS of the commercial 5754 Al-alloy from 70 μm to about 5 μm due to 6 passes. The microhardness (HV) of the alloy increased abruptly after the first pass, but thereafter it increased slowly with the following passes (up to 6). The observed increase in the HV of the alloy obviously resulted from the grain-size refinement, followed by an advanced spatial grain packing. The HV of AA5754 increased 3–4 times upon 5–6 ECAP passes, while the grains were refined from 70 μm to about 5–6 μm. The tensile tests showed that the elongations due to the applied force were significantly reduced after the ECAP processing. The stress grew from about 80 MPa to about 240 MPa upon a single pass.

5 REFERENCES

[1] V. M. Segal, Materials Science and Engineering, A2 (**1999**) 71, 322–333

[2] Y. Iwahashi, Z. Horita, M. Nemoto, T. G. Langdon, Metall. Mater. Trans., 29A (**1998**), 2503–2510

[3] O. E. Hall, Proceedings of Royal Society, B 64 (**1951**), 747–753

[4] H. Gleiter, Progress in Materials Science, 33 (**1989**), 223–315

[5] N. J. Patch, Journal of Iron Steel Institute, 174 (**1953**), 25–28

[6] R. Z. Valiev, A. V. Korznikov, R. R. Mulyukov, Materials Science and Engineering, A1 (**1993**), 223–248

[7] O. V. Mishin, V. Y. Gertsman, R. Z. Valiev, G. Gottstein, Scripta Materialia, 35 (**1996**) 7, 873–878

[8] V. V. Rubin, Large plastic deformation and destruction of metals, Metalurgia, Moscow 1987

[9] J. G. Sevillano, P. Van Houtte, E. Aernoudt, Progress in Materials Science, (**1980**), 25–69

[10] R. Z. Valiev, I. V. Islamgaliev, I. V. Alexandrov, Progress in Mat. Sci., 45 (**2000**), 103–189

[11] Y. Saito, H. Utsunomiya, N. Tsuji, T. Sakai, Acta Materialia, 47 (**1999**), 579–583

[12] Y. T. Zhu, T. C. Lowe, T. G. Langdon, Scripta Materialia, 51 (**2004**) 8, 825–830

[13] M. Zehetbauer, H. Stuwe, A. Vorhauer, E. Schafler, J. Kohout, Advanced Engineering Materials, 5 (**2003**), 330–337

[14] R. Z. Valiev, T. G. Langdon, Progress in Materials Science, 51 (**2006**), 881–981

[15] N. Izairi, F. Ajredini, A. Vevecka-Priftaj, M. Ristova, Acta Metallurgica Slovaca, 19 (**2013**) 4, 302–309

[16] A. A. Salem, T. G. Langdon, T. R. McNelley, C. R. Kalidindi, S. I. Semiatin, Metallurgical Materials Transactions A, 37A (**2006**), 2879–2891

[17] T. G. Langdon, Materials Science and Engineering, A 462 (**2007**), 3–11

[18] A. Vevecka-Priftaj, A. Böhner, J. May, H. W. Höppel, M. Göken, Materials Science Forum, 584–586 (**2008**), 741–747

[19] M. Prell, C. Xu, T. G. Langdon, Materials Science and Engineering, A 480 (**2008**), 449–455

[20] M. Kawasaki, Z. Horita, T. G. Langdon, Material Science and Engineering, A524 (**2009**), 143–150

[21] C. Xu, S. Schroeder, P. Berbon, T. G. Langdon, Acta Materialia, 58 (**2010**), 1379–1386

UDK 536.2:519.61/.64
Original scientific article/Izvirni znanstveni članek

ISSN 1580-2949
MTAEC9, 48(3)389(2014)

THERMAL EFFECTS OF A HIGH-PRESSURE SPRAY DESCALING PROCESS

TOPLOTNI UČINKI POSTOPKA ODŠKAJANJA Z VISOKOTLAČNIM BRIZGANJEM

Mária Čarnogurská[1], Miroslav Příhoda[2], Zdeněk Hajkr[2], René Pyszko[2], Zdeněk Toman[2]

[1]Technical University of Košice, Faculty of Mechanical Engineering, Vysokoškolská 4, 042 00 Košice, Slovakia
[2]VŠB – Technical University of Ostrava, Faculty of Metallurgy and Materials Engineering, 17. listopadu 15, 708 33 Ostrava-Poruba, Czech Republic
miroslav.prihoda@vsb.cz

Prejem rokopisa – received: 2013-07-16; sprejem za objavo – accepted for publication: 2013-09-04

The article deals with the possibilities to remove scale from a slab surface by means of a hydraulic spray using pressurized water as well as with an analysis of the influence of the employed removal method on the thermal field of flat rolled products. The effect of spray descaling on the temperature field of the rolled material was established experimentally in a real mill in semi-operational conditions during the process of secondary spray descaling. The experiment was carried out with two sample slabs. The dimensions of a slab were 400 mm × 400 mm × 30 mm and the chemical composition was 0.20 % C, max. 1.4 % Mn, 0.045 % P, 0.045 % S and 0.009 % N. The temperature data for different depths below the surface of the slab being sprayed, obtained during the experiment, were processed using IHCP1D, a software developed on the basis of the Beck minimization-principle algorithm. The obtained values of the heat transfer coefficient represent the boundary condition for a numerical model of the spraying process. Its mean value established in the experiment was 18460 W/(m^2 K).

Keywords: spray, scales, temperature field, heat transfer coefficient, boundary condition

Prispevek obravnava možnost hidravličnega odstranjevanja škaje s površine litih slabov z visokotlačnim brizganjem vode in tudi analizo vpliva načina odstranitve na toplotno polje ploščatih valjancev. Eksperimentalno je bil preizkušen vpliv visokotlačnega odstranjevanja škaje na temperaturno polje valjanega materiala na proizvodni liniji valjarne med sekundarnim odstranjevanjem škaje. Preizkus je bil izveden z dvema vzorcema. Dimenzija valjanca je bila 400 mm × 400 mm × 30 mm, kemijska sestava pa 0,20 % C, maksimalno 1,4 % Mn, 0,045 % P, 0,045 % S, 0,009 % N. Eksperimentalno pridobljene podatke o toploti na posamezni globini pod površino valjanca smo nato obdelali s programsko opremo IHCP1D, ki deluje po algoritmu Beckovega minimalizacijskega principa. Navedeni faktor je hkrati mejni pogoj za numerični model odškajanja. Eksperimentalno določena povprečna vrednost faktorja je 18460 W/(m^2 K).

Ključne besede: visokotlačno brizganje, škaja, temperaturno polje, koeficient prenosa toplote, mejni pogoji

1 INTRODUCTION

The present development of high-quality new compositions of rolled steels combined with the fluctuating furnace atmosphere lead to a formation of scales that are very thin, adhesive and hard to remove from the surface of the rolled material. Descaling issues have been examined by a number of authors presenting the results of their experiments across a wide spectrum of applications. The rolled-in scales that cause defects in a billet, including visual surface faults, are discussed in[1], among other issues. In addition to the other methods, this problem can be resolved with high-pressure spray descaling using modern spray nozzle types, with which a higher operating pressure and force of the water jet per unit of area can be achieved.[2] One object of observations in the steel rolling technology research is the heat transfer coefficient.[3]

Spray descaling has an impact not only on the temperature field of the billet but also on the quality of its surface. The latter is usually associated with the determination of the heat transfer coefficient. The coefficient also represents the boundary condition for a numerical solution model of the spray based on the finite element method (FEM). Article[4] deals with the issue of surface quality of continuously cast slabs. It points to the significant impact of secondary cooling in compliance with the required surface temperature. A new element in the spray descaling theory is introduced in[5]. The paper presents the water hammer effect theory. The author argues that the drops of water falling at a speed of 100 m s^{-1} to 300 m s^{-1} over an extremely short interval (0.1–5 μs) may generate a pulse (peak) impact pressure with the maximum value of 300 MPa. It was proved that a water jet acting this way is able to descale even a cold material.

Many solutions to the temperature related heat transfer problems make an intensive use of the so-called inverse problem. In addition to determining the heat transfer coefficient by means of the inverse procedure, the inverse algorithm methodology is also used, for example, in the material defect detection after hot processing as well as in other technical applications.

2 DESCALING PRINCIPLE

A descaling process aims to achieve the best possible quality of the surface with the lowest possible reduction in the temperature of the rolled material and the lowest possible energy consumption in the production of pressurized water. The process requires a generation of large impact pressures at a low water flow rate. The quantity of the water falling to the surface of the material during spraying is evaluated by means of *SIR* (specific impingement rate) indicators defined as:

$$SIR=\frac{Q_V}{v\cdot w}\quad (\mathrm{m^3/m^2}) \tag{1}$$

The hydraulic descaling of hot rolled steel plates with a higher silicone amount can be positively influenced with increased amounts of phosphorus and sulfur. Phosphorus reduces the binary eutectic temperature of a FeO/Fe_2SiO_4 compound. Sulfur forms a eutectic, a low melting point FeO/FeS compound on the metal plate surface.

3 HEAT TRANSFER COEFFICIENT DETERMINATION METHODOLOGY

The hydraulic descaling process involves not only the descaling itself, but also the cooling of the surface of the rolled material. The knowledge of the temperature field of the material is still rather relevant since it allows an optimization of the rolling process in real operational conditions in terms of the dimensional tolerances, the resulting structure and the surface quality of a rolled product. Slabs feature two dimensions substantially larger than the third dimension, i.e., the thickness and, therefore, we can assume a unidimensional thermal transfer in the major part of their volume.

Basically, two methods are available to address the issue of the changes in the temperature fields of rolled materials. They are the *analytical* method and the *numerical* method. The analytical method is based on either the temperature balance or, in the case of an application of an inverse problem, the so-called Beck's minimization principle.[6] The basis of the numerical method is a determination of the heat transferred to an elementary volume per interval of time, $\Delta\tau$, through a transmission from the adjacent volumes. Its undoubted advantage is in that it respects the dependence between the material properties and the temperature.

3.1 Heat balance

A change in the temperature field of a slab being sprayed results from the heat transfer conditions of spray descaling. The heat transfer coefficient, *h,* is an inevitable boundary condition needed for a direct problem calculation. The coefficient calculation procedure using the heat balance method can be summarized as follows.

The total amount of the heat removed by the spray is expressed with the following formula:

$$\Delta Q=\sum Q_{\mathrm{be}}-\sum Q_{\mathrm{af}}\quad (\mathrm{J}) \tag{2}$$

The amount of the heat before spraying can be expressed with the formula below:

$$\sum Q_{\mathrm{be}}=\sum m\cdot c_p\cdot t_{i,\mathrm{be}}\quad (\mathrm{J}) \tag{3}$$

The amount of the heat after spraying can be expressed with the formula below:

$$\sum Q_{\mathrm{af}}=\sum m\cdot c_p\cdot t_{i,\mathrm{af}}\quad (\mathrm{J}) \tag{4}$$

Using the heat transfer theory, the amount of the heat transferred by the spray can be expressed as:

$$\Delta Q=h\cdot(t_0-t_{\mathrm{w}})\cdot S\cdot\tau_{\mathrm{adm}}\quad (\mathrm{J}) \tag{5}$$

The heat transfer formula follows from relations (2) and (5):

$$h=\frac{\Delta Q}{(t_0-t_{\mathrm{w}})\cdot S\cdot\tau_{\mathrm{adm}}}\quad \mathrm{W/(m^2\ K)} \tag{6}$$

3.2 Inverse problem

An inverse problem is based on a direct problem solution. A determination of the boundary conditions of operational experiments is often rather problematic. However, experimental observations of the time behavior of the temperature are available for several points of the examined body. The temperature data serve as the input values for the calculation of the unknown boundary conditions and this approach is referred to as an *inverse problem*. The inverse problem solution procedure is based on the minimization principle. In hydraulic descaling, the temperatures in the given points of a cooled body are measured and the variable sought is the heat transfer coefficient *h*. The accuracy of an inverse problem solution depends primarily on how the amount of the temperature variations observed in a point of the examined body approximates the accuracy, with which the temperatures of that body are measured. The inverse problem calculation result is, thus, affected by a number of factors such as the properties of the measuring instrument, the temperature measurement method, the material composition of the thermocouple employed, etc. An inappropriate selection of the input parameters for an inverse problem may cause an impairment of the required information about the temperature changes occurring on the surface. Measurement errors may induce a situation where the measured value of the temperature in the body being examined is higher than any

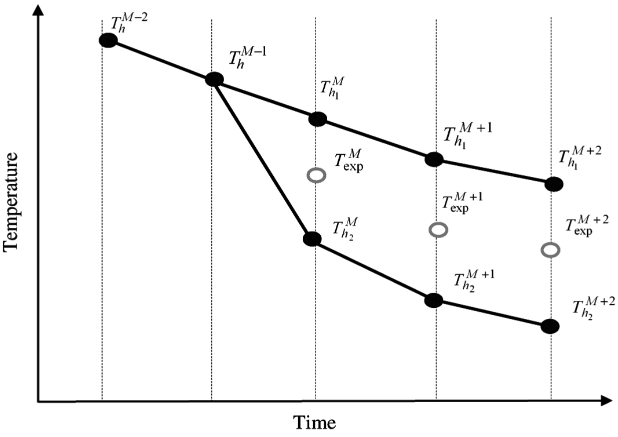

Figure 1: Inverse-calculation diagram
Slika 1: Inverzni računski diagram

temperature caused by any change in the boundary condition of the body, or the time derivative of the temperature is higher than any derivative caused by any swift change in the boundary condition. In such a case no solution to the inverse problem can be found. An inverse calculation diagram is shown in **Figure 1**.

The inverse problem solution is based on an assumed derivative of the temperature, *D,* which is defined as follows:

$$D^i=\frac{\partial T_h^i}{\partial h} \tag{7}$$

where *i* is a forward time step and *h* is the corresponding designation of the heat-transfer coefficient at a given temperature. The calculation of the actual heat transfer coefficient h^* (for point *M*) relies also on the coefficient values for points $M+1$ and $M+2$. The calculations for the initial point $M-1$ will be made using the estimated values of h_j, where $j = 1, 2, \dots r$ (*r* is the number of forward steps).

The result of the calculation is temperature $T_{h_1}^i$ where the upper index *i* designates the time step and the lower index *h* designates the heat transfer coefficient. In **Figure 1**, the temperatures from the experiment are designated as $T_{\exp}$. The heat transfer coefficient value h^* minimizes the mean square deviation between the calculated $T_{h_1}^i$ and the temperature obtained in the experiment, $T_{\exp}^i$, according to relation (8):

$$F=\sum_{i=1}^{r}(T_{\exp}^i-T_{h_1}^i)^2 \tag{8}$$

Let us assume that the derivative of *F* with respect to h_j is zero and replace h_j with the h^* being sought:

$$0=\sum_{i=1}^{r}(T_{\exp}^i-T_{h^*}^i)^2\cdot D^i \tag{9}$$

The calculation may also be made using a time consuming method based on calculating three temperature branches for the estimated values of h_1, h_2 and h_3. These calculated values are then used to calculate the coefficients of the second degree polynomial that can be easily derived.

Numerical tests showed that a simpler approach would be a substitution of the derivation with a differentiation, in which only two branches would be needed to obtain a sufficiently accurate result:

$$D^i=\frac{T_{h_1}^i-T_{h_2}^i}{h_1-h_2} \tag{10}$$

The temperature field in time step *i* can be characterized with the Taylor development around h_j*:*

$$T_{h^*}^i=T_{h_j}^i+(h^*-h_j)\frac{\partial T_{h_j}^i}{\partial h_j}+\frac{(h^*-h_j)^2}{2!}\frac{\partial^2 T_{h_j}^i}{\partial h_j^2}+\dots \tag{11}$$

In equation (9), we can substitute the first two Taylor development elements and consider only one estimated value of coefficient *h*; the outcome is:

$$0=\left[\sum_{i=1}^{r}(T_{\exp}^i-T_{h_1}^i)^2-(h^*-h_1)\cdot D^i\right]\cdot D^i \tag{12}$$

Formula (12) can be translated into the following heat transfer coefficient (h^*) equation:

$$h^*=\frac{\sum_{i=1}^{r}h_1\cdot(D^i)^2+\sum_{i=1}^{r}(T_{\exp}^i-T_{h_1}^i)\cdot D^i}{\sum_{i=1}^{r}(D^i)^2} \tag{13}$$

The determination of the heat transfer coefficient using the inverse procedure is a non-linear problem even if the thermo-physical properties of the material are temperature independent. The calculation should be carried out by way of iteration and stopped at the point where the predefined number of iterations has been reached or the condition for the maximum deviation between the new solution and the previous one has been fulfilled.

4 EXPERIMENTAL WORK

The methodology of the experimental research into the heat transfer coefficient carried out in semi-operational conditions does not allow the accuracy of the measurements made in laboratory conditions. However, it is able to produce the temperature data that correspond to the real spray descaling process.

The product selected for the experiment was a heavy metal plate (slab) with the dimensions of 400 mm × 400 mm × 30 mm and the material grade in line with the CSN 11 375 standard, whose chemical composition was 0.20 % C, max. 1.4 % Mn, 0.045 % P, 0.045 % S and 0.009 % N. Thermocouples were installed in the plate (**Figure 2**) according to the layout diagram in **Figure 3**. The distances of the thermocouples from the sprayed surface were (4.8, 8, 15, 22 and 25.6) mm. The thermocouple installation depths in the sample were verified with a Krautkramer USN-2 ultrasonic probe. In order to provide a unidirectional thermal field of the test speci-

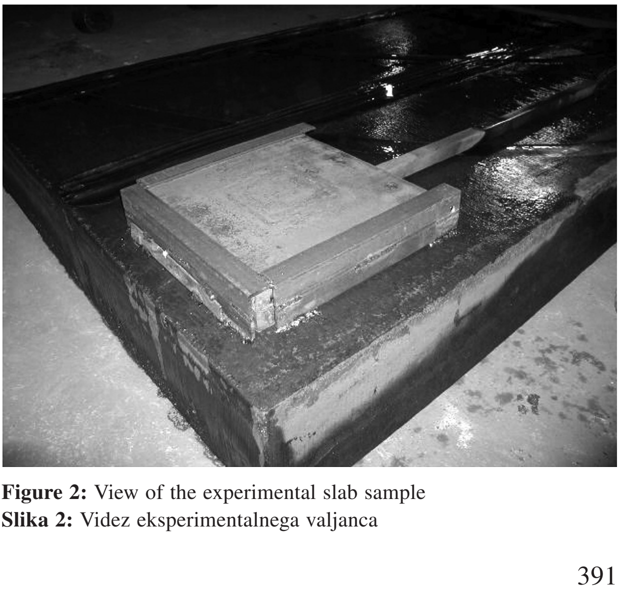

Figure 2: View of the experimental slab sample
Slika 2: Videz eksperimentalnega valjanca

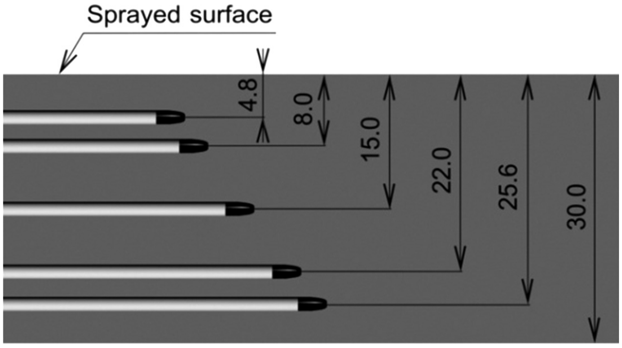

Figure 3: Layout diagram of the thermocouples installed in the sample
Slika 3: Prikaz razporeditve termoelementov v vzorcu

men, its lateral walls were insulated with a fibrous material.

The thermocouples were routed through a milled groove to the surface of the test plate. The thermocouples were protected from the mechanical effects of pressurized water with a thick wall tube. The thermocouple cold ends were routed through the protective tube to the terminal board. The signals from the thermocouples were transmitted to an OMEGA 180 recorder with the Pronto application software. The temperatures were measured with the shielded K-type Ni-NiCr grounded-end thermocouples with 3 mm diameters. The accuracy of this type of thermocouple is ± 2.2 °C at 0 °C.

The test sample (heavy metal plate) was fitted for heating in a pusher furnace and heated to 1000 °C. After the heating, the plate was transferred onto an accessory slab with the dimensions of 2360 mm × 1500 mm × 240 mm and then placed in a structure securing its stability during the spraying. Six sprays were applied during the experiment with the plate moving underneath the nozzles at a speed of 1 m s^{-1}. The spraying was performed only with the upper secondary descaling nozzles. Two thermocouples, out of the total of five, were damaged during the experiment. These were the thermocouples placed at the depth of 8 mm and 25.6 mm.

The graphical presentation of the time behavior of the temperature during the spraying (**Figure 4**) indicates that the temperature of the temperature field at the depths of 15 mm and 22 mm from the sprayed surface ceased to fluctuate with the motion of the plate underneath the spray nozzles. Only a slow, gradual decrease in the temperature was observed.

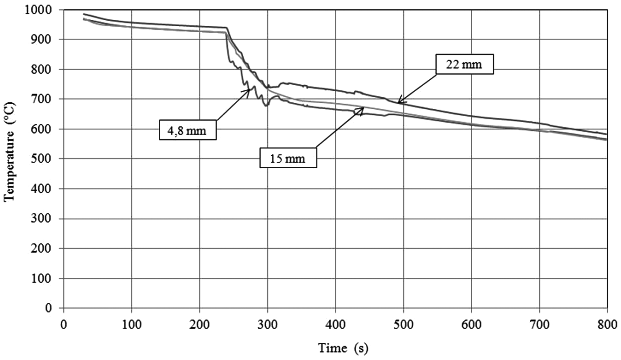

Figure 4: Time behavior of the temperature during the spraying
Slika 4: Časovna odvisnost temperature med brizganjem

It follows from the inverse problem solution principle that it is not possible to use any arbitrary point under the sprayed surface for the temperature measurement in the body being sprayed. The experiment indicates that as the distance from the sprayed surface grows, the information about the changes in the temperature diminishes. The reason for this is the fact that the material has a lower temperature gradient in the depth than on the surface. In view of this finding, the experiment was repeated with a new metal plate sample of the same steel grade but with a double thickness.

The second temperature measurement was done with a model slab with the dimensions of 400 mm × 400 mm × 60 mm. The thermocouples were prepared and routed towards the sensing apparatus in the same manner as for the first measurement. Eight K-type thermocouples were installed in the slab, out of which six were exposed-end (open-end) thermocouples with a diameter of 1.58 mm. The other two (grounded-end) thermocouples had a diameter of 3.0 mm. The distances of the thermocouples from the sprayed surface are summarized in **Table 1**. Two thermocouples were installed at the depth of 2 mm. Like in the first measurement, the thermocouple position depth was controlled by means of a Krautkramer USN-2 ultrasonic probe.

Table 1: Distances of the thermocouples from the sprayed surface
Tabela 1: Oddaljenost toplotnih senzorjev od površine, na katero se brizga

Hole diameter	Thermocouple type	Distance from the sprayed surface (mm)				
1.6 mm	Exposed-end	2.0	3.0	4.0	5.0	7.5
3.0 mm	Grounded-end	10.0	20.0			

The reason for using the exposed-end thermocouples in the measurement was the assumption that the temperature response is faster during the spraying. The prerequisite for their proper functioning was a precise installation of the open connection in contact with the measured material. A 1.58 mm thermocouple diameter was chosen because of a lower effect on the homogeneity of the measured material and improved measurement accuracy. The thermocouples at the depths of 10 mm and 50 mm were of a classic, grounded-end type, like for the first measurement, since the response to the pressurized water spray was assumed not to be equivalent to that occurring in the top layers. This assumption was confirmed with the measurement.

The temperature measurement was performed during eight passes of the slab sample under the spray nozzles. The slab moved at a speed of 1 m s^{-1}. The time interval between two sprays was 100 s.

Only the two thermocouples at the depth of 2 mm and those at the depths of 4 mm and 50 mm survived this difficult experiment without any damage. The thermocouples installed at the depths of (3, 5, 7.5 and 10) mm

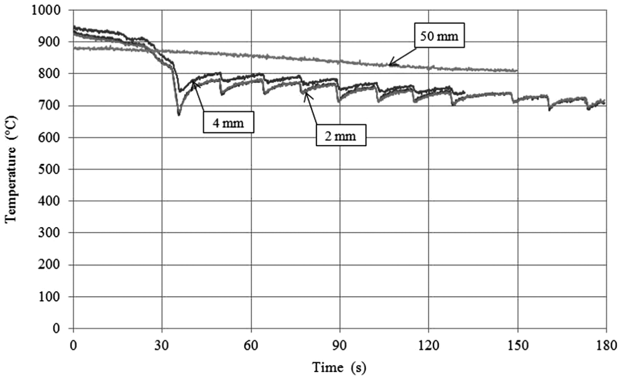

Figure 5: Time behavior of the temperatures in the slab sample during the spraying

Slika 5: Časovna odvisnost temperature v valjancu med brizganjem

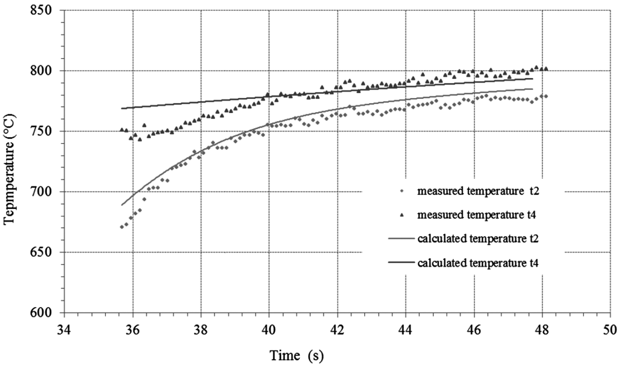

Figure 7: Temperature behavior after Spray 1 obtained from the check calculation

Slika 7: Potek temperatur iz kontrolnega izračuna po brizganju 1

were damaged either during their installation in the slab sample, or while handling the slab sample during the heating, or during the spraying. The first three temperature behavior curves obtained with the measurement were used in the evaluation.

During this measurement, each spray was followed by a short phase in order for the temperatures in the experimental slab sample to balance.

The measurement time step was 0.1 s. The temperature behavior at different measurement depths is shown in **Figure 5**. A detail of the temperature behavior at the depths of 2 mm and 4 mm during the spraying is provided in **Figure 6**.

5 RESULTS AND DISCUSSION

The data obtained through the experiment at different depths below the surface of the sprayed slab were subsequently processed using IHCP1D, a software developed on the basis of the Beck minimization principle algorithm at Beck Engineering Consultants Company.[6] This product is able to perform temperature analyses and cooling related calculations for an unknown heat flow and an unknown heat transfer coefficient based on the inverse solution procedure, using the known material properties of the body being cooled, the properties of the ambient environment and the temperatures experimentally measured in the body. The temperature values obtained in the experiment were applied in the above mentioned algorithm to calculate the heat transfer coefficient *h* for the first three sprays. Its mean value is 18.46 kW/(m^2 K). The lowest coefficient value was 17.65 kW/(m^2 K) and the highest value was 19.90 kW/(m^2 K).

The heat transfer coefficient values obtained during the spraying were used in the reverse check calculation of the temperature behavior of the experiment slab sample. The calculation results for Spray 1 are summarized in **Figure 7**.

A comparison between the measured values and calculated values indicates that the temperature difference is within a range of 10 °C to approximately 15 °C. The difference is higher for the temperature measured at the depth of 4 mm from the sprayed surface, as compared to the temperature at the depth of 2 mm. This can be attributed to a larger impact of the temperature measurement inaccuracy at the lower temperature levels as compared to the measurements at the depth of 2 mm. For example, for Spray 1 the temperature obtained through direct measurement at the depth of 2 mm below the surface, at the measurement time $\tau = 42.09$ s, was 762.8 °C. The temperature obtained through the calculation using

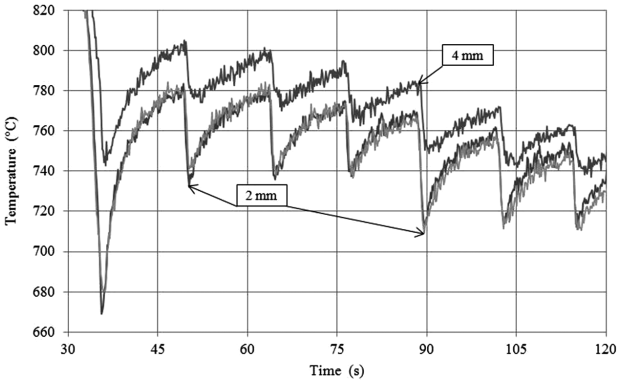

Figure 6: Detail of the time behavior of the temperatures captured by the functional thermocouples

Slika 6: Detajl časovne odvisnosti temperature, zajete s termoelementi

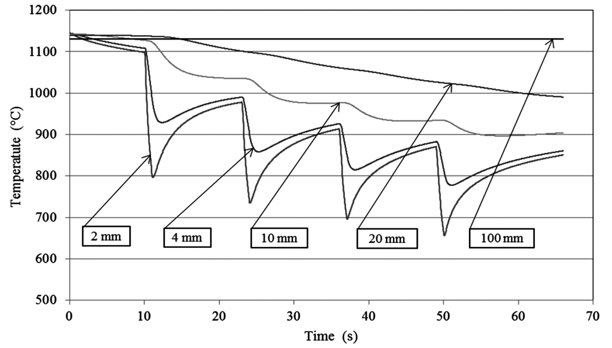

Figure 8: Temperature at the selected points acquired with the numerical simulation

Slika 8: Temperatura v izbranih točkah, ki je bila dobljena z numerično simulacijo

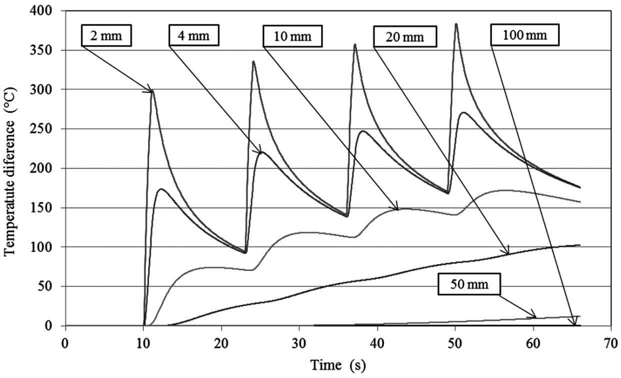

Figure 9: Temperature difference between a freely cooled and a sprayed slab

Slika 9: Razlika v temperaturah med prostim ohlajanjem in pri brizganju slaba

the heat transfer coefficient of 18.46 kW/(m^2 K) was 767.5 °C. The temperature deviation is 0.7 %.

The acquired values of the heat transfer factor was used for the calculation of the slab thermal field with a thickness of 200 mm made from steel with a steel grade identical to the test specimen. The heat transfer theory shows that if the slab length and width are, e.g., 6 m and 2 m, we can then assume a unidirectional heat transfer in more than 75 % of the material volume.

An initial surface temperature of 1145 °C was chosen for the solution, a parabolic temperature distribution was chosen for the cross-section, and the heating non-uniformity was 1.5 K cm^{-1}, while the thermo-physical steel properties depended on the temperature. The thermal field kinetics for the distances of (2, 4, 10, 20 and 100) mm from the slab surface in the course of four subsequent sprays are shown in **Figure 8**.

The numerical simulation has confirmed that the cyclical material temperature changes due to spraying are demonstrated only in the thin layer under the slab surface, approximately up to 10 mm. The temperature fluctuations due to spraying are practically not present in deeper layers. Nevertheless, this does not mean that the spraying does not influence the thermal field of the material in the mentioned areas. The temperature difference for individual spots of a freely cooled and sprayed slab is shown in **Figure 9**. The surface layers show the temperature differences of the order of 10^2 °C. However, at a depth of 20 mm, each spray also causes the temperature to drop by approximately 25 °C, unlike in the case of the freely cooled material. Even at the depth of 50 mm, the temperature drops by 2 °C to 3 °C per each spray. Only in the very centre of a slab the temperature is the same with both cooling methods.

6 CONCLUSION

A high-pressure spray descaling process has a significant impact on the temperature field of a rolled material, closely related to the quality of the final product. The research into the boundary and initial conditions needed for the solution of the temperature field problems, in controlled rolling operations in particular, has not been finished yet, but the results obtained through the on-site observations are precious and relevant for rolled product manufacturers.

An experimental measurement and the subsequent numerical simulations have confirmed that a high-pressure spray descaling process influences, to a significant extent, the surface layers of slabs. The cyclical temperature change due to the spray practically does not affect the remaining volume of the rolled material at a depth of more than 10 mm from the surface. However, the spray influences the speed of the slab cooling down also at larger distances. Only at the depths exceeding 50 mm, the temperature differences between the freely cooled and sprayed slabs are lower than 3 °C per spray.

Acknowledgments

This paper was completed in the frame of the tasks related to the projects VEGA 1/0004/14 SjF TUKE, SP2014/46 FMMI VŠB TUO and ITMS 2620220044 SjF TUKE.

Nomenclature

c_p	specific heat capacity J/(kg K)
h	heat transfer coefficient W/(m^2 K)
i	forward time step 1
m	weight of the rolled material kg
Q_V	volumetric flow rate m^3/s
ΔQ	total amount of the heat removed by the spray J
Q_{be}; Q_{af}	heat present in different layers of the material before/after the spray J
S	area being sprayed m^2
$t_{i,\mathrm{be}}$; $t_{i,\mathrm{af}}$	mean temperature in different layers of the material before/after the spray °C
t_0	surface temperature before the spray °C
t_{w}	spray-water temperature °C
v	rolling speed m s^{-1}
w	width of the material being rolled m
τ_{adm}	spraying time s

7 REFERENCES

[1] S. Yamaguchi, T. Yoshida, Improvement in Descaling of Hot Strip by Hydrochloric Acid, ISIJ International, 34 (**1994**) 8, 670–678

[2] J. N. Mukadi, P. C. Pistorius, Mould flux residues aid descaling of reheated austenitic stainless steel, Ironmaking & Steelmaking, 37 (**2010**) 1, 57–62

[3] M. Raudenský, M. Hnízdil, J. Y. Hwang, S. H. Lee, S. Y. Kim, Influence of the water temperature on the cooling intensity of mist nozzles in continuous casting, Mater. Tehnol., 46 (**2012**) 3, 311–315

[4] J. Štětina, T. Mauder, L. Klimeš, F. Kavička, Minimization of surface defects by increasing the surface temperature during the straightening of a continuously cast slab, Mater. Tehnol., 47 (**2013**) 3, 311–316

[5] J. Boháček, A. Horák, Numerical study of droplet dynamics impinging onto steel plate covered with scale layer, Front. Mech. Eng. China, 5 (**2010**) 4, 389–398

[6] www.beckeng.com

UDK 620.193:624.012.45:519.61/.64
Original scientific article/Izvirni znanstveni članek

ISSN 1580-2949
MTAEC9, 48(3)395(2014)

EFFECT OF REBAR CORROSION ON THE BEHAVIOR OF A REINFORCED CONCRETE BEAM USING MODELING AND EXPERIMENTAL RESULTS

VPLIV KOROZIJE BETONSKEGA ŽELEZA NA ARMIRANOBETONSKI STEBER Z UPORABO MODELIRANJA IN EKSPERIMENTALNIH REZULTATOV

Ali Ghods, Mohammad Reza Sohrabi, Mahmoud Miri
University of Sistan and Baluchestan, Faculty of Engineering, Department of Civil Engineering, P.O. Box 9816745563-162, Zahedan, Iran
ali.ghods@pgs.usb.ac.ir

Prejem rokopisa – received: 2013-07-21; sprejem za objavo – accepted for publication: 2013-09-13

Reinforcement corrosion in concrete may cause adverse effects, such as the area reduction of rebars, concrete cracking, a reduction of the bond strength and a change in the bond-slip behavior between concrete and rebars. All these effects will finally lead to the inappropriate performance of concrete structures. In this paper a corroded reinforced concrete beam, whose experimental results are available, is modeled based on the finite-element method using ANSYS. The results are then compared with the available and confirmed results. A reduction of the reinforcement area and a change in the bond strength between the concrete and the reinforcement are seen in the model. The effect of reinforcement corrosion on the force-displacement curve and the modeled beam are also studied and compared with the results from reinforced concrete made in the laboratory. It was observed that with an increase of the reinforcement corrosion rate, the load-carrying capacity of the concrete beam and the bond strength decreases. In addition, the area under the load-displacement curve of the concrete beam decreases with the increase of the reinforcement corrosion.

Keywords: corrosion, beam, modeling, force–displacement

Korozija armature v betonu lahko vpliva škodljivo, tako kot zmanjšanje prereza betonskega železa, pokanje betona, zmanjšanje sile vezanja in sprememba vedenja vezave in drsenja med betonom in armaturo; vse to privede do neprimernih lastnosti betonske konstrukcije. V tem članku je bil modeliran z uporabo metode končnih elementov in ANSYS korodiran betonski steber s poznanimi eksperimentalnimi podatki. Rezultati so bili primerjani z razpoložljivimi in preverjenimi rezultati. Iz modela je razvidno zmanjšanje področja utrditve in sprememba v sili vezanja med betonom in armaturo. Preučevan je bil tudi vpliv korozije armature na krivuljo sila – raztezek in modeliran steber ter primerjan z laboratorijskimi rezultati pri armiranem betonu. Ugotovljeno je, da se z naraščanjem hitrosti korozije armature zmanjšujeta nosilnost betonskega stebra in sila vezanja. Področje pod krivuljo obremenitev – raztezek armiranega betonskega stebra se zmanjšuje z večanjem korozije armature.

Ključne besede: korozija, steber, modeliranje, sila – raztezek

1 INTRODUCTION

Reinforcement corrosion is one of the major factors in the deterioration of reinforced concrete structures, such as bridges, parking and coastal structures. This phenomenon may lead to area reduction of rebars, cracking, concrete scaling, reduction of bond strength and change in the bond-slip behavior between concrete and rebars. All of these factors will eventually lead to the adverse function of concrete structures.

The area reduction of rebars is the most evident result of rebar corrosion. Although carbonate corrosion in concrete occurs uniformly, chloride corrosion usually causes local corrosion known as 'pitting'.[1] It causes a considerable area reduction of rebars, which sometimes occurs without any noticeable signs.[2–4]

Some parts of the earlier literature focused on the bond reduction between concrete and rebar and its effect on the strength of beams and reinforced concrete slabs.[5,6] In fact, the reduction of the bond strength between the concrete and the rebar occurs in two stages. During the early stage, corrosion products gather on the rebar surface and increase its diameter. This phenomenon increases the radial stresses between the concrete and the rebar, which intensifies the factor of cohesive friction.[4] During the next stage, longitudinal cracks reduce the confinement of corrosion products, which in turn reduces the bond strength. The more the corrosion proceeds, the more the bond-strength reduction will emerge.

Similar to any other engineering issue, studies concerning corrosion were conducted through three general methods, including experimental, analytical, and numerical simulation. A few studies have been carried out using numerical studies and applying some known finite-element software aiming to study the effects of reinforcement corrosion in concrete. For instance, Berra et al.[7] investigated the effect of corrosion on the bond deterioration between concrete and rebar using ABAQUS. Lundgren[8] used DIANA finite-element software for the numerical simulation of the experimental creation of cracks, caused by corrosion, and corroded rebar pullout tests. Saether and Sand[9] also modeled a corroded reinforced concrete beam, for which the experimental results were available. Meanwhile, they used DIANA and obtained similar results with the created sample. Most of the earlier finite-element models were two-dimensional.[10] An attempt is made in the current research to present a 3D model using ANSYS for a beam, for which the experimental results are available. The results obtained from the finite-element analysis of this beam are compared with the available ones. After verification of the model, a parametric study is carried out on the beam. It means that the load-displacement curve is drawn at different percentages of the corrosion and variations in the load-carrying capacity of the beam are studied. They are then compared with the load-displacement curve of the beams made in the laboratory. Finally, the reinforcement slip in the concrete is studied for various percentages of the corrosion using the model.

2 ELEMENTS USED IN ANSYS

2.1 Element for concrete

The SOLID65 element is a 3D element with eight nodes and three degrees of freedom (transmission on *x*, *y*, *z* directions) in each node. The element is capable of modeling the fissures and breaks of concrete.[11,12] A major aspect of the element is the nonlinear performance of its materials. Reinforcement can be defined in this element as well; of course, the reinforcements are defined individually here. Multi-linear isotropic hardening under the von Mises fracture criteria is used in this element. Generally, five coefficients are used to determine its smooth break, which include one-axis tensile strength, one-axis compressive strength, two-axis compressive strength, and one- and two-axis compressive strength under a specific confining pressure. Moreover, the shear transmission coefficients can also be applied as the inputs for open and close cracks. **Figure 1** exhibits the geometrical specifications of the SOLID64 element.

2.2 Element for Reinforcement

All the tensional and compressive reinforcements and stirrups are modeled in this study using the LINK8 element. This element is a 3D element, only with tensional and/or compressive axial forces.[11,12] The element has two nodes with three degrees of freedom in each node, including transmission for the *x*, *y*, *z* directions. The input of this element is the cross-section. **Figure 2** presents the specifications for this element.

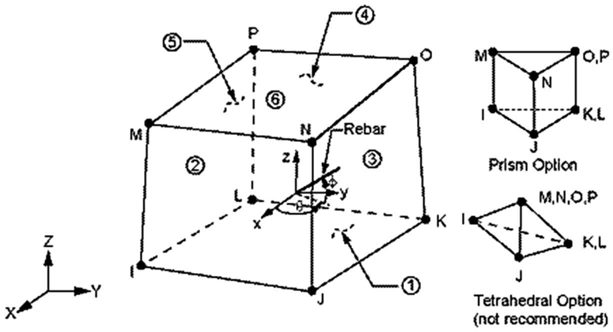

Figure 1: Geometry and specifications of the SOLID65 element
Slika 1: Geometrija in podrobnosti elementa SOLID65

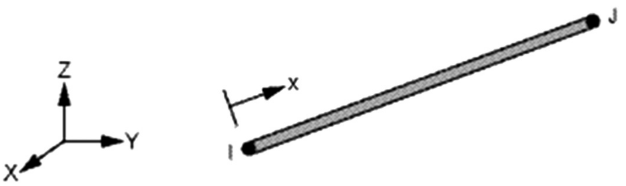

Figure 2: Geometry and specifications of the LINK8 element
Slika 2: Geometrija in podrobnosti elementa LINK8

2.3 Element for cohesion

The COMBIN39 element is applied for modeling the cohesion between the concrete and the rebar. This element is a uni-directional element capable of determining the force-displacement nonlinearity equation.[11,13] In addition, it has axial and torsional capability in one-, two- and three-dimensional analyses. Its axial option, which is used here, has a maximum of three degrees of freedom in each node. This element can have zero length, i.e., the start and end nodes can be defined as on each other. **Figure 3** exhibits a sample of the load-displacement diagram of the element.

3 CONTROL BEAM OF MODELING

3.1 The Beam Tested by Rodriguez et al.

Here, we discuss one of the reinforced concrete beams with corroded rebars tested by Rodriguez et al.[14] The test series of Rodriguez et al.[14] include 31 beams with various details of reinforcement, different shear reinforcement and a range of corrosion percentages. **Figure 4** shows the geometry and specifications of the beam reinforcement for modeling is this paper.

As shown in the figure, this beam has both tensional and compressive reinforcement and stirrups. In the beams tested by Rodriguez et al.,[14] the concrete had a compressive strength of between 48 MPa and 55 MPa. In order to accelerate the corrosion in the rebars, 3 % of calcium chloride (by mass of cement) was added to the concrete mix design. A compressive strength ranging from 31 MPa to 37 MPa was recorded for the concrete with the calcium chloride. The beams were cured under humid conditions for 28 d. Then a current of about 0.1 mA/cm^2 was applied to create an accelerated corrosion during the aging of the specimens, ranging from 100 d to 200 d.

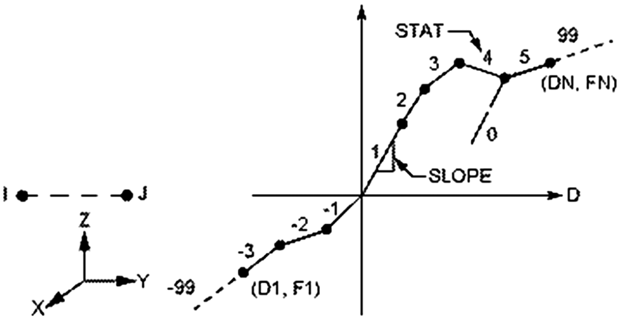

Figure 3: Geometry and specifications of the COMBIN39 element
Slika 3: Geometrija in podrobnosti elementa COMBIN39

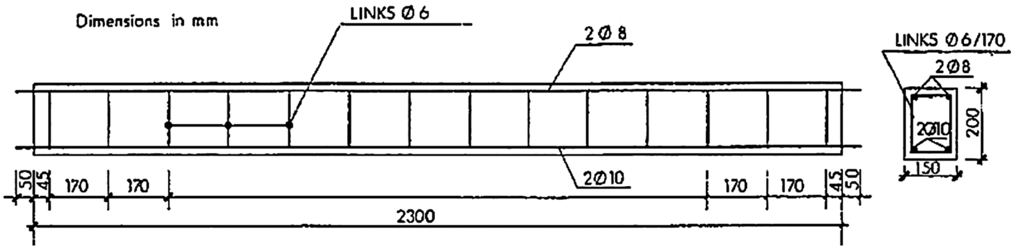

Figure 4: Geometry and specifications of the beam for modeling[14]
Slika 4: Geometrija in podrobnosti stebra za modeliranje[14]

It should be noted that due to the presence of stirrups, the corrosion was not uniformly distributed along the longitudinal rebars and the corrosion rate for the tensional and compressive rebars and stirrups was different in each beam. After the completion of the accelerated corrosion process, the beams were exposed to a four-point bending test. **Table 1** lists the complete characteristics of the beams for modeling. The non-corroded and corroded beams tested by Rodriguez et al.[14] are shown by Rod.01 and Rod.02 respectively in the remainder of the paper

Table 1: Specifications of the beams for modeling[14]
Tabela 1: Podrobnosti za modeliranje stebra[14]

Parameter			Beam with Corrosion	Beam without Corrosion
			Rod.02	Rod.01
One-axis compressive strength of concrete		f_c/MPa	31.4	50
One-axis tensile strength		f_t/MPa	2.8	3.5
Percentage of reinforcement		ρ/%	0.5	0.5
Concrete elasticity modulus		E_c/MPa	28300	32200
Steel elasticity modulus		E_s/GPa	206	206
Steel elastoplastic tangent modulus		E_{st}/MPa	824	824
Tensile steel	Area reduction percentage due to corrosion	%	13.9	–
Compressive steel		%	12.58	–
Stirrup		(%)	23.15	–

4 LABORATORY-MADE REINFORCED CONCRETE BEAM

Six reinforced concrete beams were made by the authors, using the same dimensions and reinforcement conditions as used by Rodriguez et al.[14] Three beams were tested for a further validation of the modeled beam and evaluating the effect of the corrosion on the behavior of the reinforced concrete under test. A concrete mixer was used for concreting and the modularity of the beams. In addition, after pouring the concrete into the mold, it was compacted using a 1.5 cm diameter rod. The beams were extracted from the mold after 24 h and cured using sacks for 28 d. Two-layer pressure-resistance and humidity-resistance string wires were used to create an electric current and to measure the corrosion in the concrete. The ends of the wires were taken out of the concrete. To protect the wires from corrosion and humidity, their ends were covered by an appropriated cohesive material before conducting the test. After 28 d of curing, the beam was placed in a distilled water basin containing 3 % of calcium chloride (by mass of distilled water). Then a negative current was applied in the basin to analyze salt to chlorine. To create the corrosion, a maximum 100 mA/cm^2 DC current was applied using wires. The other conditions are almost the same as those mentioned for the Rod.02 beam in **Table 1**. Hereinafter, these specimens are shown by Gh.03. **Figure 5** shows an image of these samples.

5 MODELING OF BEAMS BY CORROSION

5.1 Reinforcement Model

Uniform corrosion does not have a considerable effect on the stress-strain properties of the reinforcements and it is convenient to model it by reducing the cross-section of the steel rebars. Pitting corrosion may cause a significant reduction in the mechanical behavior of the steel reinforcement due to the local concentration of stress. Generally, if a reinforcement rebar initially has a diameter of φ_0, its diameter will be reduced due to the corrosion. The remaining cross-section of the tension rebar affected by uniform corrosion can be calculated from Eq. (1):[9]

$$A_{res}=\frac{\pi\varphi_R^2}{4}=\frac{\pi(\varphi_0-\alpha x)^2}{4} \qquad (1)$$

Where φ_R is the remaining diameter of the reinforcement, α is a coefficient dependent on the type of corrosion and x shows the penetration rate of the corrosion.[9]

Figure 5: Reinforced concrete beams made by the authors (Gh.03)
Slika 5: Armiranobetonski steber, ki so ga izdelali avtorji (Gh.03)

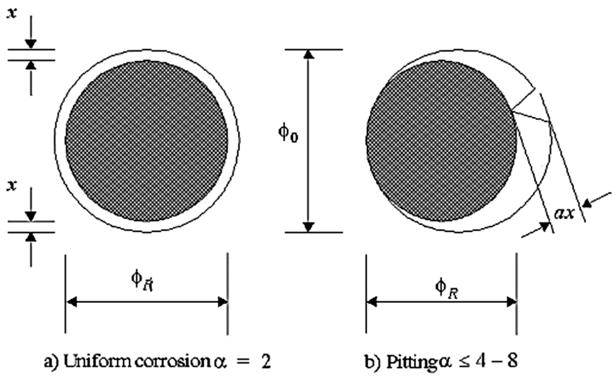

Figure 6: Remaining cross-section of the corroded rebar
Slika 6: Preostali prerez korodiranih palic v armaturi

For uniform corrosion it is assumed that the coefficient α is equal to 2. For pitting corrosion the cross-section becomes irregular and the area reduction may be considerably greater than the uniform corrosion (**Figure 6**). The above relation can be used for estimating the reinforcement cross-section in the pitting corrosion by introducing the circular cross-sectional diameter as φ_R. In this condition, the α coefficient is considered within the range of 4 to 8.[9]

In this study it is assumed that the corrosion is uniform. Therefore, no reduction is considered for the mechanical properties of the steel and only the area reduction is considered for the corroded reinforcements in the calculations. The stress-strain relation of the steel, in tension, was considered as an elastoplastic material with a linear hardness, which is shown in **Figure 7**.

5.2 Concrete Model

Cracked concrete, due to the corrosion under the effect of compressive stresses, shows a lower performance when compared with the un-cracked concrete. In this condition, the reduced compressive strength is used for the beams whose compression rebars are affected by corrosion. The amount of reduced compressive strength is suggested by Eq. (2):[15]

$$f_c^{\mathrm{D}} = \frac{f_c}{\left[1 + k\left(\frac{\varepsilon_1}{\varepsilon_{\mathrm{co}}}\right)\right]} \tag{2}$$

In this equation, f_c^{D} is the compressive strength of the cracked concrete, f_c is the specified compressive strength of the un-cracked concrete, k is a coefficient equal to 0.1 ($k = 0.1$), $\varepsilon_{\mathrm{co}}$ is the strain of the concrete under the maximum load, and ε_1 is the lateral strain caused by the crack, which is a function of the corroded reinforcements number, the volume expansion of the corrosion products on the rebar, and the average amount of corrosion influence.

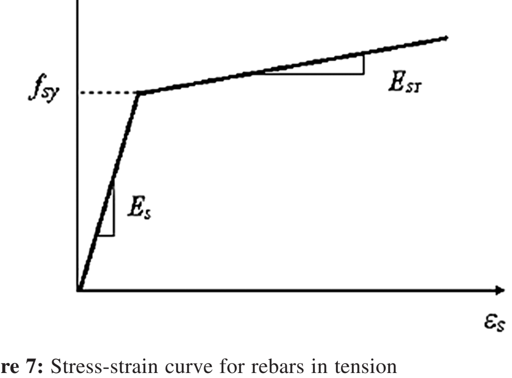

Figure 7: Stress-strain curve for rebars in tension
Slika 7: Krivulja napetost – raztezek pri natezni obremenitvi palice iz armature

In modeling reinforcement beam by ANSYS, it is necessary to define the stress-strain curve for concrete. This relation depends on several factors. The most common forms are used here. One simple model to introduce a concrete stress-strain relation is the application of an idealized elastoplastic relation, which is shown in **Figure 8a**. Another model, which is more realistic, is the parabolic model, like that shown in **Figure 8b**. In both models, the tensional behavior of the concrete is shown by a two-linear estimation in which the tensile stress increases up to the tensile strength f_t and then it is followed by a softening behavior.

5.3 Bonding Model

Before the development of cracks in the concrete, low rates of corrosion may increase the bond strength between the reinforcement and the concrete. The bond strength starts decreasing with the formation of corrosive cracks, which normally occur along the reinforcement. There are numerous experimental results on corrosive reinforcements. However, the presence and development of corrosion products were proved to be the main parameter in weakening the bond strength between the corroded reinforcement and the concrete. Various relations have been offered for the bond strength. In the present study, the following relation is used for the bond strength. This relation considers the effects of both the concrete and the stirrups:[16]

$$u_{\max}^{\mathrm{D}} = R \cdot \left[0.55 + 0.24\left(\frac{c}{d_{\mathrm{b}}}\right)\right]\sqrt{f_{\mathrm{c}}} + 0.191\left(\frac{A_{\mathrm{st}} f_{\mathrm{yt}}}{s_{\mathrm{S}} d_{\mathrm{b}}}\right) \tag{3}$$

$$R = A_1 + A_2 X$$

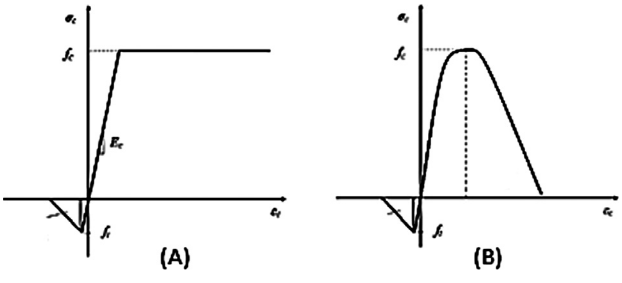

Figure 8: Different types of stress-strain curves for concrete
Slika 8: Različne krivulje napetost – raztezek za beton

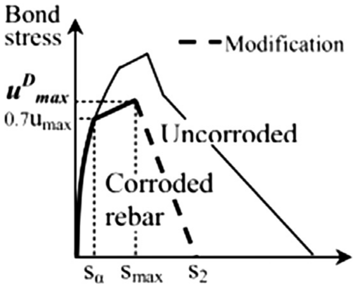

Figure 9: Diagram of the relation proposed for the bond-slip strength[17]
Slika 9: Diagram predlagane odvisnosti trdnosti za vezavo – drsenje[17]

Where u^D_{max} is the reduced bond strength, c is the thickness of concrete cover, d_b is the reinforcement diameter, f_c is the specified compressive strength of concrete, A_{st} is the area of shear reinforcement, f_{yt} is the yield strength of the stirrups, s_s is the stirrup spacing, and R is a factor that considers the reduction of the bond strength in which A_1 and A_2 are coefficients reflecting the rate of corrosion in an accelerated corrosion process. For corrosion process of 0.09 mA/cm², the values of these coefficients were determined as $A_1 = 1.104$, $A_2 = -0.024$. Finally, X is the corrosion rate, which is stated as a percentage of the rebar mass loss.

The advantage of this model for the bond strength between the concrete and the rebar is that it is capable of modeling the increase of the bond strength at low rates of corrosion. Obviously, this depends on the corrosion rate.

Studies show that the relation between the bond strength and the slip is controlled by the corrosion rate in longitudinal rebars and the rate of corrosion products. A modified relation was proposed for bond-slip rule by Harajli et al.,[17] which is shown in **Figure 9**.

In this diagram $S_2 = 0.35c_0$, where c_0 is the distance between the rebar ribs, which is assumed to be 8 mm. Other specifications of the diagram are defined in the following relations:[17]

$$u = u_1 \left(\frac{s}{s_1} \right)^{0.3} \tag{4}$$

$$s_\alpha = s_1 \left(\frac{\alpha u^D_{max}}{u_1} \right)^{1/0.3} \tag{5}$$

$$s_{max} = s_1 e^{(1/0.3)\ln(u^D_{max}/u_1)} + s_0 \ln\left(\frac{u_1}{u^D_{max}} \right) \tag{6}$$

In these relations $S_1 = 0.15C_0$, $u_1 = 2.57(f_c)^{0.5}$, $\alpha = 0.7$, and the s_0 for plain and steel-reinforced concrete is 0.15 and 0.4, respectively.[17]

In this research the above diagram is used for modeling the bond stress between concrete and rebar. Of course, the element applied for bond modeling is COMBIN39. As explained in Section 2, this element needs a force-displacement curve. Therefore, the following equation is introduced for this purpose:[17]

$$F(s) = u(s)\pi dl \tag{7}$$

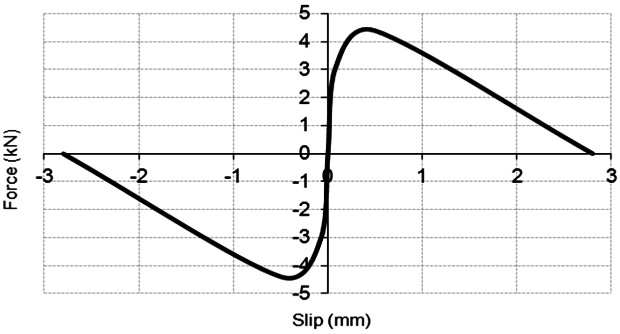

Figure 10: Force-slip diagram for the COMBIN39 element where the tension reinforcements are located
Slika 10: Diagram sila – zdrs za element COMBIN39 pri natezni obremenitvi armature

In this relation, $F(s)$ is the shear force between the reinforcement and the concrete, $u(s)$ is the bond strength, d is the reinforcement diameter, and l is the distance between two adjacent COMBIN39 elements (**Figure 10**).

For instance, the relation between the force-slip for the corroded tension reinforcements is as follows, which is in fact the same force-slip diagram of COMBIN39 element where the tension reinforcements are located.

This diagram is obtained assuming a reduction of the reinforcement mass by 10 percent ($x = 10$ %). The corresponding force-slip diagrams for different percentages of reduction of the reinforcement mass are shown in **Figure 11**.

5.4 The Model Created using ANSYS

As explained in the earlier sections, a finite-element model of the control beam tested by Rodriguez et al.[14] was made using ANSYS (**Figure 12**).

Because of the symmetrical condition, half of the beam was considered during modeling. It should be noted that it is a complicated task to make a precise model for a corroded reinforced beam. This is due to the fact that the corrosion rate along longitudinal rebars, caused by stirrups, is not constant. In addition, the average rate of corrosion in each beam for tensile and com-

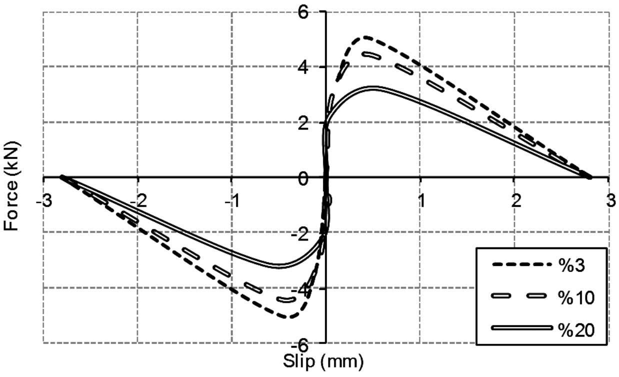

Figure 11: Force-slip diagram for COMBIN39 for different percentages of corrosion
Slika 11: Diagram sila – zdrs za element COMBIN39 pri različnih deležih korozije

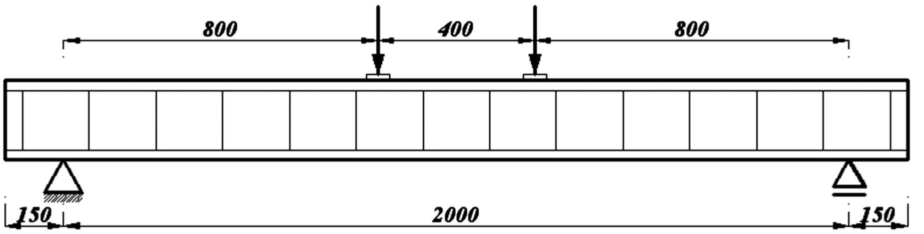

Figure 12: Supports and loading conditions for the control beam
Slika 12: Podpore in obremenitev kontrolnega stebra

pressive reinforcements and stirrups is different. However, in the beam selected for modeling, the average rates of corrosion in the tensile and compressive reinforcements are almost equal.[14] As shown in **Table 1**, the rates of corrosion in tensile and compressive reinforcements are 13.9 % and 12.6 %, respectively. It is noteworthy that in the finite-element model made here, changes to the reinforcement area were considered as mentioned in Section 1-4 and the changes of the bond stress were taken in to account, according to the remarks of Section 3-4 (**Figures 13** and **14**).

Finally, the load was applied to the model incrementally. Attempts were made to choose smaller incremental steps of load to obtain a better convergence. The load could be increased as long as it was not be possible to increase it any more due to the model instability, using the Newton-Raphson method for the non-linear analysis.

In order to observe the sensitivity of the meshing size as a result of the existing model it is also investigated with mesh seeds of 100, 200 and 300 in each direction. After that the results were compared and it has clear that the differences were negligible; therefore, a mesh size of 100 was used in the ANSYS because of the speed and comfort.

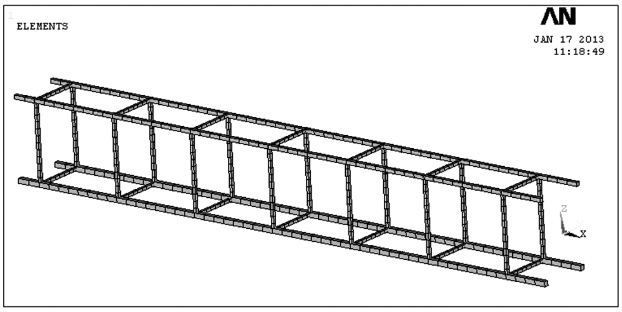

Figure 13: Modeled reinforcements
Slika 13: Modelirana armaturna mreža

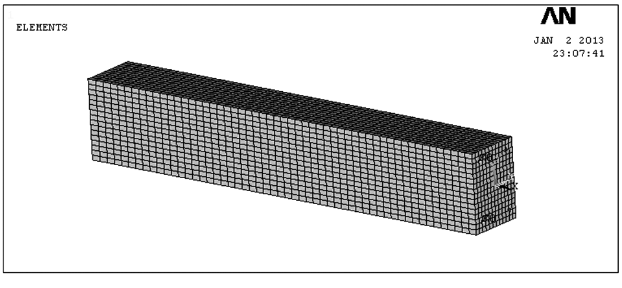

Figure 14: Control beam model on ANSYS
Slika 14: ANSYS-model kontrolnega stebra

6 MODELED BEAM RESULTS vs. EXPERIMENTAL RESULTS

Here, we continue the discussion by comparing the load–displacement curve at the mid-span of the modeled and the experimental beam. **Figure 15** compares the results of the numerical analysis of the corrosion-free Rod.01 modeled beam with its experimental results. It is clear that the numerical modeling has a favorable precision, especially for estimating the factored load.

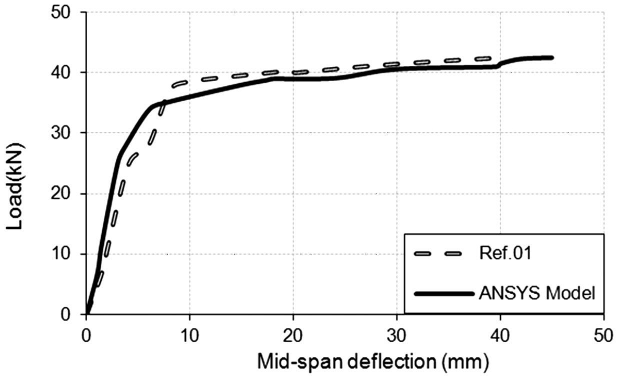

Figure 15: Numerical and experimental results of the load-displacement curves for the Rod.01 beam
Slika 15: Numerični in eksperimentalni rezultati obtežbe – raztezka pri stebru Rod.01

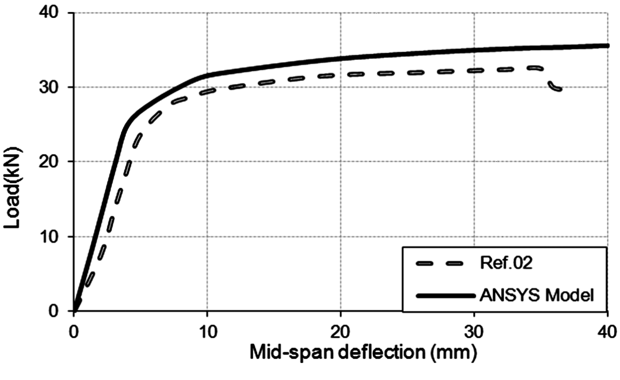

Figure 16: Numerical and experimental results of load-displacement curves for the Rod.02 beam (with corrosion)
Slika 16: Numerični in eksperimentalni rezultati obtežbe – raztezka pri stebru Rod.02 (s korozijo)

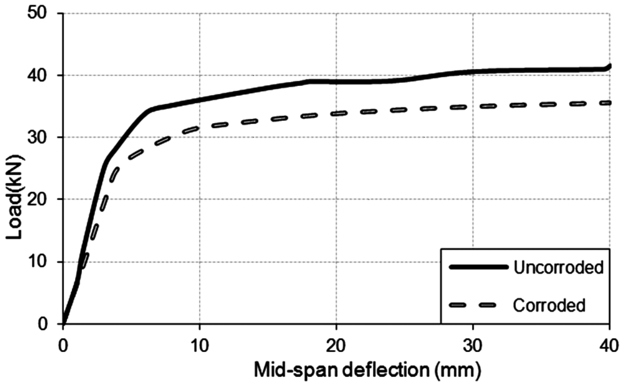

Figure 17: Numerical results of the load-displacement for the corroded and non-corroded model beam
Slika 17: Numerični rezultati obtežbe – raztezka za modelni steber s korozijo in brez nje

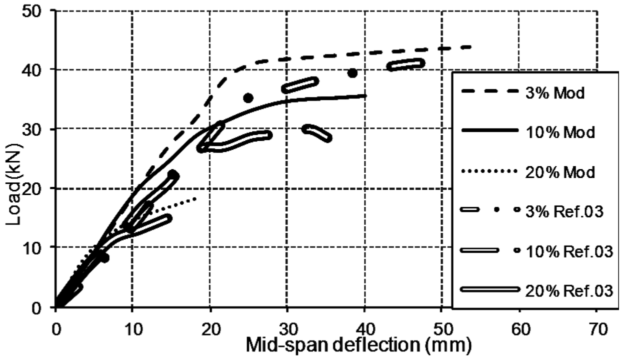

Figure 19: Results of load-displacement for different rates of corrosion in the model beam and Gh.03
Slika 19: Rezultati obtežbe – raztezka pri različnih stopnjah korozije pri modelnem stebru Gh.03

Figure 16 also shows the mid-span load-displacement relationships for the Rod.02 modeled beam and its experimental results, which are affected by the reinforcement corrosion. Comparing the results indicates a favorable precision between the results of the modeled beam by the authors and Rodriguez's experimental results. The corroded beam in the model estimates the factored load with an error close to 9 % more than the Rod.02 beam. With respect to the specific complexities of the model and the approximations used in modeling, the numerical result has a favorable precision.

Figure 17 shows the results of the load-displacement for the corroded and non-corroded beams, obtained from the modeling, in a diagram.

It should be noted that the finite-element model underestimates the results of the non-corroded beam and overestimates the results of the corroded beam. Therefore, the difference of the load-carrying capacity between the corroded and non-corroded beams is underestimated as compared with the experimental results.

The results of the load-carrying capacity at different percentages of corrosion for the modeled beams and those created by the authors (Gh.03) are explained subsequently. Four-point loading is used, as shown in **Figure 18**, to achieve the load-carrying capacity of the beams in the laboratory. It should be noted that the parameter here introduced as an index to show the corrosion rate has the same percentage of mass for the reinforcements earlier introduced as the parameter *x* in the previous sections. **Figure 19** shows the amounts of load-displacement in (3, 10, and 20) % corrosion in the created beams (Gh.03) and the modeled beams.

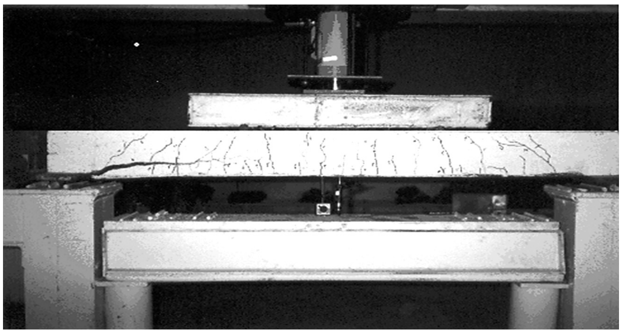

Figure 18: Four-point loading for corroded beam
Slika 18: Štiritočkovna obremenitev stebra s korozijo

Figure 19 shows that the increase of the corrosion rate reduces the ultimate load-carrying capacity and the ultimate displacement. In addition, the length of the nonlinear area in the beam increases with lower rates of corrosion. Failure of the beams with a high rate of reinforcement corrosion will probably tend to approach a brittle fracture; of course, such a question requires a separate study. It means that their fracture mechanism can be studied through examining the formation of cracks and their positions at the time of the beam fracture with different rates of corrosion. The very good precision of the offered model can be observed by examining the results obtained from the force-displacement curve in the modeled and experimental beams. The differences among the precisions may be due to the variations in the rate of corrosion along the longitudinal rebars related to the existence of stirrups. In this figure, the results of the numerical analysis of the model are overestimated as compared with the experimental ones.

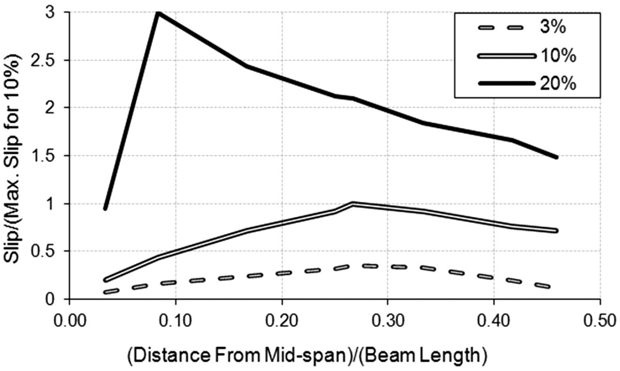

Figure 20: Rate of reinforcement slip in proportion to concrete for different rates of corrosion
Slika 20: Razmerje drsenja armature in betona pri različnih stopnjah korozije

With respect to the favorable precision of the modeled beam, the rate of reinforcement slip in proportion to concrete can be studied. In fact, it is the same displacement in the nonlinear spring element, which is placed for modeling the bonding strength between the concrete and the reinforcement. **Figure 20** shows the rate of reinforcement slip in proportion to the concrete along the beam. The diagram is drawn for different rates of corrosions.

The figure shows that the rate of slip increases with the increase of the rate of corrosion in the reinforcement. In fact, according to **Figure 11**, with an increase of the rate of corrosion, the concrete-reinforcement bond strength decreases. This leads to an increase of the slip. As **Figure 20** shows, the place with maximum slip in a beam with 20 % corrosion approaches the center of the beam.

7 CONCLUSION

A reinforced concrete beam with reinforcement corrosion was modeled in this paper. The area reduction of the reinforcement and the bond-strength reduction was observed between the concrete and the reinforcement. The results obtained from the finite-element analysis of this beam were compared with those achieved by Rodriguez.[14] It was shown that there was a good agreement between the load-displacement diagram and the experimental work.

The reinforcement corrosion rate in the model was altered as a parameter, and its effect on the load-carrying capacity was studied. The results were then compared with those experienced by the authors.

It was revealed that with an increase of the reinforcement corrosion rate, the load-carrying capacity of the concrete beam decreases.

The area under the load-displacement curve of the concrete beam decreases with the increase of the reinforcement corrosion. This may be an indication for the reduction of the concrete beam's ductility. Therefore, it can be expected that the concrete beam will become more brittle with an increase of the corrosion.

By comparing the results obtained from the model with the beams made by the authors, very good precision of the model is realized. The difference may be due to the lack of uniform corrosion of the longitudinal rebars caused by stirrups, and the use of different methods for accelerating the corrosion by the authors and Rodriguez et al.[14]

It was observed that the bond strength reduces with an increase of the corrosion rate. This leads to an increase of reinforcement slip in reinforced concrete beams.

8 REFERENCES

[1] A. Kocijan, M. Jenko, Inhibition of the pitting corrosion of Grey cast Iron using carbonate, Mater. Tehnol., 40 (**2006**) 1, 3–6

[2] A. R. Boga, Ý. B. Topçu, M. Öztürk, Effect of Fly-Ash amount and Cement type on the corrosion performance of the steel embedded in concrete, Mater. Tehnol., 46 (**2012**) 5, 511–518

[3] J. Cairns, Consequences of reinforcement corrosion for residual strength of deteriorating concrete structures, Proc. of the First Inter. Conference on Behavior of Damaged Structures, Rio de Janeiro, 1998

[4] CEB Task Group 2.5, Bond of Reinforcement in Concrete, State-of-the art report, fib Bulletin No. 10, 2000

[5] L. Chung, H. Najm, P. Balaguru, Flexural behavior of concrete slabs with corroded bars, Cement and Concrete Composites, 30 (**2008**), 184–193

[6] K. Toongoenthong, K. Maekawa, Multi-mechanical approach to structural assessment of corroded RC members in shear, J. Advanced Concrete Technology, 3 (**2005**) 1, 107–122

[7] M. Berra, A. Castellani, D. Coronelli, S. Zanni, G. Zhang, Steel-concrete bond deterioration due to corrosion: finite-element analysis for different confinement levels, Magazine of Concrete Research, 55 (**2003**) 3, 237–247

[8] K. Lundgren, Bond between ribbed bars and concrete Part 1: Modified model, Magazine of Concrete Research, 57 (**2005**) 7, 371–382

[9] I. Saether, B. Sand, FEM simulation of reinforced concrete beams attacked by corrosion, ACI Structural J., 39 (**2009**) 3, 15–31

[10] K. Narmashiri, M. Z. Jumaat, Reinforced steel I-beams: A comparison between 2D and 3D simulation, Simulation Modelling Practice and Theory, 19 (**2011**) 1, 564–585

[11] Ansys 11, Help Manual, 2011

[12] M. L. Bennegadi, Z. Sereir, S. Amziane, 3D nonlinear finite element model for the volume optimization of a RC beam externally reinforced with a HFRP plate, Construction and Building Materials, 38 (**2013**), 1152–1160

[13] A. Pozolo, B. Andrawes, Analytical prediction of transfer length in prestressed self-consolidating concrete girders using pull-out test results, Construction and Building Materials, 25 (**2011**) 2, 1026–1036

[14] J. Rodriguez, L. M. Ortega, J. Casal, J. M. Diez, Assessing structural conditions of concrete structures with corroded reinforcement, In: R. K. Dhir, M. R. Jones (editors), Concrete repair, rehabilitation and protection, E&FN Spon, 1996, 65–78

[15] D. Coronelli, P. Gambarova, Structural assessment of corroded reinforced concrete beams: modelling guidelines, J. Structural Engineering, 130 (**2004**) 8, 1214–1224

[16] T. E. Maaddawy, K. Soudki, T. Topper, Analytical model to predict nonlinear flexural behaviour of corroded reinforced concrete beams, ACI Structural J., 102 (**2005**) 4, 550–559

[17] M. H. Harajli, B. S. Hamad, A. A. Rteil, Effect of confinement on bond strength between steel bars and concrete, ACI Structural J., 101 (**2004**) 5, 595–603

UDK 678.7
Original scientific article/Izvirni znanstveni članek

ISSN 1580-2949
MTAEC9, 48(3)403(2014)

MICROCELLULAR OPEN-POROUS POLYSTYRENE-BASED COMPOSITES FROM EMULSIONS

MIKROCELIČNI ODPRTOPOROZNI POLISTIRENSKI KOMPOZITI IZ EMULZIJ

Sebastjan Huš[1,2], Mitja Kolar[2], Peter Krajnc[2]
[1]Polymer Technology College, Ozare 19, 2380 Slovenj Gradec, Slovenia
[2]University of Maribor, Faculty of Chemistry and Chemical Engineering, Smetanova 17, 2000 Maribor, Slovenia
peter.krajnc@um.si

Prejem rokopisa – received: 2013-08-21; sprejem za objavo – accepted for publication: 2013-09-11

Series of cross-linked polystyrene samples were prepared using an emulsion templating approach, where monomers were contained in the continuous phase of the emulsion, while the droplet aqueous phase induced primary pores, connected with a number of secondary pores. Emulsions with a high fraction of the droplet phase (HIPEs) were used and stabilised with a combination of a surfactant (sorbitan monooleate) and various types of particles (charcoal powder, copper powder and carbon nanopowder). The morphology of the resulting porous polymer depends on the type and amount of the particles added to the emulsion; however, in all the cases open-cellular morphology was formed. The size of the primary pores (cavities) ranged from 5 μm to 25 μm, while the size of the secondary interconnecting pores was from 1 μm to 5 μm. The materials were investigated using scanning electron microscopy and nitrogen adsorption/desorption.

Keywords: polyHIPE, porous polymers, nanocomposites, porosity, polystyrene

Z uporabo emulzij z visokim deležem notranje faze smo pripravili serijo zamreženih polistirenskih vzorcev. Monomeri so bili vsebovani v kontinuirni fazi emulzije, kapljice notranje vodne faze pa so povzročile poroznost materiala z vrsto primarnih por, povezanih s povezovalnimi porami. Emulzije z visokim deležem notranje faze (HIPE) smo stabilizirali z uporabo surfaktanta v kombinaciji z različnimi delci (oglje v prahu, baker v prahu in ogljikov nanoprah). Na morfologijo pripravljenih odprtoporoznih materialov sta vplivala tako vrsta kot tudi količina dodanih delcev. Velikost primarnih por je bila v območju med 5 μm in 25 μm, medtem ko je bila velikost sekundarnih povezovalnih por v območju med 1 μm in 5 μm. Materiale smo karakterizirali z uporabo vrstičnega elektronskega mikroskopa in adsorpcijo/desorpcijo dušika.

Ključne besede: poliHIPE, porozni polimeri, nanokompoziti, poroznost, polistiren

1 INTRODUCTION

As a template for the preparation of highly porous polymers, high internal-phase emulsions (HIPEs) can be used. They are defined as the emulsions, whose internal phase exceeds 74.05 % of the total volume[1] and which are formed by mixing together two immiscible liquids and a stabilizer. With a polymerisation of HIPEs, highly porous polymers, termed polyHIPEs, are produced, usually having an interconnected structure and a high porosity, up to 99 %.[2] PolyHIPEs are usually prepared in the form of monoliths; however, polyHIPE beads[3–5] or even membranes[6–8] can be produced. With their exceptional properties, such as a high porosity and surface area and a low density, they find use in various applications, such as tissue engineering[9–11], filtration[12], separation[13,14], gas storage[15], catalyst supports[16–18], etc.

HIPEs are thermodynamically unstable systems and their stability is affected by flocculation, sedimentation, coalescence, Ostwald ripening and phase inversion.[1] Their stabilization is usually done by adding an appropriate amount of a suitable surfactant, resulting, after the polymerisation, in an open and interconnected porous structure. The quantities of the surfactant can vary between less than 1 %[19,20] and 50 %.[21,22]

Emulsions can also be stabilized by incorporating solid particles instead of a surfactant and such systems are termed the Pickering or Ramsden emulsions.[23,24] The stability of emulsions in such cases depends on the particle size and shape, while the interactions between the particles and the wetting ability can be improved by modifying the particle surfaces.[25] The Pickering HIPEs have similar properties as the surfactant-stabilized emulsions and are used for the applications where the surfactants are difficult to remove or have a negative influence on the final product, for example, the irritancy. When polymerised, the Pickering emulsions usually tend to have a closed porous structure, but they possess other interesting futures such as electrical conductivity, magnetic properties, better mechanical properties, etc.[26,27] Preparations of polymer materials from the Pickering HIPEs were reported for several applications and, without a surfactant, they usually result in a closed-cellular porous morphology.[25,28,29] On the other hand, the Pickering emulsions, in combination with surfactants, can give open-porous materials.[30,31] Particles and nanoparticles are added to a polymer matrix for several reasons like to influence the mechanical properties or surface area by inducing additional pores, introduce novel properties to a matrix polymer material, such as magnetic, electrical or optical properties. However, in the case of porous polymers, an addition of particles can significantly influence the resulting morphology. It is, therefore, worth investigating the influence of added particles on the morphology of porous composite materials.

In this paper we report on the preparation of highly porous polyHIPEs based on styrene and divinylbenzene and with added particles, namely, the charcoal powder, copper powder and carbon nanopowder.

2 EXPERIMENTAL SECTION

2.1 Materials

A monomer styrene (Sigma Aldrich) and divinylbenzene (DVB, Sigma Aldrich) were passed through a layer of basic alumina (Al_2O_3, Fluka) to remove the inhibitors. The initiator potassium persulfate (KPS, Fluka), the surfactant sorbitan monooleate (Span 80, HLB (hidrophilicity-lipophilicity balance) = 4.3, Fluka), calcium chloride hexahydrate ($CaCl_2 \cdot 6H_2O$, Merck), ethanol (Merck), charcoal powder (Sigma Aldrich, 10–40 μm), copper powder (Sigma Aldrich, < 10 μm), and carbon nanopowder (Sigma Aldrich, < 50 nm (BET)) were used as received without any further purification. In all the experiments deionized water was used.

2.2 PolyHIPE preparation

PolyHIPEs were prepared by slowly adding the internal phase to the continuous phase under constant stirring. The continuous phase consisted of styrene and DVB monomers, surfactant Span 80 and an appropriate amount of the particles (**Table 1**). It was placed in a 250 mL three-necked reactor, fitted with an overhead stirrer. The aqueous phase was prepared separately by dissolving $CaCl_2 \cdot 6H_2O$ and the initiator KPS in degassed and deionised water and was added dropwise to the continuous phase under constant stirring at 300 r/min. After a completed addition of the appropriate amount of the aqueous phase, stirring was continued for another 60 min to produce a stable emulsion. The emulsions were transferred into polypropylene tubes and exposed to 60 °C for 24 h. The resulting monoliths were being extracted in a Soxhlet apparatus using water for 24 h and ethanol for another 24 h and then dried in a vacuum at 40 °C for 24 h. A series of 16 emulsions of varying solid-particle concentrations were prepared (**Table 1**).

Table 1: HIPE formulations and morphological features of polyHIPEs
Tabela 1: Formulacije HIPE-ov in morfološke lastnosti poliHIPE-ov

Sample	Particle type	Amount (%)	Cavity diameter (μm)	Interconnecting pore diameter (μm)
S0	/	/	/	/
C1	charcoal powder	0.5	25	5
C2	charcoal powder	1.5	20	5
C3	charcoal powder	2	12	2.5
Cu1	copper powder	0.5	14	4
Cu2	copper powder	1	/	/
Cu3	copper powder	1.5	5	1
Cu4	copper powder	2	/	/
CNP1	carbon nanopowder	0.1	/	/
CNP2	carbon nanopowder	0.35	20	5
CNP3	carbon nanopowder	1	/	/
CNP4	carbon nanopowder	3	5	2
CNP5	carbon nanopowder	5	9	1.5
CNP6	carbon nanopowder	7	/	/
CNP7	carbon nanopowder	10	/	/
CNP8	carbon nanopowder	15	9	2

*all emulsions consisted of volume fractions 70 % styrene, 30 % DVB, 20 % Span80 – oil phase (20 %) and KPS, $CaCl_2 \cdot 6H_2O$ and deionized water – water phase (80 %)

2.3 Characterisation

Typical polyHIPE morphology was determined using a scanning electron microscope (SEM), Quanta 200 3D (FEI Company). Samples were mounted on a sample holder using a graphite tape and sputter coated with a layer of gold. Nitrogen adsorption/desorption measurements were done on a Micromeritics TriStar II 3020 porosimeter using a BET model for the surface-area evaluation.

3 RESULTS AND DISCUSSION

In order to examine the effect of different particle additions to the emulsion on the morphology of the resulting polymers, polyHIPE samples from styrene and divinylbenzene (DVB) with added particles were prepared (**Table 1**). To avoid a misinterpretation of the influences on the morphology, the basic matrix always consisted of a high internal-phase emulsion with styrene and DVB (volume fractions 70 % styrene and 30 % DVB). The continuous phase of all the emulsions consisted of monomers and surfactant Span 80 (the volume fraction 20 % of the monomer content). The internal aqueous-phase volume was kept at 80 % in all the cases consisting of deionized water, $CaCl_2$ and the initiator (potassium persulfate). A sample without any added particles was also prepared (S0) as a reference for comparison. For the other experiments three different types of particles were used: charcoal powder, copper powder and carbon nanopowder.

Charcoal powder was first tried as an additive to the monomer containing the continuous phase of the emulsion. As predicted, the addition of solid particles to the oil phase showed a significant effect on the resulting polyHIPEs morphology. By increasing the amount of the charcoal powder from 0.5 % to 2 %, the cavity diameter decreased from 25 μm to 12 μm and the interconnecting pore diameter from 5 μm to 2.5 μm, which suggests an increased stability of the particle-stabilized emulsions caused by the Pickering effect. No visible particle agglo-

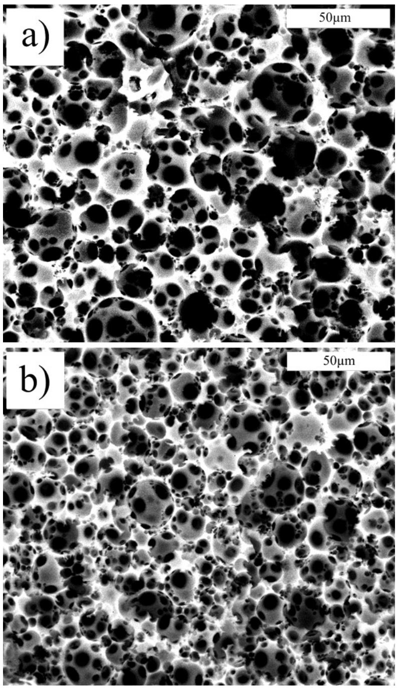

Figure 1: SEM images of: a) 1.5 % charcoal and b) 2 % charcoal polyHIPEs
Slika 1: SEM-posnetka poliHIPE-a z: a) 1,5 % oglja in b) 2 % oglja

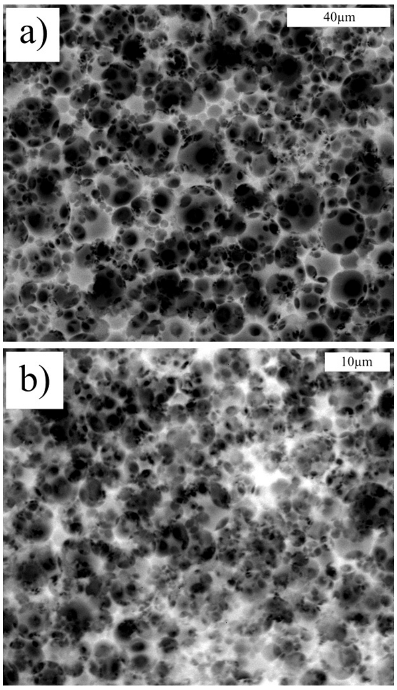

Figure 2: SEM images of: a) 0.5 % copper and b) 1.5 % copper polyHIPEs
Slika 2: SEM-posnetka poliHIPE-a z: a) 0,5 % bakra in b) 1,5 % bakra

merates can be seen on the SEM images (**Figure 1**). As it is known from the previous studies that a stabilization of high internal-phase emulsions with particles only usually results in a polyHIPE material with a closed-cellular morphology,[28,29] the combination of the surfactant and the particle-stabilized emulsion, in our case, leads to an open-cellular morphology. The role of the particles as emulsion stabilizers is different from the role of the surfactant; the latter causes a thinning of the polymer film during the phase separation and gelation, having, therefore, a detrimental effect on the mechanical properties.

A similar effect on the morphology was also found when incorporating copper powder and carbon nanopowder into the oil phase of a HIP emulsion. In the case of copper powder, by increasing its mass fraction amount from 0.5 % to 1.5 %, the cavity diameter changed from 14 μm to 5 μm and the interconnecting pore diameter changed from 4 μm to 1 μm. An agglomerate is seen on the SEM images (**Figure 2b**) where the concentration of the incorporated copper powder is 1.5 %.

The mass fraction amount of the carbon nanopowder used for the investigation of the effect on the morphology was changed from 0.35 % to 15 %. However, an addition of more than 3 % of carbon nanopowder caused agglomerates in the polyHIPE matrix (**Figure 3**) and had a slight reverse effect on the cavity and interconnecting-pore diameters (**Table 1**). By varying the amount of the carbon nanopowder used (from 0.35 % to 3 %), the average cavity diameter of polyHIPE changed from 20 μm to 5 μm and the interconnecting-pore diameter changed from 5 μm to 1.5 μm. At lower particle concen-

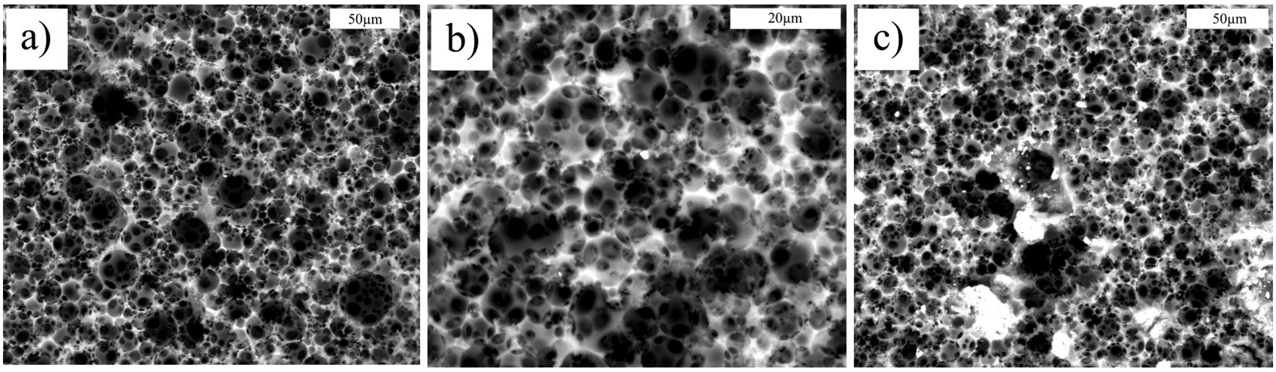

Figure 3: SEM images of: a) 0.35 % carbon nanopowder, b) 3 % carbon nanopowder and c) 15 % carbon-nanopowder polyHIPEs
Slika 3: SEM-posnetki poliHIPE-a z: a) 0,35 % , b) 3 % in c) 15 % ogljikovega nanoprahu

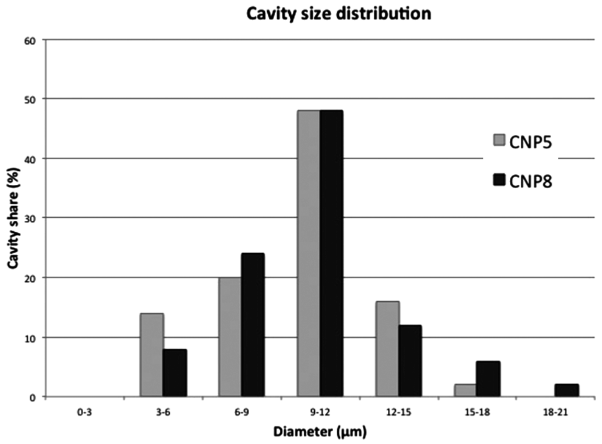

Figure 4: Cavity-size distribution of CNP5 and CNP8 samples
Slika 4: Porazdelitev velikosti por v vzorcih CNP5 in CNP8

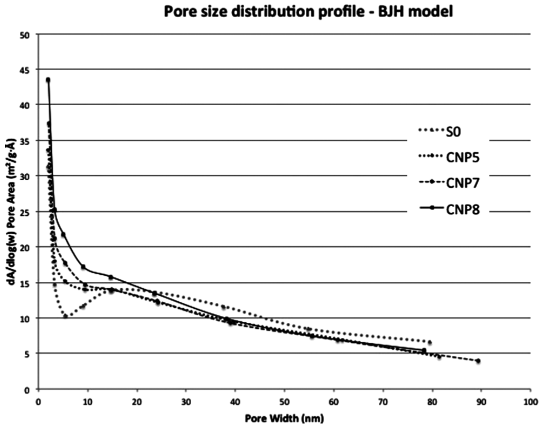

Figure 5: Pore-size-distribution profile (*r* < 100 nm) of S0, CNP5, CNP7 and CNP8 samples
Slika 5: Porazdelitev velikosti por (*r* < 100 nm) v vzorcih S0, CNP5, CNP7 in CNP8

trations the effect of an agglomeration is not as evident as in the case of higher amounts of the incorporated particles, which is mainly the result of high specific-surface area of the particles. After reaching the concentration maximum, the added particles do not have a stabilising effect but tend to form agglomerates (**Figure 4**).

Additionally, nitrogen adsorption/desorption experiments were carried out to determine the surface area and pore-size distribution of the prepared polyHIPEs. A BET model was used for the surface-area determination while a BJH model was applied for the pore-size-distribution profile. As shown in **Table 2**, the surface area of the polyHIPEs stabilized using a combination of the surfactant and solid particles (samples CNP5, CNP7 and CNP8) is between 23.6 m^2/g and 29.2 m^2/g, which is similar to the surface area of the styrene-based polyHIPEs stabilized with the surfactant only (22 m^2/g, sample S1). This is surprising because we predicted that, due to the high specific-surface area of the incorporated particles, the surface area would increase with the increasing amount of solid particles. Obviously, the addition of the particles did not produce any additional pores within the meso or micro range of the pore size (below 50 nm; **Figure 5**) that would significantly increase the surface area of polyHIPEs.

Table 2: Surface areas of polyHIPEs with different carbon-nanopowder amounts
Tabela 2: Površina poliHIPE-ov z različno vsebnostjo ogljikovega nanoprahu

Sample	Particle amount	*BET*/(m^2/g)
S0	0 %	22.03
CNP5	5 % C	23.58
CNP7	10 % C	25.84
CNP8	15 % C	29.22

4 CONCLUSIONS

We have demonstrated that it is possible to prepare styrene-based polyHIPEs stabilized with a combination of a surfactant and various solid particles. Their interconnecting open-porous morphology can be successfully controlled by changing the amount of the incorporated solid particles until they start to agglomerate. We have also shown that the amount of solid particles has no significant effect on the polyHIPE specific-surface area. The ability of controlling the morphology by changing the concentration of the particles is important with respect to the applicability of polyHIPE materials. Further experiments are needed to determine the effect of incorporated particles on the mechanical properties of the obtained polyHIPEs.

5 REFERENCES

[1] K. J. Lissant (Ed.), Emulsions and Emulsion Technology, Part 1, Marcel Dekker, New York 1974

[2] I. Pulko, P. Krajnc, Macromolecular Rapid Communications, 33 (**2012**), 1731–1746

[3] A. Desforges, M. Arpontet, H. Deleuze, O. M. Monval, Reactive & Functional Polymers, 53 (**2002**), 183–192

[4] D. Štefanec, P. Krajnc, Reactive & Functional Polymers, 65 (**2005**), 37–45

[5] D. Štefanec, P. Krajnc, Polymer International, 56 (**2007**), 1313–1319

[6] U. Sevšek, S. Seifried, Č. Stropnik, I. Pulko, P. Krajnc, Mater. Tehnol., 45 (**2011**) 3, 247–251

[7] I. Pulko, P. Krajnc, Chemical Communications, 37 (**2008**), 4481–4483

[8] I. Pulko, V. Smrekar, A. Podgornik, P. Krajnc, Journal of Chromatography A, 17 (**2011**), 2396–2401

[9] W. Busby, N. R. Cameron, C. A. B. Jahoda, Biomacromolecules, 2 (**2001**), 154–164

[10] E. M. Christenson, W. Soofi, J. L. Holm, N. R. Cameron, A. G. Mikos, Biomacromolecules, 8 (**2007**), 3806–3814

[11] A. Barbetta, M. Dentini, E. M. Zannoni, M. E. De Stefano, Langmuir, 21 (**2005**), 12333–12341

[12] D. C. Walsh, J. I. T. Stenhouse, L. P. Kingsbury, E. J. Webster, Journal of Aerosol Science, 27 (**1996**), 629–630

[13] P. Krajnc, N. Leber, D. Štefanec, S. Kontrec, A. Podgornik, Journal of Chromatography A, 1065 (**2005**), 69–73

[14] I. Pulko, M. Kolar, P. Krajnc, Science of the Total Environment, 386 (**2007**), 114–123

[15] M. G. Schwab, I. Senkovska, M. Rose, N. Klein, M. Koch, J. Pahnke, G. Jonschker, B. Schmitz, M. Hirscher, S. Kaskel, Soft Matter, 5 (**2009**), 1055–1059

[16] H. F. M. Schoo, G. Challa, B. Rowatt, D. C. Sherrington, Reactive Polymers, 16 (**1992**), 125–136

[17] S. Ungureanu, H. Deleuze, O. Babot, M. F. Achard, C. Sanchez, M. I. Popa, R. Backov, Applied Catalysis A: General, 390 (**2010**), 51–58

[18] I. Pulko, J. Wall, P. Krajnc, N. R. Cameron, Chemistry – A European Journal, 16 (**2010**), 2350–2354

[19] H. Kunieda, C. Solans, N. Shida, J. L. Parra, Colloids and Surfaces, 24 (**1987**), 225–237

[20] V. G. Babak, M. J. Stebe, Journal of Dispersion Science and Technology, 23 (**2002**), 1–22

[21] J. M. Williams, D. A. Wrobleski, Langmuir, 4 (**1988**), 656–662

[22] J. M. Williams, Langmuir, 7 (**1991**), 1370–1377

[23] R. Aveyard, B. P. Binks, J. H. Clint, Advances in Colloid and Interface Science, 100 (**2003**), 503–546

[24] A. Menner, V. Ikem, M. Salgueiro, M. S. P. Shaffer, A. Bismarck, Chemical Communications, (**2007**), 4274–4276

[25] I. Gurevitch, M. S. Silverstein, Journal of Polymer Science Part A: Polymer Chemistry, 48 (**2010**), 1516–1525

[26] S. Zou, Y. Yang, H. Liu, C. Wang, Colloids and Surfaces A: Physicochemical and Engineering Aspects, 436 (**2013**), 1–9

[27] M. Claire Hermant, B. Klumperman, C. E. Koning, Chemical Communications, (**2009**), 2738–2740

[28] V. O. Ikem, A. Menner, A. Bismarck, Langmuir, 26 (**2010**), 8836–8841

[29] V. O. Ikem, A. Menner, A. Bismarck, Angewandte Chemie International Edition, 47 (**2008**), 8277–8279

[30] S. Kovacic, G. Ferk, M. Drofenik, P. Krajnc, Reactive and Functional Polymers, 72 (**2012**), 955–961

[31] S. Kovacic, N. B. Matsko, G. Ferk, C. Slugovc, Journal of Materials Chemistry A, 1 (**2013**), 7971–7978

UDK 621.785.616: 620.178:004.032.26
Original scientific article/Izvirni znanstveni članek

ISSN 1580-2949
MTAEC9, 48(3)409(2014)

PREDICTION OF THE HARDNESS OF HARDENED SPECIMENS WITH A NEURAL NETWORK

NAPOVED TRDOTE KALJENIH VZORCEV Z NEVRONSKIMI MREŽAMI

Matej Babič[1], Peter Kokol[2], Igor Belič[3], Peter Panjan[4], Miha Kovačič[5,6], Jože Balič[7], Timotej Verbovšek[8]
[1]Ph. D. Researcher, Slovenia
[2]University of Maribor, Faculty of Electrical Engineering and Computer Science, Smetanova 17, 2000 Maribor, Slovenia
[3]Institute of Metals and Technology, Lepi pot 11, 1000 Ljubljana, Slovenia
[4]Jožef Stefan Institute, Jamova 39, 1000 Ljubljana, Slovenia
[5]Štore-Steel, d. o. o., Železarska 3, 3220 Štore, Slovenia
[6]University of Nova Gorica, Laboratory for Multiphase Processes, Vipavska 13, 5000 Nova Gorica, Slovenia
[7]University of Maribor, Faculty of Mechanical Engineering, Smetanova 17, 2000 Maribor, Slovenia
[8]University of Ljubljana, Faculty of Natural Sciences and Engineering, Aškerčeva 12, 1000 Ljubljana, Slovenia
babicster@gmail.com

Prejem rokopisa – received: 2013-11-05; sprejem za objavo – accepted for publication: 2014-02-20

In this article we describe the methods of intelligent systems to predict the hardness of hardened specimens. We use the mathematical method of fractal geometry in laser techniques. To optimize the structure and properties of tool steel, it is necessary to take into account the effect of the self-organization of a dissipative structure with fractal properties at a load. Fractal material science researches the relation between the parameters of fractal structures and the dissipative properties of tool steel. This paper describes an application of the fractal dimension in the robot laser hardening of specimens. By using fractal dimensions, the changes in the structure can be determined because the fractal dimension is an indicator of the complexity of the sample forms. The tool steel was hardened with different speeds and at different temperatures. The effect of the parameters of robot cells on the material was better understood by researching the fractal dimensions of the microstructures of hardened specimens. With an intelligent system the productivity of the process of laser hardening was increased because the time of the process was decreased and the topographical property of the material was increased.

Keywords: fractal dimension, laser, hardening, neural network

V tem članku je uporabljena metoda inteligentnih sistemov za napovedovanje trdote kaljenih vzorcev. Uporabljena je matematična metoda fraktalne geometrije v laserski tehniki. Za optimiranje strukture in lastnosti orodnega jekla je treba upoštevati vpliv samoorganizacije strukture z lastnostmi fraktalov. Fraktalna znanost o materialu raziskuje odnos med parametri fraktalne strukture in disipativnimi lastnostmi orodnega jekla. Članek opisuje uporabo fraktalne dimenzije pri robotskem laserskem kaljenju vzorcev. Z uporabo fraktalne dimenzije se lahko določi sprememba v sestavi, ker je fraktalna dimenzija pokazatelj kompleksnosti oblike vzorcev. Orodno jeklo je bilo kaljeno z različnimi hitrostmi z različnih temperatur. Učinek parametrov robotske laserske celice na orodno jeklo se da boljše razumeti z raziskovanjem fraktalne dimenzije mikrostrukture kaljenih vzorcev. Z inteligentnimi sistemi je bila povečana produktivnost procesa laserskega kaljenja, ker se zmanjša trajanje procesa in se povečajo topografske lastnosti materialov.

Ključne besede: fraktalna dimenzija, laser, kaljenje, nevronske mreže

1 INTRODUCTION

Of all the microscopic methods, electron-microscopy images give the best resolution, the most accurate information of the distribution of crystals in a building, the best morphology of various structural types and the best structural surface topography. Fractal geometry provides a new approach in describing the structures of various irregular facilities. Fractal theory is also used in the field of materials science. Models of fractal lines and surfaces are created to describe the properties of the microstructures of materials. The subject of fractals can be used to assist in an analysis of the surfaces encountered in robot laser hardening. It should be noted that the morphology of a surface will change if the material is hardened with robot laser cells. An analysis of fractal dimensions is a method used to study the surface properties of materials. A fractal dimension[1,2] is a property of fractals that is maintained with all the magnifications and is, therefore, well-defined but, in addition, it also reveals the complexity of the fractal. In general, we cannot calculate the fractal dimension for the above-mentioned procedure, as this is possible only for purely mathematical constructs and not in reality. In practical terms, to determine the dimensions the most used method is that 'of counting the boxes' (the box-counting dimension) that studies a fractal cover using a square grid, which is then reduced and the change in the number of the squares needed to cover the entire crowd is observed. The result is, of course, an approximation, which is calculated using the desired number of places. In this research, a fractal analysis is used to determine how the parameters of robot laser hardening affect the hardness of a hardened material. Robot laser surface-hardening heat treatment[3–6] is complementary to the conventional flame or inductive hardening. The energy source for laser hardening is a laser beam that heats up very quickly achieving the metal surface area of points up to 1.5 mm and a hardness of 65 HRc. Laser hardening is a process of projecting the features such as non-controlled energy intake, high performance constancy and accurate positioning process. A hard martensitic microstructure provides improved surface properties such as wear resistance and high strength.[7,8] A fractal analysis[9,10] is useful when classical geometry cannot be sufficiently useful to precisely describe the results of irregular facilities. A profound feature of fractals is the fractal dimension D[11–13] providing an important view of the physical properties of various materials. This article describes the fractal structure[14,15] of robot laser-hardened tool steel. Fractal patterns were found in different mechanical properties of hardened materials (Mandelbrot 1982, Feder 1988). Fractal features were also observed in a mechanical computer simulation, which can be explained with Gauss-Marc fractal random fields. In this work, we have used a scanning electron microscope (SEM)[16,17] to search and analyse the fractal structure of the robotic-laser-hardened material. The aim of the research is to ascertain how the robotic-laser-cell parameters for an optimum tempering affect the fractal dimension of the hardened material.

2 MATERIAL PREPARATION AND EXPERIMENTAL METHOD

2.1 Material preparation

The study was undertaken using the tool steel of DIN standard 1.7225. The chemical composition of the material included 0.38 % to 0.45 % C, 0.4 % maximum Si, 0.6–0.9 % Mn, 0.025 % maximum P, 0.035 % maximum S and 0.15–0.3 % Mo. The specimen test section was in a cylindrical form with the dimensions of 25 mm × 10 mm. After hardening the test specimen was cut into smaller parts. The tool steel was forged with laser at different speeds and different powers. So, we changed two parameters, speed $v \in 2,5$ mm/s with the steps of 1 mm/s and temperature $T \in (1000, 1400)$ °C in 50 °C steps. In all these tests we recorded the microstructure.

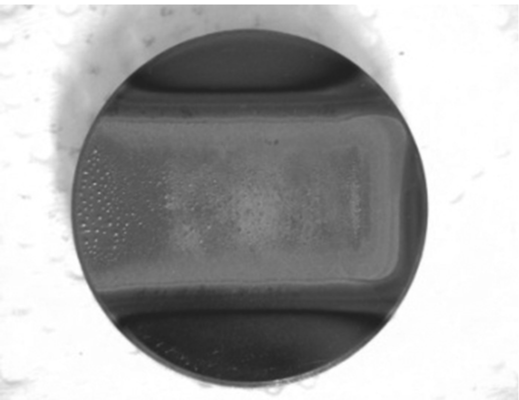

Figure 1: Hardened specimen
Slika 1: Kaljen vzorec

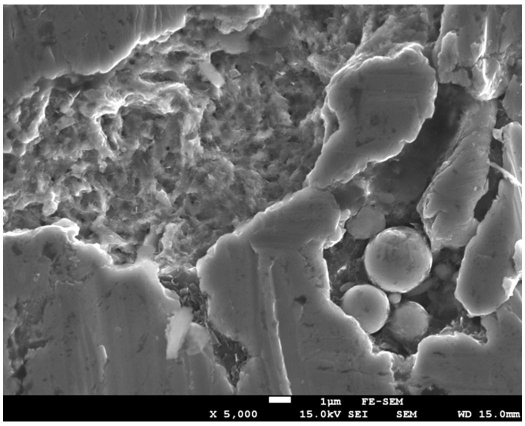

Figure 2: SEM image of a hardened specimen
Slika 2: SEM-posnetek kaljenega vzorca

We recorded the hardened surface area as well as the deep hardened zone of the clips. Of interest to us was whether the robotic laser-hardening parameters for different fractal structures resulted in microparticles. Also, we wanted to understand or ascertain the fractal structure of the optimum hardening parameters. **Figure 1** shows the longitudinal and transverse cross-section of the hardened tool steel. **Figure 2** shows the microstructure of the hardened tool steel. Prior to testing, the specimens were first subjected to mechanical and then to electrolytic polishing[18] in $H_3PO_4 + CrO_3$. After polishing the microstructure was examined with a light microscope and with field-emission scanning electron microscope, JEOL JSM-7600F. Irregular surface textures with a few breaks, presented as black islands, are seen in **Figure 2**.

2.2 Experimental method

The porosity was determined from the SEM images of the microstructure. It is known that in a homogenously porous material the area of the pores is equal to the volume of the pores in specimens. The SEM pictures were converted to binary images (**Figure 3**), from which we calculated the areas of the pores for all the pictures using the ImageJ program (ImageJ is a public domain, a Java-based image processing program developed at the National Institutes of Health). The area of the pores on each picture of the material was calculated and then the arithmetic mean and the standard deviation of the porosity were determined. To analyze the possibility of an application of the fractal analysis[11–16] to the heat-treated surface, we examined the relation between the surface porosity and fractal dimensions depending on various parameters of the robot laser cell. In fractal geometry, the key parameter is fractal dimension D. The relationship between fractal dimension D, volume V and length L can be indicated as follows:

$$V \sim L^D \qquad (1)$$

Fractal dimensions were determined using the box-counting method which has been proven to have a higher

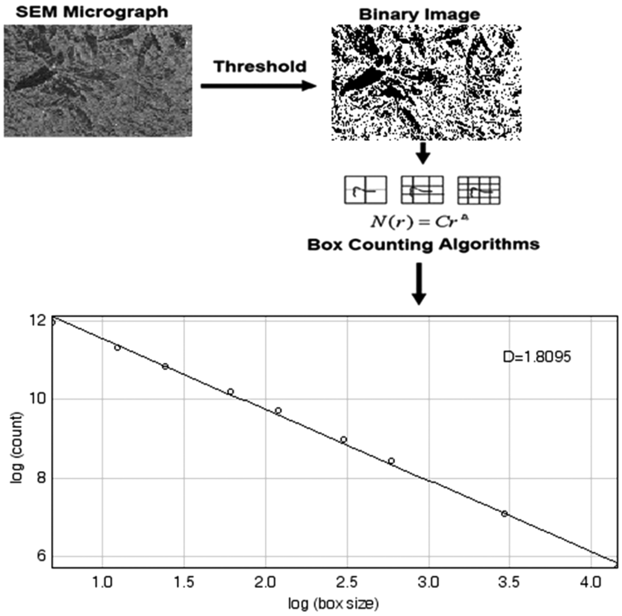

Figure 3: Calculation of fractal dimensions with the box-counting method
Slika 3: Računanje fraktalne dimenzije z metodo rezanja škatel

calculation speed and better accuracy by Dougan[19] and Shi[20].

To analyse the results we used one method of the intelligent system: the neural network.[21] Artificial neural networks (ANNs) are simulations of collections of model biological neurons. A neuron operates by receiving signals from the other neurons through the connections called synapses. A combination of these signals, in excess of a certain threshold or activation level, will result in the neuron firing, i.e., sending a signal to another neuron, to which it is connected. Some signals act as excitations and others as inhibitions of neuron firing. What we call thinking is believed to be a collective effect of the presence or absence of firings in the patterns of the synaptic connections between neurons. In this context, neural networks are not simulations of real neurons, as they do not model the biology, chemistry or physics of a real neuron. The basic building element of the neural network used is an artificial-neural-network cell (ANN) (**Figure 4**).

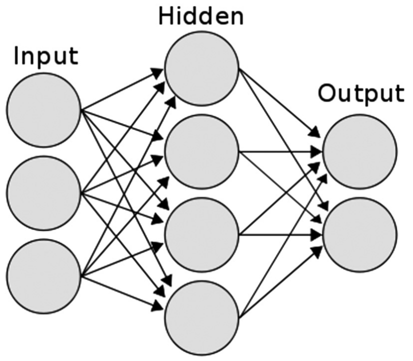

Figure 4: General multi-layer neural-network system
Slika 4: Splošni sistem večplastne nevronske mreže

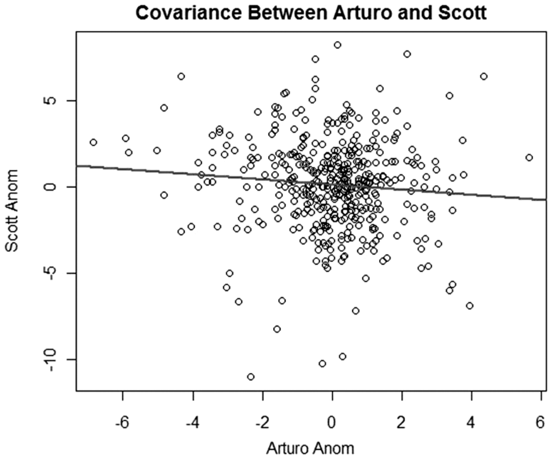

Figure 5: Analysis of covariance
Slika 5: Analiza kovariance

The analysis of covariance (generally known as ANCOVA) is a technique that brings together the analysis of variance and regression analysis. Covariance is a measure of how much two variables change together and how strong the relationship is between them. ANOVA can be extended to include one or more continuous variables that predict the outcome or dependent variable. **Figure 5** presents the analysis of covariance.

3 RESULTS AND DISCUSSION

3.1 Results

Table 1 presents the parameters of the hardened specimens that have an impact on the hardness. We marked the specimens with the codes from P1 to P19. Code *X*1 stands for the parameter of the temperature (°C), *X*2 is the speed of hardening (mm/s), *X*3 is the fractal dimension and *X*4 is the base hardness (the hardness before hardening). The last parameter, *Y*, is the measured hardness of the robot laser-hardened specimens. **Table 2** lists the experimental and prediction hardnesses of the robot laser-hardened specimens. With the fractal dimension we described the complexity of the hardened specimens. In **Table 1**, we can see that specimen P11 has the largest fractal dimension, 1.978 4. Thus, specimen P11 is the most complex. Specimen P1 has the highest hardness after hardening, that is 60 HRc. Specimen P17 has the lowest hardness after hardening, that is 52 HRc. **Figure 6** shows a graph presenting the measured and predicted hardnesses of the robot laser-hardened specimens. This figure also presents a model of regression. **Table 2** lists the experimental and prediction data. The first column gives the codes of the hardened specimens. The column for Hardness (experimental data) gives the experimental data for the hardness after hardening. The predictions with a neural network are presented in the column for Hardness (prediction with NN 36 %); in our case we

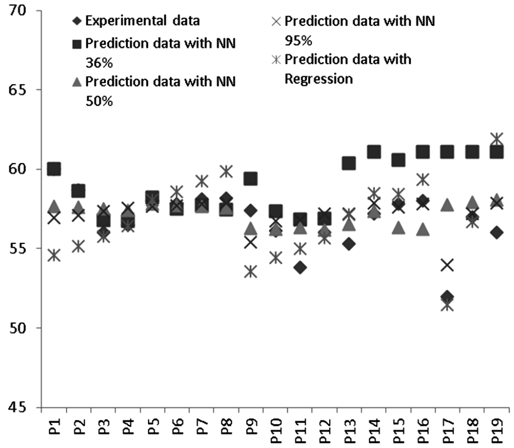

Figure 6: Measured and predicted hardnesses of the hardened specimens
Slika 6: Izmerjene in napovedane trdote kaljenih vzorcev

used 12 datasets for the learn test set and 7 datasets for the test set. In the column for Hardness (prediction with NN 52 %) we used 10 datasets for the learn test set and 9 datasets for the test set; and in the column for Hardness (prediction with NN 95 %) we used 18 datasets for the learn test set and 1 dataset for the test set; we used the leave-one-out method. We used program Neuralyst. Neuralyst is a general-purpose neural-network engine that was integrated with Microsoft® ExcelTM in the WindowsTM or MacintoshTM systems. Neuralyst provides a user-friendly interface and a powerful, flexible neural network that is self-programming. A researcher acts as a coach to Neuralyst providing it with data and letting it know the goals it should learn. Neuralyst will then train itself on the data and goals the researcher has set. During its training, it will report on how well it is doing. We used a 4-layer network, learning at the rate of 0.6, with the moment of learning being 0.5, the tolerance of the test set being 0.01 and the tolerance of the learning set being 0.3. The neural-network modelling with the 36 % training data shows a 7.7 % deviation from the measured data, the modelling with the 52 % training data shows a 5.2 % deviation from the measured data and the modelling with the 95 % training data shows a 2.3 % deviation from the measured data. The regression model shows a 4.7 % deviation from the measured data.

Table 1: Parameters of the hardened specimens
Tabela 1: Parametri kaljenih vzorcev

Specimen	$X1$	$X2$	$X3$	$X4$	Y
P1	1000	2	1.9135	34	60
P2	1000	3	1.9595	34	58.7
P3	1000	4	1.9474	34	56
P4	1000	5	1.9384	34	56.5
P5	1400	2	1.9225	34	58
P6	1400	3	1.9781	34	57.8
P7	1400	4	1.954	34	58.1
P8	1400	5	1.9776	34	58.2
P9	1000	2	1.972	60	57.4
P10	1000	3	1.858	58.7	56.1
P11	1000	4	1.9784	56	53.8
P12	1000	5	1.941	56.5	56
P13	1400	2	1.9782	58	55.3
P14	1400	3	1.581	57.8	57.2
P15	1400	4	1.965	58.1	57.8
P16	1400	5	1.8113	58.2	58
P17	800	0	1.9669	34	52
P18	1400	0	1.9753	34	57
P19	2000	0	1.9706	34	56

Table 2: Experimental and prediction data
Tabela 2: Eksperimentalni in napovedani podatki

Specimen	Hardness (experimental data)	Hardness (prediction with NN 36 %)	Hardness (prediction with NN 52 %)	Hardness (prediction with NN 95 %)	Hardness (prediction with regression)
P1	60	60.04404	57.66478	56.95868	54.56465
P2	58.7	58.65453	57.60106	57.12015	55.12693
P3	56	56.79983	57.5164	57.37326	55.7891
P4	56.5	56.75793	57.42825	57.5548	56.44594
P5	58	58.21552	57.79482	57.63685	58.04714
P6	57.8	57.48934	57.73722	57.68834	58.5924
P7	58.1	57.72849	57.65605	57.80268	59.27572
P8	58.2	57.478	57.58361	57.85767	59.87651
P9	57.4	59.39293	56.29186	55.42167	53.57422
P10	56.1	57.33137	56.21767	56.71604	54.4561
P11	53.8	56.83125	56.31979	56.76928	54.98285
P12	56	56.89147	56.19585	57.17863	55.67142
P13	55.3	60.36785	56.5345	57.19434	57.12963
P14	57.2	61.11235	57.35906	57.85592	58.46115
P15	57.8	60.55724	56.33986	57.59233	58.43199
P16	58	61.11235	56.2168	57.84021	59.33421
P17	52	61.11235	57.76515	53.96322	51.44111
P18	57	61.11235	57.93535	57.20306	56.67362
P19	56	61.11235	58.0907	57.87076	61.92865

3.1.1 Model regression

$$Y = 48.99076743 + 0.008744915 \cdot X1 + 0.641369094 \cdot X2 - 1.71942784 \cdot X3 - 0.034224818 \cdot X4$$

We checked the reliability model with pattern P20 heat treated at 1200 °C at a speed of 6 mm/s. We calculated the fractal dimension of the sample, which had a value of 1.9692. Sample P20 had a hardness of 57 HRc. The data were inserted into the model and we determined the deviations of the experimental values from the model values. **Table 3** shows the deviation of the predicted value for sample P20 from the experimental measurements after heat treatment.

Table 3: Deviation of the predicted values for specimen P20 from the experimental measurements after heat treatment
Tabela 3: Odmik napovedanih vrednosti vzorca P20 od eksperimentalnih meritev po toplotni obdelavi

Specimen	Hardness (prediction with NN 36 %)	Hardness (prediction with NN 50 %	Hardness (prediction with NN 95 %)	Hardness (prediction with regression)
Deviation	4.32 %	2.91 %	1.23 %	3.12 %

3.2 Discussion

The hardness structure of the material is an important mechanical property that affects the hardness of materials. We cannot apply Euclidian geometry to describe the porosity of hardened specimens because porosity is very complex. Here we use fractal geometry to describe the hardness of the robot laser-hardened specimens. In this paper we describe how the parameters (speed and temperature) of a robot laser cell affect the hardness of metal materials using a new method, fractal geometry. Hardness has a large impact on the mechanical properties of a material. The fractal approach is more appropriate for characterizing complex and irregular surface microstructures observed in the surfaces of robot laser-hardened specimens and can be effectively utilized for predicting the properties of the material from the fractal dimensions of the microstructures. The fractal analysis of a series of digitized surface microstructures of the robot laser-surface-modified specimens indicated that useful correlations can be derived between the fractal dimensions and the surface microstructural features such as hardness. Specimen P17 has the minimum hardness after hardening, which is 52 HRc. We used two methods of intelligent systems to make a prediction of the hardness of the robot laser-hardened specimens. The neural-network model gave us a better prediction than the regression.

4 CONCLUSION

The paper presents the use of the method of an intelligent system to predict the hardness of hardened specimens. We used fractal geometry to describe the mechanical property, the hardness of robot laser-hardened specimens. Fractal structures were also found in the robot laser-hardened samples when viewed under sufficient magnification. The hardening of various metal alloys has shown that when the melting occurs, fractal geometry can be used to calculate the fractal dimension. Using the box-counting method, we analysed the samples of equal-tempered metal, after subjecting them to the robot laser hardening using various parameters. The main findings can be summarized as follows:

- A fractal structure is found after the robot laser hardening.
- The box-counting method allows us to calculate the fractal dimensions for different parameters of laser hardening robotic cells.
- The optimum fractal dimensions of different-parameter robot-laser-hardened tool steel have been identified.
- As in the robot-laser-hardening heat treatment of the material, a deformation occurs, which is a self-similar fractal dimension and can be used to describe the level irregularity.
- The fractal dimension varies between 1 and 2. By increasing the temperature of the robot laser cell, the fractal dimension becomes larger and the grain size becomes smaller. Consequently, we can use the fractal dimension as an important factor to define the grain shape.
- The dependence of the fractal dimension on the hardness was ascertained. This finding is important if we know that certain alloys mix poorly because they have different melting temperatures, but such alloys have much higher hardnesses and better technical characteristics. By varying different parameters (temperature and speed) robot laser cells produce different fractal patterns with different fractal dimensions.
- Materials with higher fractal dimensions are less porous than those with lower fractal dimensions.
- Specimens with lower fractal dimensions are the hardest.
- With the correlation coefficients we show a connection between the hardness and the fractal dimensions of the robot laser-hardened specimens.
- For the prediction of the porosity of hardened specimens we used a neural network, a genetic algorithm and multiple regressions.

5 REFERENCES

[1] C. C. Barton, Fractal analysis of scaling and spatial clustering of fractures, In: C. C. Barton, P. R. La Pointe (eds.), Fractals in the earth sciences, Plenum Press, New York 1995, 141–178

[2] B. B. Mandelbrot, The fractal geometry of nature, W. H. Freeman, New York 1982, 93

[3] M. Babič, M. Milfelner, S. Stepišnik, Robot, 2010, Laser hardening metals, In: T. Perme, D. Švetak, J. Balič (ur.), Proceedings of the IRT Industrial Forum, Portorož, 2010

[4] M. Babič, Optimal parameters of a robot cell for laser hardening of metals at different angles, 19. Proceedings of the International Electrotechnical and Computer Conference ERK 2010, Portoroz 2010 (in Slovene)

[5] M. Babič, T. Muhič, Fractal structure of the robot laser hardened materials, In: 18th Conference on Materials and Technology, Portoroz, Slovenia, 2010, Program and abstracts book, Institute of Metals and Technology, Ljubljana, 2010, 73 (in Slovene)

[6] M. Babič, Fractal dimension of the robot laser hardening tool steel, In: M. Robnik, D. Korošak (ur.), 9th Symposium of Physicists at the University of Maribor, Maribor, 2010, Book of Abstracts, London: CAMTP, 2 F., 2010 (in Slovene)

[7] J. Grum, P. Žerovnik, R. Šturm, Measurement and analysis of residual stresses after laser hardening and laser surface melt hardening on flat specimens, Proceedings of the Conference "Quenching ’96", Ohio, Cleveland, 1996

[8] P. A. Gillespie, C. B. Howard, J. J. Walsh, J. Watterson, Measurement and characterisation of spatial distributions of fractures, Technophysics, (**1993**), 113–141

[9] J. Feder, Fractals, Plenum Press, New York 1988

[10] P. S. Addison, Fractals and Chaos, IOP, London 1997

[11] J. Palis, M. Viana, On the continuity of the Hausdorff dimension and limit capacity for horseshoes, Lecture Notes in Mathematics, 1331 (**1988**), 150–160

[12] J. Palis, F. Takens, Hyperbolicity and sensitive chaotic dynamics at homoclinic bifurcations, Fractal dimensions and infinitely many attractors, Cambridge University Press, Cambridge 1993

[13] P. Mattila, Geometry of sets and measures in Euclidean spaces, Fractals and rectifiability, Cambridge University Press, Cambridge 1995

[14] A. Chaudhari, Y. Ch-Ch Sanders, S. Lee, Multifractal analysis of growing surface, Applied Surface Science, 238 (**2004**), 513–517

[15] P. R. La Pointe, A method to characterize fracture density and connectivity through fractal geometry, International Journal of Rock Mechanics and Mining Science & Geomechanics Abstracts, 25 (**1988**), 421–429

[16] Y. Hui-Sheng, S. Xia, L. Shou-Fu, W. Young-Rui, W. Zi-Qin, Multifractal spectra of atomic force microscope images of amorphous electroless Ni-Cu-P alloy, Applied Surface Science, 191 (**2002**), 123–127

[17] Z. W. Chen, J. K. L. Lai, C. H. Shek, Multifractal spectra of scanning electron microscope images of SnO2 thin films prepared by pulsed laser deposition, Physics Letters A, 345 (**2005**), 218–223

[18] M. Soković, J. Mikula, L. A. Dobrzanski, J. Kopač, L. Koseč, P. Pandan, J. Madejski, A. Piech, Cutting properties of the Al_2O_3 + SiC(w) based tool ceramic reinforced with the PVD and CVD wear-resistant coatings, Proceedings of the 13th International Scientific Conference "Achievements in Mechanical and Materials Engineering" AMME'2005, Gliwice-Wisla, 2005, 606–610

[19] L. T. Dougan, P. S. Addison, Estimating the cut-off in fractal scaling of fractured concrete, Cement and Concrete Research, 31 (**2001**), 1043–1048

[20] Y. Shi, X. P. Lou, S. H. Quan, Fractal dimension computation methods for gas diffusion layer of PEM fuel cells (in Chinese), Journal of Wuhan University of Technology, 29 (**2005**), 79–82

[21] M. El Hafnawi, M. Mysara, Recurrent Neural Networks and Soft Computing, Intech, Rijeka 2012

UDK 669.14:532.613
Professional article/Strokovni članek

ISSN 1580-2949
MTAEC9, 48(3)415(2014)

INTERFACIAL TENSION AT THE INTERFACE OF A SYSTEM OF MOLTEN OXIDE AND MOLTEN STEEL

MEDFAZNA NAPETOST NA STIKU STALJEN OKSIDNI SISTEM – STALJENO JEKLO

Silvie Rosypalová, Rostislav Dudek, Jana Dobrovská, Ludovít Dobrovský, Monika Žaludová

VŠB – Technical University of Ostrava, Faculty of Metallurgy and Materials Engineering, 17. listopadu 15/2172, 708 33 Ostrava, Czech Republic
silvie.rosypalova@vsb.cz

Prejem rokopisa – received: 2012-08-30; sprejem za objavo – accepted for publication: 2013-07-16

This paper is focused on a study of the interfacial tension between selected oxide and metal phases. The experimental research on the interfacial tension was performed in a horizontal resistive graphite Tamman furnace using an original method of measuring. This method consists of fixing both liquid phases in a horizontal position using a mandrel made of tungsten wire in a corundum cover. In this work the influence of the carbon content in the steel on the interfacial tension was studied. For this purpose a steel with 0.411 % of mass fraction of carbon and a steel with 2.64 % of carbon were used. Because of the wide variety of oxide systems used in industry, a characteristic system of casting powder was chosen for this study. This system contains dominant components, i.e., SiO_2, CaO, Al_2O_3 and MgO, as well as a range of attendant mixtures, e.g., Fe_2O_3, TiO_2 and Na_2O. Simultaneously, the influence of SiO_2 on the temperature dependence of the interfacial tension was observed. For this reason a concentration series with gradual additions of SiO_2 was created. It was found that an increasing content of carbon in the steel significantly decreases the interfacial tension between the oxide system and the steel. The interfacial tension was found to decrease slightly with an increase in the content of SiO_2 in the oxide system.

Keywords: steel, casting powder, interfacial tension

Članek predstavlja študijo medfazne napetosti med izbranim oksidom in kovinsko fazo. Določanje medfaznih napetosti je bilo izvršeno z originalno metodo v horizontalni uporovni grafitni Tammanovi peči. Ta metoda sestoji iz zadržanja obeh talin v horizontalnem položaju s trnom iz volframove žice in korundnega pokrova. V tem delu je bil preučevan vpliv ogljika v jeklu na medfazno napetost. Uporabljeno je bilo jeklo z masnim deležem 0,411 mas. % ogljika in jeklo z 2,64 % ogljika. Zaradi velike raznolikosti oksidnih sistemov, ki se uporabljajo v industriji, je bil za študij izbran livni prašek. Ta vsebuje glavne komponente, ki so SiO_2, CaO, Al_2O_3 in MgO, ter vrsto primesi, kot so na primer Fe_2O_3, TiO_2 in Na_2O. Hkrati je bil opažen vpliv SiO_2 na temperaturno odvisnost medfazne napetosti. Zato je bila pripravljena serija z naraščajočo vsebnostjo SiO_2. Ugotovljeno je, da naraščanje vsebnosti ogljika v jeklu občutno zmanjša medfazno napetost med oksidnim sistemom in jeklom. Za medfazno napetost je ugotovljeno, da se nekoliko zmanjša, če se povečuje vsebnost SiO_2 v oksidnem sistemu.

Ključne besede: jeklo, livni prašek, medfazna napetost

1 INTRODUCTION

Interfacial phenomena play an important role in many metallurgical processes in which two immiscible liquid phases co-exist. Numerous steps in primary processing and the refining of materials include a mass transfer through an interface, which significantly affects the rate of individual reactions. Surface and interfacial tensions can accelerate these reactions, or completely dampen them. It is, therefore, necessary to know the properties of the interface, which together with the other physicochemical properties[1] forms the properties of the resulting product. Although various methods[2,3] have been developed for the research of interface phenomena, any experimental investigation remains very difficult. For this reason the literature data for a determination of the interface phenomena, particularly the interface phenomena for slag–metal, are not commonly available.

The aim of this research was to study the interfacial tension in the system involving an oxide phase and a metallic phase. The interfacial tension was calculated using the following equation:

$$\sigma_{(0)-(s)} = \sqrt{\sigma^2_{(0)-(g)} + \sigma^2_{(s)-(g)} - 2\sigma_{(0)-(g)} \cdot \sigma_{(s)-(g)} \cdot \cos\theta} \quad (1)$$

where $\sigma_{(s)-(g)}$/(mN/m) is the the surface tension of oxide system, $\sigma_{(o)-(g)}$/(mN/m) is the surface tension of the molten steel, and θ is the wetting angle of the liquid phases.

2 EXPERIMENTAL

2.1 Material

For the investigation of the interfacial tension a casting powder was chosen as a representative of an oxide system. Its composition is given in **Table 1**.

Within this system we investigated the influence of the carbon in the steel on the interfacial tension. For this purpose we choose, as representatives of the metallic phase, the steel (I) containing 0.411 % of carbon, and the steel (II), containing 2.64 % of carbon. The chemical compositions of both steels are given in **Tables 2** and **3**.

Table 1: Chemical composition of oxide system in mass fractions, *w*/%
Tabela 1: Kemijska sestava oksidnega sistema v masnih deležih, *w*/%

casting powder	component	SiO_2	CaO	MgO	Al_2O_3	TiO_2	Fe_2O_3	MnO_2
		37.10	29.00	1.70	12.50	0.50	0.64	0.10
	component	Na_2O	K_2O	P_2O_5	F^-	$C_{tot.}$	CO_2	
		5.10	0.40	0.10	4.10	7.20	4.40	

Table 2: Chemical composition of steel (I), *w*/%
Tabela 2: Kemijska sestava jekla (I), *w*/%

Steel (I)	component	C	Si	Mn	S	P	Cu
		0.41	0.375	0.344	0.011	0.016	0.076
	component	Ni	Cr	Mo	Ti	W	Fe
		0.218	12.392	0.027	0.013	0.084	75.6

Table 3: Chemical composition of steel (II), *w*/%
Tabela 3: Kemijska sestava jekla (II), *w*/%

Steel (II)	component	C	Si	Mn	S	P	Cu
		2.64	2.04	0.57	0.031	0.043	0.020
	component	Ni	Cr	Mo	Ti	W	Fe
		0.022	0.051	0.008	0.034	–	94.5

The influence of SiO_2 on the interfacial tension in an oxide/steel system was also investigated. For this research a concentration series was prepared with gradual additions of (3, 6, 9 and 15) % of SiO_2 to the measured system of casting powder, within the concentration range from 37.1 % to 52.1 %.

2.2 Experimental methods

Differential Thermal Analysis (DTA) was used to obtain the melting temperature of the steel samples.[4] The analysis was performed with the suse of the laboratory system Setaram SETSYS 18_{TM}. The samples with masses of approximately 200 mg were analysed using a controlled rate of heating equal to 15 °C/min. A dynamic atmosphere of Ar (purity > 99.9999 %) was maintained in the furnace during the analysis.

For the calculation of the interfacial tension according to Equation (1) the surface tension and the wetting angle of the liquid phases were determined experimentally. The surface tension of the casting powder, the steel and the concentration series with the addition of SiO_2 was measured using the method of sessile drop. This method is based on a recognition of the geometrical shapes of a drop of melt sessile on a non-wetting pad.[5] A graphite pad was used for the oxide systems and a corundum pad was used for the steel. The experimental measurements were performed in a horizontal resistance furnace under an Ar atmosphere (purity > 99.9999 %).

In order to determine the wetting angles of both liquid systems an original experimental methodology was used. This is schematically represented in **Figure 1a**. The principle of this methodology consists of fixing both liquid phases in a horizontal position.[6]

A sample of steel was put into a corundum pad of the appropriate shape. Afterwards, a tablet of oxide material was put on the steel. For the fixation of both phases in the horizontal position a mandrel formed by a tungsten wire in corundum protection was passed through the centre of the whole sample, as shown in **Figure 1b**. After the melting of both systems the wetting angle was calculated on the basis of the determined contours of the steel and oxide system, as can be seen in **Figure 1c**.

3 RESULTS AND DISCUSSION

The liquidus temperatures of the steels, determined by a DTA analysis, were 1455 °C for steel (I) and 1158 °C for the steel (II).

Figure 1: a) Schematic diagram of experimental method, b) a prepared sample before the experiment, c) image of molten phases
Slika 1: a) Shematski prikaz eksperimentalne metode, b) pripravljen vzorec pred preizkusom, c) posnetek staljenih faz

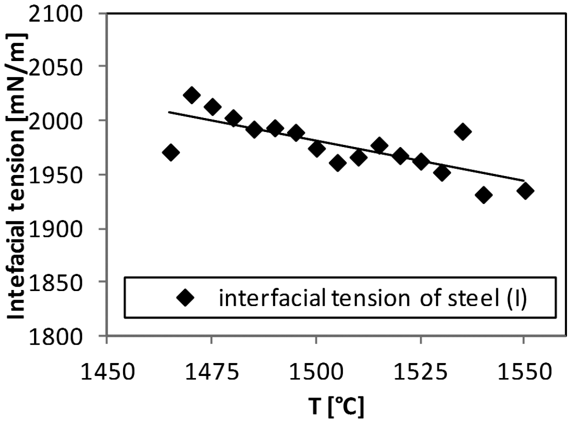

Figure 2: Temperature dependence of interfacial tension of system oxide – steel (I)
Slika 2: Temperaturna odvisnost medfazne napetosti oksidni sistem – jeklo (I)

For the calculation of the interfacial tension according to Equation (1), first of all the surface tensions of the steel and the casting powder were measured. The surface tension of steel (I) was measured within the temperature interval 1465–1550 °C. The surface tension decreased with the temperature in the interval 1770–1680 mN/m. The surface tension of steel (II) was measured within the temperature interval 1185–1550 °C and the values were in the interval 1409–1205 mN/m. From the measured values it is evident that the surface tension of the steel containing 0.411 % of carbon is on average higher by 350 mN/m, compared to the steel containing 2.64 % of carbon. The surface-tension measurements of the oxide system were performed in the temperature interval 1180–1550 °C and the obtained values ranged within the interval 390–370 mN/m.

During the next stage of the experimental research the wetting angles were measured in the interface systems oxide/steel (I) and oxide/steel (II). The values of the wetting angles for steel (I) increased slightly with the temperature in the range of 2–2.4 rad; in contrast to that in steel (II) the values decreased slightly in the interval 2–1.75 rad.

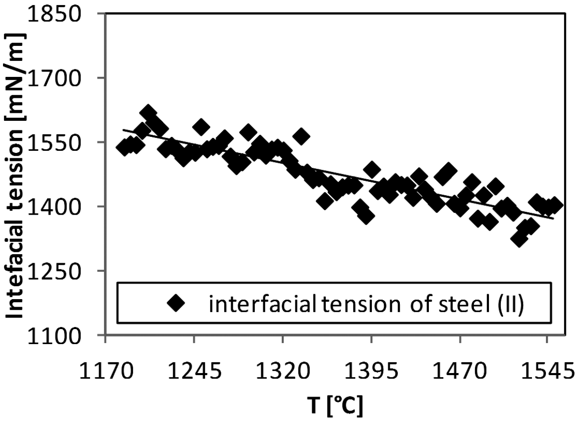

Figure 3: Temperature dependence of interfacial tension of system oxide – steel (II)
Slika 3: Temperaturna odvisnost medfazne napetosti oksidni sistem – jeklo (II)

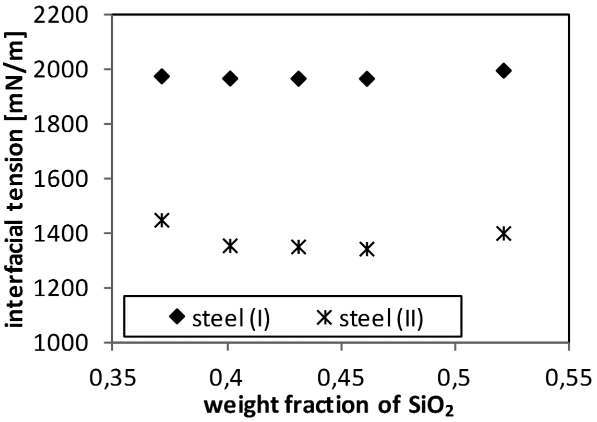

Figure 4: Dependence of interfacial tension on mass fraction of SiO_2 at a temperature of 1500 °C
Slika 4: Odvisnost medfazne napetosti od masnega deleža SiO_2 pri temperaturi 1500 °C

From the experimental data the interfacial tension was calculated according to Equation (1). **Figures 2** and **3** show the temperature dependences of the interfacial tension of steel (I) and steel (II).

From **Figures 2** and **3** it is evident that the interfacial tension in both systems decreases with the temperature. The values of the interfacial tension of steel (I) varied from 2020 mN/m to 1930 mN/m. The values of the interfacial tension of steel (II) were in the interval 1540–1330 mN/m. From these temperature dependences it follows that the values of the interfacial tension are, in steel (II), on average lower by 25.5 % (505 mN/m) in comparison with the values of the interfacial tension of steel (I).

Moreover, the influence of SiO_2 on the interfacial tension in both steels was determined experimentally. **Figure 4** shows the dependence of the interfacial tension of the system oxide/steel (I) or oxide/steel (II) on the content of SiO_2 at a temperature of 1500 °C. It is generally true that in the case when the melt contains the ions Si^{4+}, they will have a decisive influence on its structure, since silicon is the most electronegative of all the elements of the system, and with oxygen it creates stable complexes with a strong covalent bond.

The ions Al^{3+} also play an important role in formation of polyanion networks. It is evident from **Figure 4** that the trend of influence of the SiO_2 content on the interfacial tension is the same in both steels. The interfacial tension in the systems with additions of (0, 3, 6 and 9) % of SiO_2 decreases slightly. This confirmed the theory about SiO_2 functioning as a networks former. In the case of the system with the addition of 15 % of SiO_2 the values of the interfacial tension increase slightly. This phenomenon may be caused by the formation of phases with shorter chains and a change of the coordination of the Al^{3+} cations.

4 CONCLUSIONS

We can summarise the obtained results as follows:

- The interfacial tension between the molten steel and the molten casting powder with dominant components of SiO_2, CaO, Al_2O_3 and MgO decreases with temperature.
- A higher content of carbon in steel decreases the values of the interfacial tension at the interface system involving molten oxide and molten steel.
- The interfacial tension of the system involving molten casting powder and molten steel decreases with an increasing content of SiO_2 in the concentration interval 37.1–46.1 %.

Acknowledgements

The work was carried out within the scope of the student projects SP 2012/25, entitled "Experimental study of inorganic heterogeneous systems", and SP 2012/196, entitled "Specific research in metallurgy, materials and process engineering". It was financed from the specific research resources of the Faculty of Metallurgy and Materials Engineering, VŠB – Technical University of Ostrava, Czech Republic and of the project No. CZ.1.05/2.1.00/01.0040 "Regional Materials Science and Technology Centre" within the frame of the operation programme "Research and Development for Innovations" financed by the Structural Funds and from the state budget of the Czech Republic.

5 REFERENCES

[1] B. Smetana et al., Application of High Temperature DTA to Micro-Alloyed Steels, Metalurgija, 51 (**2012**) 1, 121–124

[2] E. J. Jung, W. Kim, I. Sohn, D. J. Min, A study on the interfacial tension between solid iron and CaO-SiO_2-MO system, J. Mater. Sci., 45 (**2010**), 2023–2029

[3] J. Elfsberg, T. Matsushita, Measurements and calculation of interfacial tension between commercial steels and mould flux slags, Steel research, 82 (**2011**) 4, 404–414

[4] M. Žaludová et al., Experimental study of Fe–C–O based system below 1000 °C, Journal of thermal Analysis and Calorimetry, 111 (**2013**) 2, 1203–1210

[5] R. Dudek, L. Dobrovsky, J. Dobrovska, Interpretation of inorganic melts' surface properties on the basis of chemical status and structural relations, International Journal of Materials Research, 99 (**2008**) 2, 1369–1374

[6] R. Dudek et al., Possibilities of study of the inorganic melts interphase tension, Proceedings of 19th International Metallurgical and Materials Conference, Metal 2010, Brno, 2010, 138–143

UDK 666.3/.7:620.178.1
Professional article/Strokovni članek

ISSN 1580-2949
MTAEC9, 48(3)419(2014)

WEAR PROPERTIES OF CERAMIC BODIES PRODUCED WITH NATURAL ZEOLITE

VEDENJE KERAMIČNIH TELES, IZDELANIH IZ NARAVNEGA ZEOLITA, PRI OBRABI

Ayşe Şükran Demırkiran
Sakarya University, Faculty of Engineering, Department of Metallurgical and Materials Engineering, Esentepe Campus, 54187 Sakarya, Turkey
dkiran@sakarya.edu.tr

Prejem rokopisa – received: 2012-08-31; sprejem za objavo – accepted for publication: 2013-09-04

In this study, the wear and friction behaviours of a ceramic disk produced from natural zeolite were studied using a ball-on-disk arrangement. Samples were fired in an electric furnace with a heating rate of 10 °C/min at 1150 °C for a period of 60 min. Friction and wear tests were carried out in dry test conditions under the (2.5, 5 and 7.5) N loads at the (0.1, 0.3 and 0.5) m/s sliding speeds.

Keywords: zeolite, friction, wear, ceramic

V tej študiji je predstavljeno vedenje keramične ploščice, izdelane iz naravnega zeolita, pri obrabi in trenju na napravi krogla na disku. Vzorci so bili žarjeni v električni peči s hitrostjo ogrevanja 10 °C/min, 60 min pri temperaturi 1150 °C. Preizkusi trenja in obrabe so bili izvršeni v suhih razmerah z obremenitvami (2,5, 5 in 7,5) N pri hitrostih drsenja (0,1, 0,3 in 0,5) m/s.

Ključne besede: zeolit, trenje, obraba, keramika

1 INTRODUCTION

At present, there is a large interest in the application of moving ceramic parts in the constructions without lubrication.[1] Ceramics have high mechanical properties, including hardness, general chemical inertness, excellent wear resistance, the ability to work in severe thermal conditions and relatively low densities in comparison with metallic or polymeric materials.[2,3] The wear of ceramics is one of the important issues for designers.[1] The wear of ceramics depends on operating conditions (such as normal load, sliding velocity, sliding distance and temperature), material properties (such as mechanical and thermal material properties) and structural properties (such as bulk density, impurity content, grain size, grain-boundary microstructure, porosity and glassy phase).[1,4,5]

In recent years, there has been a great demand for new materials produced using different raw materials. Zeolites are crystalline aluminosilicates with a three-dimensional framework structure based on the repeated units of silicon-oxygen (SiO_4) and aluminium-oxygen (AlO_4) tetrahedra. Natural zeolites are abundant raw materials in many countries. They can be used as raw material to produce ceramic, and the ceramics produced from natural zeolites have interesting properties.[6–9]

In this study, the wear behaviour of the ceramic bodies made of natural zeolite was investigated. The wear tests were carried out using an AISI 52100 ball by means of a ball-on-disc system in ambient and dry-friction conditions under the (2.5, 5 and 7.5) N loads with the (0.1, 0.3 and 0.5) m/s sliding speeds.

2 EXPERIMENTAL PROCEDURE

The zeolites used in the present study were supplied from ETİ Holding Company, located in Turkey. The chemical composition of zeolite as raw material is given in **Table 1**. The raw material was ground and sieved through a mesh 75 µm. Then, water was added as a binder and disc samples (Ø = 25 mm, 5 mm thick) were shaped by uniaxial dry pressing at a pressing pressure of 1.5 t. After shaping, the samples were dried at 110 °C for 24 h in an oven. Dried samples were fired in an electric furnace at a heating rate of 10 °C/min at 1150 °C for a period of 60 min and the fired samples were cooled down to room temperature in the furnace.

Before the wear test, the sintered disc samples were metallographically prepared and polished. Then, the balls and disc were ultrasonically cleaned in acetone. A ball-on-disc system was used for the friction and wear

Table 1: Chemical composition of zeolite as raw material
Tabela 1: Kemijska sestava zeolita kot surovine

Components (*w*/%)										
SiO_2	Al_2O_3	Na_2O	K_2O	Fe_2O_3	CaO	MgO	TiO_2	SrO	Rb_2O	ZnO
79.28	11.22	0.15	4.22	1.20	2.52	1.22	0.08	0.06	0.03	0.02

tests. The wear tests were carried out at ambient and dry-friction conditions under the (2.5, 5 and 7.5) N loads at the (0.1, 0.3 and 0.5) m/s sliding speeds. Hardened AISI 52100 steel balls with a 9 mm diameter against a ceramic disk were used in the system.

3 RESULTS AND DISCUSSION

The microstructural investigations, carried out by SEM, of the sintered samples revealed various features including very small cracks, undissolved quartz grains and porosity. In order to understand the microstructural changes and correlate them with the other results, an XRD analysis was performed. The XRD patterns of the samples sintered at 1150 °C for 60 min are shown in **Figure 1**. The XRD patterns consisting of kyanite, albite and silicon oxide peaks confirm the SEM results. In addition to these crystalline phases, a glassy phase also exists in the microstructure.

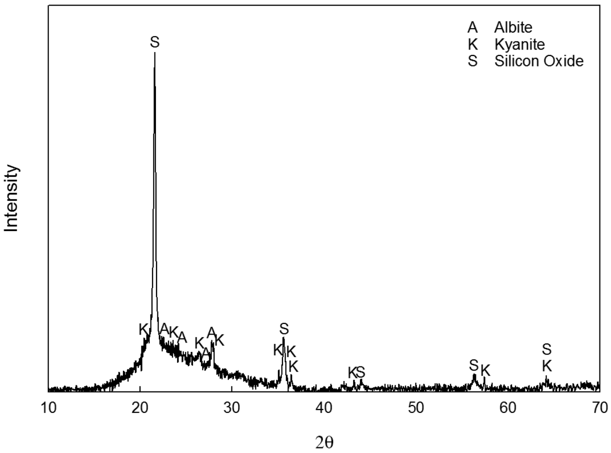

Figure 1: XRD pattern of the samples sintered at 1150 °C for 60 min

Slika 1: XRD-posnetek vzorca, sintranega pri 1150 °C, 60 min

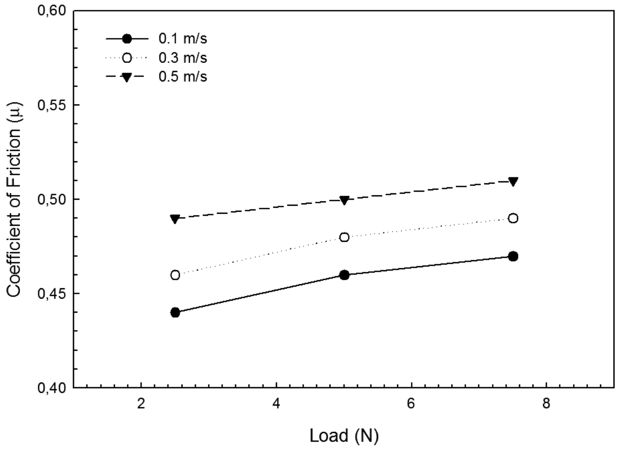

Figure 2: Variation of the friction coefficient with the applied load at different sliding speeds

Slika 2: Spreminjanje koeficienta trenja od uporabljene obtežbe pri različnih vrednostih hitrosti drsenja

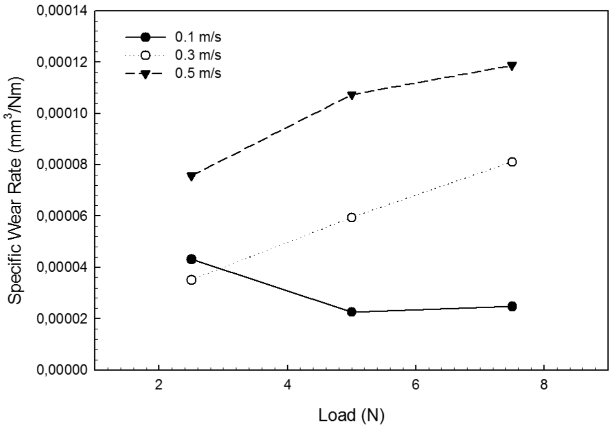

Figure 3: Variation of the specific wear rate with the applied load at different sliding speeds

Slika 3: Spreminjanje specifične hitrosti obrabe od uporabljene obtežbe pri različnih vrednostih hitrosti drsenja

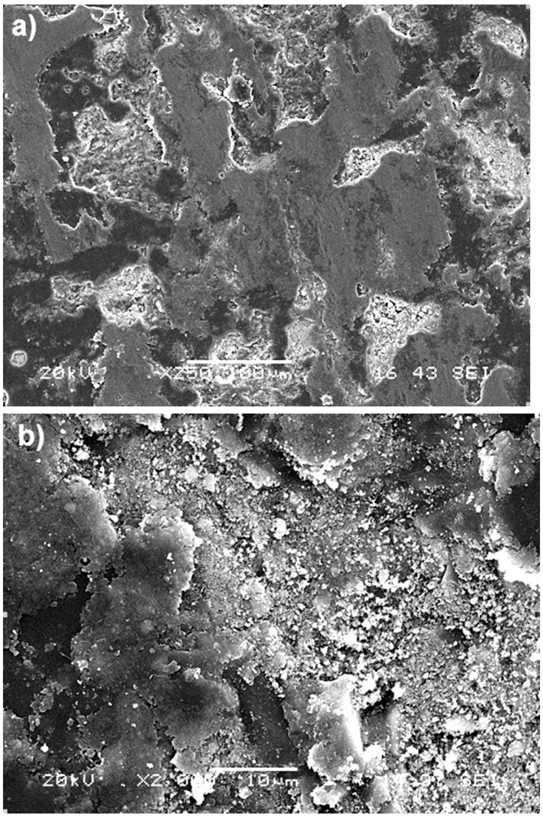

Figure 4: SEM micrographs of the worn surfaces at the 0.1 m/s sliding speed under the normal load of 5 N at different magnifications

Slika 4: SEM-posnetka obrabljene površine pri hitrosti drsenja 0,1 m/s pri obremenitvi 5 N pri različnih povečavah

Figure 2 presents a variation in the friction coefficient with an applied load at different sliding-speed values. It clearly shows that the friction coefficient increases linearly with an increase in the applied load and sliding speed. However, there is no significant change in the friction-coefficient values. **Figure 3** shows a variation in the specific wear rate with an applied load at different sliding-speed values. It is shown that specific-

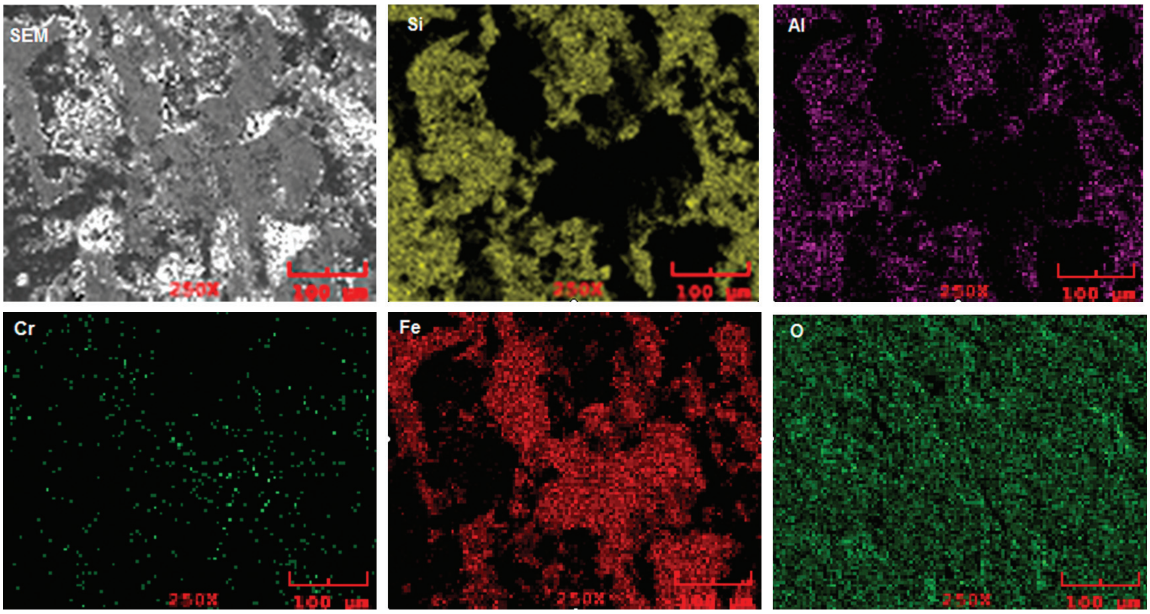

Figure 5: Elemental maps of the worn surfaces at the 0.1 m/s sliding speed under the normal load of 5 N
Slika 5: Razporeditev elementov na obrabljeni površini pri hitrosti drsenja 0,1 m/s pri obremenitvi 5 N

wear-rate values increase with the increasing applied load at the (0.3 and 0.5) m/s sliding speeds, but, at the 0.1 m/s sliding speed, the specific wear rate first decreases and then increases with the increase in the applied load.

Figure 4 shows SEM micrographs of the worn surfaces at the 0.1 m/s sliding speed under a normal load of 5 N at different magnifications. The worn surface of a sintered sample was covered by a layer formed with a densification of the oxidized wear debris from the steel ball on the sintered sample. However, a local spalling took place in this layer. Furthermore, the wear tracks consist of the wear debris as shown in **Figure 4b**. **Figure 5** presents elemental maps of the wear tracks of the sintered samples. It is clearly shown that the wear track of the disk includes iron, chromium and oxygen. However, as shown in **Table 1**, the chemical composition of the raw material does not include these elements. In this case, the wear debris from the AISI 52100 steel balls oxidizes with the heat resulting from the friction and then it adheres on the sample surfaces. In the light of these findings, it can be said that the wear mechanism of these samples is the adhesive wear. The wear mechanism of the AISI 52100 steel ball is also the abrasive wear.

4 CONCLUSIONS

The phases formed in the sintered samples are kyanite, albite and silicon oxide.

The coefficients of friction for all the combinations increase with an increase in the load.

The friction-coefficient values for the ceramic disks against the AISI 52100 steel balls vary between 0.44 and 0.51.

The specific wear rate also ranged between 2.267×10^{-5} mm^3/(N m) and 1.187×10^{-4} mm^3/(N m).

The wear mechanism of the sintered samples is the adhesive wear.

Acknowledgments

The author thanks Sakarya University, Engineering Faculty for supporting this work. The author also wishes to thank Mehmet İlhan Bayazıt for his experimental assistance.

5 REFERENCES

[1] H. R. Pasaribu et al., The transition of mild to severe wear of ceramics, Wear, 256 (**2004**), 585–591

[2] Y. Sun et al., Unlubricated friction and wear behaviour of zirconia ceramics, Wear, 215 (**1998**), 232–236

[3] E. Medvedovski, Wear-resistant engineering ceramics, Wear, 249 (**2001**), 821–828

[4] K. Adachi et al., Wear map of ceramics, Wear, 203–204 (**1997**), 291–301

[5] C. P. Doğan et al., Role of composition and microstructure in the abrasive wear of high-alumina ceramics, Wear, 225–229 (**1999**), 1050–1058

[6] E. A. Ortega et al., Properties of alkali-activated clinoptilolite, Cement and Concrete Research, 30 (**2000**), 1641–1646

[7] S. Chandrasekhar et al., Thermal studies of low silica zeolites and their magnesium exchanged forms, Ceramics International, 28 (**2002**), 177–186

[8] A. S. Demirkıran et al., Effect of natural zeolite addition on sintering kinetics of porcelain bodies, Journal of Materials Processing Technology, 203 (**2008**), 465–470

[9] A. S. Demirkıran et al., Electrical resistivity of porcelain bodies with natural zeolite addition, Ceramics International, 36 (**2010**), 917–921

UDK 536.65
Professional article/Strokovni članek

ISSN 1580-2949
MTAEC9, 48(3)423(2014)

THERMAL STORAGE AS A WAY TO ATTENUATE FLUID-TEMPERATURE FLUCTUATIONS: SENSIBLE-HEAT VERSUS LATENT-HEAT STORAGE MATERIALS

SHRANJEVANJE TOPLOTE KOT POT ZA ZMANJŠANJE NIHANJA TEMPERATURE: OBČUTLJIVI MATERIALI PROTI MATERIALOM ZA SHRANJEVANJE LATENTNE TOPLOTE

Pavel Charvat[1], Lubomir Klimes[1], Josef Stetina[1], Milan Ostry[2]
[1]Brno University of Technology, Faculty of Mechanical Engineering, Technicka 2896/2, 616 69 Brno, Czech Republic
[2]Brno University of Technology, Faculty of Civil Engineering, Veveri 331/95, 602 00 Brno, Czech Republic
charvat@fme.vutbr.cz

Prejem rokopisa – received: 2012-08-31; sprejem za objavo – accepted for publication: 2013-09-04

A stable fluid temperature is quite important in many technical applications and thermal storage is one of the ways to attenuate fluid-temperature fluctuations. Both sensible- and latent-heat storage materials can be used for this purpose. A theoretical study comprising numerical simulations was conducted in order to investigate the behaviors of sensible- and latent-heat storage for attenuating fluid-temperature fluctuations. The studied case was a circular channel, through which a fluid passed, surrounded by a thermal-storage material. Two sensible-heat storage materials (copper and concrete) and two latent-heat storage materials (n-octadecane and calcium chloride hexahydrate) were considered in the performed study. Water was the fluid in all the studied cases. The main goal of the investigations was to assess the thermal response of each variant under the same conditions. The length of the channel, the flow rate of water and the volume of the heat-storage material were the same in all the variants.

Keywords: temperature stability, thermal storage, phase-change materials

Stabilna temperatura tekočine je pomembna na mnogih tehničnih področjih uporabe, shranjevanje toplote pa je ena od poti za zmanjšanje nihanja temperature. Za ta namen je mogoče uporabiti občutljive materiale in materiale za shranjevanje latentne toplote. Izvršena je bila teoretična študija, ki je obsegala numerično simulacijo, z namenom preučitve vedenja občutljivih materialov in materialov za shranjevanje latentne toplote za zmanjšanje nihanja temperature tekočine. Preučevan primer je bil okrogel kanal, skozi katerega je tekla tekočina, obdan z materialom za shranjevanje toplote. V študiji sta bila obravnavana dva občutljiva materiala za shranjevanje toplote (baker in beton) in dva materiala za shranjevanje toplote (n-oktadekan ter kalcijev klorid heksahidrat). V vseh preučevanih primerih je bila tekočina voda. Glavni namen študije je bil ugotoviti toplotni odgovor v enakih razmerah za vsako varianto.

Ključne besede: stabilnost temperature, shranjevanje toplote, materiali s faznimi premenami

1 INTRODUCTION

A constant fluid temperature plays an important role in many applications from laboratory experiments to the extracorporeal blood circulation. Some deviations from the desired fluid temperature can occur due to a number of reasons such as an imperfect temperature control or a fluctuating heat load. Temperature fluctuations can be either stochastic or they can follow a certain pattern (e.g., depending on the dead band of a temperature controller). Thermal storage with both sensible- and latent-heat storage materials can be employed to attenuate fluid-temperature fluctuations. The behavior of a sensible-heat storage used for this purpose is rather independent of the fluid temperature (the same material can be used to attenuate the fluid-temperature fluctuations at various temperatures). Another advantage of sensible-heat storage is a rather good thermal conductivity of many sensible-heat storage materials, metals in particular. Latent-heat storage materials (phase-change materials – PCMs) provide a high thermal-storage capacity in a narrow temperature interval around the phase-change temperature. If a PCM is used for attenuating fluid-temperature fluctuations, it needs to be chosen with regard to the fluid temperature in order to make use of that high thermal capacity (a fluid temperature needs to fluctuate within the melting range of a material). A schematic presentation of an application of heat storage for attenuating fluid-temperature fluctuations is shown in **Figure 1**. There are harmonic oscillations of the fluid temperature at the inlet of the attenuator because that was the case in the numerical investigations presented in this paper.

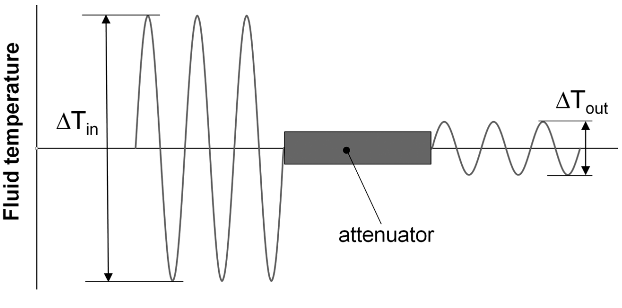

Figure 1: Attenuation of the fluid-temperature fluctuation
Slika 1: Zadrževanje nihanja temperature tekočine

Some studies into the attenuation of temperature gradients or temperature instabilities have been published in the last decade. Lawton et al.[1] reported theoretical analyses and experimental observations of the thermal performance of direct-contact packed-bed thermal-gradient attenuators. The packed bed in this case was a cylindrical canister filled with spheres. The authors presented the attenuator transfer functions for various parameters such as the diameter of the canister, the diameter of the spheres, the number of the spheres and the fluid-flow rate. The attenuator in the form of a 100 mm diameter plastic canister containing 10000 steel spheres with the diameter of 6.4 mm reduced the harmonic variations of the water temperature with the peak-to-peak amplitude of 150 mK at the input to the variations of just 0.6 mK at the output. Alawadhi[2] presented a numerical study evaluating the thermal performance of a fluid-temperature regulation unit. The unit was a two-dimensional channel with a phase-change material on each side. The author numerically investigated the thermal characteristics of the unit for a step function change and a periodic change of the inlet temperature.

2 PROBLEM DESCRIPTION

The idea behind the use of thermal storage for attenuating fluid-temperature fluctuations is the increase in the thermal inertia of the system. A thermal-storage material, in this case, behaves as both the heat sink and the heat source. When the fluid temperature is higher than the temperature of the heat-storage material, the heat flows from the fluid to the thermal-storage material. Similarly, when the fluid temperature is lower than that of the heat-storage material, the heat flows in the opposite direction. Since the overall thermal-storage capacity of such a thermal mass is limited, there are some constraints for the attenuation characteristics of this approach in terms of the amplitudes and frequencies of the temperature fluctuations. **Figure 2** shows one period of the square-wave, sine-wave and triangle-wave temperature changes with the same amplitude and the same frequency. If the temperature of the fluid at the inlet of the attenuator followed one of the waveforms, the heat would flow from the fluid to the thermal-storage material during the first half of the period and it would flow from the heat storage material to the fluid during the second half of the period. The mean value of the heat flux for the whole period (or any number of periods) would be zero and the mean fluid temperatures at the inlet and the outlet of the attenuator would be the same. The amplitude of the fluid-temperature fluctuations at the outlet of the attenuator depends on many parameters, mostly related to heat transfer – the attenuator is a kind of a heat exchanger in this case. If the attenuator only contains sensible-heat storage material, its attenuation characteristic will be almost independent of the mean fluid temperature at the inlet since the thermophysical properties such as the thermal conductivity and heat capacity do not significantly change with the temperature (in the range of ± 20 K). The situation changes considerably when latent-heat storage is used. PCMs provide a large thermal-storage capacity in their melting ranges but their thermal-storage capacity is much smaller outside the melting range. This paper reports on the numerical investigations of a thermal response of an attenuator of fluid-temperature fluctuations containing sensible- and latent-heat storage materials under various conditions.

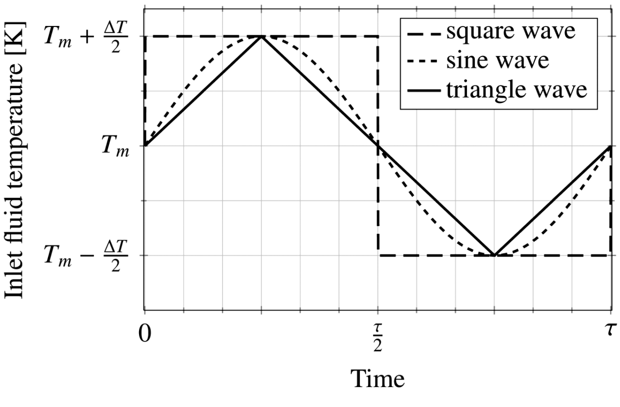

Figure 2: Inlet temperature oscillations (waveforms)
Slika 2: Spreminjanje vstopne temperature (v obliki valov)

3 CASE STUDY

The studied attenuator of the fluid-temperature fluctuation was a circular tube, through which the fluid flowed, surrounded by a thermal-storage material. Water was the fluid in all the studied cases. Two sensible-heat storage materials and two latent-heat storage materials were considered in the study. The schematic view of the attenuator is in **Figure 3**. The main goal of the investigations was to assess the thermal response of each variant under the same conditions. For this reason the same dimensions of the attenuator as well as the same water flow rate were considered in all the studied cases. The length of the attenuator was 10 m. In practice, an attenuator can be built of shorter modules arranged in the meander-flow fashion. The internal diameter of the tube was 25 mm and the thickness of the annular layer of the heat-storage material surrounding the tube was 25 mm (the volume of the heat-storage material was about 60 L). A suitable geometry of the attenuator for specific conditions can be obtained through a multi-parameter

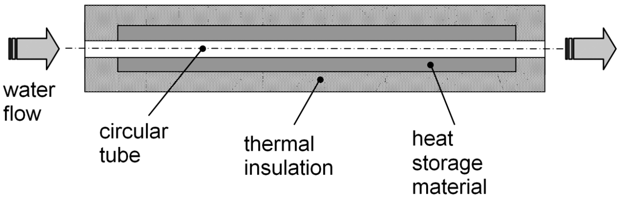

Figure 3: Thermal-storage attenuator
Slika 3: Zadrževalnik za shranjevanje toplote

optimization.[3] The thermal insulation on the external side of the heat-storage material was replaced with an adiabatic boundary condition in the numerical model. This simplification was justified with a rather small difference between the fluid temperature and the ambient air temperature.

A number of papers dealing with thermal-storage materials, techniques and related phenomena have been published in the last couple of years.[4–6] There is a variety of both sensible- and latent-heat storage materials that can be used in the devices for attenuating fluid-temperature fluctuations. Copper was chosen as one of the sensible-heat storage materials in this numerical study because of its very good thermal conductivity. The other sensible-heat storage material was concrete. Concrete is a very common and inexpensive material that can be used for many purposes. The alkanes (paraffins) with the formula C_nH_{n+2} are probably the most common category of organic phase-change materials. The melting temperature of an alkane depends on the number of carbon atoms. That makes alkanes usable in many thermal-storage applications (both in heat and cold storage). For example, nonane (C_9H_{20}) has a melting temperature of –53 °C, while dotetracontane ($C_{42}H_{86}$) has a melting temperature of 86 °C. N-octadecane ($C_{18}H_{38}$) that has a rather high latent heat of fusion was chosen to represent organic PCMs in this study. As for the inorganic PCMs, calcium chloride hexahydrate ($CaCl_2 \cdot 6H_2O$) was selected as it is one of the most common salts that can be used as a PCM. Tyagi and Buddhi[7] carried out a thermal cycle test of calcium chloride hexahydrate with the aim to assess the stability of its thermophysical properties with a number of melting cycles. They found a little change in the properties even after 1000 melting-solidification cycles. The stability of its thermophysical properties was another reason for including $CaCl_2 \cdot 6H_2O$ in the numerical study of the fluid-temperature attenuation. Some of the properties of the heat-storage materials chosen for this study are in **Table 1**. It should be pointed out that the thermophysical properties of the considered materials (especially of the PCMs) vary in various literature sources.

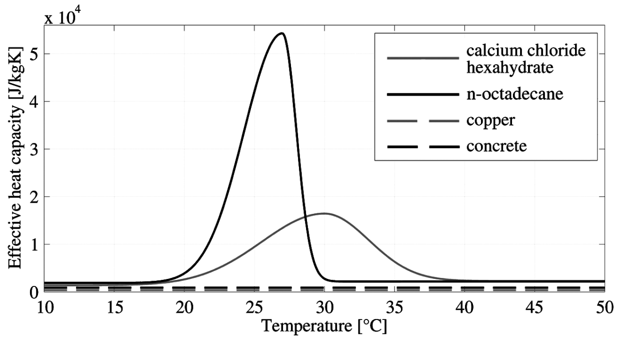

Figure 4: Effective-heat capacities
Slika 4: Efektivna toplotna kapaciteta

Table 1: Material properties
Tabela 1: Lastnosti materiala

	copper	concrete	n-octadecane	calcium chloride hexahydrate
ρ/(kg/m^3)	8940	2200	780	1400
c/(kJ/(kg K))	0.385	0.88	2.89	1.4 (s) 2.1 (l)
k/(W/(m K))	401	1.4	0.16	1
Latent heat (kJ kg^{-1})	n. a.	n. a.	244	140

4 NUMERICAL MODEL

The numerical model of the attenuator was created in MATLAB with using the control-volume method. The model consisted of two parts (sub-models). The first sub-model addressed the fluid flow in the tube and the convective heat transfer associated with it. The second sub-model dealt with the heat transfer inside the heat-storage material. The governing equation for the heat and mass transfers in the fluid flow expressed in the cylindrical coordinate system has the following form:

$$\frac{1}{r}\frac{\partial}{\partial r}\left(k_{\mathrm{f}}\, r\frac{\partial T}{\partial r}\right)+\frac{1}{r^2}\frac{\partial}{\partial \varphi}\left(k_{\mathrm{f}}\, r\frac{\partial T}{\partial r}\right)+\frac{\partial}{\partial z}\left(k_{\mathrm{f}}\, r\frac{\partial T}{\partial z}\right)+ \\ +w\rho_{\mathrm{f}}\, c_{\mathrm{f}}\,\frac{\partial T}{\partial t}=\rho_{\mathrm{f}}\, c_{\mathrm{f}}\,\frac{\partial T}{\partial t} \qquad (1)$$

where r, φ and z are the coordinates, w/(m/s) is the fluid velocity, ρ_{f}/(kg/m^3) is the fluid density and c_{f}/(J/(kg K)) is the fluid thermal capacity. The governing equation for the heat transfer in the heat-storage material is rather similar:

$$\frac{1}{r}\frac{\partial}{\partial r}\left(kr\frac{\partial T}{\partial r}\right)+\frac{1}{r^2}\frac{\partial}{\partial \varphi}\left(kr\frac{\partial T}{\partial r}\right)+\frac{\partial}{\partial z}\left(kr\frac{\partial T}{\partial z}\right)=\rho c_{\mathrm{eff}}\,\frac{\partial T}{\partial t} \qquad (2)$$

Considering the rotational symmetry of the attenuator, the studied problem is reduced to a 2D model with only the radial r and longitudinal z coordinates. The circumferential coordinate φ is not taken into account assuming that the heat flux in the circumferential coordinate equals zero. As can be seen in equation (2) an effective heat-capacity method[8] was adopted to address the phase change of the latent-heat storage materials. The effective heat capacities of the four materials involved in the numerical study are shown in **Figure 4**.

The value of the heat-transfer coefficient for the convective heat transfer between the fluid and the inner surface of the tube was determined according to the convective heat-transfer correlations:[9]

$$Nu=\frac{\frac{Nu}{\mathrm{Re}}(\mathrm{Re}-1000)\,\mathrm{Pr}^{2/3}}{1+12.7\left(\frac{Nu}{\mathrm{Re}\,\mathrm{Pr}^{1/3}}\right)^{1/2}(\mathrm{Pr}^{2/3}-1)} \qquad (3)$$

The correlation expressed with equation (3) is valid for the Reynolds number in the range of $3000 < Re < 5 \times 10^5$

and for the Prandtl number in the range of $0.5 < Pr < 2000$. Both conditions were satisfied for the investigated conditions. Heat-transfer coefficient h was then obtained from the definition of the Nusselt number:

$$Nu = h(D/k_f) \qquad (4)$$

where D/m is the diameter of the tube and k_f/(W/(m K)) is the thermal conductivity of the fluid. The value of the heat-transfer coefficient was h = 1000 W/(m^2 K) in the investigated cases.

5 RESULTS AND DISCUSSION

All the numerical simulations were carried out for the water-mass flow rate of 0.1 kg/s (360 kg/h) and the harmonic oscillations of the inlet water temperature (the sine wave). As can be seen in **Figure 2**, the waveforms differ in the amount of heat carried in the temperature fluctuations. This amount of heat is proportional to the area of the wave. For the same frequency (period) and amplitude of the waves, it is the largest for the square wave and the smallest for the triangle wave.

The first set of numerical experiments addressed the peak-to-peak amplitudes. Two peak-to-peak amplitudes of the water temperature variations at the inlet of the attenuator, ΔT_{in} = 10 K and ΔT_{in} = 2 K, were investigated. The wave period was 60 s. The mean value of the water temperature at the inlet of the attenuator was 30 °C in the case of copper, concrete and calcium chloride hexahydrate. The mean value of the inlet water temperature in the case of n-octadecane was 27 °C. The mean values of the inlet water temperature for the PCMs were chosen at the peaks of their effective heat capacities (**Figure 4**). Additional cases with the mean value of the water inlet temperature of 10 °C were investigated. At this temperature both PCMs are in the solid state, behaving as sensible-heat storage materials. The results of the simulations are shown in **Table 2**.

Table 2: Simulation results
Tabela 2: Rezultati simulacije

	copper	concrete	octadecane	calcium chloride hexahydrate
inlet peak-to-peak temperature amplitude	outlet peak-to-peak temperature amplitude ΔT_{out} /K			
ΔT_{in} = 10 K	1.167	3.153	0.187	0.231
ΔT_{in} = 2 K	0.231	0.627	0.039	0.044
ΔT_{in} = 10 K (solid PCMs)	n. a.	n. a.	2.569	1.563
ΔT_{in} = 2 K (solid PCMs)	n. a.	n. a.	0.510	0.309

Consequently, the influence of the temperature-change frequency (period) was numerically investigated. Simulations were done for the inlet peak-to-peak temperature amplitude of 10 K. As can be seen in **Figure 5**, the attenuation improves with the increasing frequency (shorter periods). With the shortening period of the wave less heat needs to be exchanged between the fluid and the heat-storage material and, as a result, the outlet temperature amplitude decreases.

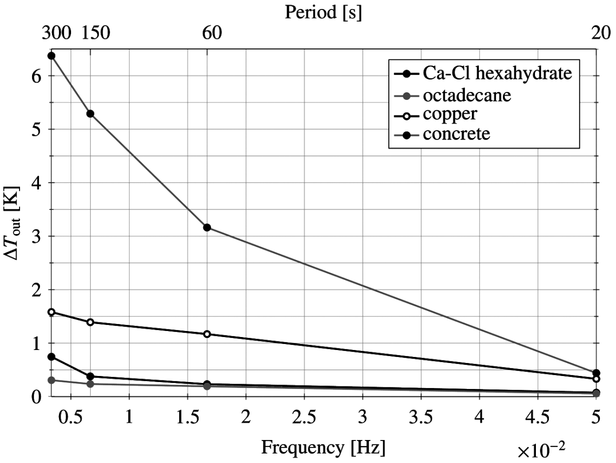

Figure 5: Influence of the wave frequency (period)
Slika 5: Vpliv frekvence vala (dolžina trajanja)

The last set of numerical investigations focused on the offset of the sine wave – the differential between the mean inlet fluid temperature and the peak of the effective heat capacity of the PCMs. Since the effective-capacity curves of the PCMs are not symmetrical, both positive and negative offsets were investigated. The results of this scenario are presented in **Figure 6**. The peak-to-peak amplitude was 10 K in this case and the period of the sine wave was 60 s. The sensible-heat storage materials (copper and concrete) have the same specific heat in the investigated temperature interval; therefore, the value of the mean inlet fluid temperature had no effect on the attenuation characteristic.

The results of all the studied cases show that the attenuation effect was the strongest in the case of n-octadecane when the inlet water temperature oscillated around the peak of its effective capacity. The attenuation effect

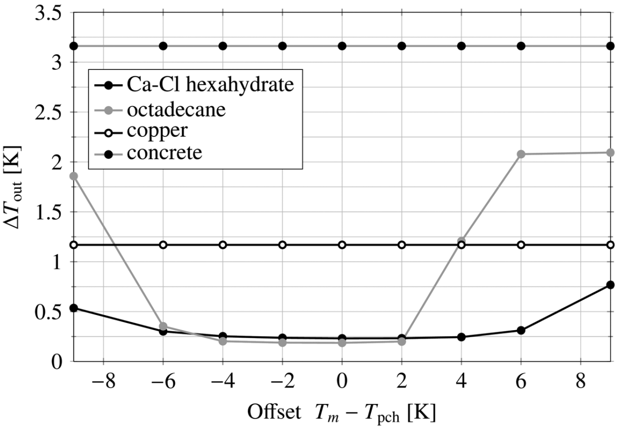

Figure 6: Influence of an offset
Slika 6: Vpliv odmika

of n-octadecane decreased with the increasing offset of the sine-wave temperature fluctuations. The same applies to calcium chloride hexahydrate. For large offsets, when the mean inlet temperature gets outside the PCM melting range, the PCM starts to behave as a sensible-heat storage material. Copper had a stronger attenuation effect on the fluid-temperature oscillations than the PCMs in the solid or liquid state.

6 CONCLUSION

The numerical investigations of the attenuation of water temperature fluctuations by means of a heat-storage-based attenuator were carried out. A numerical model of the attenuator created in MATLAB using the control-volume method was employed in the investigations. Two sensible-heat storage materials (copper and concrete) and two latent-heat storage materials (n-octadecane and calcium chloride hexahydrate) were considered in this study. The results showed that the effective heat capacity of a thermal-storage material played a more important role than its thermal conductivity in the studied scenarios. The latent-heat storage materials (PCMs) were more effective in dampening the water temperature oscillations than the sensible-heat storage materials when the water temperature oscillated around the peak values of their effective heat capacities (the water temperature oscillating in the melting range of the PCMs). The attenuation properties of the PCMs decreased very significantly when the PCMs were only in the solid or liquid state.

Acknowledgement

The research leading to the presented results was supported by the Czech Science Foundation under the contract number P101/11/1047 and by the BUT junior project FSI-J-13-1977 for young researchers. The authors also gratefully acknowledge the financial support from the project ED0002/01/01 NETME Centre and NETME CENTRE PLUS (LO1202).

7 REFERENCES

[1] K. M. Lawton, S. R. Patterson, R. G. Keanini, Direct contact packed bed thermal gradient attenuators: Theoretical analysis and experimental observations, Review of Scientific Instruments, 74 (**2003**) 5, 2886–2893

[2] E. M. Alawadhi, Temperature regulator unit for fluid flow in a channel using phase change material, Applied Thermal Engineering, 25 (**2005**) 2–3, 435–449

[3] L. Klimes, P. Charvat, Heuristic optimization of fluid temperature attenuator design with phase change material, Proceedings of International conference on soft computing MENDEL 2012, Brno, 2012, 338–343

[4] E. Oró, A. de Gracia, A. Castell, M. M. Farid, L. F. Cabeza, Review on phase change materials (PCMs) for cold thermal energy storage applications, Applied Energy, 99 (**2012**), 513–533

[5] M. Delgado, A. Lázaro, J. Mazo, B. Zalba, Review on phase change material emulsions and microencapsulated phase change material slurries: Materials, heat transfer studies and applications, Renewable and Sustainable Energy Reviews, 16 (**2012**), 253–273

[6] H. Shmueli, G. Ziskind, R. Letan, Melting in a vertical cylindrical tube: Numerical investigation and comparison with experiments, International Journal of Heat and Mass Transfer, 53 (**2010**) 19-20, 4082–4091

[7] V. V. Tyagi, D. Buddhi, Thermal cycle testing of calcium chloride hexahydrate as a possible PCM for latent heat storage, Solar Energy Materials & Solar Cells, 92 (**2008**), 891–899

[8] L. Klimes, P. Charvat, M. Ostry, Challenges in the computer modeling of phase change materials, Mater. Tehnol., 46 (**2012**) 4, 335–338

[9] F. P. Incropera, D. P. DeWitt, T. L. Bergman, A. S. Lavine, Fundamentals of Heat and Mass Transfer, Sixth edition, John Wiley and Sons, 2006, 1024 p.

UDK 678.7:66.017
Professional article/Strokovni članek

ISSN 1580-2949
MTAEC9, 48(3)429(2014)

CHARACTERIZATION OF A POLYMER-MATRIX COMPOSITE SUPPORT BEAM

KARAKTERIZACIJA KOMPOZITNEGA NOSILCA S POLIMERNO OSNOVO

Neva Štrekelj, Matevž Maren, Iztok Naglič, Andrej Demšar, Evgen Dervarič, Boštjan Markoli

Faculty of Natural Sciences and Engineering, University of Ljubljana, Aškerčeva 12, 1000 Ljubljana, Slovenia
neva.strekelj@omm.ntf.uni-lj.si

Prejem rokopisa – received: 2012-12-06; sprejem za objavo – accepted for publication: 2013-08-27

This paper deals with the characterization of a polymer-matrix composite support beam designed for the automotive industry. The discussed composite polymer-matrix material was characterized using light microscopy (LM), scanning electron microscopy (SEM), energy-dispersive X-ray spectroscopy (EDS), Vickers hardness (HV) measurements and mechanical testing under tensile loads. Using these characterization methods the diameter, distribution and arrangement of the fibres in the composite material were determined. The type of fibres used in this composite material was also established from the chemical composition determined by EDS. The mechanical properties of the discussed composite material under a tensile load were determined on proportional, sub-sized, tensile specimens prepared from the support beam.

Keywords: polymer-matrix composite, fibre, microstructure, tensile properties

Članek obravnava preiskavo kompozitnega nosilca na polimerni osnovi, namenjenega avtomobilski industriji. V ta namen so bile opravljene analize z metodami svetlobne mikroskopije (SM), vrstične elektronske mikroskopije (SEM), energijsko disperzijske spektroskopije (EDS), merjenja trdote po Vickersu (HV) in nateznega preizkusa. Omenjene metode so omogočile ugotavljanje povprečnega premera vlaken, površinskega deleža ter porazdelitve vlaken v kompozitu. Vrsta vlaken v kompozitu je bila ugotovljena s kemijsko sestavo po metodi EDS. Mehanske lastnosti so bile opredeljene na proporcionalnih pomanjšanih nateznih preizkušancih kompozitnega nosilca.

Ključne besede: kompozit s polimerno osnovo, vlakno, mikrostruktura, mehanske lastnosti

1 INTRODUCTION

The use of composite materials in automotive components and parts continues to grow, because the structural weight is becoming increasingly important in automotive vehicles.[1,2] A composite material is a macroscopic (nowadays also microscopic or nanoscopic) combination of two or more distinct materials, having a recognizable interface between them. Composites are used for their structural, electrical, thermal, etc. properties. Modern composite materials are usually optimized to achieve a particular balance of properties for a given range of applications.[3]

In general, the composites consist of a matrix and a reinforcement. To a large extent the matrix gives the shape and monolithic property to the composite. It ensures an even distribution of the reinforcement, it provides a suitable composite loading capacity by transferring the loads to the reinforcement (fibres), which is the main bearing element.[4,5]

Composites are commonly classified at two distinct levels. The first level of classification is usually made with respect to the matrix constituent. The major composite classes include organic-matrix composites (OMCs, which include polymer-matrix composites (PMCs) and carbon-matrix composites), metal-matrix composites (MMCs), and ceramic-matrix composites (CMCs). The second level of classification refers to the reinforcement form – particulate reinforcements, whisker reinforcements, continuous-fiber laminated composites and woven composites (braided and knitted fiber architectures are included in this category.[3,4] This kind of composite (with continuous fibres) represents the most important and common type of composites that have the potential to be used in the automotive industry, too. They are characterized by a high strength and stiffness at a very low density.[3]

The main objective of this work was to characterize the composition and the properties of a polymer-matrix composite part (support beam) designed for the automotive industry.

2 EXPERIMENTAL

A polymer-matrix composite support beam was manufactured using supplied fiberglass mats, which were placed into the mould and then impregnated with the resin (polycarbonate – PC).[2]

This step was followed by an air evacuation process in order to remove any residual air bubbles. Then the composite was placed in a furnace where the polymerization reactions took place above the glass-transition temperature (above 150 °C).[2] In this way the support beam permanently retains the shape of the mould.

The samples for the metallographic analyses and the hardness measurements were cut from the composite part presented in **Figure 1** in such a way that the fibres were either perpendicular or parallel to the surface of the observation. Samples cut from the part were mounted in a polymeric material, ground and polished. Light micro-

Figure 1: Composite support beam
Slika 1: Kompozitni nosilec

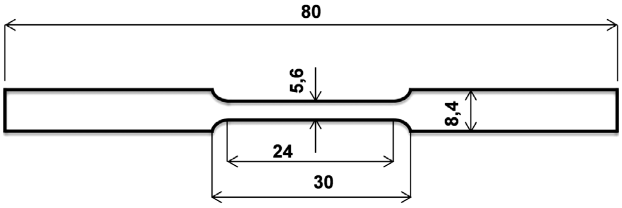

Figure 2: Dimensions of the test specimen used in the tensile test[5]
Slika 2: Dimenzije preizkušanca za natezni preizkus[5]

scopy (LM) was performed using an Axio Imager.A1m ZEISS.

LM was used for the microstructure observation and determining the average diameter of the fibres. The Vickers hardness (HV) was performed using a Shimadzu Microhardness Tester with a mass of 25 g and loading times of 10 s. This rather small load was chosen due to the small diameter of the fibres.

Scanning electron microscopy (SEM) and energy-dispersive X-ray spectroscopy (EDS) were performed with a JEOL JSM-5610. The samples for scanning electron microscopy were additionally coated with carbon due to the fact that the composite material is nonconductive.

Tensile tests were also executed to determine the tensile mechanical properties of the composite part.[6] Sub-sized test specimens were used as presented in **Figure 2** due to the dimensions of the composite part.[7] The test specimens were cut in such a way that the fibres were either perpendicular or parallel to the tensile load. An INSTRON 5567 was employed to perform tensile tests and determine the tensile strength, the elongation and the modulus of elasticity.

3 RESULTS AND DISCUSSION

3.1 Microstructure

The microstructure of the composites' main wall cross-section with a thickness of 3 mm showed that the fibre bundles were arranged almost perpendicular to each other and intertwined (plain weave, yarn interlacing), as presented in **Figure 3**. A single bundle consists of several thousands of individual fibres and has dimensions of approximately 3 mm (parallel to the fibres) and 0.3 mm to 0.5 mm (perpendicular to fibres). The intersection of the main wall contains approximately six layers of intertwined bundles.

The average diameter of the fibres in a single bundle was also estimated and the results of individual measurements of the fibres' diameters are compiled in **Table 1**. The average diameter of the fibres was found to be 18.5 µm.

Table 1: Average fibre diameter measurement (**Figure 4**)
Tabela 1: Povprečne vrednosti meritev premera vlaken (**slika 4**)

Measurement no.	Diameter (µm)
1	17.7
2	15.5
3	15.7
4	18.9
5	20.8
6	19.8
7	21.4
Average Value	18.5

The average surface fraction of the fibres in the bundle was also assessed from the backscattered electron image presented in **Figure 4**. These were then reformatted in binary images and processed using ZEISS (AXIO Imager.A1m) software for an assessment of the phase amount. As presented in **Table 2**, the average surface fraction of the fibres in a single bundle was around 65.7 %.

3.2 Hardness

The relation between the hardness and the number of fibres examined in **Figure 5** summarizes the results of the hardness measurements using the Vickers method. The average hardness of the fibres was around 537 HV and that of matrix, 20 HV. The hardness values of the fibres ranged between 513 and 572 HV, whereas for the matrix these values were between 19.3 HV and 21.9 HV.

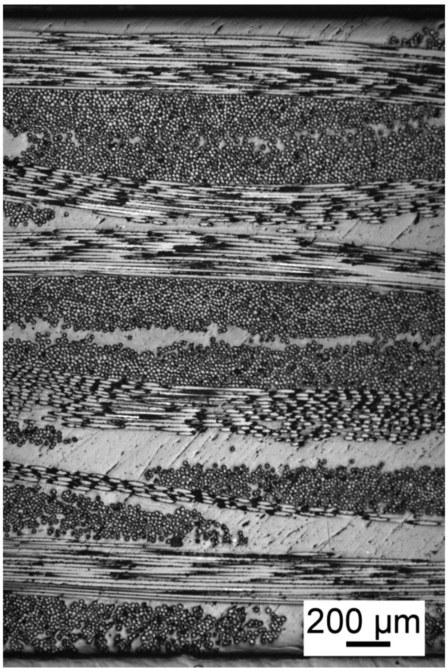

Figure 3: LM image of composite part's cross-section
Slika 3: SM-posnetek prereza dela kompozita

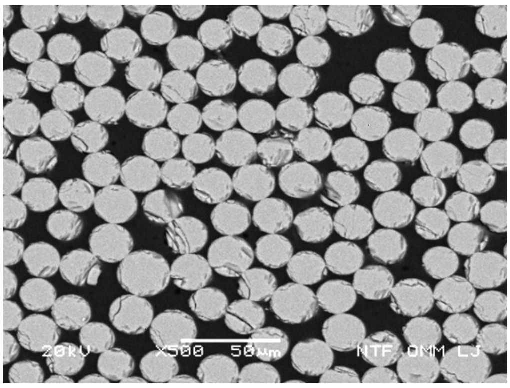

Figure 4: BSE (backscattered electron image) of composite part for estimation of fibre fraction in a single bundle
Slika 4: BSE-posnetek (povratno sipani elektroni) kompozita, namenjenega za ugotavljanje deleža vlaken v posameznem snopu

Table 2: Average surface fraction of the fibres in a single bundle (**Figure 4**)
Tabela 2: Povprečni površinski delež vlaken v posameznem snopu (**slika 4**)

Sample no.	Fibres fraction (%)
1	66.5
2	66.8
3	63.1
4	67.4
5	64.8
Average value	65.7

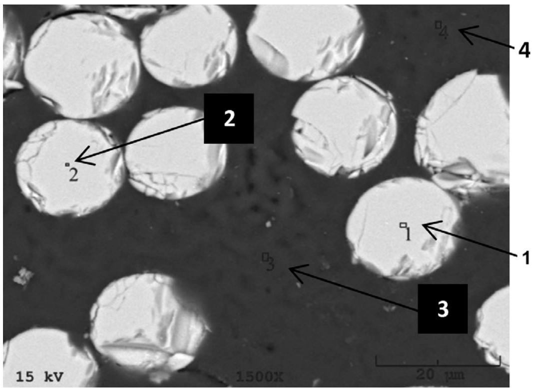

Figure 6: BSE (backscattered electron image) of micro-analysed fibres (points 1 and 2) and matrix (points 3 and 4)
Slika 6: BSE-posnetek (povratno sipani elektroni) analiziranih vlaken (točki 1 in 2) in osnove (točki 3 in 4)

Table 3: Chemical analyses of the fibres presented in **Figure 6**, mole fractions, *x*/%
Tabela 3: Kemijska analiza vlaken, prikazanih na **sliki 6**, molski deleži, *x*/%

	1	2
O	15.86	15.12
Na	0.26	0.33
Mg	1.70	1.85
Al	10.85	11.02
Si	46.01	46.23
K	0.42	0.46
Ca	24.90	25.00

3.3 Chemical composition of fibres

The chemical composition of the fibres was determined using EDS analyses, as presented in **Figure 6** and **Table 3**. Both analyses showed very similar fibre compositions. It was found that silicon, calcium, oxygen, aluminium, magnesium, potassium and sodium are present for both cases of the analysed fibres. The oxygen content was not determined quantitatively (only qualitatively), and due to this fact it was assumed that these elements form oxides such as SiO_2, CaO, Al_2O_3, MgO, K_2O and Na_2O.[3,8,9] According to this assumption a new composition was calculated, as presented in **Tables 4** and **5**.

Based on the results presented in **Tables 4** and **5** the average fraction of the oxides in the fibres was estimated to be in mass fractions 57.4 % SiO_2, 28.9 % CaO, 11.6 % Al_2O_3, 1.5 % MgO, 0.4 % K_2O and 0.2 % Na_2O. It is known that some glasses also contain boron[3]. The EDS detector used in this study was not able to detect boron and consequently this analysis could not evaluate the presence of boron. A comparison of these data with the literature[3] shows that the composition of the fibres was similar to the compositions in the literature designated as E-glass fibres for general purpose.

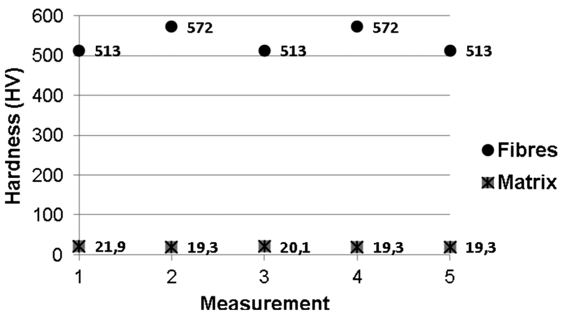

Figure 5: Hardness measurements
Slika 5: Izmerjene trdote

3.4 Tensile test

Tensile test results are presented in **Figure 7** as diagrams of load versus elongation. The backscattered

Table 4: Calculated oxide contents in fibre 1 (**Figure 6**, point 1)
Tabela 4: Izračunane vsebnosti oksidov v vlaknu 1 (**slika 6**, točka 1)

Element	Element content (*x*/%)	Oxides	Oxide content (*w*/%)
Si	46.01	SiO_2	57.5
Ca	24.90	CaO	29.0
Al	10.85	Al_2O_3	11.5
Mg	1.70	MgO	1.4
K	0.42	K_2O	0.4
Na	0.26	Na_2O	0.2

Table 5: Calculated oxide contents in fibre 2 (**Figure 6**, point 2)
Tabela 5: Izračunane vsebnosti oksidov v vlaknu 2 (**slika 6**, točka 2)

Element	Element content (*x*/%)	Oxides	Oxide content (*w*/%)
Si	46.23	SiO_2	57.3
Ca	25.00	CaO	28.9
Al	11.02	Al_2O_3	11.6
Mg	1.85	MgO	1.5
K	0.46	K_2O	0.4
Na	0.33	Na_2O	0.2

electron images in **Figure 8** show fractured samples after a tensile test. The fracture of the fibres after the tensile test occurred in those fibres oriented parallel to the direction of the load. The fractured fibres show smooth surfaces, which is a characteristic of brittle fracture. In **Figure 8** the decohesion of the fibres can also be observed.

The tensile properties determined by the tensile tests are presented in **Table 6**. Both samples show similar properties. It was found that the average tensile strength of the composite material is 332 MPa, with an elongation of 3.5 % and a modulus of elasticity of 11.87 GPa.

The tensile strength of the investigated composite samples was around 332 MPa, which is about a tenth of the tensile strength of a typical E-glass fibre for general purposes.[3] The modulus of elasticity of the composite was between six and seven times lower than the modulus of elasticity for a typical E-glass fibre for general purposes.[3]

4 CONCLUSIONS

The characterization of a polymer matrix composite material revealed that the material consists of intertwined bundles of fibres arranged perpendicular to each other (plain weave, yarn interlacing). Each bundle consists of several thousands of fibres with the fraction of the fibres within the bundle being 65.7 %. The average diameter of the fibres was found to be 18.5 μm and the average hardness was 537 HV. The average composition of the fibres, determined by EDS analyses and calculations, was in mass fractions 57.4 % SiO_2, 28.9 % CaO, 11.6 % Al_2O_3, 1.5 % MgO, 0.4 % K_2O and 0.2 % Na_2O. This composition corresponds well to the composition of E-glass fibres for general purposes[3]. The presence of boron could not be confirmed or refuted.

The tensile tests of composite parts performed parallel or perpendicular to the direction of the fibres gave a tensile strength of 332 MPa, an elongation of 3.5 % and a modulus of elasticity of 11.87 GPa.

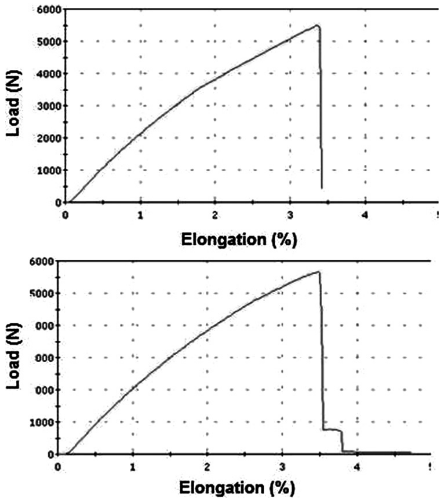

Figure7: Tensile load in dependence of elongation for two testing composite samples

Slika 7: Sila v odvisnosti od raztezka za dva preizkusna vzorca kompozita

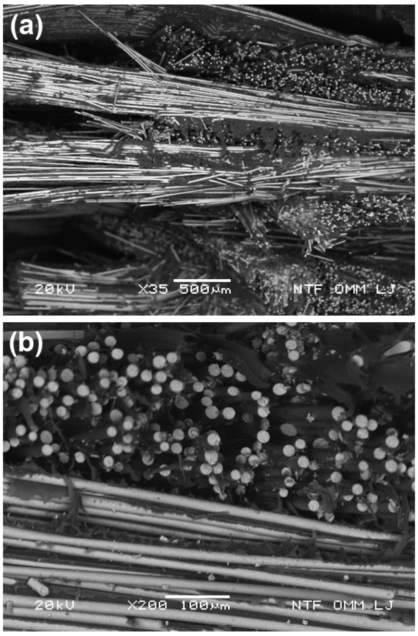

Figure 8: BSE (backscattered electron image) of composite sample after achieved tensile test

Slika 8: BSE-posnetek (povratno sipani elektroni) vzorca kompozita po izvedenem nateznem preizkusu

Table 6: Results of tensile test

Tabela 6: Rezultati nateznega preizkusa

	Maximal load (N)	Tensile strength (MPa)	Elongation (%)	Modulus of Elasticity (MPa)
Test 1	5494.7	327	3.4	11974
Test 2	5665.6	337	3.5	11768
Average value		332	3.5	11871

Acknowledgment

The authors would like to thank Mr. Tomaž Stergar for the tensile testing.

5 REFERENCES

[1] R. F. Gibson, Principles of composite material mechanics, 2nd ed., CRC Press, 2007

[2] U. Vaidya, Composites for Automotive, Truck and Mass Transit, DEStech Publications, Inc., 2010

[3] D. B. Miracle, S. L. Donaldson, ASM Handbook, Vol. 21, Composites, ASM International, 2001

[4] M. Maren, Characterization of the Composite Support Beam, Diploma work, Ljubljana, 2011 (in Slovene)

[5] W. D. Callister, Jr., D. G. Rethwisch, Fundamentals of Materials Science and Engineering, 3rd ed., John Wiley & Sons, Inc., 2008

[6] B. Kosec, L. Kosec, F. Kosel, M. Bizjak, Metall, 54 (**2000**), 186–188

[7] H. Kuhn, D. Medlin, ASM Handbook, Vol. 8, Mechanical Testing and Evaluation, ASM International, 2000

[8] J. K. Kim, Y. W. Mai, Engineered Interfaces in Fiber Reinforced Composites, 1st ed., Elsevier Science Ltd, 1998

[9] D. Hartman, M. E. Greenwood, D. M. Miller, High Strength Glass Fibers, Agy, LIT-2006-111, 2006

UDK 669.14.018.8:519.233.5
Professional article/Strokovni članek

ISSN 1580-2949
MTAEC9, 48(3)433(2014)

REGRESSION ANALYSIS OF THE INFLUENCE OF A CHEMICAL COMPOSITION ON THE MECHANICAL PROPERTIES OF THE STEEL NITRONIC 60

REGRESIJSKA ANALIZA VPLIVA KEMIJSKE SESTAVE NA MEHANSKE LASTNOSTI JEKLA NITRONIC 60

Almaida Gigović-Gekić, Mirsada Oruč, Hasan Avdušinović, Raza Sunulahpašić

University of Zenica, Faculty of Metallurgy and Materials Science, Zenica, Bosnia and Herzegovina
almaida.gigovic@famm.unze.ba

Prejem rokopisa – received: 2013-06-27; sprejem za objavo – accepted for publication: 2013-09-04

Nitronic 60 (UNS S21800) is a highly alloyed austenitic stainless steel with increased amounts of manganese and silicon that has good mechanical and corrosion properties. This paper presents the results of a regression analysis of the influence of the chemical composition, i.e., the alphagenic (Si and Cr) and gamagenic (Mn and Ni) elements on the tensile properties of the steel. The results of the analysis are the equations with which we can calculate the strength for a given chemical composition when a measurement is disabled. The regression analysis showed that the strength of the steel can be increased with an increased amount of alphagenic elements and that the influence of Mn on the strength depends on the Si amount.

Keywords: austenitic stainless steel Nitronic 60, alphagenic elements, gamagenic elements, tensile properties, regression analysis

Nitronic 60 (UNS S21800) je visoko legirano avstenitno nerjavno jeklo s povečano vsebnostjo mangana in silicija ter z dobrimi mehanskimi in korozijskimi lastnostmi. Ta članek predstavlja rezultate regresijske analize vpliva kemijske sestave, to je alfagenih (Si in Cr) in gamagenih (Mn in Ni) elementov na natezno trdnost jekel. Rezultati analiz so enačbe, s katerimi lahko izračunamo trdnost jekla iz dane kemijske sestave, če meritev ni mogoča. Regresijska analiza je pokazala, da se trdnost povišuje z naraščanjem vsebnosti alfagenih elementov in tudi, da je vpliv Mn na trdnost odvisen od vsebnosti Si.

Ključne besede: avstenitno nerjavno jeklo Nitronic 60, alfageni elementi, gamageni elementi, natezna trdnost, regresijska analiza

1 INTRODUCTION

Microstructure stability is the most important requirement for obtaining proper mechanical properties of an austenitic stainless steel (ASS).[1] The microstructure of Nitronic 60 is primarily monophasic, i.e., austenitic, but a precipitation of the delta ferrite (δ-ferrite) in an austenite matrix is possible, too. A higher volume fraction of the δ-ferrite in a microstructure can be achieved by changing the chemical composition. The main alloying elements in austenitic stainless steel can be classified as alphagenic and gamagenic elements. The alphagenic elements (Cr, Si, Ti, Al, Mo, V, Nb and W) stabilize and support the formation of δ-ferrite, while the gamagenic elements (Ni, Mn, C, N, and Cu) stabilize the austenitic phase.[2,3] The presence of δ-ferrite with a BCC crystalline structure slows down the grain growth and increases the strength properties of the steel because the interphase boundaries act as strong barriers to the dislocation motion.[4] This paper presents the testing results for the mechanical properties (the tensile and yield strengths) of the austenitic stainless steel Nitronic 60, and the regression analysis of the relationships between the chemical composition and mechanical properties of the steel Nitronic 60.

2 DESIGN OF THE EXPERIMENT

The plan of the experiment predicted a programming of the amounts of the basic alphagenic (Cr and Si) and gamagenic (Ni and Mn) elements in the experimental melts. The plan required that the amounts of the alloying elements in the experimental melts should have a range of values equal to ± 0.5 % for Ni, Mn, Si and ± 1.0 % for Cr in relation to the mean value of the chemical amount prescribed by standard A276. Another requirement is that the amounts of the other chemical elements (C, N, P and S) should be kept at approximately the same level, i.e., 0.05 % C, 0.15 % N, 0.06 % P and 0.03 % S. The number of melts (N) is determined with a fragmented dynamic planning model as $N = 2^{k-1}$ (the k-number of independent variables). The checking of the reproducibility of the results includes a randomization and a double repetition of each experimental melt. This means that the total number of the produced melts was 16. The chemical compositions of the produced melts are in accordance with the standard of ASTM A276-96, **Table 1**. After forging and rolling the melts into Ø 15 mm bars, the produced bars were heat treated at 1020 °C for 1 h and quenched in water to obtain austenitic microstructures. The testing of the tensile properties was carried out on the samples in the heat-treated state according to standards EN 10002-1/02 and EN 10002-5/01. The results of testing are given in **Table 1**.

3 ANALYSIS AND DISCUSSION OF THE EXPERIMENTAL RESULTS

3.1 Regression analysis

A multifactorial experiment was used for the analysis of the influence of alphagenic and gamagenic elements on the tensile properties. The MATLAB software (version 7) and its module Model-Based Calibration Toolbox was used for the regression analysis and graphical interpretation.[5] A second-order mathematical model, i.e., a square regression model was assumed. This approach enabled an analysis of not only the individual effects of the factors but also of their mutual, i.e., coupled effects.[6,7] On the basis of the testing and statistical data, the regression equations for R_m and $R_{p0.2}$ are as follows:

$$R_m/\text{MPa} = 3997.21 - 758.84x_1 - 962.44x_2 - 1759.93x_3 + 3020.52x_4 + 89.64x_1^2 - 16.02x_1x_2 + 92.26x_1x_3 - 35.87x_1x_4 + 30.45x_2^2 + 17.48x_2x_3 - 12.30x_2x_4 + 43.36x_3^2 + 49.55x_3x_4 - 181.30x_4^2 \quad (1)$$

$$R_{p0.2}/\text{MPa} = 3\,695.62 - 484.99x_1 - 280.03x_2 - 1225.70x_3 + 1011.87x_4 + 50.59x_1^2 - 17.83x_1x_2 + 113.22x_1x_3 - 48.53x_1x_4 + 14.90x_2^2 + 5.50x_2x_3 - 17.76x_2x_4 + 27.88x_3^2 + 28.19x_3x_4 - 44.07x_4^2 \quad (2)$$

Note: $x_1/\% = w(\text{Si})$; $x_2/\% = w(\text{Cr})$; $x_3/\% = w(\text{Mn})$; $x_4/\% = w(\text{Ni})$ (mass fractions: w)

The values of the tensile properties calculated with regression equations (1) and (2) have a very good match with the values obtained experimentally. **Table 1** shows the deviations of the tensile values (R_m and $R_{p0.2}$) obtained using the regression model (K_M) from the experimentally obtained values (K_E) according to the following equation:

$$Deviation = \frac{(K_M - K_E)}{K_E} \cdot 100(\%) \quad (3)$$

From **Table 1**, it can be seen that the deviations of the $R_{p0.2}$ values are slightly higher than the deviations of the R_m values. The maximum deviation of the $R_{p0.2}$ value is 2.5 %. The deviation of the R_m value does not exceed 0.6 %, which is the maximum deviation obtained for No. 5. In terms of mathematical precision, small deviation values indicate that the model is suitable. The statistical data confirming the adequacy of the model is given in **Table 2.**

3.2 Graphical interpretation of the results

The MATLAB software with module Model-Based Calibration Toolbox was also used for a graphical interpretation. Considering that a three-dimensional space can be represented with only two independent variables and their impact on the dependent variable, in this case, it is not possible to graphically present the impact of four independent variables on the dependent variable. The

Table 1: Chemical composition of steel Nitronic 60 and a review of the experimental and model-based values of the tensile properties with the corresponding deviations
Tabela 1: Kemijska sestava jekla Nitronic 60 in pregled eksperimentalnih ter modelnih vrednosti za natezno trdnost s pripadajočimi odmiki

Melt	Chemical composition, w/%				R_m/MPa		Deviation /%	$R_{p0.2}$/MPa		Deviation /%
	Si	Cr	Mn	Ni	K_E	K_M		K_E	K_M	
1	4.25	16	8.4	8.8	749	747.45	–0.21	385	381.5	–0.89
2	4.41	18	7.4	8.1	821	821.13	0.02	467	467.29	0.062
3	3.81	18	7	8	791	790.17	–0.10	463	461.20	–0.39
4	3.74	18	8.6	8	750	747.22	–0.37	400	393.98	–1.50
5	3.69	17.8	8.2	8	706	710.21	0.60	365	374.13	2.50
6	3.5	16.9	7.9	8.6	681	677.55	–0.51	331	323.52	–2.26
7	3.5	16.9	7.2	8.6	716	720.02	0.56	366	374.70	2.38
8	4.5	16	8.6	8	793	792.20	–0.10	442	440.27	–0.39
9	4.54	16	7.5	9	718	718.06	0.01	365	365.13	0.03
10	3.8	17.3	7.4	8.6	724	719.94	–0.56	387	378.22	–2.27
11	3.5	16.6	7.2	8	707	706.35	–0.09	357	355.59	–0.39
12	4.39	16.8	8	8.8	746	747.34	0.18	394	396.91	0.74
13	4.39	16	7.9	8	734	734.81	0.11	378	379.75	0.46
14	3.8	17	8.9	9	708	707.76	–0.03	356	355.49	–0.14
15	3.7	17.7	7.9	8.6	734	736.16	0.29	378	382.68	1.24
16	3.9	16	9	8.7	731	732.64	0.22	340	343.55	1.04

Table 2: Statistical data for the model
Tabela 2: Statistični podatki za model

Tensile property	Coefficient correlation R	R^2	Adjusted R square	Standard error	SS regression	SS residual
R_m	0.998	0.996	0.938	9.173	20262.79	84.143
$R_{p0.2}$	0.992	0.984	0.755	19.868	23785	394.753

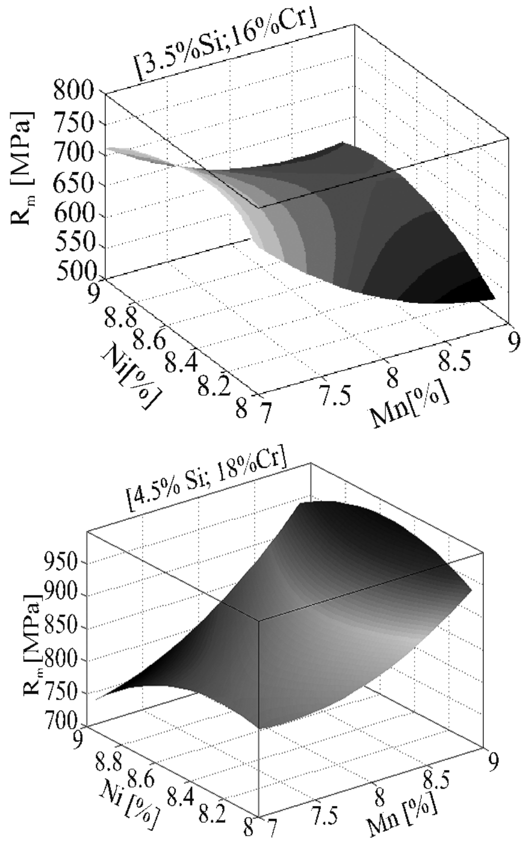

Figure 1: Functional dependence of R_m on the amounts of Mn and Ni
Slika 1: Funkcionalna odvisnost R_m od vsebnosti Mn in Ni

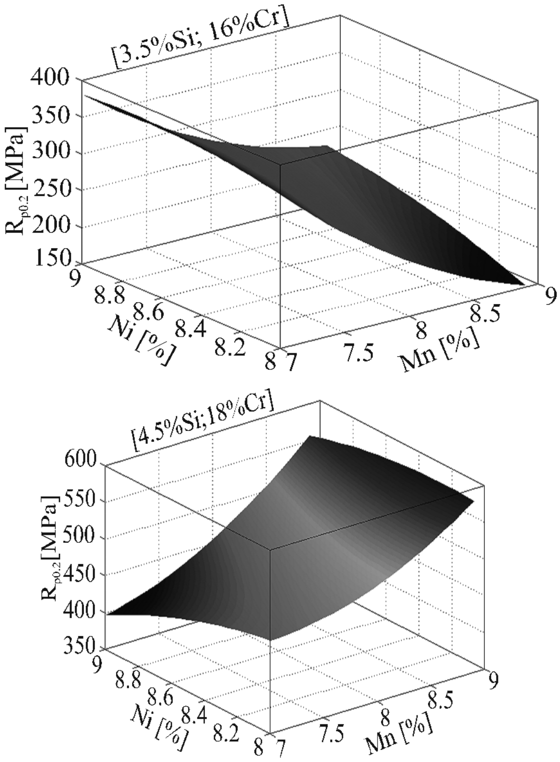

Figure 2: Functional dependence of $R_{p0.2}$ on the amounts of Mn and Ni
Slika 2: Funkcionalna odvisnost $R_{p0.2}$ od vsebnosti Mn in Ni

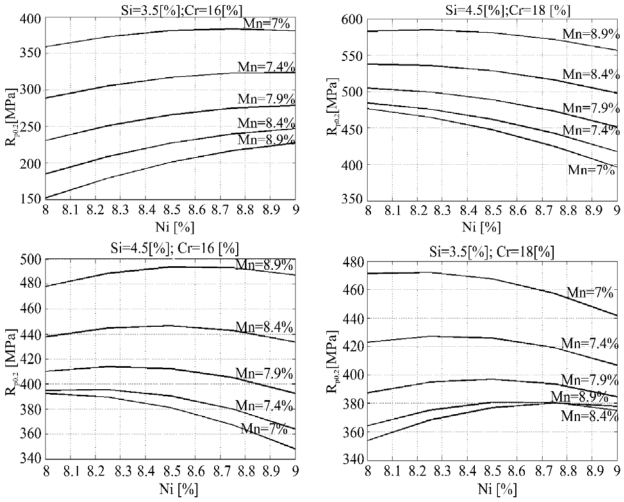

Figure 3: Interaction between alphagenic and gamagenic elements
Slika 3: Interakcije med alfagenimi in gamagenimi elementi

analysis of the results was based on the observation of the impact of alphagenic elements on the strength because of their tendency to form δ-ferrite that increases the strength. The studies have shown that the amount of δ-ferrite can be up to 10 % if the amount of alphagenic elements is maximum and the amount of gamagenic elements is minimum.[8] However, the δ-ferrite amount in

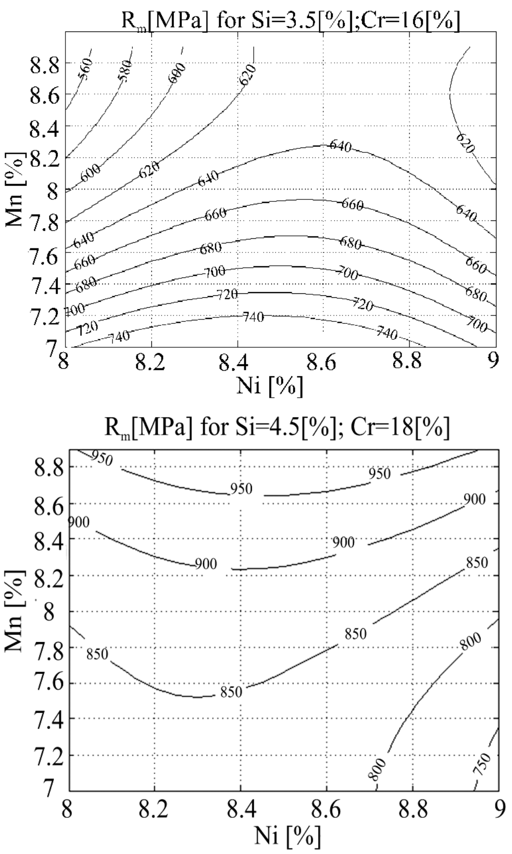

Figure 4: Graphical presentation of the tensile-strength curves according to equation (1)
Slika 4: Grafična predstavitev krivulj natezne trdnosti po enačbi (1)

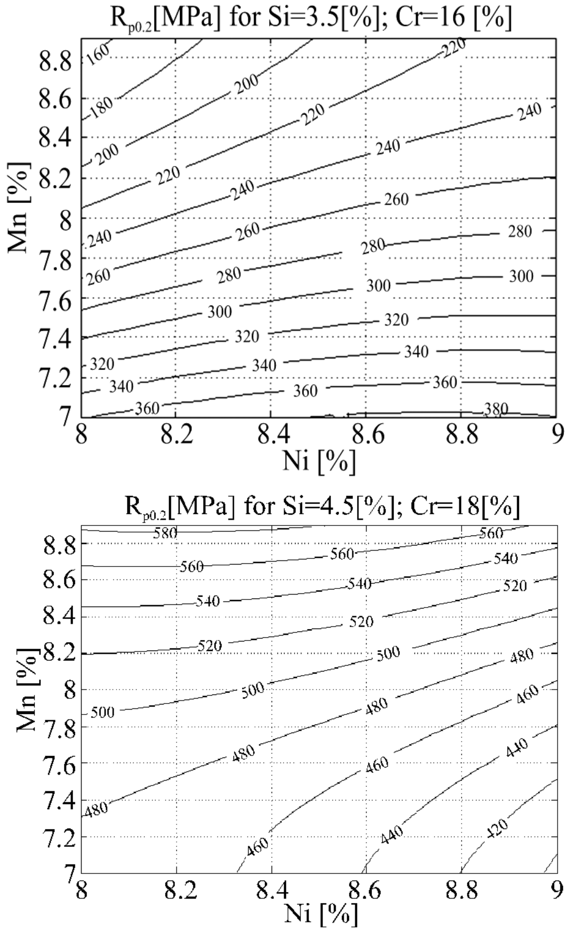

Figure 5: Graphical presentation of the tensile-strength curves according to equation (2)
Slika 5: Grafična predstavitev krivulj natezne trdnosti po enačbi (2)

this steel is limited to 2 %, which has to be taken into consideration. In the opposite case, δ-ferrite would have a negative influence on the ductile properties.[9] **Figures 1** and **2** show the influences of the minimum and maximum amounts of alphagenic elements on the strength of the steel Nitronic 60.

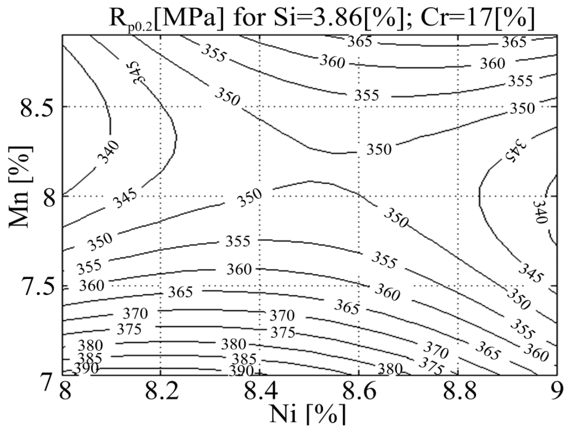

Figure 6: Graphical presentation of the tensile-strength curves according to equation (2)
Slika 6: Grafična predstavitev krivulj natezne trdnosti po enačbi (2)

The tensile properties of the steel Nitronic 60 increase with the increasing amount of alphagenic elements. However, the effect of Mn on the tensile properties changes with the increasing amount of alphagenic elements. At a lower amount of alphagenic elements, Mn decreases the tensile strength, but when their amount is increased, Mn increases the strength. Ni decreases the strength of the steel independently of the influence of alphagenic elements, especially when the amount is higher than 8.5 %. Observing the interaction between alphagenic and gamagenic elements, we can see that Si has a significant influence on the effect of Mn (**Figure 3**). The role of Mn changes with the increasing amount of Si. The effect of Cr is not so significant; only at the maximum values of Cr its interaction with Mn can be seen. **Figure 3** shows an interaction in the case of determining $R_{p0.2}$; however, the same interaction was observed in the case of determining R_m.

These surfaces (**Figures 1** and **2**), belonging to a three-dimensional space, can be easily represented and interpreted by designers and technologists in the steel industry. Especially, it is possible to use the curves presented in **Figures 4** and **5**. The curves are presented in the form of a graph resulting from the intersection of the surface (**Figures 1** and **2**) correlation with the parallel planes. In each plane there is a part of the plane of the intersection. Thanks to this graph, a designer or a technologist can easily determine an expected value of the strength for a given chemical composition without executing the calculation.

From **Figures 4** and **5**, it can be seen that for the minimum amounts of Cr and Si, the amount of Ni can range from its maximum to the minimum value, but the amount of Mn should be minimal in order to obtain the strength values prescribed by standard A276. The standard minimum value for R_m is 655 MPa and the minimum value for $R_{p0.2}$ is 345 MPa. In the case of the middle values for the amounts of Si and Cr, the amount of Ni should be in the range of 8.2 to 8.8 % in order to obtain the values of $R_{p0.2}$ prescribed by the standard (**Figure 6**). It was already mentioned that with the maximum amounts of Si and Cr, the strength values will be maximum.

4 CONCLUSIONS

The regression analysis allows us to find a connection between one or more independent variables and one dependent variable, if the latter exists. The equations linking the dependent variable with the independent variables were obtained with a regression analysis. These equations represent a mathematical model, called the regression function that can be obtained only by respecting certain limitations and assumptions.[10] Since the main problem of this paper is a quantification of the effect of alphagenic and gamagenic elements on the mechanical properties of the steel Nitronic 60, the regression analysis was used as a method for predicting these influences. The practical benefit of the regression analysis is the ability to evaluate the dependent variable in the case when its measurement is difficult. In this paper we examine the effect of a chemical composition on the mechanical properties using the regression analysis. On the basis of the analysis we can conclude the following:

- On the basis of the statistical data (correlation coefficients, standard errors and deviations), it can be concluded that the obtained mathematical model satisfies the set requirements.
- The deviations of the mathematical model compared to the experimental values for R_m are below 1 %, and for $R_{p0.2}$ the maximum deviation is 2.5 %.
- On the basis of the graphic presentation of the results it can concluded that with an increase in alphagenic elements (Si and Cr) the strength increases. Increasing the amounts of these elements increases the amount of δ-ferrite, which leads to an increase in the strength but reduces the ductility.[8,9]
- Gamagenic elements decrease the strength, especially at the minimum amount of alphagenic elements.
- With an increased amount of alphagenic elements (especially Si) the influence of Mn on the strength is changed, i.e., Mn increases the strength.
- The graphical model showed that in order to reduce the cost of production (especially for Ni, whose price changes on the market), it is possible to produce a melt with minimum amounts of all the elements and, at the same time, obtain the strength values prescribed in the standard. The minimum amount of alphagenic elements decreases the amount of δ-ferrite below 2 %.
- The maximum amount of alphagenic elements gives the maximum strength values.

5 REFERENCES

[1] J. Janovec, B. Šuštaršič, J. Medved, M. Jenko, Mater. Tehnol., 37 (**2003**) 6, 307–312

[2] Metals Handbook: Properties and Selection: Iron, Steels and High-Performance, 10th edition, Alloys, vol. 1, ASM American Society for Metals, 1990

[3] F. Tehovnik, F. Vodopivec, L. Kosec, M. Godec, Hot ductility of austenite stainless steel with a solidification structure, Mater. Tehnol., 40 (**2006**) 4, 129–137

[4] A. A. Astafev, L. I. Lepekhina, N. M. Batieva, Metal Science and Heat Treatment, 31 (**1989**) 12, 880–884

[5] R. H. Brian, L. L. Ronald, M. R. Jonathan, A Guide to MatLab, Cambridge University Press, 2006

[6] R. Sunulahpašić, M. Oruč, M. Hadžalić, M. Rimac, Mater. Tehnol., 46 (**2012**) 3, 263–267

[7] D. Montgomery, Design and analysis of experiments, John Wiley& Sons, Inc., New York 2001

[8] A. Gigović-Gekić, M. Oruč, M. Gojić, Determination of the content of delta ferrite in austenitic stainless steel Nitronic 60, 15th International Research/Expert Conference "TMT 2011", Prague, 2011

[9] A. Gigović-Gekić, M. Oruč, S. Muhamedagić, Mater. Tehnol., 46 (**2012**) 5, 519–523

[10] S. Ekinović, Metode Statističke analize u Microsoft Excelu, Mašinski fakultet u Zenici, Univerzitet u Zenici, Zenica, 2008

UDK 669.715:621.762
Professional article/Strokovni članek

ISSN 1580-2949
MTAEC9, 48(3)439(2014)

MORPHOLOGICAL AND MICROSTRUCTURAL FEATURES OF Al-BASED ALLOYED POWDERS FOR POWDER-METALLURGY APPLICATIONS

MORFOLOŠKE IN MIKROSTRUKTURNE ZNAČILNOSTI KOVINSKIH PRAHOV NA OSNOVI ALUMINIJA ZA IZDELAVO IZDELKOV PO POSTOPKIH METALURGIJE PRAHOV

Borivoj Šuštaršič[1], Irena Paulin[1], Matjaž Godec[1], Srečko Glodež[2], Marko Šori[2], Jože Flašker[2], Albert Korošec[3], Stanko Kores[3], Goran Abramovič[3]

[1]Institute of Metals and Technology, Lepi pot 11, 1000 Ljubljana, Slovenia
[2]University of Maribor, FNM, Koroška cesta 160, 2000 Maribor, Slovenia
[3]Talum, Factory of Aluminium, Tovarniška cesta 10, 2325 Kidričevo, Slovenia
borivoj.sustarsic@imt.si

Prejem rokopisa – received: 2013-12-16; sprejem za objavo – accepted for publication: 2014-02-20

Besides advanced nano steels, polymers and ceramics, recently also light metals, i.e., Al, Mg and Ti based materials, have been recognized as future materials for different kinds of advanced applications. Al and its alloys have an acceptable price, excellent corrosive resistance, good mechanical and other physical properties. Therefore, they are also used in the powder-metallurgy (P/M) field. The P/M technology of Al materials is very demanding and has its own specifics compared to the sintering technology of iron and steel. A relatively large quantity of Al-based alloy powder is formed during the sand blasting of slugs and discs in the Talum Al factory, Kidričevo, Slovenia. Therefore, we analysed and investigated its practical usability for a production of advanced products using P/M technology. The formed Al-based powder was compared with the commercially available Al-based powders that are generally used for conventional sintering technology. In the first part of this paper we explain which types of Al-based powders are used for the production of sintered parts, what the required parameters are and why we considered them. Then, the results of theoretical thermodynamic analyses and investigations of the morphological and microstructural characteristics of the selected commercial Al-based powders are given, as well as their comparison with the Al powder formed during the sand blasting and its potential for P/M applications.

Keywords: Al-based alloy powders, morphology and microstructure, LM and SEM/EDS characterisation

Postopki metalurgije prahov (P/M) so med najučinkovitejšimi tehnologijami za velikoserijsko izdelavo majhnih izdelkov kompliciranih oblik. Med vsemi P/M-postopki je najbolj uveljavljen t. i. konvencionalni sinter postopek. Z njim izdelujemo predvsem izdelke na osnovi železa. To so sintrani jekleni zobniki, zaklepi, puše, porozni filtri, ležaji, kakor tudi drugi strojni ali konstrukcijski elementi strojev in naprav. Zelo popularni so tudi sintrani izdelki na osnovi Fe za mehko- in trdomagnetne aktuatorje in senzorje. Največji odjemalec sintranih izdelkov je avtomobilska industrija. Najdemo pa jih tudi v pohištveni industriji, beli tehniki, precizni mehaniki, v izdelkih za šport in razvedrilo, kakor tudi za zelo zahtevne letalske, vojaške, vesoljske in druge aplikacije. Na vseh teh področjih se v novejšem času uveljavljajo poleg polimerov in keramike tudi lažji kovinski materiali, kot so zlitine na osnovi Al, Mg in Ti. Aluminij oz. njegove zlitine se zaradi svojih odličnih mehanskih, korozijskih in drugih fizikalnih lastnosti uveljavljajo tudi na področju P/M-tehnologij. Ta tehnologija Al-materialov je zelo zahtevna, ima svoje specifičnosti in se precej razlikuje od sinter tehnologije Fe in jekla. V tovarni aluminija Talum kot stranski produkt peskanja rondelic nastaja legiran Al-prah. Zato smo analizirali njegovo praktično uporabnost in možnosti izdelave zahtevnih izdelkov s P/M-postopkom. Nastajajoči Al-prah smo primerjali s komercialno dosegljivimi Al-prahovi, ki se standardno uporabljajo za konvencionalno sinter tehnologijo Al. V prispevku predstavljamo tudi, kakšni prahovi so uporabni za izdelavo sintranih izdelkov, kaj se od njih zahteva in zakaj. Predstavljeni so rezultati teoretičnih termodinamskih analiz in raziskav s poudarkom na morfoloških in mikrostrukturnih značilnostih komercialno dosegljivih prahov na osnovi Al in primerjava z Al-prahom peskanja. Ocenili smo tudi njegovo uporabnost za izdelavo izdelkov s P/M-tehnologijo.

Ključne besede: kovinski prahovi zlitine na osnovi Al, morfologija in mikrostruktura, preiskave s svetlobnim in elektronskim mikroskopom

1 INTRODUCTION

The powder-metallurgy process (P/M) is one of the most efficient technologies for a mass production of small complex functional and structural products. Conventional sintering technology (**Figure 1**) is the most convenient and popular technology among all the P/M processes. A fine metal-powder mixture is first automatic die compacted (ADC) into the final shape of the product with automatic mechanical or hydraulic presses and then sintered in a protective atmosphere at the temperatures between approximately 0.8 and 0.9 of the melting point of the metal powder. The result of this procedure is a partly porous or completely dense metal product that can be additionally improved with heat and/or mechanical treatments. Iron- and steel-based P/M products are mainly produced with this procedure. These are sintered steel gears, spurs, locking mechanisms, porous filters, sliding bearings, as well as other machine and structural elements. Sintered soft/hard magnetic actuators and sensors are also very popular. The automotive industry is the most important end user of sintered parts. However, small complex sintered parts can be frequently used also in the furniture and household industry, precision mecha-

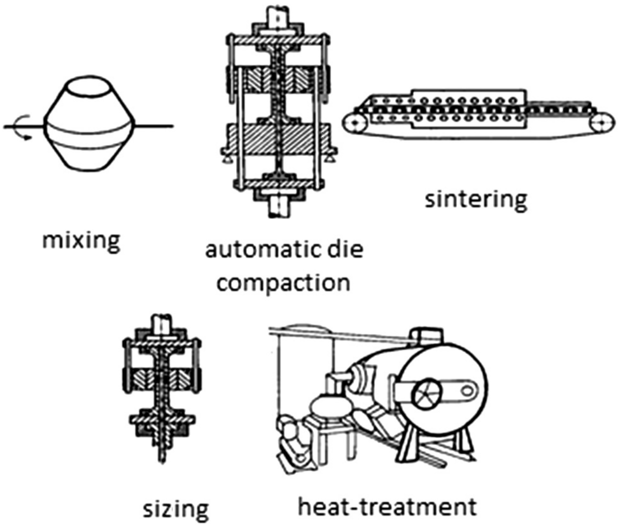

Figure 1: Schematic presentation of conventional sintering process
Slika 1: Shematski prikaz konvencionalnega postopka sintranja

nics, the articles for leisure, recreation and sports, etc. High-alloyed sintered metal parts can also be used for very demanding marine, aeronautic, military and space applications.[1]

Besides advanced nano steels, polymers and ceramics, recently also light metals, i.e., Al, Mg and Ti based materials, have been recognized as future materials for different kinds of advanced applications.[2,3] Aluminium and its alloys have an acceptable price, excellent corrosive resistance, good mechanical and other physical properties (non-magnetic, excellent thermal and electrical conductivity, etc.). Therefore, they are also used in the P/M technology field (**Figure 2**).[4]

However, the P/M technology of Al materials is very demanding and has its own specifics compared to the sintering technology of iron and steel.[5,6] The Al-based alloyed powders, appropriate for a sintering procedure (powder metallurgy, P/M) contain the alloying elements (Cu, Zn, Mg, etc.) with a high solid solubility in Al, enabling reaction and liquid-phase sintering, respectively. The high solid solubility of these elements is also important for an additional improvement of mechanical properties, enabling precipitation hardening during a heat treatment. Generally, Al powders are surface oxidised because of the high affinity of Al to oxygen. Besides, these types of powders also contain approximately the mass fraction 1.5 % of polymeric lubricant (wax) that reduces the friction at die walls, while the powders are being ADC into the final compact shapes of the products. This lubricant has to be removed slowly during the first stage of sintering in order to prevent deformations and cracking of the product. Therefore, its sintering is very complex. Generally, these types of powders are sintered in pure nitrogen (N_2, 5.9) with a low dew point (below –40 °C). The optimum sintering conditions are commonly determined on the basis of light (LM) and scanning electron microscopy (SEM) combined with a micro-chemical analysis based on the measurement of the dispersed kinetic energy of X-rays (energy dispersive X-ray spectrometer, EDS). The investigation can also be completed very successively with hot microscopy, as well as with differential scanning calorimetry and thermogravimetry (DSC/TG).[7]

A relatively large quantity of Al-based alloy powder is formed as a bypass product during the sand blasting of slugs (**Figure 3**) and discs in the Talum Al factory, Kidričevo, Slovenia.[8] Therefore, we analysed and investigated its practical usability for the production of the advanced products made with the P/M technology. The formed Al-based powder was compared with the commercially available Al-based powders that are generally used for conventional sintering technology. In the first part of this paper we explain which types of Al-based powders are generally used for the production of sintered parts, what the required parameters are and why we con-

Figure 3: Slugs produced in the Talum Al factory used as semi-products in the production of tubes and containers in the pharmaceutical, food and cosmetic industries[8]
Slika 3: Rondelice, izdelane v tovarni aluminija Talum, ki se uporabljajo kot polproizvod v proizvodnji tub in posodic za kozmetiko ter v farmacevtski in prehrambeni industriji[8]

Figure 2: Some small complex Al-based sintered parts[4]
Slika 2: Nekaj majhnih in kompliciranih sintranih izdelkov na osnovi Al[4]

sidered them. Then, the results of the theoretical thermodynamic analyses and investigations of the morphological and microstructural characteristics of the selected commercial Al-based powders are presented and their comparison with the Al powder formed during the sand blasting, together with its potential for P/M applications, are given. Henceforth, this Al powder will be designated as the SB powder.

2 CHEMICAL AND THERMODYNAMIC CHARACTERISTICS OF THE Al POWDERS

In the frame of the present project,[9] three commercial Al-based powders (Alumix 123, 231 and 432) appropriate for the sintering technology were purchased at Ecka Granules, Germany.[10] Henceforth, these three commercial alloys will be designated as alloys *A*, *B* and *C*. The powder producer has already provided some recommendations for the sintering of these alloy powders. However, in some cases these data are not enough to get all the necessary information for their comparison with the SB powder. Therefore, first, a complete theoretical thermodynamic analysis as well as morphological and microstructural characterisations of the selected commercial powders were performed.

Table 1 shows the nominal and actual chemical compositions of the investigated powders. One can notice that the chemical compositions of these alloys are very simple. Wrought Al alloys (extruded, forged) of similar types usually have more complex compositions with additional amounts of alloying elements (Cr, Ti, Zr, V, etc.) and, generally, lower amounts of impurities and oxygen. The chemical composition of the SB powder differs significantly from the commercial alloys. It has much higher amounts of Cu, Fe and Mn but lower amounts of Mg and Zn. Only its Si content is comparable with the amount in alloy *A,* but it does not contain Zn. In view of the above, it is practically impossible to dilute the SB powder with additional corrections (by adding appropriate amounts of Al and other elements) in order to prepare an alloy similar to the one of the commercial alloys given in **Table 1**.

In the first phase of the investigation, to understand the sintering process, it is necessary to be acquainted at least with the experimentally determined binary-phase diagrams of Al with the basic alloying elements (Al-Cu, Al-Si, Al-Mg, Al-Zn) and with their mutual congruency (Si-Cu, Si-Mg, Mg-Cu, Mg-Zn).[11] Such information gives us the appropriate data about the temperature solid-state solubility of an individual alloying element in Al, the basic temperature stability of the formed binary phases and the melting points. Certain ternary-phase diagrams with known multi-component intermetallic phases are also available in the professional, but relatively expensive, databases.[12]

From the considerably complex (eutectic-peritectic/peritectoid) Al-Cu equilibrium binary-phase diagram[11] one can see that the solid solubility of Cu in Al is maximal at 548 °C (approximately 5.7 %). The eutectic reaction ($L \Rightarrow \alpha\mathrm{Al} + \theta$) is carried out at 67 % of Al. All our three commercial alloys have such Cu amounts that all the Cu is soluble in the fcc αAl solid solution during the sintering. At the same time, it follows from the Cu-Si binary diagram that Cu has a good solubility for Si, while Cu is not soluble in Si.

The Al-Si equilibrium binary-phase diagram is of the pure eutectic type.[11] The eutectic (αAl + Si) is formed at 577 °C and approximately 87.5 % Al. The solid solubility of Si in Al is small. It is maximal at the eutectic temperature (1.56 %). One can see in **Table 1** that the composition of alloy *A* enables practically all the Si to be soluble in the αAl solid solution during the sintering. On the other hand, alloy *B* has a much higher amount of Si, and, therefore, one can expect the presence of hard Si crystals in the metal matrix, enabling a high hardness and good wear resistance of this alloy. The third alloy, alloy *C*, does not contain Si.

The Al-Mg equilibrium binary-phase diagram is of the double eutectic type.[11] The solid solubilities of Mg in Al and Al in Mg are good. At the eutectic temperatures of 450 °C and 437 °C the solid solubilities are approximately 17 % of Mg and approximately 12 % of Al, respectively. Mg is present as an alloying element in all three commercial alloys and one can expect that almost all of it is dissolved in the αAl solid solution during the sintering. Why almost? Because a certain part of an

Table 1: Nominal and actual average bulk chemical compositions of the investigated powders
Tabela 1: Nazivna in dejanska povprečna kemijska sestava preiskovanih prahov

Chemical composition		Cu	Si	Mg	Zn	Al	Other elements	Remark
Name		mass fractions, *w*/%						
Alloy *A*	nominal[10]	4.2–4.8	0.5–0.7	0.4–0.6	–	bal.	–	type 2××× (2014)
	actual	4.5	0.62	0.48	–	n. d.*	0.08 Fe	
Alloy *B*	nominal[10]	2.4–2.8	14–16	0.5–0.8	–	bal.	–	Hypereutectic high Si (wear resistant)
	actual	2.7	15.0	0.58	–	n. d.	–	
Alloy *C*	nominal[10]	1.4–1.8	–	2.2–2.8	5.0–5.8	bal.	–	type 7××× (7075)
	actual	1.6	–	2.4	5.8	n. d.	0.29 Sn	
SB powder	actual	7.74	0.83	0.1	1.57	87.0	1.6 Fe 0.48 Mn	Bypass product of sand blasting

* n. d.……. not determined

alloying element is also present in the liquid phase during the liquid-phase sintering.

From the considerably complex (eutectic-eutectoid) Al-Zn equilibrium binary-phase diagram[11] one can see that Zn has a large solid solubility in Al. The maximum solubility at 382 °C is 83 %. At approximately 340 °C a spinodal decomposition occurs ($\alpha \Rightarrow \alpha + \alpha'$) followed (at the lower temperatures) by the phase transformations of $\alpha + \gamma$ and $\alpha + \beta$. The Zn alloying element is present only in commercial alloy *C*. This alloy also has a small amount of tin (Sn) that has a very low melting point (232 °C) and a good solubility in solid Cu (bronzes) and in Mg, but it is not soluble in Zn and Al.

However, recent modern CALPHAD-based (Calculation of Phase Diagrams)[13] computer tools (Thermocalc, Dictra, etc.)[13–15] enable a faster and more reliable insight into complex multi-component systems. The thermodynamic analysis of alloy *A* with ThermoCalc[15] shows (**Figure 4**) that it mostly contains the solid crystals of the αAl phase (from room temperature up to 637.81 °C) and intermetallic θ phase (Al_2Cu) up to 500.96 °C. The first liquid appears at 525.04 °C. The theory also predicts a formation of small amounts of the intermetallic phases of $Al_5Cu_2Mg_8Si_6$ (up to 500 °C), Al_7Cu_2M (M = Fe, up to 565.04 °C), βAlFeSi (up to 223.2 °C) and Si to approximately 396 °C. The exact chemical composition of each individual phase can also be determined for the whole temperature region. A two-phase region ($L + \alpha$Al) exists between 525.04 °C and 637.81 °C. At the beginning of this temperature region (somewhere between 570 °C and 600 °C) where a small quantity of liquid is already formed, there is the appropriate optimum (maximum) sintering temperature. The powder producer recommends a sintering temperature between 590 °C and 600 °C for 20 min, which is in good agreement with the theoretical thermodynamic calculation.

Unfortunately, the limited scope of this article does not allow us to show all the results of the performed thermodynamic analyses of the investigated alloys. Therefore, only the main results will be presented. The thermodynamic analysis of alloy *B* shows[9] that the alloy in equilibrium mostly contains the solid crystals of the αAl phase (from room temperature up to 562.64 °C), the crystals of Si (up to 619.72 °C) and the intermetallic phases of Al_2Cu (up to 447.85 °C) and $Al_5Cu_2Mg_8Si_6$ (up to 526.04 °C). The first liquid is formed at 532.65 °C. This alloy does not have a two-phase L + αAl region because of a high amount of Si and its high temperature stability. Therefore, there is only the three-phase L + αAl + Si temperature region (between 532.65 °C and 562.65 °C) appropriate for the liquid-phase sintering. The powder producer recommends the sintering temperatures between 540 °C and 560 °C for 60 min, which is again in good agreement with the theoretical calculations. A longer sintering time may be prescribed to the low solubility of Si.

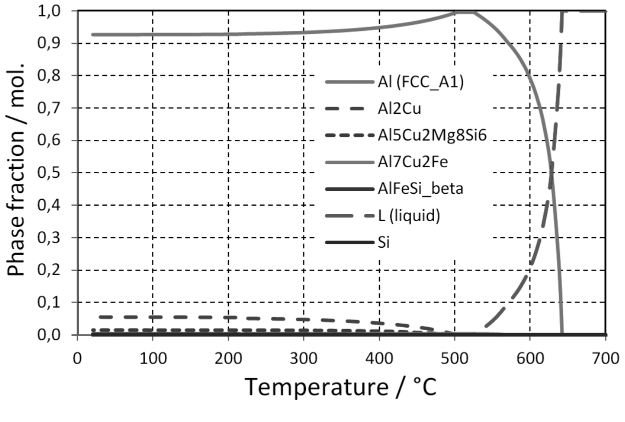

Figure 4: Theoretical equilibrium thermodynamic phase stability of alloy *A*, calculated with ThermoCalc[15]

Slika 4: Teoretična ravnotežna termodinamska stabilnost faz zlitine *A*, izračunana z orodjem ThermoCalc[15]

The thermodynamic analysis of alloy *C* shows[9] that, in equilibrium, this alloy mostly contains the solid crystals of the αAl phase (from room temperature up to 630 °C) and intermetallic phases of Mg2X_C1 (X = Sn, up to 511.13 °C), S_Al_2CuMg (up to 442.70 °C), $MgZn_2$ (up to 409.71 °C) and T_AlCuMgZn (up to approximately 250 °C). The first liquid is formed at 516.54 °C. A two-phase region (L + αAl) exists between 516.54 and 630 °C. This temperature region is relatively wide. At the beginning of this temperature region (somewhere between 530 °C and 560 °C) where a small amount of liquid is already formed, there is the appropriate optimum sintering temperature predicted by ThermoCalc. However, the powder producer recommends a higher sintering temperature (between 600 °C and 610 °C for 20 min), which is still in agreement with the theoretical calculation. A higher sintering temperature is possible with a slightly shorter sintering time (for example, 15 min instead of 20 min). But, there is always the issue of the final optimization of the sintering process that is, unfortunately, still primarily based on the experimental work.

From the thermodynamic analyses of the selected alloys it is also clear that after the sintering (designated as T1a) all three alloys can be additionally heat treated with the conventional standardized precipitation-strengthening (also age-hardening) procedure, i.e., solid-solution annealing combined with fast cooling (quenching) and natural (T4) or artificial ageing (T6, T76, etc.). In this case the temperature of solid-solution annealing must be below the formation temperature of the first liquid in the region of the maximum solid solubility of the alloying elements in Al, typically 500 °C for 20 min. After homogenization very fast cooling must be performed, enabling a formation of a supersaturated solid solution of the αAl phase with the alloying elements. The final step of the heat treatment is natural (ambient conditions) or artificial (at an elevated temperature) ageing, typically 150 °C for 15 min. A precipitation of a very fine dispersion of intermetallic phases occurs during this step. An ageing temperature that lasts for too long and is too high can cause an unwanted growth of the precipitates decreasing the hardness and strength of the alloy. As in the case of sintering, the final optimization of the age-hardening process is unfortunately still based on the expensive and time-consuming experimental work. However, new computer tools[13–15] calculating theoretical CCT (continuous cooling temperature) and isothermal TTT (time-temperature transformation) diagrams can significantly reduce the experimental work. At the cooling rate of 10^5 °C/h (approximately 28 °C/s) a fine precipitation of GP (Guiner-Preston) zones and the theta prime (θ') phase are predicted.[9] In the case of lower cooling rates other (unwanted) intermetallic phases would also develop.

Figure 5 shows the theoretical thermodynamic phase stability in the system with the chemical composition of the SB powder. One can see that in this system, depending on the temperature, there can be eleven (11) phases, compared to only seven (7) in alloy *A*, five (5) in alloy *B* and six (6) in alloy *C*. The liquid and αAl are stable together in the temperature region between approximately 527 °C and 617 °C. However, besides αAl the most temperature-stable solid phases in this system are Al$_6$Mn and Alfa (Al-Fe-Mn-Si-Cu) that are still solid above 645 °C and 609 °C, respectively. For the optimum liquid-phase sintering conditions it would be recommendable that these two phases are also dissolved in the αAl solid solution. Unfortunately, in this alloying system a two-phase region (αAl + L) does not exist and the optimum sintering conditions cannot be assured.

This theoretical thermodynamic analysis shows that commercial Al powders have designed chemical compositions that enable reactive liquid-phase sintering. However, the SB powder has a more complex chemical composition that is not accommodated for the optimum sintering process. By analogy with the determination of the sintering temperatures of the commercial Al powders (approximately 10 % to 20 % of the liquid phase present), the optimum sintering temperature of the SB powder is somewhere between 550 °C and 590 °C. But in this temperature region, besides the liquid and αAl, there is still a relatively large amount of the intermetallic phases of AlFeSi-Beta, Al$_6$Mn and Alpha. All these intermetallic phases are only dissolved in the liquid phase above 645 °C, but then the αAl phase also completely disappears, i.e, only the liquid phase is present and complete melting of the material occurs. On the other hand, it is necessary to know that the sinterability of a metal powder does not depend only on the chemical composition and thermodynamic conditions but also on the other parameters (particle-surface oxidation, particle shape and size, homogeneity of the powder mixture, sintering atmosphere, etc.) that control the sintering kinetics and cannot be fully covered in this theoretical study.

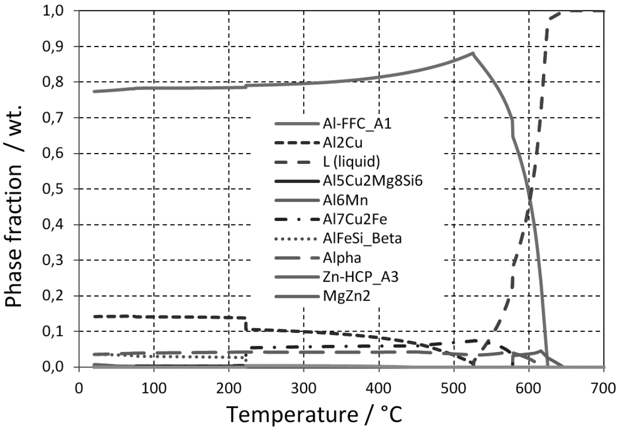

Figure 5: Theoretical equilibrium thermodynamic phase stability of the alloy with the SB-powder composition, calculated with Thermo-Calc[15]

Slika 5: Teoretična ravnotežna termodinamska stabilnost faz v sistemu s kemično sestavo SB-prahu, izračunana z orodjem ThermoCalc[15]

3 MORPHOLOGICAL CHARACTERISTICS OF THE POWDERS

For a successful industrial mass production of small complex parts, besides a good final densification of a powder compact with sintering, the preceding processing step, i.e., the automatic uniaxial cold or warm die compaction (ADC) in the metal mould with automatic mechanical or hydraulic presses is also important. The selected metal powder must flow fast and continuously from the powder container through the filling tube and the shoe into the die cavity, where it is fast compacted with as low as possible pressure into a green compact with a high green density and strength, as well as without any internal or surface defects (cracks, flaws). The powder must completely fill all the parts of the die cavity. For this reason, besides a suitable chemistry, the metal powder must also have an appropriate particle morphology (the size distribution and shape). This is mainly controlled with the powder production process (atomisation, milling, powder heat treatment, etc.). Several standardized tests and investigations make it possible to evaluate the usability of the powder mixture for an ADC process and its technological properties.[16] The most important are the apparent and tap densities, the flowability and compressibility that are controlled with the particle morphology, as well as chemical and metallurgical conditions of a powder production. For example, the results of an atomization[17] are hard particles generally formed during fast cooling of the droplets of a melt; a mixture of pure soft elemental and hard alloyed particles gives a better compressibility than a prealloyed, chemically uniform powder, etc. The type and amount (1 % to 2 %) of a lubricant influence, to some extent, the technological properties of a powder mixture. The apparent density and flowability of a powder are determined with a Hall flowmeter.[16] Through a funnel of a standardized size, 50 g or 100 g of powder flows for a defined period. The flow time is measured (for example,

Table 2: Main technological properties of the investigated Al powders important for the ADC process

Tabela 2: Glavne tehnološke lastnosti izbranih Al-prahov, pomembne za uspešno avtomatsko hladno enoosno stiskanje v surove končne oblike izdelka

Property	Powder type	Alloy *A*	Alloy *B*	Alloy *C*	SB powder
Apparent density (g/cm^3)	nominal[10]	1.05–1.15	1.05–1.25	1.1–1.25	n. d.
	actual	1.08	1.12	1.14	1.20
Tap density (g/cm^3)	nominal[10]	1.2–1.5	1.2–1.5	1.2–1.5	n. d.
	actual	1.32	n. d.	n. d.	1.25
Flowability (seconds/50g)	nominal[10]	< 30	n. d.	< 30	n. d.
	actual	24	n. d.	n. d.	not flowable
Green density (g/cm^3)	nominal[10]	2.65 at 400 MPa	2.56 at 620 MPa	2.65 at 400 MPa	not defined
	actual	2.68 at 440 MPa	2.52 at 600 MPa	2.61 at 430 MPa	2.37 at 516 MPa
Fine fraction (< 45 μm), *w*/%		max. 20	25–40	max. 35	45

(30 s)/(50 g)) and the value is designated as the powder flowability. At the same time this powder is collected in a small copper pot with a known volume (25 cm^3), weigh and apparent density of the loose powder, calculated in g/cm^3 (typically approximately 3 g/cm^3 for the Fe- and 1.2 g/cm^3 for the Al-based powders). The loose powder is generally densified, to some extent, with mechanical vibration. The tap density is a result of 100 mechanical vibrations of the loose powder. The compressibility of a powder is determined with a standardized tool measuring the mechanical pressure needed for a certain green density of a compact (typically approximately 600 MPa for the green density of 7.0 g/cm^3 of a steel-powder compact and 400 MPa for the green density of 2.6 g/cm^3 of an Al-powder compact, respectively).[17]

Table 2 shows the main technological properties of the investigated powders. It can be clearly noticed that the commercial powders have smaller parts of the fine fraction of powder particles, better flowability and compressibility than the SB powder.

Figures 6 and **7** show the results of the complete sieving analyses of the investigated powders. The SB powder mainly consists of two fractions. The fine < 45 μm fraction is a result of the sand blasting of discs and slugs, i.e., small-scale particles (worn parts), and the coarse-particle fraction of 160–200 μm is a result of the incompletely worn sand-blasting media. On the other hand, the commercial Al powders have a relatively uniform natural-particle-size distribution with a regular *S* curve of the cumulative-particle-size distribution (**Figure 7**). The SB powder also has a lower mean particle size; as observed from the *S* curve, d_{50} is approximately 53 μm for the SB powder in comparison with alloys *A* (80 μm), *B* (60 μm) and *C* (78 μm).

4 MICROSTRUCTURAL CHARACTERISTICS OF THE POWDERS

The revealed technological properties of the investigated powders are the results of their micromorphological and microchemical characteristics. The microstructural and microchemical investigations of the powders performed with LM and SEM/EDS are shown below. The observations under the microscopes were performed in a loose condition (powder particles stacked on a special tape), as well as in cross-section (polished and etched metallographic samples). **Figures 8** and **9** show the SEM micrographs of loose powders *A* and *B* at two different magnifications. Powder *C* has a similar particle morphology.

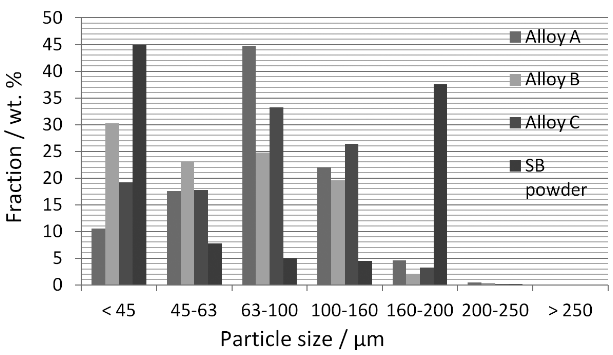

Figure 6: Particle-size-distribution histogram of the investigated Al-based powders based on the performed sieving analyses

Slika 6: Histogram velikostne porazdelitve delcev preiskovanih prahov, izdelan na osnovi sejalne analize

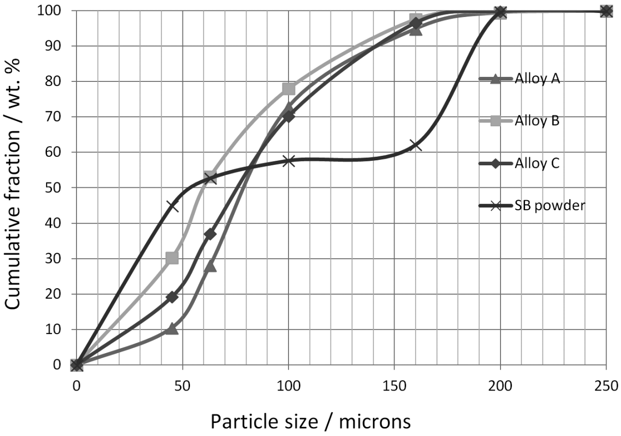

Figure 7: Cumulative-particle-size distribution of the investigated Al-based powders based on the performed sieving analyses

Slika 7: Kumulativne velikostne porazdelitve delcev preiskovanih prahov, izdelane na osnovi sejalne analize

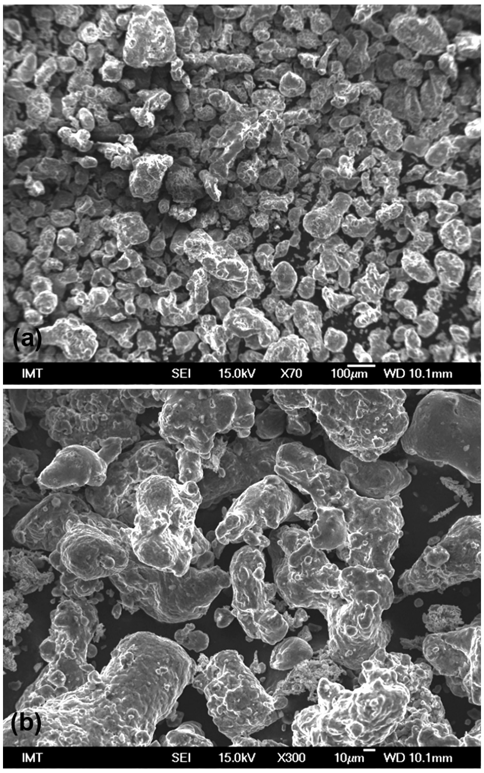

Figure 8: SEI micrographs of loose powder *A* made at two different magnifications

Slika 8: SEI-posnetka nasutega prahu *A*, narejena pri dveh različnih povečavah

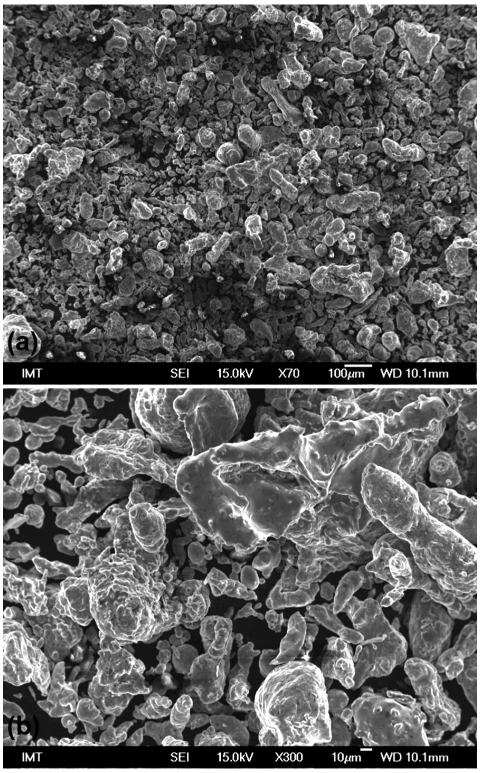

Figure 9: SEI micrographs of loose powder *B* made at two different magnifications

Slika 9: SEI-posnetka nasutega prahu *B*, narejena pri dveh različnih povečavah

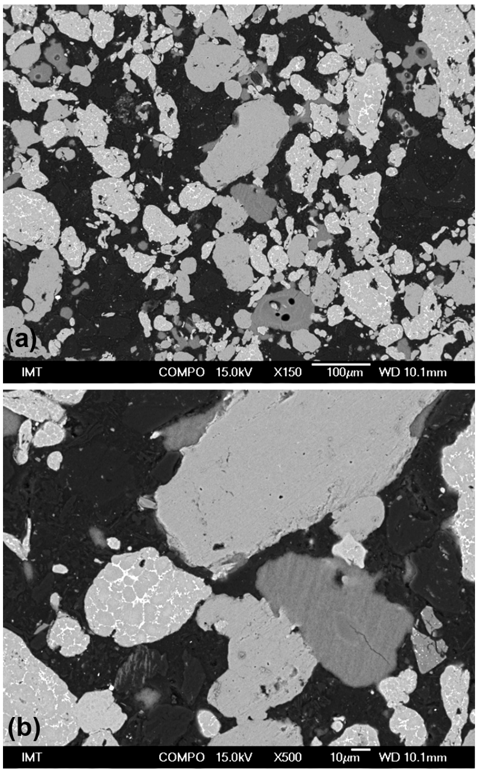

Figure 10: SEM/BEI micrographs of powder *B* in cross-section, made at two different magnifications

Slika 10: SEM/BEI-posnetka nasutega prahu *B* v prerezu, narejena pri dveh različnih povečavah v povratno sipanih elektronih

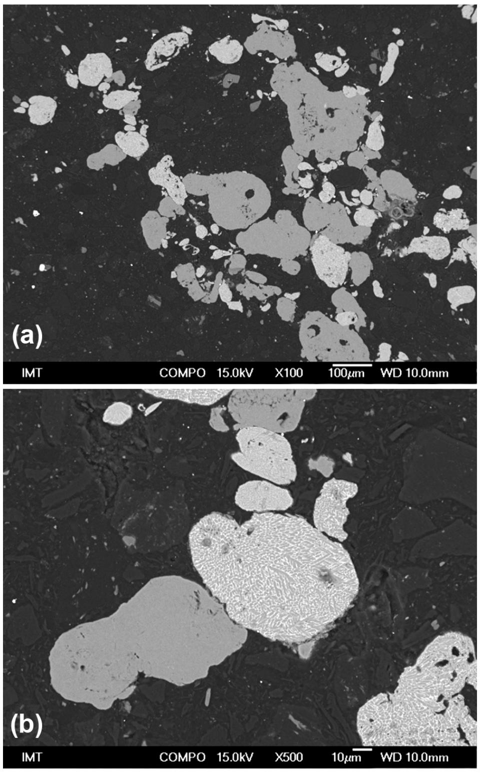

Figure 11: SEM/BEI micrographs of powder *C* in cross-section, made at two different magnifications

Slika 11: SEM/BEI-posnetka nasutega prahu *C* v prerezu, narejena pri dveh različnih povečavah v povratno sipanih elektronih

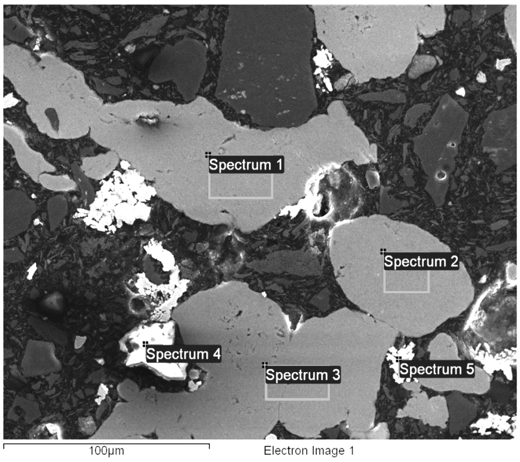

Figure 12: SEM/BEI micrograph of individual particles of powder *A* in cross-section where the EDS microanalysis was performed

Slika 12: Posnetek mest na posameznih delcih prahu *A*, kjer je bila izvedena SEM/EDS-mikroanaliza

It can be seen that the commercial powders have irregular particle shapes (rounded droplets) with smooth vitreous surfaces and different sizes from approximately 1 µm to 200 µm. This particle morphology is typical for gas (air) atomized Al powders.

Figures 10 and **11** show the SEM/BEI (backscatter electron image mode) micrographs of the powder particles of alloys *B* and *C* in cross-section at two different magnifications. In both powders it can be clearly seen that the particles are of different colours (shades of grey). This means that they have different chemical compositions. It can also be seen that small white irregular shapes are present in powder *A*. The microchemistry of the powders was checked with the SEM/EDS microanalyses of individual powder particles.

It has been shown that all the commercial powders consist of the powder particles with different chemical compositions. In the case of powder *A* (**Figure 12** and **Table 3**), the powder mixture contains the particles of pure soft Al, the Al-Si alloy (approximately 90 % Al and 10 % Si) and the Cu-Al alloy (approximately 95 % Cu and 5 % Al). It is also confirmed that the small white clusters of particles are oxides (mainly SiO_2, some Al_2O_3 and CaO).

The SEM/EDS analysis of some particles of powder *B* has shown that this powder is also a powder mixture of pure Al as well as the alloyed particles of Al-Si-Mg-Cu and Si-Al. All the particles are considerably surface oxidized. Powder *C* is a mixture of pure Al particles and the alloyed particles with the approximate composition of Al-12Zn-5Mg-4Cu. This powder is the least oxidized of all the commercial powders.

Figures 13a and **13b** show SEM micrographs of the loose SB powder at two different magnifications. In **Figure 13a**, made at a lower magnification, large round particles of the sand-blasting media are clearly visible. However, at larger magnifications (**Figure 13b**) we clearly see small irregular particles (scales or shells) formed due to the sand blasting of discs and slugs. The SB powder has a low flowability and compressibility because of its particle morphology.

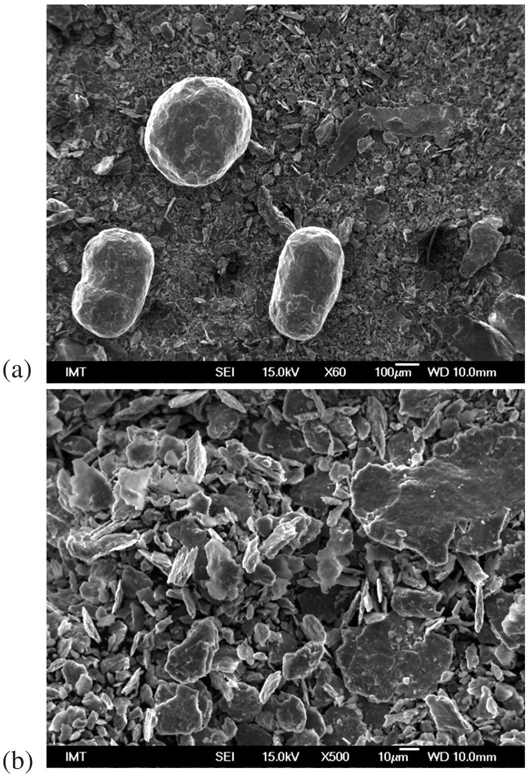

Figure 13: SEI micrographs of the loose SB powder, made at two different magnifications

Slika 13: SEI-posnetka kovinskega SB-prahu, narejena pri dveh različnih povečavah

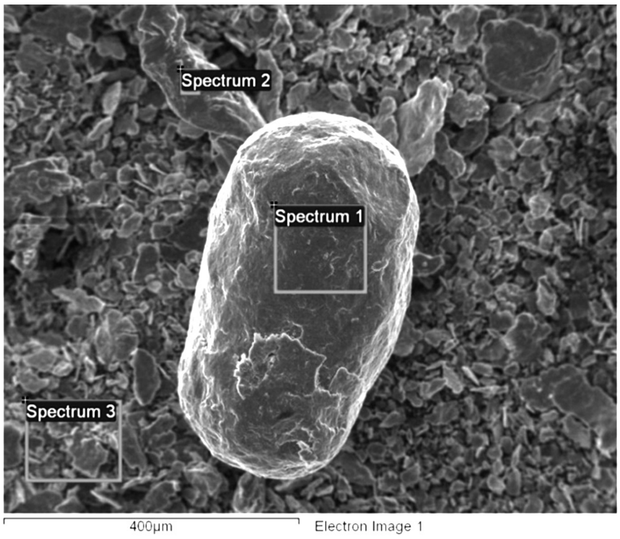

Figure 14: SEM/EDS analysis of a larger spherical particle and smaller-scale particles with designated locations of the performed analyses (connected with **Table 4**)

Slika 14: SEM/EDS-analiza večjih sferičnih in manjših luskinastih delcev z označenimi mesti izvršene analize in tabelarično podanimi rezultati analize delcev (**tabela 4**)

Table 3: Microchemical compositions of individual powder particles of powder mixture *A* (connected with **Figure 12)**

Tabela 3: Mikrokemijska sestava posameznih delcev prašne mešanice *A* (vezano na **sliko 12**)

Spectrum	O	Al	Si	Ca	Cu	Total
Spectrum 1		100.00				100.00
Spectrum 2		89.32	10.68			100.00
Spectrum 3		100.00				100.00
Spectrum 4	55.69	2.28	41.04	0.98		100.00
Spectrum 5		5.45			94.55	100.00

Figure 14 shows the SEM/EDS analysis of a larger spherical particle (Spectrum 1) in the region where small-scale particles are also present (Spectrum 3). As it can be seen in **Table 4**, the large spherical particle is surface oxidized and, besides Al, it also contains Si, Mn, Fe, Cu and Zn, which is in accordance with the chemical analysis of the sand-blasting media (**Table 5**). However, the larger flat particle is practically pure Al (Spectrum 2) but also surface oxidized.

Table 4: Microchemical compositions of individual powder particles of the SB powder (connected with **Figure 14**), *w*/%

Tabela 4: Mikrokemijska sestava posameznih delcev SB-prahu (vezano na **sliko 14**), *w*/%

Spectrum	O	Al	Si	Mn	Fe	Cu	Zn	Ag
Spectrum 1	17.11	74.39	0.77	0.27	0.94	4.97	1.14	0.41
Spectrum 2	4.12	95.88						
Spectrum 3	15.29	76.29	0.66		1.02	5.59	1.16	

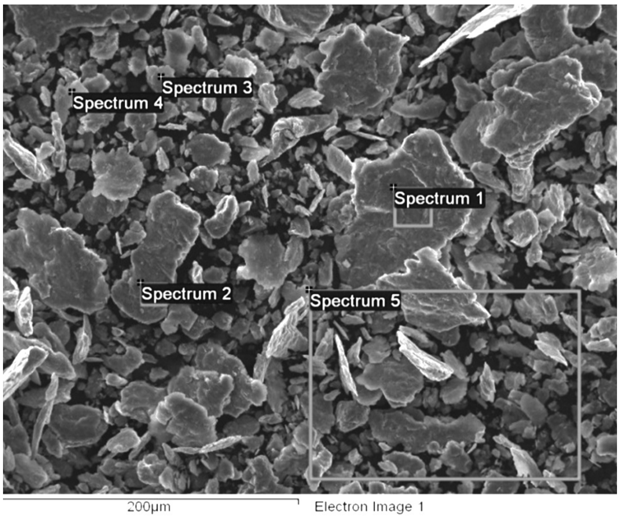

Figure 15: SEM/EDS analysis of smaller-scale particles with designated locations of the performed microanalyses (connected with **Table 6**)

Slika 15: SEM/EDS-analiza manjših luskinastih delcev z označenimi področji, kjer je bila izvršena analiza (v povezavi s **tabelo 6**)

Figure 15 and **Table 6** show the results of SEM/EDS analyses of the regions where mainly fine particles are present. Fine-scale particles are substantially surface oxidized and, as a result of the sand blasting, they contain all the elements present in discs and slugs as well as in the residuals of the sand-blasting media.

Table 6: Microchemical compositions of individual fine-powder particles of the SB powder (connected with **Figure 20**), *w*/%

Tabela 6: Mikrokemijska sestava posameznih finih delcev SB-prahu (vezano na **sliko 20**), *w*/%

Spectrum	O	Al	Si	Mn	Fe	Cu	Zn	Ag
Spectrum 1	16.62	75.76	0.93	0.39	0.92	4.51	0.87	
Spectrum 2	13.86	77.85	0.89	0.33	1.16	4.71	0.75	0.46
Spectrum 3	17.45	74.87	1.37		0.89	4.51	0.92	
Spectrum 4	9.70	82.49	1.07		0.94	4.42	0.93	0.44
Spectrum 5	15.45	76.02	0.79	0.47	1.17	5.16	0.95	

5 COMPACTION AND SINTERING OF THE POWDERS

The investigated commercial powders were compacted into standard[11,16,17] tensile-test specimens (35 pieces

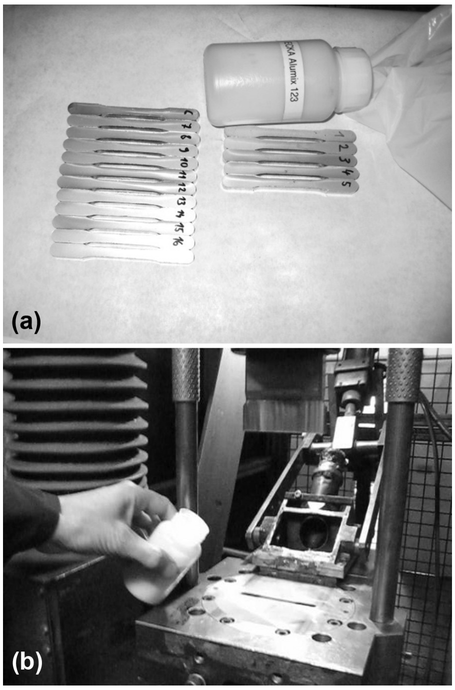

Figure 16: Powder-compaction experiments: a) standardized tensile-test specimens compacted from Al-based commercial powders and b) manual pouring of the powder into a die cavity

Slika 16: Preizkusi stiskanja prahov: a) standardni natezni preizkušanci, stisnjeni iz komercialnih Al-prahov in b) ročno nasipanje Al-prahu v orodje

Table 5: Chemical composition and properties of the sand-blasting media

Tabela 5: Kemijska sestava in lastnosti peskalnega sredstva

Element	Si	Mn	Fe	Cu	Zn	Pb	Mg	Particle size (μm)	Apparent density (g/cm^3)	Hardness HV$_{0.2}$
Composition (*w*/%)	0.6–1.2	0.3–0.6	1.0–1.5	6.0–6.5	1.0–1.5	< 0.15	< 0.3	150–400	1.65	90–120

of each powder, **Figure 16a**) with a 60 MN Dorst mechanical press, Germany, in the Unior factory, Zreče. The powders were manually dosed (poured) into the die cavity (**Figure 16b**). Powders *A* and *C* were compacted at approximately 450 MPa. Powder *B* has a lower compressibility and was, therefore, compacted at approximately 600 MPa. The corresponding average green densities are given in **Table 7**. The samples were then sintered in a batch lab furnace under the prescribed sintering conditions. The obtained average sintered densities and mechanical properties are also given in **Table 7** and they are in accordance with the expectations (the nominal values for the T4 condition are given in parentheses). As a case study, the LM micrographs of the green and sintered compacts of powder *B* are given in **Figures 17a** and **17b**. It is well visible that the remaining porosity of the green compact after cold compaction is still relatively large. However, after the sintering a good densification is obtained and only a small amount of residual porosity remains. One can also notice that the compacted powder mixture mainly consists of two types of particles (pure Al and alloyed particles of Al-Si-Mg-Cu), which was also confirmed with SEM/EDS analyses. This chemical inhomogeneity with the traces of a different initial-particle composition also remained after the sintering.

The SB powder was also experimentally compressed and sintered. However, because of its low compressibility observed already in the case of green compacts, at high compaction pressures (at 520–620 MPa only 2.25–2.37 g/cm^3) flaws are formed. The sinterability of the powder is also low; therefore, a low sintering density was obtained together with a high porosity and a significant amount of different defects (**Figure 18**).

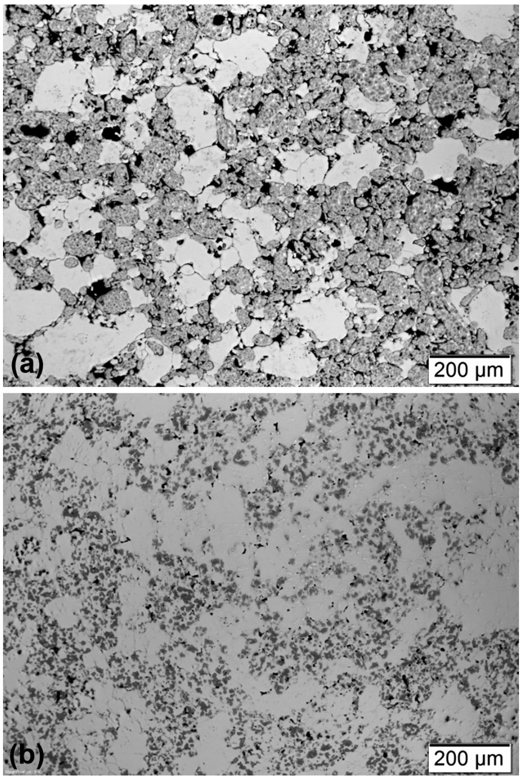

Figure 17: Microstructure of powder *B*: a) after cold compaction and b) after sintering, visible under a light microscope

Slika 17: Mikrostruktura vzorca iz prahu *B*, vidna pod svetlobnim mikroskopom: a) po hladnem stiskanju in b) po sintranju

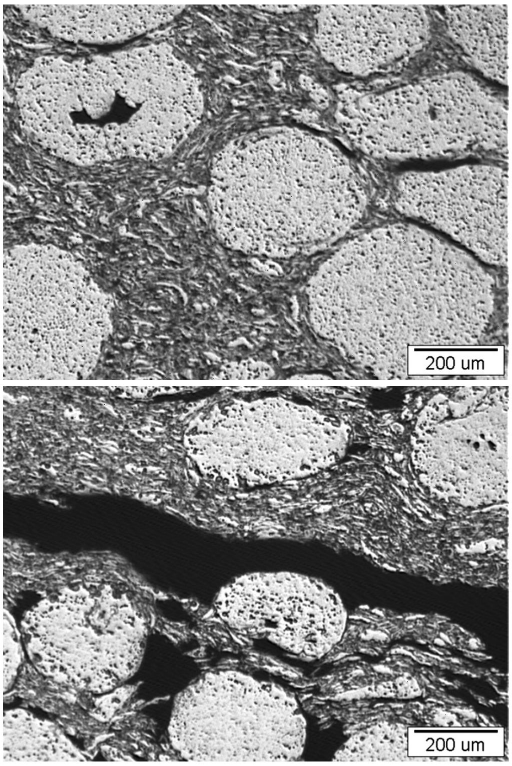

Figure 18: Microstructure of the SB powder after sintering with a well visible, irregular particle morphology and local defects (pores, lunkers and flaws)

Slika 18: Mikrostruktura sintranega SB-prahu, vidna pod svetlobnim mikroskopom z dobro vidno neregularno morfologijo delcev in lokalnimi napakami (pore, lunkerji in plastne razpoke)

Table 7: Results of the compaction and sintering of the tensile-test specimens of commercial Al-based powders (average values)

Tabela 7: Rezultati stiskanja in sintranja epruvet iz preiskovanih Al-prahov (povprečne vrednosti)

Powder designation	Green density	Sintered density	Hardness HB$_{2.5/31.25}$	Tensile strength	Yield strength	Module of elasticity	Elongation at fracture
	g/cm^3			MPa			
Alloy *A*	2.62	2.60	65 (60)	202 (190)	156	3834	2.23 (5)
Alloy *B*	2.52	2.62	104 (100)	239 (200)	219	4399	0.70 (1)
Alloy *C*	2.61	2.73	102 (100)	325 (270)	250	4102	3.90 (5)

Our morphological and microstructural investigations confirmed that the SB powder has an inappropriate chemical and particle morphology. It would have to have more suitable morphological properties in order to be appropriate for the use in conventional ADC and sintering technology. Firstly, the flowability and compressibility of the powder have to be improved. This could be achieved by adding an appropriate amount (approximately 50 % to 60 %) of soft, commercially available, pure Al powder (> 99.8 % of Al) with a suitable particle shape and size distribution. An additional procedure should be a removal of the remaining coarse particles of the sand-blasting media with 180 μm or 250 μm sieves. The sand-blasting media contains relatively large amounts of Fe, Mn and Zn, and sieving would probably significantly decrease the amounts of these elements in the SB powder. However, the correct chemical composition similar to that of the standardized Al-Cu-Si-Mg alloy (for example, type 2××) would still not be attained and additional corrections of the chemical composition would be necessary. In spite of this, the final target composition will be very difficult to obtain completely. Therefore, it seems that SB powder can be more suitable for the production of selected dispersion-strengthening alloys.

6 USE OF SB POWDER FOR DISPERSION STRENGTHENING

SB powder is a relatively good raw material with approximately 86 % to 87 % of Al. But it also contains a significant amount of oxides. Therefore, it seems that SB powder is more usable for the production of Al/Al_2O_3 composites using the modified oxygen-dispersion-strengthening (ODS) technology than for conventional sintering technology. The technology of preparing ODS alloys was started already in the early 1950s by A. V. Zeerlder and R. Irmann.[11,17] As a matter of fact, it was originally developed for the use of the Al scrap containing a lot of metallic oxides. The appropriate powder mixture for the initial sintering (sintered aluminium powder, SAP) was obtained by grinding and milling the scrap and the end result was a semi-final or final extruded or forged composite with the oxide-particle size of 10 μm to 100 μm. However, later a lot of modifications and improvements of the technology were introduced using atomized powders and high-energy reaction ball milling (**Figure 19**). In this way various Al-based composites with a fine micro/nano dispersion of complex oxides, nitrides and borides can be formed, such as Al/Me_xO_y (for example, Al_2O_3), Al/M_xC_y (Al_4C_3, SiC), Al/M_xN_y (BN, TiN, ZrN, TiB_2, etc.) or their combinations. Nowadays, high-quality Fe- and Ni-based ODS superalloys with a fine dispersion of thermally stable oxides (Y_2O_3) or intermetallics are also produced.

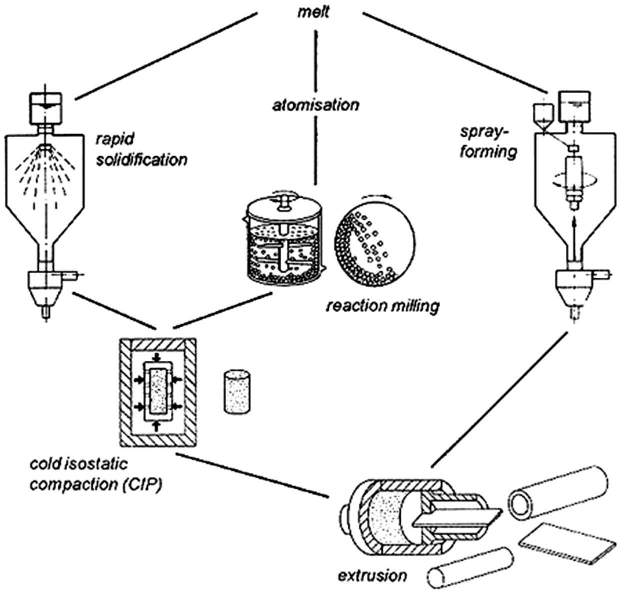

Figure 19: Three different but related P/M technologies for the production of high-strength, thermally stable ODS Al-based alloys[17]
Slika 19: Trije različni, toda sorodni P/M-postopki izdelave visoko trdnih disperzijsko utrjenih Al-zlitin[17]

In our case, to use the SB powder only the last steps (high-energy reaction ball milling, CIP and warm/hot extrusion) given in **Figure 19** could be used and some additional steps (initial sieving of the powder, pre-sintering of CIP preforms) would have to be introduced. Fine Al powders are very reactive and very dangerous with respect to self-ignition and explosion, therefore, a highly inert protective atmosphere has to be used.[18] A modification of this procedure would also be useful for the production of Al foams introducing the foaming reagents such as TiH_2 or $CaCO_3$.[19] This process is very complex, but it generally gives an excellent microstructure with good mechanical properties and a thermal stability of the material. However, a lot of technical and market-related questions remain to be solved in the frame of a new project introducing this technology using SB powder.

7 CONCLUSIONS

In the frame of our investigations, practical usability of the Al powder formed as a bypass product of the sand blasting of slugs and discs was analysed. The so-called SB powder was compared with commercially available Al-based powders used for conventional sintering technology. Our theoretical thermodynamic analyses as well as morphological and microstructural investigations have shown that the investigated Al powder has inappropriate chemical and particle morphologies for conventional sintering technology. It seems that it is a much more suitable raw material for the production of Al/Al_2O_3 composites using modified ODS technology. This still has to be confirmed in the frame of a new, additional experimental research.

Acknowledgement

Authors wish to thank to the Slovenian Research Agency for the financial support in the frame of the project No. L2-4283, as well as the powder producer of Ecka Granules, Germany, and the Unior Forging Industry, Zreče, for their assistance with the experiments.

8 REFERENCES

[1] R. M. German, Powder Metallurgy Science, Metal Powder Industries Federation (MPIF), 1st and 2nd edition, Princeton, New Jersey 1984, 1994

[2] M. J. F. Gándara, Aluminium, The metal of choice, Mater. Tehnol., 47 (**2013**) 3, 261–265

[3] P. Lichý, M. Cagala, J. Beňo, Investigation of the thermomechanical properties and microstructure of special magnesium alloys, Mater. Tehnol., 47 (**2013**) 4, 503–506

[4] Indiamart, web pages: http://sourcing.indiamart.com/engineering/articles/aluminum-gears/) and http://dir.indiamart.com/cgi/catprd-search.mp?ss=aluminium+gears

[5] Aluminium Powder Metallurgy, web page: http://www.aluminum.org/Content/NavigationMenu-/The-Industry/PowderandPaste/PowderMetallurgy.PDF, Al Association Inc.

[6] Powder Metallurgy of Al and Al alloys, Powder Metal Technologies and Applications, Vol. 7, ASM Handbooks

[7] B. Šuštaršič, J. Medved, S. Glodež, M. Šori, A. Korošec, DSC/TG of Al-based Alloyed Powders for P/M Applications, Presentation at 21st international conference on Materials and Technology, Portorož, Slovenia, 2013

[8] Talum, Factory of Aluminium, Kidričevo, Slovenia, web page: http://www.talum.si/en/slugs

[9] B. Šuštaršič, I. Paulin, M. Godec, S. Glodež, M. Šori, J. Flašker, A. Korošec, Morphological and microstructural features of Al-based powders appropriate for P/M applications, University of Maribor, Slovenian Research Agency, project L2-4283 (2012–2014), phase report (in Slovenian language) and oral presentation at 21st international conference on Materials and Technology, Portorož, Slovenia, 2013

[10] ECKA Granules, web page: http://www.ecka-granules.com/en/ecka-granules/products/

[11] E. A. Brandes, G. B. Brook, Smithells Metals Reference Book, 7th edition, Butterworth Heinemann, Oxford, UK 1992

[12] ASM Alloy Phase Diagram Database, P. Villars, editor-in-chief, H. Okamoto and K. Cenzual, section editors, ASM International, Materials Park, OH, 44073, USA, 2006–2013

[13] U. R. Kattner, Thermodynamic Modeling of Multicomponent Phase Equilibria, JOM, 49 (**1997**) 12, 14–19

[14] J. F. Chinella, Z. Guo, Computational Thermodynamics Characterization of 7075, 7039, and 7020 Aluminum Alloys Using JMatPro, ARL-TR-5660, USA, 2011

[15] Thermocalc, web page: http://www.thermocalc.com/, software package for thermodynamic calculations

[16] Metal Powder Industries Federation, web page: http://www.mpif.org/

[17] Powder Metallurgy CD, Materials Processes and Applications, Leonardo project, EPMA Education Working Group, 2001

[18] General Safety Recommendations for storage and handling of Al powder and pastes, http://www.aluminum.org/Content/NavigationMenu/TheIndustry/PowderandPaste/TR2_2006.pdf

[19] I. Paulin, Synthesis and characterisation of Al foams, Ph. D. thesis, Ljubljana, 2011